FUNCTIONALIZATION AND INVESTIGATION OF NANODIAMONDS FOR BIOMEDICAL AND SENSOR APPLICATIONS

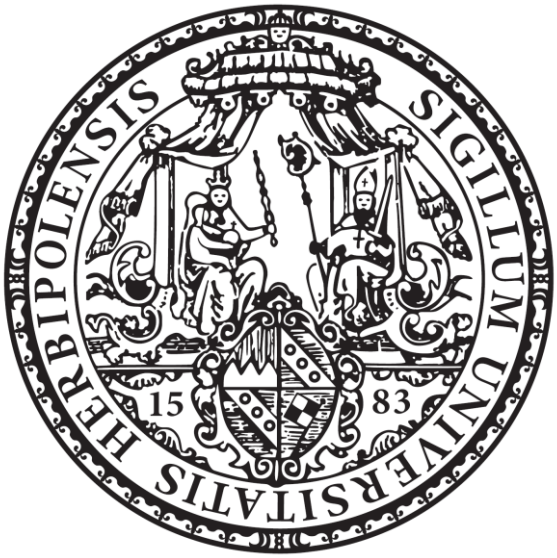

Dissertation zur Erlangung des naturwissenschaftlichen Doktorgrades
der Julius-Maximilians-Universität Würzburg

vorgelegt von

Viktor Merz
aus Schortandy/Zelinograd, Kasachstan

Würzburg 2021

Eingereicht bei der Fakultät für Chemie und Pharmazie am

_____

Gutachter der schriftlichen Arbeit

1. Gutachterin: Prof. Dr. Anke Krueger

2. Gutachterin: Jun.-Prof. Dr. Ann-Christin Pöppler

Prüfer des öffentlichen Promotionskolloquiums

1. Prüferin: Prof. Dr. Anke Krueger

2. Prüferin: Jun.-Prof. Dr. Ann-Christin Pöppler

3. _____

Datum des öffentlichen Promotionskolloquiums

_____

Doktorurkunde ausgehändigt am

_____

Für meine Familie

Woof woof, woff, awooooo!

- Loki

Die Experimente zur vorliegenden Arbeit wurden in der Zeit von November 2015 bis Februar 2021 am Institut für Organische Chemie der Julius-Maximilians-Universität Würzburg unter der Aufsicht von Prof. Dr. Anke Krueger durchgeführt.

Danksagung

Zunächst einmal möchte ich mich bei Frau **Prof. Dr. Anke Krüger** bedanken, dass sie sich getraut hat, die Katze im Sack zu kaufen, indem sie einen frechen Paderborner in ihren AK gelassen hat. Ich weiß nicht, ob es ehrlich wäre sich für die Wahl des Themas zu danken, wenn man bedenkt, wie viele schlaflose Nächte ich deswegen hatte. Ganz zu schweigen von dem Sprint, den wir vor der Deadline der Publikation hatten. Ohne Sie hätte ich die Arbeit sicherlich nie abgeschlossen! Wofür ich mich aber auf jeden Fall bedanken möchte, ist die Freiheit, die mir gegeben wurde, alles ausprobieren zu dürfen (fast alles, Explosionen – oder wie wir es seit dem OC-Brand nennen: "Verpuffung" – sind in Würzburg nicht erwünscht, naja wahrlich sind die nirgendwo erwünscht…) und sogar einen fast absurden Themenwechsel von der biomedizinischen Schiene zur Wasseranalytik vorzunehmen, bei dem ich immer voll unterstützt wurde. Alles in Allem bleiben nur zwei Sachen zu sagen: "Danke Anke und Danke Anke 2(!)“.

Also, I would like to thank **Prof. Dr. Dr. h. c. Todd B. Marder**. From the first moment I was welcomed into the "Marder Family" and have been involved ever since. Thank you also to your wife **Anne** who took care of all the house parties and all the delicious food. Thank you that we could always talk freely about everything and that I was allowed to do so many measurements with Julia and in the end a lot of useful things came out of it.

Ich möchte **Jun.-Prof. Dr. Ann-Christin Pöppler** danken für die vielen gemeinsamen Grillfeiern mit unseren AKs und für die NMR-Messungen. Aktuell möchte ich Dir danken, dass Du die Begutachtung meiner Arbeit angenommen hast und meine Prüferin bist.

Aber auch bei den fleißigen Bienchen im Haus möchte ich mich bedanken. Insbesondere bei den **Reinigungskräften**, die sich nie aufgeregt haben, wenn man mal wieder mit dem restlichen fl. Stickstoff alle Staubbälle unter den Schränken hervorgeholt hat und sie mit herumliegenden Spielkarten verziert auf dem Boden liegen lassen hat. **Jonathan Landeck** möchte für die Bevorzugung meiner Apparaturen danken, die manchmal binnen eines Tages fertig waren, obwohl die Warteschlage für die nächsten Wochen voll war. **Michael Ramold** und **Frank Förtsch** danke ich für die vielen Reparaturen und Hilfestellungen im Labor. **Dipl. Ing. Bernd Brunner** könnte ich für die unschlagbar schnelle und immer erfolgreiche Hilfe danken, aber

viel mehr möchte ich mich für den trockenen Humor und die Lässigkeit bedanken, die Sie immer in die Konversation gebracht haben. **Markus Braun**, ich weiß gar nicht wie oft ich Dich wegen diverser Angelegenheiten angerufen habe, danke, dass Du Dir immer die Zeit genommen hast! Der Verwaltung, **Eleonore Klaus**, **Christiana Toussaint**, **Anette Krug** und **Dr. Christian Stadler** möchte ich danken, dass ich euch immer Sachen in die Hand gedrückt habe und mich drauf verlassen konnte, dass es erledigt wird.

Ein großer Dank gilt auch meiner „OP2-Crew“ **Katrin Schreiber**, **Dr. Alfons Ledermann**, **Dr. Rolf Janiak**, **Christian Possiel**, **Dr. Christian Steinmetzger**, **Sebastian Endres** und den anderen wechselnden Assistenten. Der Spaßfaktor und die Toleranz gegenüber Schabernack waren nie so groß und wichtig, wie in den sechs Wochen Praktikum jedes Semesters, dass wir begleitet haben. Ich glaube ohne euch wäre ich nicht nur aufgeschmissen im Praktikum gewesen, sondern auch ziemlich ungern wieder reingegangen.

Viele große Dinge hätten jedoch im Labor nicht stattgefunden ohne die Hilfe meiner großartigen Freunde im Labor. Mein Arbeitskreis war mir stets eine Stütze. Manchmal brauchte man jemanden der einem zeigt was man falsch macht, manchmal braucht man wen, der über ein zerbrochenes Glas mit einem lacht oder weint. Fast alle Jahre meine Promotion durfte ich mir den Abzug mit **Dr. Benjamin Kiendl** teilen. Dir verdanke ich wahrscheinlich nicht nur die meisten Ratschläge, sondern auch die schlechtesten Witze und Memes, die man im Netz finden kann. Wenn ich nochmal einen Laborpartner wählen dürfte, dann könnte es kein anderer sein. Aber auch den anderen „alten“ Doktoranden, wie **Andreas Mutza**, **Dr. Peter Buschmann**, **Dr. Rachel Buschmann**, **Dr. Sarah Schweeberg**, **Dr. Steffen Heyer** und **Dr. Stefan Wachtler** möchte ich für mein warmes Willkommen im AK Krüger bedanken. All die Tipps für verschiedenen Eigenheiten der Geräte, viele Handgriffe und Verhandlungsgeschick mit den Festangestellten habe ich von euch gelernt und hoffentlich auch an die neue Generation weitergegeben. Die Zwangskaffeepause von Sarah habe ich definitiv weitergegeben und hoffe dort werden immer noch so wertvolle Informationen über Gott und die Welt ausgetauscht, wie bei uns, **Sarah**. **Steffen**, manchmal kann ich immer noch deine extrem laute Lache in den Wänden der OC hören, ich hoffe das ändert sich nie, danke dafür. **Stefan**, ich weiß gar nicht wofür ich mich bei dir alles bedanken müsste. Am wichtigsten waren eigentlich immer die albernen Momente zusammen, als wir die Zentrifuge mit einem 5-m-Seil laufend durch das

Labor resettet haben, oder wie wir an der TGA verzweifelt sind. Aber auch die ganzen Geschichten und Legenden über die OC und die besonderen Gestalten darin, werde ich nie vergessen.

Bei dem „AK-Krüger: The next generation“: **Sinem Toksabay**, **Lena Roos**, **Julia Puck**, **Dr. Sara Ranjbar**, **Thomas Hertle**, **Christina Bauer**, **Johannes Ackermann** und **Sebastian Vettermann** möchte ich mich natürlich auch ganz herzlich bedanken. Meine morgendlichen Kaffeepausen-Truppe, **Sinem**, **Lena** und **Julia** möchte ich für den schönen Start in den Tag danken. **Sinem**, Dir bin ich dankbar für all die nützlichen türkischen Wörter, die Du mir beigebracht hast, auch wenn ich sie im realen Leben wohl nicht verwenden kann, weil keiner unseren Humor versteht. **Lena**, danke, dass ich bei Dir auf der Heizung immer mein Leid bekunden konnte, ohne immer dafür ausgelacht zu werden (haha). **Julia**, was würde ich bloß ohne deine lustigen Geschichten aus dem Labor machen. Ich erinnere mich noch wie Du das Praktikum bei mir gemacht hast und ich bin so glücklich, dass Du im AK geblieben bist.

Thomas, Dir möchte ich für die deine Fairness und Hand-On-Mentalität danken. Das klingt nach all den Bewerbungen/Stellenausschreibungen sehr abgedroschen, aber wenn es auf einen zutrifft, dann auf Dich! An **Christian** geht ein besonderer Dank. Du hast mir gezeigt, und das auf deine spezielle unverblümte und doch etwas schüchterne, aber gleichzeitig durchdachte Art und Weise, dass es keine dummen Fragen gibt. Ich bin Dir sehr dankbar, dass Du alles verstehen und hinterfragen möchtest. Wie oft hast Du mir damit die Augen für ein bisher nicht wahrgenommenes Problem geöffnet. **Johannes** möchte ich herzlich für all seine Ratschläge und lustige Anekdoten danken, aber ganz besonders für die SEM-Messungen, die mir den verlängerten Rücken bei der Revision-Deadline gerettet haben. **Basti**, es gab keinen Abend, an dem man nicht mit Dir für eine LAN-Runde rechnen konnte. Es war immer wieder schön die gebrochene Säule, das heruntergefallene Produkt, die fehlerhafte Messung oder die kaputte TGA bei einem Bier am Abend zu vergessen oder das endlich perfekt saubere Produkt, die reparierte TGA oder super Messung zu feiern. Danke euch allen für die viele Unterstützung!

Allgemein geht ein großer Dank an das zweite Stockwerk (**AK Seibel** und **AK Lambert**) für den Chemikalienaustausch, wenn die Chemobar schon zu hatte, den vielen Spaß mit den kleinen Gärten, Kartenschlachten, Eppi-Bomben und nicht zu vergessen der Duplo-Abzocke alias Einwohnerzahl-„Ratespiel“ in der Küche. Aber auch für die vielen Pizza-Abende, spontane

Spieleabende oder allgemein Feiern möchte ich mich bedanken. Besonders möchte ich mich bei **Jürgen Mut** bedanken, der nicht nur auf Loki aufgepasst hat, sondern auch immer für ein Gespräch über dem neuen Manga zu haben war. Für die kurzfristigen Biomessungen und die Co-Autorschaft möchte ich mich noch beim Herrn **Prof. Dr. Jürgen Seibel** und bei **Dr. Maria E. Ortiz-Soto** bedanken. **Michael Moos**, die gute Fee des Stockwerks, möchte ich für die ganzen Hilfestellungen und Vermittlungen zu anderen Leuten, die sich mit irgendwas auskennen danken. Ich danke Dir, dass Du immer Zeit für einen genommen hast und nie eine Erklärung abgekürzt hast, um schneller fertig zu sein. Außerdem möchte ich mich für die Fluoreszenzmessungen im AK Lambert bei **Arthur Turkin** und **David Mims** bedanken, die immer Zeit hatten mir alles zu erklären und mit mir über meine Fehler zu lachen.

Zum Schluss möchte ich meinen Bacheloranden und Austauschstudenten danken. **Yvonne Vonhausen** möchte ich für ihre unglaubliche Organisation im Labor danken, Du hast meine Arbeitserwartungen um einiges übertroffen und hast immer mit einem Lächeln auf dem Gesicht dich für neue Aufgaben begeistern können. **Maximilian Kirchner** Dir möchte ich danken, dass Du mir so viele Sachen beigebracht hast. Zum Beispiel, dass ein Produkt erst im zerbrochenen Kolben auf dem Boden gewesen sein muss, um damit weiter arbeiten zu können. Trotzdem warst Du nie aufgebracht oder hast aufgegeben. Es gab keinen Tag, an dem ich nicht erstaunt war, wie das Du das alles meisterst. Ich bin froh, dass **Julian Lenhart** mein Azubi war. Ich habe Dir nicht nur zahlreiche Synthesen und Untersuchungen für meine Paper zu verdanken, sondern auch eine besondere Freundschaft. Zuletzt möchte ich **Harsh Dongre** danken, weil Du mit so viel Leichtigkeit an die organische Synthese gegangen bist, dass es mich gefreut hat dich bei der Arbeit zu begleiten. Nie habe ich jemanden so schnell in ein fremdes Thema einarbeiten sehen.

Meinen Geschwistern, **Andreas**, **Lena**, **Eduard und Valentina**, die nie aufgehört haben zu fragen, wann ich denn endlich fertig bin, möchte ich für die gemeinsamen Feiern und Treffen danken, die mich stets auf den Boden der Tatsachen zurückgeholt haben, und mich begreifen ließen, dass Uni nicht immer alles im Leben ist.

Meiner Mutter, **Katharina**, die stets an mich geglaubt hat, mich unterstützt und sich immer darum gekümmert hat, dass genug Marmelade im Vorratsschrank war, und wenn nicht, mich

stets mit frisch gepflückten Beeren und anderen Gartenerträgen nach Hause gelockt hat möchte ich für Ihre Liebe und Fürsorglichkeit danken.

Loki, mein großer Bär, Dir möchte ich ganz besonders danken, auch wenn du das nie lesen wirst. Du bringst so viel Freude in mein Leben und lehrst mich jeden Tag wie wundervoll die kleinen Dinge des Lebens sind. Außerdem wüsste ich nicht wie fett ich schon wäre, wenn wir nicht jeden Tag zusammen bei unseren Spaziergängen die Gegend unsicher machen würden. Danke, dass Du immer tapfer im Flur gewartet hast, bis ich meine Arbeit fertig hatte und allen Vorbeigehenden den Tag versüßt hast.

Meiner besten Freundin, Reisepartnerin, Co-Autorin, Weggefährtin und Ehefrau, **Dr. Julia Merz**, gilt unbestritten der größte Dank. Von der ersten Vorlesung in Paderborn, über die Bachelorarbeit in Shanghai und zur Doktorarbeit in Würzburg (und jetzt den neuen Stellen in Antwerpen) hältst Du mich immer noch aus. Zusammen haben wir so viele Abenteuer bestritten und zusammen werden wir noch mehr Abendteuer bestreiten. Mit Dir an meiner Seite fühle ich mich geborgen und unbesiegbar.

Liste der Publikationen

Teile dieser Dissertation wurde bereits in Fachjournalen publiziert und werden in der folgenden teilkumulativen Arbeit, mit der Genehmigung von Wiley-VCH, wiedergegeben und in der Zusammenfassung übersetzt.

Publikation
Viktor Merz, Julian Lenhart, Yvonne Vonhausen, Maria E. Ortiz Soto, Juergen Seibel, Anke Krueger, Zwitterion-Functionalized Detonation Nanodiamond with Superior Protein Repulsion and Colloidal Stability in Physiological Media. ***Small*** 2019, 1901551. **https://doi.org/10.1002/smll.201901551**
Viktor Merz, Julia Merz, Maximilian Kirchner, Julian Lenhart, Todd B. Marder, Anke Krueger, Pyrene-Based "Turn-Off" Probe with Broad Detection Range for Cu^{2+}, Pb^{2+} and Hg^{2+} Ions. ***Chem. Eur. J.*** 2021, *27*, 8118–8126. **https://doi.org/10.1002/chem.202100594, Cover Bild: https://doi.org/10.1002/chem.202101582**

List of Abbreviations

4-DMAP	*N*,*N*-Dimethylpyridin-4-amine
ASAP	atmospheric solids analysis probe
ATR	attenuated total reflection
BH	Benesi-Hildebrand
CV	cyclic voltammetry
CVD	chemical vapor deposition
DBCO	diarylcyclooctyne
DCC	*N,N'*-dicyclohexylcarbodiimide
DCM	dichlormethane
DD-water	double distilled water
DLS	dynamic light scattering
DMEM	Eagle's Minimal Essential Medium
DND	detonation nanodiamond
DOX	doxorubicin hydrochloride
DRIFTS	Diffuse reflectance infrared spectra
$D_v(XX)$	hydrodynamic diameter (volume) of the smalles XX % particles
EDTA	ethylenediamine tetraacetic acid
ESI	electrospray ionization
FBS	fetal bovine serum
fND	fluorescent nanodiamonds
FRET	Förster resonance energy transfer
FT-IR	Fourier-transform infrared spectroscopy
HG	head group
HOMO	highest occupied molecular orbital
HPHT	high-pressure-high-temperature
HRMS	high-resolution mass spectrometry
IRF	instrument response function
K_a	binding constant
K_{SV}	Stern-Volmer constant

LLOQ	lower limit auf quantification
LOD	limit of detection
LUMO	lowest unoccupied molecular orbital
MALDI	matrix assisted laser desorption/ionization
MeCN	acetonitrile
ND	nanodiamond
NHS	*N*-hydroxysuccinimide
NIR	near infrared
NMR	nuclear magnetic resonance
NV	nitrogen vacancy
PAH	polycyclic aromatic hydrocarbon
PBS	phosphate buffered saline
PEG	polyethylene glycol
ppm	parts per million
r.t.	room temperature
RPM	rounds per minute
SiV	silicon vacancy
SR	super resolution
STED	stimulated emission depletion
STORM	stochastic optical reconstruction microscopy
TCSPC	time-correlated single-photon counting method
TEG	tetraethylene glycol
TGA	thermogravimetric analysis
THF	tetrahydrofuran
TLC	thin-layer chromatography
TNT	trinitrotoluene
ULOQ	upper limit of quantification
UPCNPs	upconversion nanoparticles
UV	ultraviolet
Vis	visible range of light

Table of Contents

Chapter 1

Introduction and State of Knowledge

1.1 Nanodiamond as a Functional Material

When the detonation synthesis of diamond nanoparticles was discovered in 1960s, probably no one could have imagined the impact it would have on research some 60 years later.[1] Despite the already known promising properties of nanodiamonds (NDs) at that time, it was not until the 1980s that nanodiamond could be produced as a commercially available product on a large scale. Among a variety of different methods, the synthesis strategy by detonation of a mixture of trinitrotoluene (TNT) and hexogen/octogen in an oxygen-free chamber has been established as one of three common methods. At 15 GPa and temperatures of about 3000 K this method produces approximately 2–10 nm detonation nanodiamonds (DND) and also graphitic materials. The two other bottom-up methods are the chemical vapor deposition method (CVD-ND)[2] and the high-pressure-high-temperature method (HPHT-ND), where diamond films with crystal clusters or larger single-crystal diamonds are produced respectively, which are then broken down by milling processes to uniform sizes in the nanometer range.[3,4]

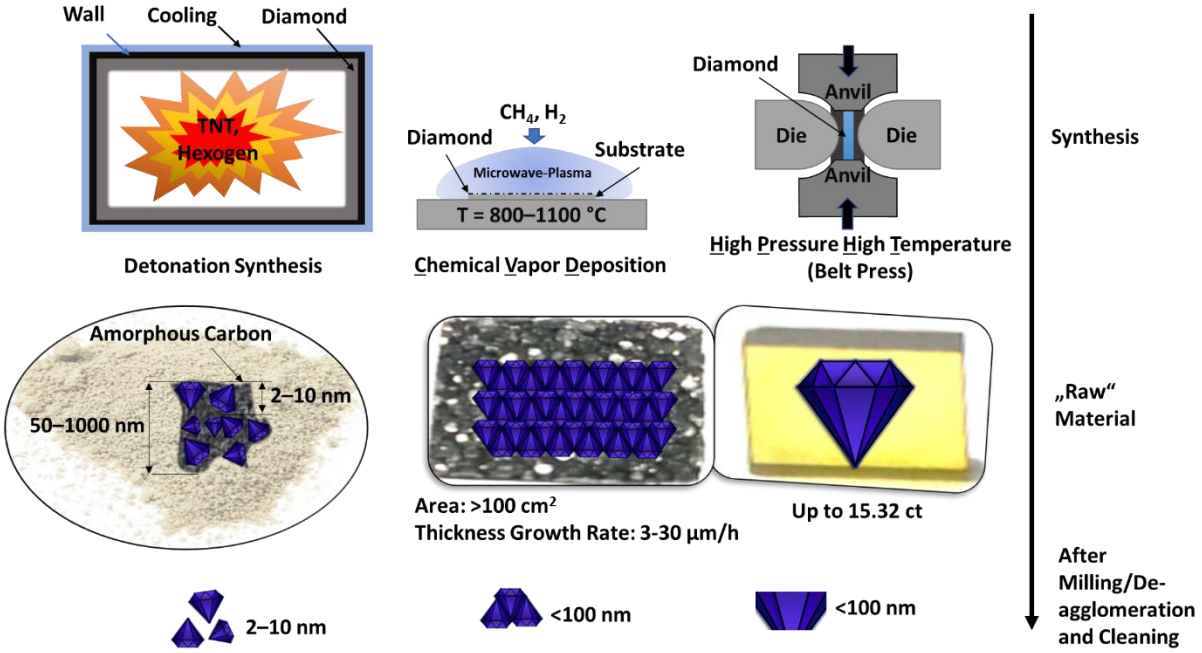

Figure 1-1. Schematic representation of the three established methods (detonation synthesis, CVD and HPHT) for the production of nanodiamond with insets showing the respective raw material.

CVD diamond is usually produced at a pressure between 1 mbar and 100 mbar in a carbonaceous atmosphere with a high hydrogen concentration at substrate temperatures between 800 °C and 1100 °C where thermal or plasma activation of the gas phase is present.[2] During this process, methane (CH_4) is cracked into CH_3 and other carbon species and reacts radically with the surface of the diamond. During the growth process atomic hydrogen in plasma is selectively etching all carbon compounds except diamond, thus suppressing graphite formation and promoting hydrogen termination of the diamond surface. The raw material is a diamond film that can coat areas larger than 100 cm² and can be grown, under suitable condition, with a growth rate of 3–30 µm/h.

HPHT diamonds, on the other side, are produced when graphite is subjected to pressures between 5.5 GPa and 7 GPa and temperatures of 1400 °C to 1800 °C in an anvil press, the so-called belt apparatus, in the presence of a catalyst. The catalysts used are mainly metals of subgroups VI, VII and VIII of the periodic table. The graphitic carbon dissolves in the catalyst, which is liquefied under these conditions, up to the saturation limit. Once this is reached, the carbon precipitates in the form of diamond crystals. The high pressure supports the conversion of delocalized π-bonds into σ-bonds (sp^3 hybridization). Another driving force is the accompanying reduction in volume. Under these conditions, graphite is at the phase boundary witch diamond and dissolves more easily in the liquid catalyst. The catalyst forms a diffusion layer between graphite and diamond and further adds carbon to the diamond crystallite due to the concentration gradient created by the precipitation of diamond-bonded carbon to the still unconverted graphite.[5] The weight of such diamonds can reach up to 15 ct.

Agglomerated DND-raw-particles (diameter: <1000 nm), large CVD-films (~100 cm² an variable thickness) and macroscopic diamonds from HPHT (typically plates of <0.5 cm² and 0.2–1.2 mm thickness) need to broke down to nanoscale by milling.[3,4] After milling the big diamond crystals down to ND, the resulting particles have many unique properties compared to other members of the carbon allotrope family. But they also share many properties with the bulk diamond, such as hardness and thermal conductivity. Additionally, NDs share properties with other nanoparticles because of their size to volume ratio. However, nanodiamond differs from all other nanoparticles due to the diamond crystal structure in its core and the versatile surface group composition.[6–9]

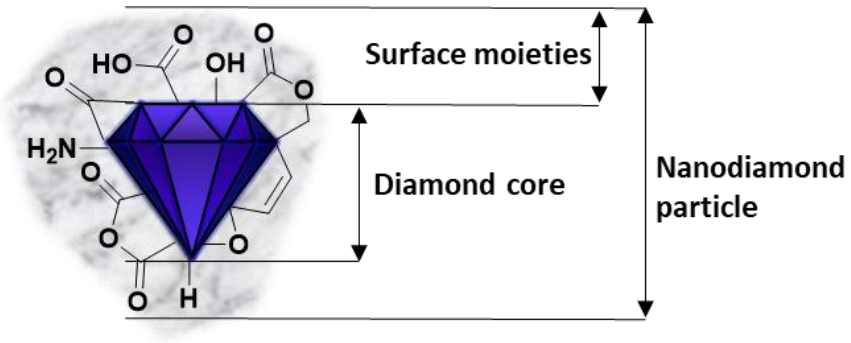

Figure 1-2. Schematic representation of the prominent surface groups of nanodiamond.

On the one hand, uniform surface groups can be generated by the various manufacturing processes and the subsequent purification. On the other hand, surface groups can be manipulated by wet chemical and gas phase modification methods. Furthermore, ND defect structures, such as nitrogen-vacancy or silicon vacancy defect centers (NV/SiV centers), or doping with boron atoms, for example, can induce many optical and electronic properties. By grafting surface groups and manipulating the diamond lattice, ND has a high potential for a wide range of applications in tribology, bioimaging, quantum sensing, drug delivery, tissue engineering, nanocomposite core material and additive for polymers.[3,10]

1.2 Nanodiamond for Biological Applications

Within the carbon nanoparticle family and compared with non-carbon nanoparticles, ND is an excellent candidate for biomedical applications.[11] Due to its largely non-toxic behavior *in vivo*, it can be used for drug delivery, biological imaging and sensing. Especially DND is an easily accessible material for bioapplication. It is cheap, can be produced in big amounts and is small enough (~2–10 nm) to be used as a drug carrier and additive in polymers for tissue engineering, nanocomposites and tribology.[12–15]

Tribology

Tribology is the study of interacting surfaces in motion and finds its application when, for example, hip joints no longer function due to high wear and tear and then need to be replaced with artificial joints. Over time, the friction and wear of these implants often causes inflammation and infection, and they are eventually replaced or removed. To extend life of such

joints, ND is used for additive/composite for metal/polymers/lubricants to adjust friction for joint implant.[16,17,18] By intraarticular injection of nanodiamond particles into the joint not only the resistance against wear and friction was enhanced significantly, but also the lubricant characteristics and antibacterial properties were adjusted.[19]

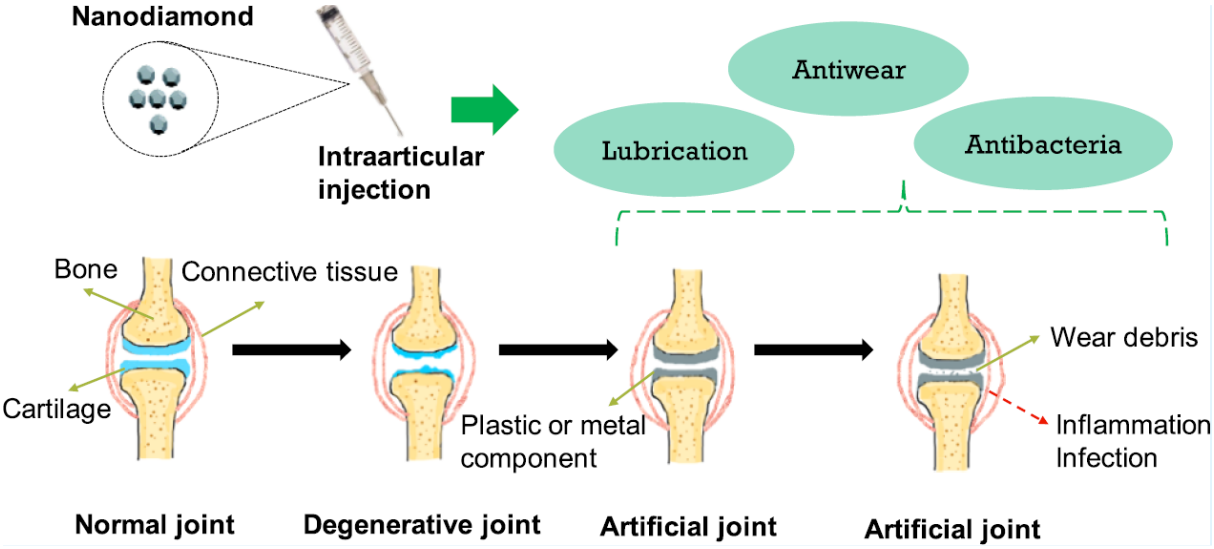

Figure 1-3. Schematic representation of using NDs for wear and frictions adjustment in artificial joints to prevent degeneration of the polymer-on-metal parts to prevent inflammation and infection and adding positive antibacterial and lubricant properties to the surface. Reprinted with permission from A. Shirani, Q. Hu, Y. Su, T. Joy, D. Zhu, D. Berman, *ACS App. Mat. Interfaces* **2019**, *11*, 43500−43508. Copyright (2019) American Chemical Society.[19]

In addition to biological applications, ND, for instance in detonation soot, lubricants such as oil in car engines, allows to reduce friction and wear by polishing the moving parts and removing unevenness. Additionally, due to the lower friction the energy consumption is reduced when used in oil for engines. The tribological properties of NDs (low surface roughness, hard core, ball-bearing effect) make them a promising candidate to reinforce polymers for mechanical adjustment.[18]

Tissue engineering, nanofiller material for nanocomposites and additive in polymers

Tissue engineering is a technique that involves the use of synthetic constructs to restore or improve tissues using the benefits of ND described above. It exploits the biocompatibility of ND to provide together with polymers improved mechanical properties compared to the tissue that is being used so far for replacement.[20] One of the most important subtypes of tissue

engineering is bone tissue engineering. The goal is to induce bone regeneration through the interaction between biomaterials, cells and factor therapy.[21,22]

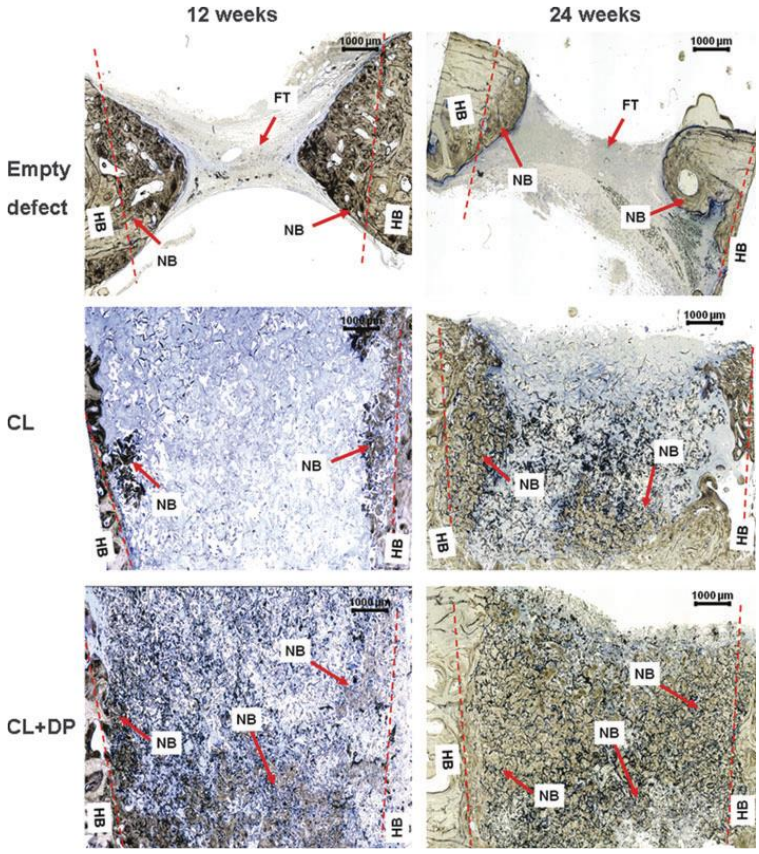

Figure 1-4. Recordings of tissue healing (longitudinal sections stained with Toluidine Blue O) after 12 and 24 weeks of implantation using ε-caprolactone (CL) and CL+diamond particle (CL+DP) for regeneration, whereby the dotted lines separating the host bone (HB) from the new bone (NB) in between new fibrous tissue (FT) is growing. Reprinted from Z. Xing, T. O. Pedersen, X. Wu, Y. Xue, Y. Sun, A. Finne-Wistrand, F. R. Kloss, T. Waag, A. Krueger, D. Steinmüller-Nethl, K. Mustafa, *Tissue. Eng. Part A* **2013**, *19*, 1783, with permission from Mary Ann Liebert, Inc. [22]

Therefore, it is important that the material is not only biocompatible, but also degradable when growing new bone while maintaining a strength comparable to bone throughout. Biopolymers can already function well as bone substitutes, but they are not as strong as bone in terms of mechanical strength.[23] ND can provide a solution here because they add not only mechanical strength but also other assets to the scaffold.[17] For example, 3D-printed selective laser melted titanium surfaces, for bone replacement, can offer two advantages with the help of ND coating. First, ND coatings provide an improved surface for mammalian cell (osteoblast and fibroblast) growth, resulting in an increase in cell density of about 30%, which is important for

osseointegration. Second, this coating provides an 88% reduction in adhesion of *Staphylococcus aureus* colonies, and thus, prevents inflammation.[24] ND functionalized with biomolecules such as cellulose or saccharides has already shown, in addition to pure ND, even higher biocompatibility for growth cells of bones and inhibits adhesion of *E.coli* bacteria.[25] Biopolymers such as poly(lactic-co-glycolic acid) can improve the Young's modulus by 100% and hardness by 550% with the addition of phospholipid-functionalized ND without being toxic, while promoting cell proliferation and osteogenic differentiation.[26] However, the use of otherwise very hydrophobic and thus not necessarily biocompatible polymers can also be improved by the addition of NDs, with NDs excelling in particular as additives or nanofillers to improve other material properties and contribute to their non-toxic interactions.[27] On the other hand, the ND can also be improved by the polymers, e.g., by forming a polymer shell around the ND that can absorb and deliver drugs.[28]

Drug Delivery

In biomedical applications, especially drug delivery, the major concern is the toxicity of the nanomaterials used. A nanomaterial that is non-toxic and biocompatible is essential for long-term clinical use. In the cell types tested, including neuronal, lung, kidney, and cervical cells, NDs show no cytotoxicity, which makes them suitable as drug delivery vehicles in bioapplications.[29,30,31] Furthermore, due to the aforementioned properties, namely the easily functionalizable surface and defect structures for bioimaging, ND is well suited for drug delivery applications.[32] For instance, in the last two decades, novel cancer therapeutics based on NDs were tested.[33,34] Here, the drugs are either covalently bound or adsorbed on the surface of the ND or the ND shell, such as a polymer.[6,20,28,35,36] A number of biomolecules such as DNA, lysozyme, cytochrome c, growth hormones, biotin, alpha-bungarotoxin, insulin and doxorubicin and several more have already been adsorbed in studies and some have been successfully desorbed under physiological conditions.[33] In one of the pioneer studies, a chemotherapy drug called doxorubicin hydrochloride (DOX) was adsorbed onto a DND surface and introduced into murine macrophages and colorectal cancer cells using the DNDs as carriers. Reversible desorption was regulated by the concentration of chloride ions.[37] However, in recent studies, the release of the drug release is regulated by pH. The surrounding pH of an ordinary cell is 7.2–7.4, while cancer cells often exhibit lower pH of 6.2–7.0. Entering the cell,

the pH of endosomes and lysosomes of a cancer cell is 4–6. If the drug carrier comes close or enters a cancer cell, this circumstance can be exploited to cleave pH-labile bonds and force a release of the drug.[38] This gives enormous advantages over the conventional way of administering the drug: On the one hand, due to long circulation times of the nanoparticles, the drug can be kept in the bloodstream until it encounters a cancer cell and then releases the drug.[39] On the other hand, there are far fewer side effects because the drug affects intact cells to a much lower extent. In addition, the dosage of the drug can be kept lower if the drug is mainly consumed by cancer cell instead of all cells.[40] In the example shown in Figure 5, it is evident that the side effects of DOX cause the mice to lose about 20 % weight after 24 days. In contrast, when DOX is administered to cancer cells in a controlled manner by conjugation to ND, the weight does not decrease with respect to the reference weight of the mouse that received only PBS. At the same time, tumor growth has been attenuated twice as well as with DOX. Additionally to that, Wang *et al.* found that the survival rate of ND-DOX treated mice was four times longer than of the mice treated with free DOX.[41]

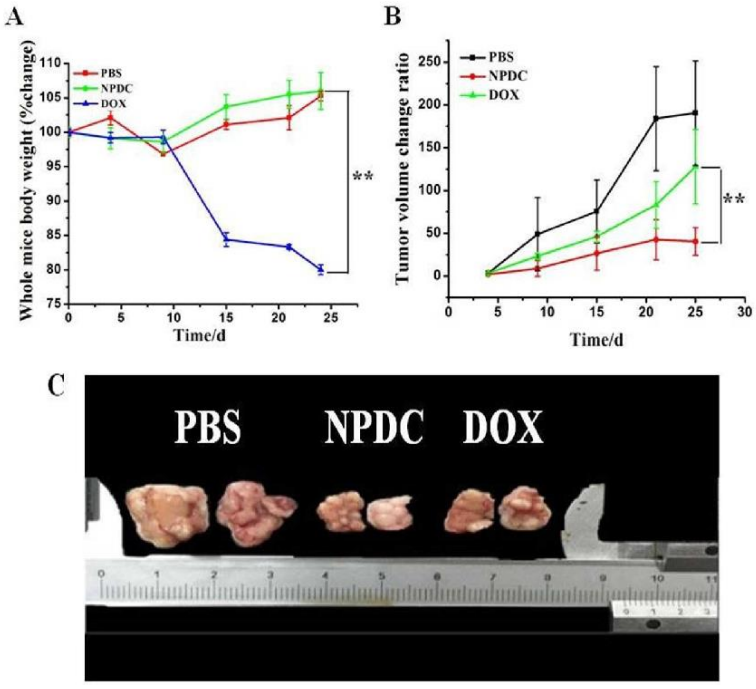

Figure 1-5. *In vivo* experimental results with ND-DOX-conjugate (NPDC) and DOX, in which phosphate-buffered saline (PBS) was used as a control. A) Average whole mice weight intravenous injections every 5 days. B) Average tumor volume change. C) Representative images of tumors from treated mice after 25 days. Reprinted in part from L. Li, L. Tian, Y. Wang, W. Zhao, F. Cheng, Y. Li, B. Yang, *J. Mater. Chem. B* **2016**, *4*, 5046, with permission from Royal Society of Chemistry.[38]

ND functionalized with polyethylene glycol (PEG) or polyglycerol and in which DOX is adsorbed/conjugated has already demonstrated high efficiency. Recent studies refine the interaction of ND surface, polymer and the release of active material.[37,38,42] Both, the ND and the ND-DOX, are not toxic to kidney, liver and spleen, while free DOX is toxic to kidney and liver.[41] In addition, due to their nature and size, NDs can cross the brain blood barrier and thus provide drug transport to the brain as well as interfere with the central nervous system.[43,44,45] Due to the high density of functional groups on the surface, especially in the case of detonation NDs, there is an enormous adsorption and desorption potential. As a result, NDs were already added to skin creams for skin care, skin cancer treatment and wound healing, among others.[46] However, the diversity of the ND functional groups seems to be crucial for adsorption. If the surface is homogenized, this may have a negative effect on the amount of drug adsorbed (but is positive in case of covalently bound drugs), as in the case of the attempt to use ND as HIV drug carriers.[47] Extending this, fluorescent nanodiamonds (fNDs) can be used to better track the proliferation of NDs and help to understand drug delivery mechanism.[44,45] Through fND, bioimaging can be achieved simultaneously to the drug delivery process, which can serve as a marker with the help of targeting molecules at the fND.[48]

Bioimaging and Quantum Sensing

In therapy and diagnostics (theranostics), fNDs , mainly with nitrogen vacancies (NV) defects, not only have the function to characterize of the stage of the disease, but they can also perform a therapeutic function. A major obstacle here is the absorption of excitation light and fluorescence signals by biomolecules, cells, tissues or organisms and body fluids. To avoid these interferences and autofluorescence of, for instance melanin, elastin, collagen, keratin, porphyrins and flavins, two regions in the near infrared (NIR) range have been identified that provide minimal or no interference. Detection in the short wavelength visible range (VIS) of around 400–700 nm can result in imaging problems caused by the compounds mentioned above. In order to avoid that hemoglobin and water are the main light absorbers, the 650–950 nm range (NIR I) was chosen as both compounds possess very low extinction coefficients in this region. In addition, in the NIR I range the light can penetrate tissue and the cell membrane and thus deep tissue imaging can be achieved. The NIR II range is located at 1000–1700 nm wavelength and can provide good imaging results in up to 1 cm of tissue.

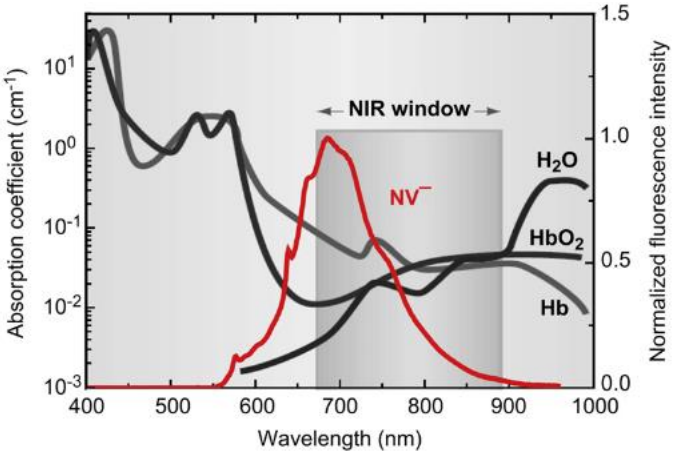

Figure 1-6. UV/Vis (black/grey curve) of hemoglobin and water and fluorescence spectra of fND with $[NV]^-$ center (red curve) with the respective NIR I window. Reprinted from V. Vaijayanthimala, P.-Y. Cheng, S.-H. Yeh, K.-K. Liu, C.-H. Hsiao, J.-I Chao, H.-C. Chang, *Biomaterials* **2012**, *33*, 7794, with permission from Elsevier.[49]

As a result of this wavelength limitation, fND for application in bioimaging need to be optimized for this to obtain meaningful results.[35,50–52] Bioimaging enables studies of organisms, at cellular and tissue level, and provides valuable information about biological processes. Nanodiamonds have been established as a contrast agent for magnetic resonance and photoacoustic imaging and as a probe for fluorescence imaging.[53] Diamond can incorporate a variety of optically and magnetically active defects in its sp^3 matrix, which are suitable for bioimaging applications. Using defect structures, diamond particles with NV-centers can be used as fNDs for photostable labeling and nanoscale sensing in living cells and organisms. Thus, green fNDs can be used for super-resolution (SR) microscopy, such as stimulated emission depletion (STED) imaging[54] and stochastic optical reconstruction microscopy (STORM).[52,55] Because of its ability to produce targeted, multispectral contrast of specific analytes over various length scales, fluorescence microscopy is an indispensable tool in biological research.[52,56] Current fluorescent labels that find application in microscopy consist mainly of small molecules, dyes, as well as larger particles that may include hybrid structures, such as polymers loaded with organic dyes, as well as other materials that are intrinsically fluorescent by various mechanisms. ND offers a new technique for bioimaging. The emission of NV and SiV centers in fNDs is located in the region of NIR I. To generate the quality and purity of fNDs with certain defect centers, HPHT-ND are mainly used for the fabrication of such fNDs. The only disadvantage of NV centers is that their excitation wavelength is 510–

560 nm, which leads to absorption of light by biomolecules and can attack tissue or lead to self-interference. One solution to this can be binding of the fND to photon upconversion nanoparticles (UCNPs), like NaYF4:Yb,Er, which excite the NV centers of the ND in the NIR-I range.[31]

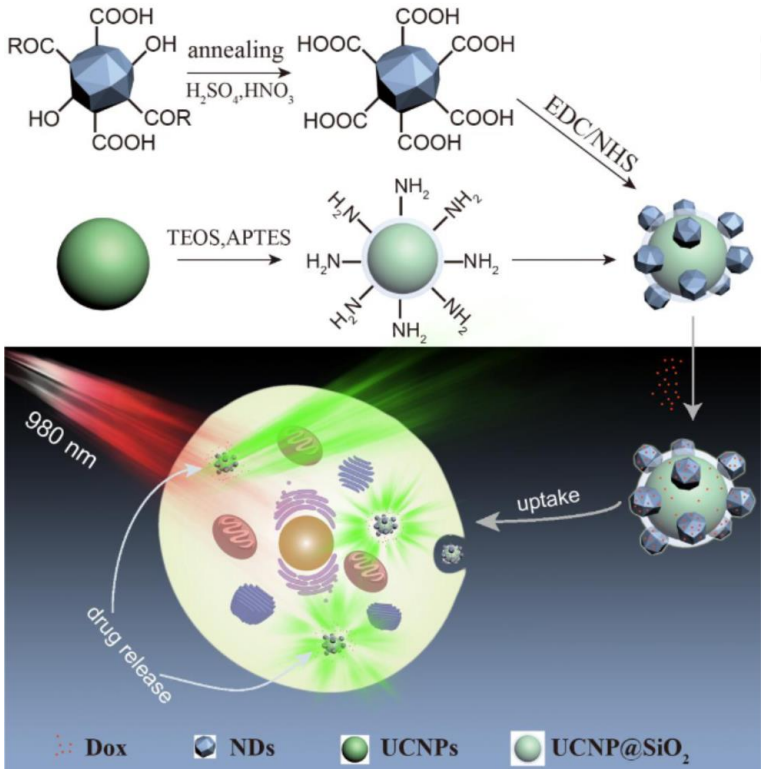

Figure 1-7. NDs on a core-shell photon upconversion nanoparticle (UCNP) @ SiO_2 with adsorbed DOX on the surface for drug delivery experiments in HeLa cells. Reprinted from K. Zhang, Q. Z. S. Qin, Y. Fu, R. Liu, J. Zhi, C. Shan, *J. Colloid Interface Sci.* 2019, *537*, 316 with permission from Elsevier.[31]

However, if the NV-center based systems cannot be modified to be able to use the needed wavelengths, then one can resort to other defect structures such as H3,[57] N3,[58] Eu-V[59] or Si-V,[60] or even bind dyes to NDs that do not have defect structures.[61]

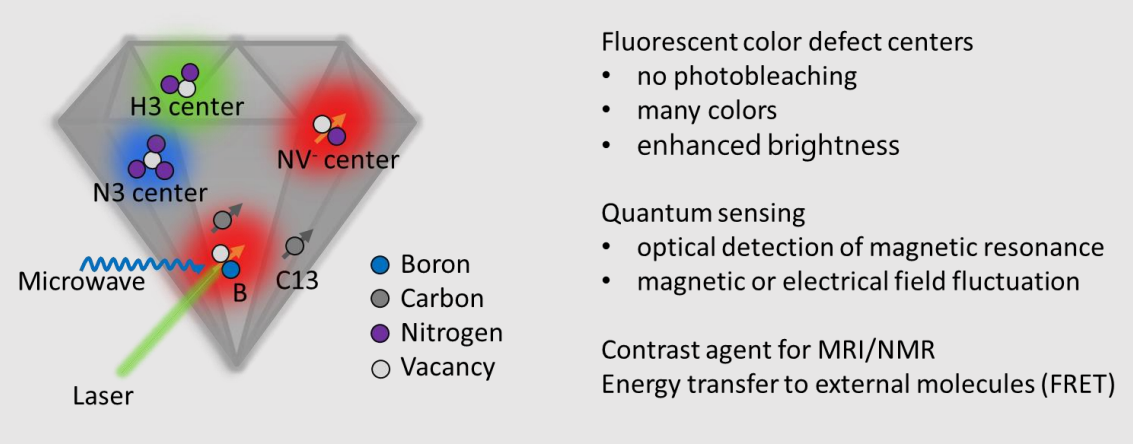

Figure 1-8. Schematic illustration of prominent defect centers, such as H3, N3, NV^-, C13, B, for bio-imaging and bio-sensing application with NDs. Figure is adapted from M. D. Torelli, N. A. Nunn, O. A. Shenderova, *Small* **2019**, 902151 with permission to reprint from John Wiley and Sons.[52]

A method that has so far only rarely found its way into bioimaging is the measurement in the NIR-II range using Raman spectroscopy of HTHP-NDs. While cells show significant signals at 2800–3200 cm^{-1} in the Raman spectrum, large HPHT-fNDs exhibit a significant peak at 1332 cm^{-1}.[62] In addition to the versatile properties of fND in imaging, the defect structures can additionally be used for sensing.[52] Through the influence of magnetic fields, the optical output of the $[NV]^-$-centers can be changed. Thus, among other things, the magnetic or electrical fluctuation in cells can be detected as well as their temperature or temperature change making fND favored for bioimaging and quantum sensing applications.[63–66]

A recent milestone in the production of fNDs is related to an expansion of multicolor capability.[67] The recently developed method of rapid thermal annealing briefly exposes irradiated synthetic diamond powder to elevated temperatures, opening up new possibilities for the controlled production of particles containing H3 and N3 centers and thus, expanding the range of different colors of fNDs.[58]

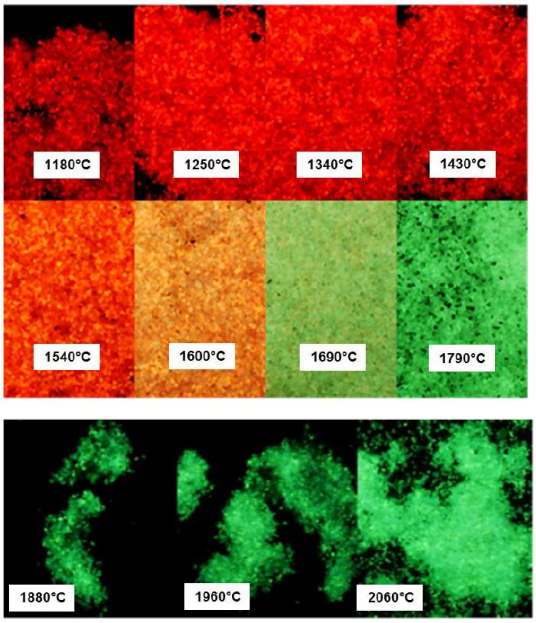

Figure 1-9. Illustration of the luminescence colors of the diamond powder as a result of rapid thermal annealing treatment at different annealing temperatures in the range from 1180 °C to 2060 °C. Reprinted from L. Dei Cas, S. Zeldin, N. Nunn, M. Torelli, A. I. Shames, A. M. Zaitsev, O. Shenderova, *Adv. Funct. Mater.* 2019, *29*, 1808362, with permission from John Wiley and Sons.[58]

Due to their photostability, nontoxicity and sensing capability fND are highly desirable fluorophores for bioimaging but also very sensitive probes used for quantum sensing.[33,35,51–53,68] Many existing methods for quantum sensing have major weaknesses, such as poor spatial and temporal resolution, low signal-to-noise ratio, unstable fluorescence emission, and limited operating time.[69] Sensing techniques based on defect-vacancy centers in diamond can be implemented at room temperature. Additionally, measurements with diamond are the only technique that allows measurements under extreme pressures. Furthermore, they have already been used in living cells, making them ideal sensors for nanoscale bioapplications.[70,71]

If the defect structures are to be used, it must be ensured that the particles do not agglomerate and find their way to the target. Due to the versatile surface groups of the ND, a large variety of reactions can be carried out and thus not only the size, the behavior, or the interactions among the NDs can be significantly influenced, but also already well researched water-insoluble active ingredients can be bound and transported with the help of the ND. However, in order to investigate such reactions, it is important to understand how the surface of the ND is structured.

1.2.1 Surface Structure and Functionalization of Nanodiamond

The surface groups of the ND are largely determined by the methods used for its purification, independent of their production by detonation synthesis or milling of CVD/HPHT diamonds.[72] As metal impurities and amorphous materials in the remain on the surface of the NDs, they are air oxidized and then etched with acid mixtures of H_2SO_4/HNO_3 or $H_2SO_4/HClO_4$.[73] Consequently, the surface is composed of multiple oxygenated moieties, such as carboxyl, carbonyl, ether and hydroxyl groups. To achieve a reaction with as many binding sites as possible on the ND surface, the surface should have as many identical groups for the coupling as possible. The surface can be modified in many ways.[4,6,8,74]

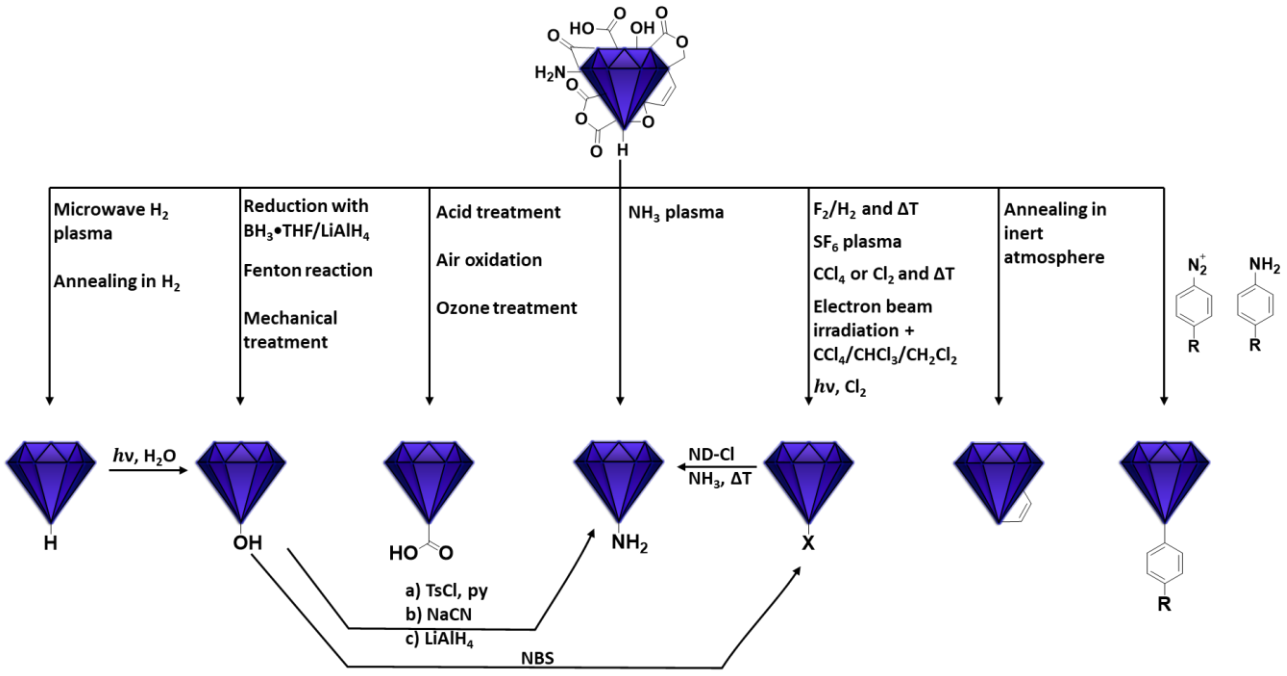

Figure 1-10. Schematic representation of typical surface reactions on ND surfaces.[35,74–76]

Hydrogen termination

Diamond films, produced via the CVD process, have a hydrogen-terminated surface. Depending on the orientation of the layer, CH (111) or CH_2 (100) groups are predominant on the surface. After the milling process, the NDs must be cleaned again, as described above, resulting in an oxygen-rich surface. The oxygen moieties must be reduced in order to get hydrogenated ND.[77] Since wet chemical methods for hydrogenation are not suitable for

diamond surface reaction, methods such as heating the NDs in a hydrogen atmosphere, hydrogen plasma or hot filament are good alternatives to reduce their surface groups to a large extent.[78]

Oxygen termination

A surface with functional groups containing oxygen is relatively easy to generate on nanodiamond. By treatment with ozone or oxidizing acids (HNO_3/H_2SO_4 or H_2O_2/H_2SO_4), or by air oxidation, some alcohol moieties but mainly ketone groups as well as acid groups can be generated.[7,79] Ozone treatment of ND at low temperature leads to ozonides on the surface which can be transformed into aliphatic alcohols, ketones and carboxylic acids.[79] At higher temperatures and UV-irradiation, ozone treatment leads mainly to C=O groups.[80] Acidic treatment, on the other hand, leads to mainly acid groups on the surface.[81] Air oxidation does not only remove non-diamond carbon and allow to remove oxidized metallic impurities but also generates carbonyl and ether groups on the surface at temperature of 420 °C for DND.[82] However, during air oxidation the temperature should be observed, otherwise the diamond core will be oxidized and consumed as well.[83] Hydroxylation of the diamond surface can be achieved by reduction of surface carbonyl groups by borane or lithium aluminum hydride, treatment with Fenton reagent or mechanical treatment.[84]

Nitrogen termination

Apart from oxygen termination, the ND surface can also be terminated with other heteroatoms such as nitrogen-containing groups (NO_2, CN, NH, NH_2) and halogens (F, Cl). Chemically, nitrogen-containing compounds, such as polymers[29] or amino acids[85], can be stably attached to the otherwise very oxygen-rich ND surface, and also directly to the diamond lattice.[86] They are a versatile anchor point regarding functionalizations for bioapplications and are therefore of high importance.[75] However, the complete exchange of oxygen moieties by nitrogen species proves to be very difficult. Not only the orientation of the ND lattice plays a role ({100} favored over {111} and {110}), also the approach (wet chemical, plasma) influences the results in surface loading but also remaining groups.[87] Besides, a full coverage of the ND surface with amino groups has not been achieved so far. However, at small scale coverage with N and N/H termination of the surface using a molecular beam has been achieved by Kawarada and coworker.[86]

Halogenation

The situation is different with halogenation. Because fluorine, for example, is a poor leaving group, harsh methods can be used to fluorinate the surface of ND. One possibility is to thermally treat the material with F_2/H_2 gas or to ignite an SF_6 plasma at the ND surface to produce C-F bonds.[85,88,89] A chlorinated surface of initially hydrogen terminated or graphitized NDs, on the other hand, can be produced by electron beam irradiation and thermal chlorination (Cl_2 at 600 °C, CCl_4 at 500 °C).[90] Here, the source of chlorine is the chlorinated solvent (CCl_4, $CHCl_3$, CH_2Cl_2).[89,91] The most unstable termination of halogenated ND surface is the brominated surface of ND, which is made from a hydroxylated surface with NBS. This creates a partially brominated surface, which can easily react, like chlorinated ND, with air humidity and oxygen.[92]

Annealing

Annealing consists of a thermal treatment of NDs at elevated temperatures in an oxygen-free atmosphere. In this process, the surface atoms reorient themselves, as surface groups and fractions thereof are cleaved as $CO_2/CO/H_2$ at higher temperatures. Depending on temperature, inert atmosphere argon/vacuum and time, a (partially) graphitized surface remains until carbon onion formation sets in. From 750 °C sp^2 carbon is formed on the surface, from 900 °C even the diamond core is graphitized under high vacuum conditions leading ultimately to carbon onions for annealing at even higher temperatures.[93]

Functionalization using diazonium salts

Reaction with aryldiazonium salts provides a very versatile method for the functionalization of carbon materials.[94] In the reaction of labile diazonium salts with NDs, nitrogen (N_2) is released while a very reactive carbocation is formed, which cannot be stabilized by the conjugated system because the positive charge is in the sp^2 orbital perpendicular to the conjugated system of p orbitals. The very reactive species is suitable for the functionalization of various carbon materials. The actual mechanism has not been fully elucidated, though. Thus, the reaction could proceed via the cationic but also through a radical species. Although the functional group in the para-position is affecting the reactivity of the diazonium salt, in most cases the reactivity is high

enough to achieve a superior surface loading under suitable conditions.[95] At the same time, a large variety of functional groups can be directly grafted onto the ND surface through the exchange/protection or subsequent reactions of the para-position, which can even be monitored by FTIR/Raman measurements.[75] Since the original functionalization with aryl diazonium salts took place on carbon nanotubes in an electrochemical synthesis, the reactive species is assumed to be a radical instead of an cation intermediate. This is also applicable to other similar structures, such as fullerenes, carbon onions or annealed NDs.[96] However, if the ND is not surface-treated and, like purified DND, still has many oxygen-containing groups on the surface, the reactive species will generally react with heteroatoms of the ND surface. In this case, it is initially irrelevant whether the diazonium salt was prepared *in situ* from an aniline derivative or whether it is present as a tetrafluoroborate salt, for example. In addition, the reactivity of the salt can be significantly improved by mechanical processes such as grinding or ultrasonic treatment of the ND.[76,97] This has the advantage of not only increasing reactivity but also of grinding/dispersing the particles into homogeneous dispersions during and after the reaction. Thereby preventing agglomeration, the surface of the particles is also kept free for reactions with the diazonium salt, thus achieving a homogeneous "coating" of the particles.[76]

Nanodiamond polymer coatings

A suitably terminated surface not only allows a variety of surface reactions, but also tailored interactions with surrounding molecules, e.g. proteins in bio-fluids. One possibility to further modify ND surfaces is the binding of polymers via van der Waals forces, hydrogen bonds, electrostatic forces etc. or covalent attachment .[20,29,98] The applications of such polymer composites are manifold, such as bone tissue engineering, imaging etc. (see above). In these composites the purpose of ND is to improve e.g. the Young's modulus, hardness, tensile stress, strain at break, cell proliferation and differentiation, thermal conductivity, decrease contact angle and to improve the friction coefficient.[20] Depending on the desired set of properties, different combinations of (functionalized) ND and polymer can be chosen. Polyethylene glycol is used to enhance the solubility of ND in physiological media but also make ND in some cases more biocompatible and help to carry drugs.[99] Polylactic acid (PLA) is nowadays known as filament material for 3D printing and is strengthened (improved hardness and Young's modulus) by adding ND as crosslinker into the polymer raw material.[100] G. Y. Ahn *et al.*

showed that only 1 wt% of ND as composite in polycaprolactone (PLC) can enhance tensile properties, proliferation and differentiation of MC3T3-E1 cells with the potential for application as bone replacement composite.[101] In poly(lactic-co-glycolic acid) (PLGA)[26,102] ND helps to enhance mechanical properties for bone tissue engineering, polyvinyl alcohol (PVA)[103] and chitosan[104] ND-composites improve in hardness and Young's modulus, while polyethylene (PE)[105] composites improve also thermal and tribological properties. Considering the advantages of ND in polymeric scaffolds, research on ND polymer composites enables a novel application for tissue engineering.[106]

1.2.2 Nanodiamond and Protein Interaction

The versatile surface of ND not only enables many reactions but also shows a high propensity to adsorb/desorb molecules. It works particularly well because hydrogen bonds are created easily between ND and biomolecules, or when opposite charges on the ND surface and biomolecules attract each other. Therefore, interaction with biomolecules, such as proteins or DNA is easily achieved.[107,108] When NDs presenting a variety of surface groups (see chapter: Surface and functionalization of nanodiamond) are exposed to a bio-liquid, numerous bio-molecules adsorb on the surface.[109] This is also the case in typical cell testing setups using fetal bovine serum (FBS), for instance. Once serum proteins are adsorbed *in situ*, this process is often irreversible due to a large number of binding sites, thus creating a shell of strongly bound proteins surrounding the actual nanoparticle. This newly formed shell around the particle is called "protein corona". This layer is not only neglected in many studies, but also intentionally induced to make ND colloidally more stable in bio-fluids in the presence of salts and to improve their uptake in cells.[108,110] The protein corona is generally divided into two zones/areas, namely the "soft corona" and the "hard corona". In the adsorption process, weakly interacting biomolecules, which however have a higher mobility due to their size, are first adsorbed on the surface (soft corona), which are subsequently replaced by molecules with stronger affinity, forming the hard corona.[111] This reorganization was already known as Vroman's model in the 1960s and has been confirmed by more recent studies.[112]

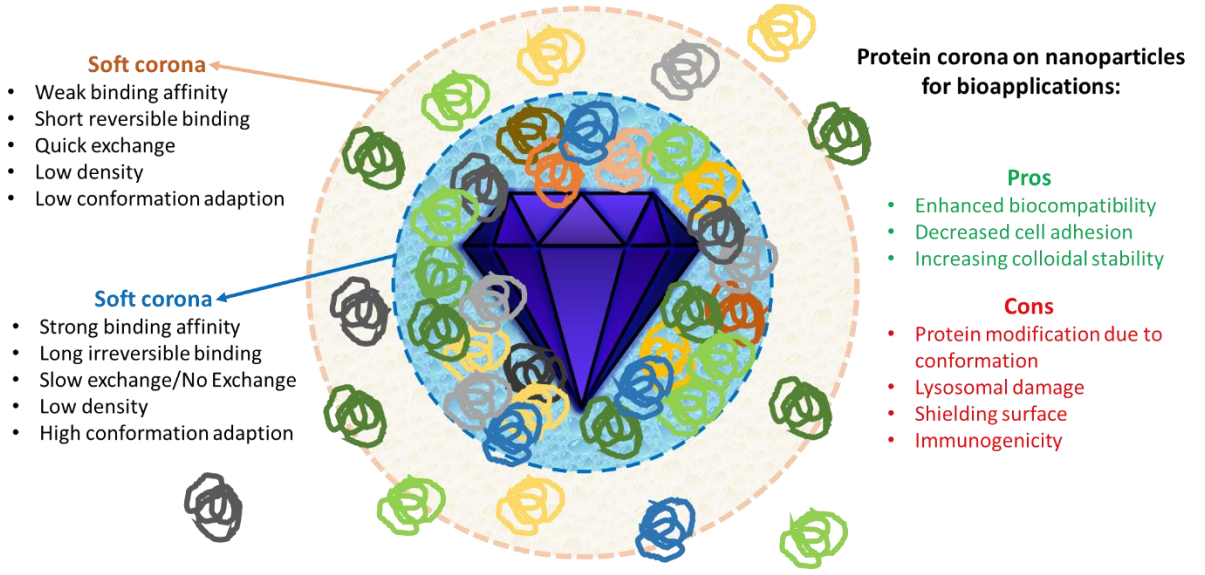

Figure 1-11. Schematic illustration of the evolution of soft and hard corona and its pros and cons on nanoparticles for bioapplications.[113]

Since NDs are often used for sensing, and therefore have targeting molecules on their surface, or are used as drug carriers, it is essential that the surface is functionalized in a controlled manner. Only in this way interactions with cell walls and membranes and targets can be assessed and controlled.[114] However, if an irreversibly bound protein corona is covering the surface of the functionalized NDs, it will inevitably result in neither drug nor targeting molecules being able to fulfill their purpose. In addition, depending on the stage of the corona, the colloidal stability and size of the particles will change.[115] To prevent such a loss of control, there are a number of ways to protect nanoparticle surfaces from uncontrolled adsorption of proteins.[116] One common method is to create a protective shell of e.g. polyethylene glycol or polyglycerol around the particles, which largely suppresses adsorption.[117] However, the same problem occurs with a polymer shell as with the corona, the original surface is largely shielded.[118,119] An alternative is an ionic layer consisting of one or more functional groups. A measure of the effectiveness of this functional groups comes from following the so-called "Whiteside rules", which state that the surface groups must 1) be hydrophilic, 2) have hydrogen bond acceptors, 3) have no hydrogen bond donors, and 4) have their overall charge neutral.[119,120,121] The resulting layer allows proteins to be repelled while controlling surface groups. One possible solution that fulfills all four rules is the use of zwitterionic groups attached

to the nanoparticle surface. A positive side effect is that the colloidal stability in aqueous medium is significantly improved, leading to prolonged circulation time. [119,122,123]

1.2.3 Nanodiamond Toxicity

With a large variety of methods available to control surface chemistry without shielding the ND surface, the question arises how biocompatible ND is. Toxic behavior results in the requirement for safe encapsulation by e.g. biocompatible polymers such as PEG. Recent studies show that ND is largely non-cytotoxic against diverse cell types such as neuronal, lung, renal, cervical cells and human breast adenocarcinoma cells.[29,33,124,125] This makes ND a promising candidate for bioapplications compared to other carbon materials.[8,126]

However, when a model insect species, *Acheta domesticus*, was exposed to ND in its diet, endpoint indices (lifespan, body weight, consumption, fecal caloric value, reproduction) showed adverse changes in ND-fed crickets compared to the control group. Oxidative stress levels in the ND-treated crickets' offspring however indicate that the toxicity of these particles is limited to the exposed individuals.[127]

A recently published study highlights the toxicity tests of fNDs using the very sensitive zebrafish embryo model *in vivo*. As a result, up to a rather high concentration of 1 mg/mL, no differences were detected between the control group and the embryos exposed to the fNDs. However, it should be noted that the two highest concentrations, 2 mg/mL and 5 mg/mL (which is an enormously high concentration), leads to a curved caudal fin of the zebrafish after hatching, which was previously attributed to a negative influence on the pharyngula stage of the embryos.[128] At the same time, a study that injected fNDs into worms (*C. elegans*) and fed them with fNDs indicated that neither oxidative stress nor disadvantages in reproduction were seen.[129] Low toxicity can only be detected at an enormous concentration of 400 mg/mL in a kidney cell, due to a moderate loss of viability of about 5–10%.[130] Analysis of various tissues and organs showed that fNDs were not toxic up to 75 mg/kg body weight. The particles were administered intraperitoneally to the live rats and these were studied for 5 months.[49] A study that investigated the dependence of toxicity on the sp^2/sp^3 ratio indicates that DND is not an inflammatory or toxic material, but suggests that sp^2 carbon contamination in DND may be a hazardous factor for biomedical application of DND.[131] In non-human primates and rats, it

was found that no toxic side effects occurred up to 25 mg/kg and it was suggested that a clinical DND monotherapy dose should be between 6.75 and 13.5 mg/kg.[132]

It can be assumed, especially in the case of DND, that a large degree of impurity associated with the manufacturing method, may influence, or even cause, a large part of the toxicity.[8] For example, a higher survival rate of bacteria can be demonstrated if the DNDs have been carefully cleaned (acid cleaning followed by air oxidation) beforehand (G02 grade).[133] Other studies also show, as summarized by Mochalin and Turcheniuk,[8] that toxicological studies with purified NDs and plausible particle concentrations, show no toxic effects[14,49,129,130,132,134], while others with NDs used without further purification or extremely high amounts/concentrations often show toxic side effects in the studies.[135]

1.2.4 Nanodiamond and Antibodies

If functionalized NDs are to be used in imaging or sensing, targeting is often required to achieve sufficient levels of ND concentrations at relevant locations. Without targeting, NDs are typically found in liver and spleen and other organ tissues, but cannot e.g. be enriched in the vicinity of tumors.[125] One way of targeting is to use antibodies that can bind, for instance, to the nuclear pore complex, and thus provide for an accumulation of the particles at the cell nucleus.[136] Successful experiments have already been performed using ND and CNT coated on silicon substrates to bind highly specific anti-Salmonella and anti-Staphylococcus aureus antibodies. By scanning electron microscopy, it was found that the binding of the hydrophilic surfaces (ND) was significantly better than that of the hydrophobic surface (CNT).[137] Examples of successful grafting of ND with antibodies have been presented in further reports.[138] Targeting using fNDs as carriers are mainly used for cancer/tumor diagnostics.[139] Recently, adsorbed antibodies on fND were used to target efficiently yeast cell nuclei and the high potential of this method can be demonstrated by monitoring the targeting by sensing with NV centers.[140]

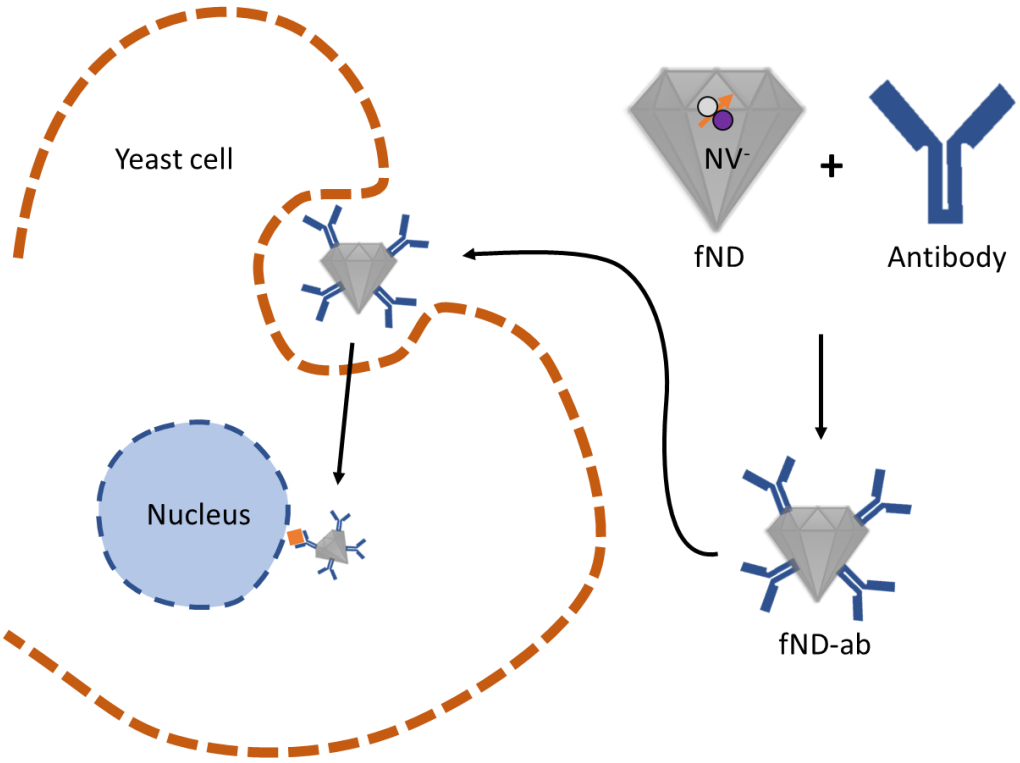

Figure 1-12. Schematic representation of the targeting strategy in a yeast cell. An antibody (ab) is linked to fluorescent nanodiamonds (fNDs). The fND–antibody (fND-ab) conjugate is ingested and accumulates at the surface of the nucleus. Adapted from A. Morita, T. Hamoh *et al.*[140]

1.3 Nanodiamond as a Sensor

NV centers in diamond can sense magnetic fields, electric fields, temperature, crystal strain, and optical near fields. Furthermore, NV centers in diamonds are outstanding for entanglement or superposition of quantum states, which so far is not achieved by any alternatives material under same conditions.[64,71,126]

When magnetic fields induced by e.g. ferritin,[71,141,142] manganese,[142] gadolinium[143] or magnetic nanoparticles[144] are causing magnetic noise close to a NV center in diamond, its T_2 spin coherence time is reduced. Consequently, biomolecules containing such magnetic field triggers can be detected. Alternatively, NV centers can measure electric field and temperature,[63–66] which can be important for cell[145] and intraneuronal[146] monitoring.[147] Using fNDs on e.g. a cantilever allows to directly sense mechanical strain.[71,148,149] In addition, very promising imaging techniques are possible when near-field energy transfer processes, such as Förster resonance energy transfer (FRET) are used to exchange energy between a donor and

acceptor. In this process, the non-radiative energy exchange will always result in reducing the excited state lifetime and fluorescence rate of the donor.[71,150] However, the process occurs only over small path lengths of <7 nm but mostly around 2 nm and is only dependent on linking of the dye to the ND, but also the position of the NV center in the ND.[50,129,150]

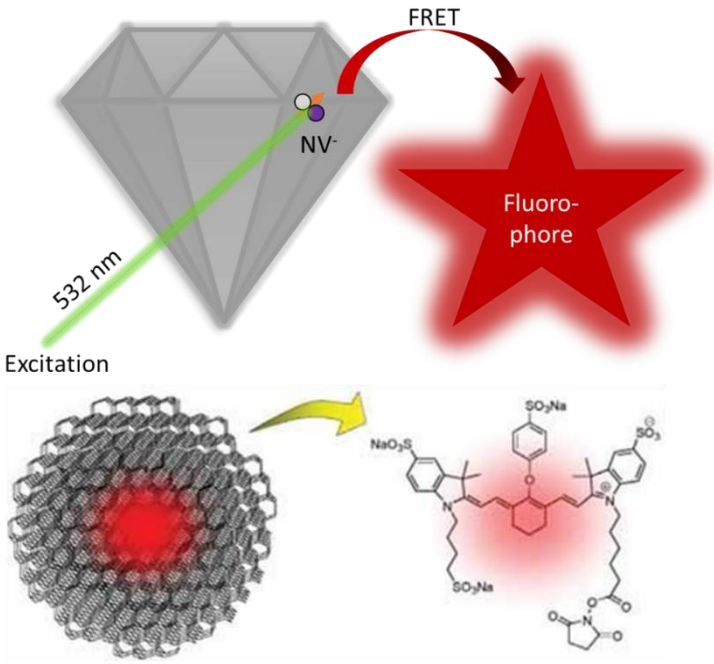

Figure 1-13. Schematic illustration of a Förster resonance energy transfer between NV^- and a fluorophore (top) and bio label example (bottom). Reprinted from N. Mohan, Y.-K. Tzeng, L. Yang, Y.-Y. Chen, Y. Y. Hui, C.-Y. Fang, H.-C. Chang, *Adv. Mater.* 2010, *22*, 843, with permission from John Wiley and Sons.[151]

Challenges related to the use of NV centers are the non-uniform fabrication methods of NV defects and their proximity to the diamond surface, which can influence defect centers.[149,152] Nevertheless, most sensing applications are still based on NV centers. Other defect centers such as the SiV center, which have a narrow emission spectrum at room temperature, in addition to their short state lifetimes (1.7 ns), may also be suitable as acceptors in the FRET process.[153]

ND, in addition to direct measurement using NV/SiV centers, can also help detect substances as part of a 2D electrode. For instance, when it comes to tracing contaminants in wastewater, nanodiamond can help to detect how much phenolic compounds are present in the water using cyclic voltammetry (CV) analysis on an electrode. However, the preparation (12 h dispersion of boron doped ND, amorphous carbon and graphene to always same size, making a

reproducible coating on the electrode, and repeating the experiments for CV) are demanding compared to conventional organic fluorescent probes, which only need to be added to the water sample and their excited state to be examined.[154] In general, probes on a ND basis (or containing ND) provide good sensitivity for heavy metals (Cd^{2+}, Ni^{2+}, Mn^{2+}, Co^{2+}, Pb^{2+}) in water,[155] and Cr^{3+} in urine[156] or can even extract Pb^{2+} and Cu^{2+} from wastewater.[157] Mostly, however, the ND is not used for detection directly through defect centers but for stabilization of non-water soluble complex conjugates of other nanoparticles, carbon nanotubes, graphite, graphene or inorganic salts in water or more complex media (cell solution, urine, salt solutions, acidic/basic conditions).[155,156]

The material mixtures for 2D electrode coatings (e.g. graphene or carbon nanotubes) with NDs described above show that they are very sensitive to certain metal ions. However, the application of such materials in wastewater has the disadvantage that e.g. graphene and carbon nanotubes can cause toxic side effects.[158] Probes, which are ND-based, can potentially offer important advantages, such as higher surface area compared to the 2D electrodes which are used for CV. But also avoiding toxic materials and colloidal stability in complex media are potential advantages of ND-based probes. When ND is covalently bound to cellulose and urease, urea is indirectly detected in an aqueous medium by the enzymatic cleavage of urea into ammonia and carbon dioxide through urease salicylate-hypochlorite method.[159] Another example are saccharides that are covalently attached to ND proved a unusually simple detection method. When these conjugates are exposed to a type 1 fimbriated uropathogenic *E. coli* in solution, mechanically stable aggregates are formed, which not only allows detection with the naked eye, but also the bacterial ND agglutinations can be removed by filtration and the ND recycled by addition of methyl α-D-mannopyranoside (a competing inhibitor of the binding of mannose by *E. coli*.).[160]

For all the promising applications developed so far with NDs to detect heavy metals or other substances of concern in wastewater, the application of NDs as a carrier for water-insoluble organic sensors has been overlooked. As already demonstrated for numerous bioapplications, NDs can be functionalized in an extremely versatile manner. Furthermore, as demonstrated by the applications in the sensor field, NDs can help many materials otherwise insoluble in water or of biological concern, such as carbon nanotubes, bound to NDs to become not only less of a

concern but also water soluble. How ND can be used as a carrier for chemosensors and how such a chemosensor system can be designed will be discussed in detail in the next part.

1.3.1 Fluorescent Sensor - Building Strategies for Cation Recognition

Heavy metals dissolved as salts in water or solvents can cause tremendous environmental pollution. Due to the ubiquitous use of such metals in industry, agriculture, households and technology, harmful effects are diagnosed in plants, animals and human.[161,162,163] If an organism is exposed to heavy metals, toxic effects can set in very quickly. Heavy metals can bind biomolecules in various oxidation states and then alter or block important functions of vital metal complexes. Control mechanisms of the organism are bypassed and toxic effects occur.[163,164] To prevent or at least notice the release of heavy metals into the environment as early as possible, monitoring mechanisms must be implemented where these metals are used.[162,165]

By analyzing and monitoring leaking liquids, such as coolant (water), a wide variety of heavy metals can be detected if there is a possibility to test all metals used. A simple method is the use of chemosensor molecules, which, after addition to the analyzing solution, change their fluorescence in a very short time due to their interaction with the metal and thus indicate the type of metal cation as well as its concentration.[166]

Such chemosensors consist for the most part of a fluorophore connected to the ionophore directly or with the aid of a spacer.[167] While the fluorophore is responsible for the signal, i.e. fluorescence change, the ionophore is responsible for the interaction with the cation. If an ion is complexed in the ionophore, energy transfer, electron transfer, charge transfer to the fluorophore, or an excimer/exciplex are formed or prevented.[168]

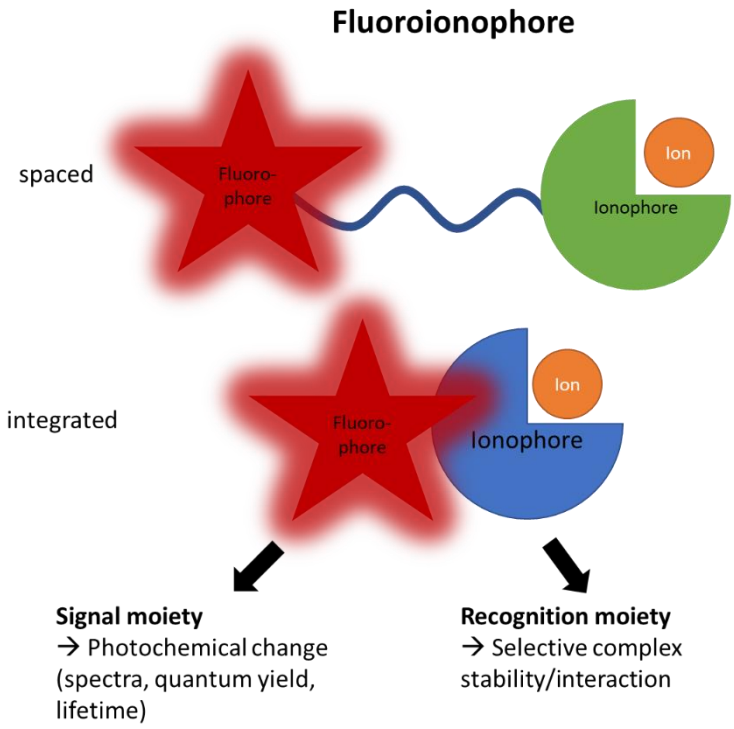

Figure 1-14. Schematic illustration of general fluoroionophore building strategies. Adapted from B. Valeur and I. Leray.[168]

A fluorophore being used extensively is pyrene, which stands out due to its unique properties.[169,170]

1.3.1.1 Fluorophore – Pyrene

Pyrene, a polycyclic aromatic hydrocarbon (PAH) that was discovered by Auguste Laurent in 1837 by extraction from coal tar, has been the focus of extensive studies due it unique photophysical properties. It is well known for its excimer and exciplex formation, its exceptionally long-lived singlet excited state of 354 ns, its high fluorescence quantum yield and sensitivity of its excitation spectra to environmental changes.[171,172] Consequently, pyrene derivatives have already been used in applications such as synthetic dye production, fluorescence labeled polymers, sensing of temperature, pressure, pH, or to detect guest molecules such as organic molecules or metals.[168,171,173,174] However, pyrenes have also been of great interest to application fields such as organic semiconductors as it possesses high chemical stability and charge-carrier mobility. Therefore, pyrene derivatives have been used in

organic light emitting diodes (OLEDs), organic field-effect transistors (OFETs) and organic photovoltaic cells (OPVs).[171,173,175]

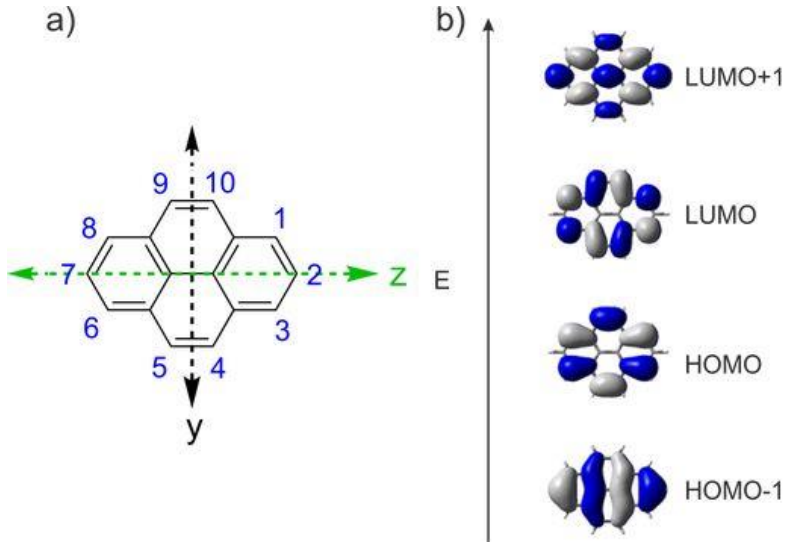

Figure 1-15. Schematic illustration of the a) Cartesian coordinate system used for pyrene, b) LUMO(+1) and HOMO(-1) of pyrene. Reprinted from J. Merz, J. Fink, A. Friedrich, I. Krummenacher, H. H. Al Mamari, S. Lorenzen, M. Haehnel, A. Eichhorn, M. Moos, M. Holzapfel et al., *Chem. Eur. J.* **2017**, *23*, 13164, with permission from John Wiley and Sons.[176]

However, most of the used pyrene derivatives involve substitution at one or more of the 1-, 3-, 6-, and 8-positions, which are the sites of maximum contributions of the HOMO and LUMO.[171,177–180] Consequently, electrophilic aromatic reactions take place at these positions whereas substituting pyrene at the 2- and 2,7-positions is rather challenging since a nodal plane in the HOMO and LUMO passes through these positions.[177,178] Nevertheless, it has been shown that the photophysical properties of pyrenes substituted at the 2- and 2,7-positions differ from those substituted at the 1-position.[178,181] However, these positions were only accessible through indirect methods until Marder and co-workers reported a general and selective method to functionalize the 2- and 2,7-positions of pyrene via a sterically controlled Ir-catalyzed C-H borylation reaction.[179,182] To understand the effect of substitution on pyrene, it is necessary to obtain a good picture of the photophysical properties of pyrene.

The absorption spectrum of unsubstituted pyrene consists of four bands with the first transition band ($S_1 \leftarrow S_0$) at 372 nm (ε = 510 mol^{-1} cm^{-1} L) being very low in intensity.[178] The reason for this is that the $S_1 \leftarrow S_0$ transition is the result of a configuration interaction between HOMO-

1→LUMO and HOMO→LUMO+1 and the respective transition dipole moments of these two contributions cancel each other. Consequently, the S_1←S_0 electronic excitation is transition dipole forbidden, which results also in a forbidden fluorescence from S_1 and, therefore, the S_1 state is long-lived. The S_2←S_0 transition at 334 nm is based on the HOMO→LUMO transition and is allowed with ε = 55 000 mol^{-1} cm^{-1} L. The higher S_3←S_0 transition at 272 nm (ε = 54 000 mol^{-1} cm^{-1} L) is also the result of a configuration interaction between HOMO-1→LUMO and HOMO→LUMO+1 of pyrene but with the respective transition dipole moments enhancing each other. The S_4←S_0 at 243 nm (ε = 88000 mol^{-1} cm^{-1} L) is based on the HOMO-1→LUMO+1 transition and strongly allowed.[183]

As the S_1←S_0 transition involves the HOMO-1 and LUMO+1 that have non-zero contributions at the 2,7-positions, substituents can influence this transition depending on the electron accepting/donating ability of the substituent.[176,178,181,184] Thus, derivatives with a S_1←S_0 transition that have larger bathochromic shifts and increased allowedness can be achieved which is reflected by higher extinction coefficients and shorter lifetimes. As the S_2←S_0 transition involves the HOMO and LUMO that have nodes at the 2,7-positions, this transition is not affected for 2- or 2,7-substituted pyrenes. In contrast, functionalizing pyrene at its 1-position has a strong influence on the S_1←S_0 and S_2←S_0 transition because all orbitals involved in these transitions have non-zero contributions. Thus, pyrene derivatives with very short lifetimes are obtained.[178] In summary, pyrenes functionalized at the 2-position are highly desirable for use as chemosensors due to their long lifetimes. However, only a few chemosensors based on pyrenes functionalized at their 2-position have been reported to date.[170,185]

1.3.1.2 Ionophore – TEG and Triazole

Poly(ethylene glycol) (PEG) is a widely used ionophore for binding alkali metal ions similar to crown ethers and it forms conjugates with biologically important substances, such as drugs.[186] Particles stabilized with PEG by coating the surface of the particles, or the polymer particles *per se*, are particularly colloidally stable and readily dispersible in aqueous media. This is based on two phenomena: On the one hand, entropic repulsion, which is based on the tendency of the polymer to maintain the freedom of a random winding, leads to steric stabilization, and on the other hand, osmotic repulsion of the PEG layer/particles increases, which ensures that "bound"

water can no longer be easily released.[121,187] However, if PEG is intended for bioapplications, metal ions and oxygen in the bloodstream or cells can cause toxic degradation products to be formed from PEG.[188,189] This can however be circumvented as a shorter glycol chain is sufficient to take advantage of the benefits of PEG. The optimal toxicity profile is obtained with a chain length between two and six glycol moieties.[189] With tetraethylene glycol (TEG), good dispersibility, colloidal stability and hydrophilicity are likewise achieved.[123]

Bound to hydrophobic molecules, TEG can render them water-soluble and conjugates can be purified by chromatography. Additionally, TEG has the property of providing crown ether-like properties leading to improved coordination with metal ions.[190]

If TEG, which like crown ethers is very good at coordinating metal ions, is extended with further heteroatoms, new coordination possibilities are opened. A good way to functionalize TEG with heteroatoms is a [3+2] cycloaddition between an azide and an alkyne using elevated temperatures for a 1,3-dipolar cycloaddition (Huisgen) or, because uncontrolled two the 1,5- and the 1,4-isomer can be formed, a Cu(I)-catalyzed click reaction leading exclusively to the 1,4-isomer.[191] After a click reaction, a 1,2,3-triazole is generated and opens up a binding possibility between fluorophore and ionophore while TEG can function as both, spacer and ionophore. The resulting triazoles are known to bind well to metal ions and, for example, dyes that are functionalized with triazoles by a click reaction can act as a chemosensor.[191,192]

1.3.2 Nanodiamond Sensors

In summary, the above discussed topics demonstrate that ND is an outstanding material with high potential as a chemosensor using additional detection principles apart from the luminescence of lattice defects. Due to their very large surface area relative to their core and their versatile surface groups, NDs are additionally highly modifiable.[6–9] Further, by grafting the surface groups with more complex molecules, such as biopolymers, targeting molecules or catalysts, and manipulating the diamond lattice, ND has a high potential for a wide range of applications such as tribology, imaging, quantum sensing, tissue engineering, nanocomposite core material and additive for polymers. Additionally, fND makes all kinds of ND applications even more interesting by enabling sensing and bioimaging.[3,10,193] Within the carbon nanoparticle family, ND is an excellent candidate for biomedical applications.[11] Studies show,

as summarized by Mochalin and Turcheniuk, that purified NDs and at plausible particle concentrations, show no toxic effects.[8] Due to its largely non-toxic behavior *in vivo*, it can be used for drug delivery, biological imaging and sensing. Especially DND is a cheap and easily accessible material for bioapplications.[12–15]

1.4 Outlook and Remaining Challenges

1.4.1 ND-Zwitterion Based Drug Delivery

In this work it is shown how advanced zwitterionic moieties on ND surface can be used to successfully prevent NDs from protein adsorption and simultaneously enhancing colloidal stability in water and physiological fluids. The key behind this advantage is overall neutral charge of the surface and the extremely high affinity towards water. Shown by Rotello and coworkers, TEG-based chains with polar headgroups on the surface can be used as shielding sphere which can also be used to entrap hydrophobic drugs inside.[194] However, due to the highly adsorbing surface of ND, the loading of such a drug can be very high. When drugs are adsorbed in hydrophobic environment, by changing the solvent water, all adsorbed drug is trapped and can be release very slowly. Whereas the unfunctionalized surface auf ND can exchange freely with surrounding solvent and therefore desorb drug molecules from the surface quicker.

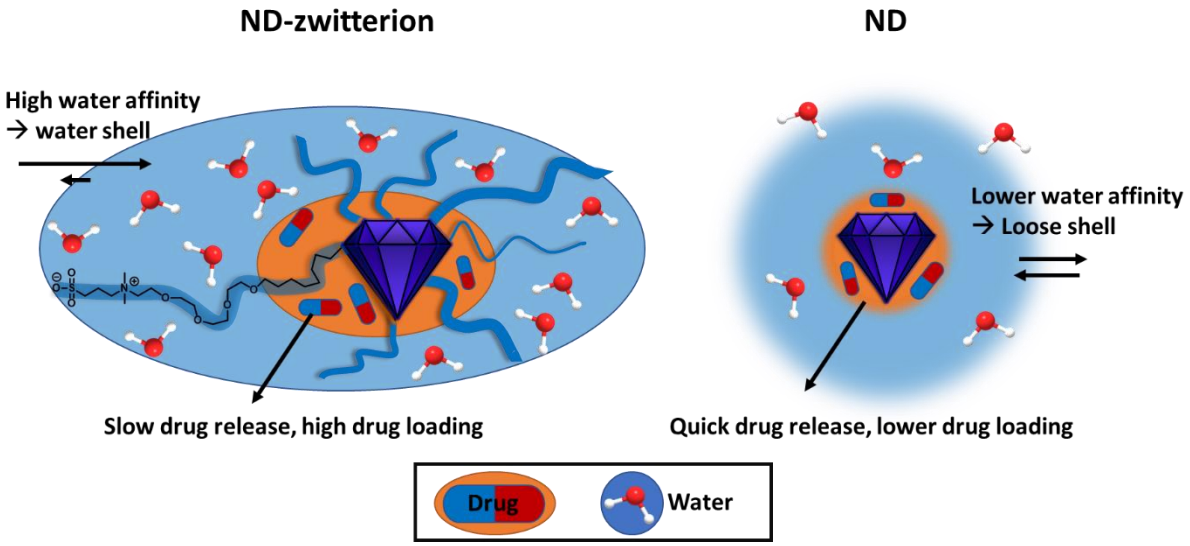

Figure 1-16. Schematic presentation of zwitterion functionalized ND compared with non-functionalized ND for drug delivery interactions in water.

For such an application, it is necessary to know how many of the zwitterions are needed to observe a positive effect on both colloidal stability/protein interaction and drug adsorption and desorption. From previous work it can be assumed that a smaller amount of zwitterionic

molecules would be sufficient to protect the surface from protein adsorption. To open the surface for targeting molecules, such as antibodies, but also covalently bound drugs, the optimal amount of zwitterions need to be determined. The structural composition of the chosen zwitterion could also be reconsidered with the aim to develop an efficient synthetic approach requiring less steps (currently, seven reactions before binding to the ND). Possibly a simple mechanochemical grafting (milling/bead-assisted ultrasonication) with amino acids could work in a similar way.

1.4.2 Chemosensors for *in vitro* and *in vivo* Investigations

The building block principle of the chain with azides has led to the construction of a sensor by click reaction of the azides with 2-ethynylpyrene. This sensor can not only detect Cu^{2+}, Hg^{2+} and Pb^{2+}, but can also be used in water if bound to the surface of ND. At the same time, excimer formation is prevented by the construction of the chain.

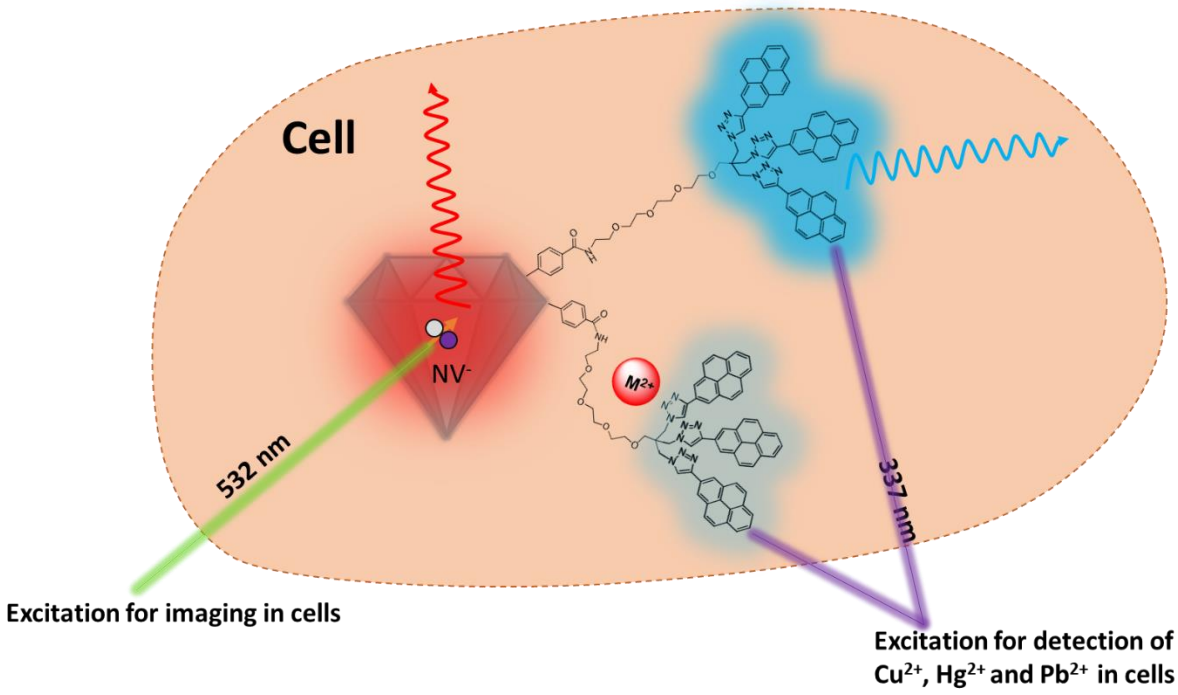

Figure 1-17. Schematic illustration of a potential multimodal ND sensors combining the usage of fND for imaging purposes and a chemosensor for simultaneous cation detection inside in a cell.

Thinking one step further, such a system could be used with fND as the nanoparticle base not only as a chemosensor but also for imaging *in vivo* or *in vitro*. Due to the absence of excimer formation of the pyrene probe (usually between ~450–600 nm) the absorption and emission wavelength (230–350 nm and 370–530 nm) of the pyrene probe does not overlap with the fND excitation wavelength (532 nm). Thus, if no other major energy transfer takes place, both systems can be excited and detected independently from each other using fluorescence microscopy. Even if the sensor loses up to 90 % of its original fluorescence intensity, for example, due to extremely high Cu^{2+} concentrations, the NV center can always be used to detect its location.

1.4.3 Modifications of the Chemosensor Molecule for more Advanced Usage

In future work, a combination of sensing ability and colloidal stabilization could be achieved using the principles presented in this work. The chain (TEG) not only connects the ND to the sensor, but also serves as an ionophore for potential complexation, and can additionally serve as a colloidal stabilizer. Analogous to the sensor from this work, the head group is formed from three 1,2,3-triazoles that connect the chain to the fluorophore in a click reaction and simultaneously act as part of the ionophores. Additionally, the pyrene head group could be equipped with a zwitterion at the 7-position that protects the fluorophore and thus the diamond surface from protein adsorption.

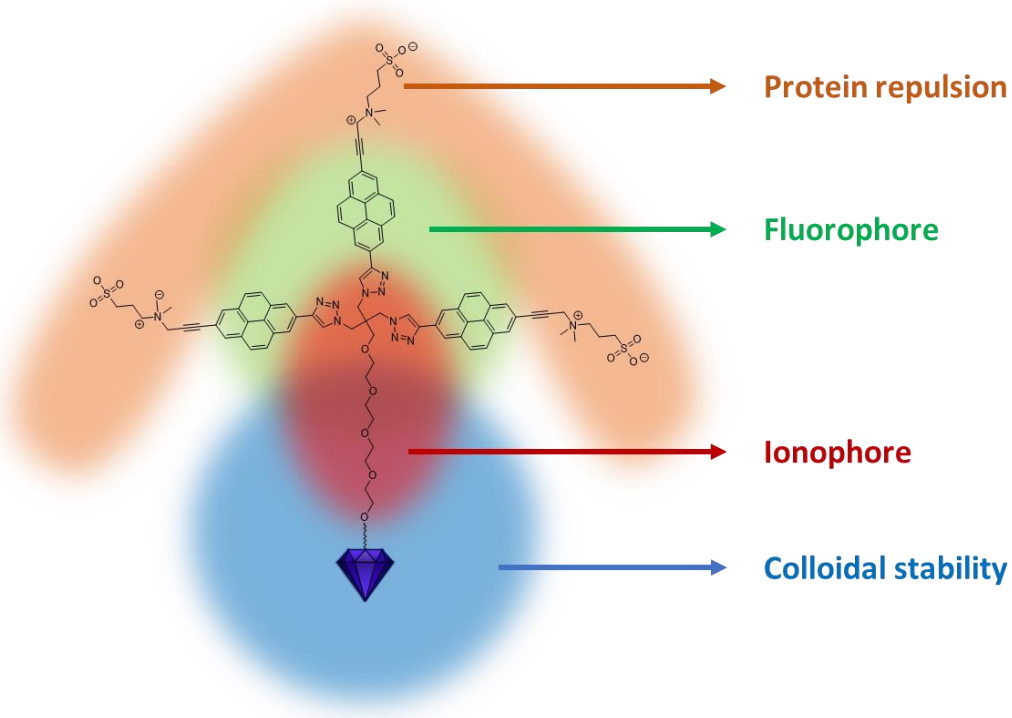

Figure 1-18. Hypothetic chemosensor system attached to ND which could potentially combine the properties of zwitterions and the sensor system.

If surface functionalization with zwitterions and a chemosensor would be combined, then potentially both positive effects, namely the prevention of protein corona and colloidal stability provided by the zwitterion headgroup and the sensor ability of the pyrene headgroup, could be merged in one functional unit. As a result, this could prevent possible blockage of sensing capability in complex media by a protein corona formed in the case of unprotected sensor moieties.

1.5 References

[1] V. V. Danilenko. On the history of the discovery of nanodiamond synthesis. *Phys. Sol. State* **2004**, *46*, 595–599.

[2] J. E. Butler, A. V. Sumant. The CVD of Nanodiamond Materials. *Chem. Vap. Deposition* **2008**, *14*, 145–160.

[3] V. N. Mochalin, O. Shenderova, D. Ho, Y. Gogotsi. The properties and applications of nanodiamonds. *Nat. Nanotechnol.* **2012**, *7*, 11–23.

[4] G. Reina, L. Zhao, A. Bianco, N. Komatsu. Chemical Functionalization of Nanodiamonds: Opportunities and Challenges Ahead. *Angew. Chem. Int. Ed.* **2019**, *58*, 17918–17929; *Angew. Chem.* **2019**, *131*, 18084–18095

[5] Y. N. Palyanov, I. N. Kupriyanov, A. F. Khokhryakov, V. G. Ralchenko in *Handbook of Crystal Growth* (Hrsg.: P. Rudolph), Elsevier Science, Burlington, **2014**, S. 671–713.

[6] D. H. Jariwala, D. Patel, S. Wairkar. Surface functionalization of nanodiamonds for biomedical applications. *Mater. Sci. Eng. C* **2020**, *113*, 110996.

[7] J. Ackermann, A. Krueger. Highly sensitive and reproducible quantification of oxygenated surface groups on carbon nanomaterials. *Carbon* **2020**, *163*, 56–62.

[8] K. Turcheniuk, V. N. Mochalin. Biomedical applications of nanodiamond (Review). *Nanotechnology* **2017**, *28*, 252001.

[9] S. Szunerits, C. E. Nebel, R. J. Hamers. Surface functionalization and biological applications of CVD diamond. *MRS Bull.* **2014**, *39*, 517–524.

[10] O. A. Shenderova, G. E. McGuire. Science and engineering of nanodiamond particle surfaces for biological applications (Review). *Biointerphases* **2015**, *10*, 30802.

[11] N. Bondon, L. Raehm, C. Charnay, R. Boukherroub, J.-O. Durand. Nanodiamonds for bioapplications, recent developments. *J. Mater. Chem. B* **2020**, *8*, 10878–10896.

[12] A. M. Panich, A. I. Shames, D. Mogilyansky, S. D. Goren, V. Dolmatov. Detonation nanodiamonds fabricated from tetryl: Synthesis, NMR, EPR and XRD study. *Diam. Relat. Mater.* **2020**, *108*, 107918.

[13] N. Panwar, A. M. Soehartono, K. K. Chan, S. Zeng, G. Xu, J. Qu, P. Coquet, K.-T. Yong, X. Chen. Nanocarbons for Biology and Medicine: Sensing, Imaging, and Drug Delivery. *Chem. Rev.* **2019**, *119*, 9559–9656.

[14] A. M. Schrand, H. Huang, C. Carlson, J. J. Schlager, E. Osawa, S. M. Hussain, L. Dai. Are diamond nanoparticles cytotoxic? *J. Phys. Chem. B* **2007**, *111*, 2–7.

[15] A. M. Schrand, S. A. C. Hens, O. A. Shenderova. Nanodiamond Particles: Properties and Perspectives for Bioapplications. *Crit. Rev. Solid. State.* **2009**, *34*, 18–74.

[16] a) Y. Jiao, S. Liu, Y. Sun, W. Yue, H. Zhang. Bioinspired Surface Functionalization of Nanodiamonds for Enhanced Lubrication. *Langmuir* **2018**, *34*, 12436–12444; b) W. Zhai, N. Srikanth, L. B. Kong, K. Zhou. Carbon nanomaterials in tribology. *Carbon* **2017**, *119*, 150–171; c) M. Ullah, A. Kausar, M. Siddiq, M. Subhan, M. Abid Zia. Reinforcing Effects of Modified Nanodiamonds on the Physical Properties of Polymer-Based Nanocomposites: A Review. *Polymer Plast Tech Eng* **2015**, *54*, 861–879.

[17] Y. Zamani, A. Zareein, L. Bazli, R. NasrAzadani, B. P. Mahammod, S. Nasibi, A. M. Chahardehi. Nanodiamond-containing composites for tissue scaffolds and surgical implants: A review. *J. Compos. Compd.* **2020**, *2*, 215–227.

[18] A. Javeed, B. John. Tribological performance of nanolubricants dispersed with graphene oxide and detonation nanodiamond. *Proc. Inst. Mech. Eng. J* **2020**, *235*, 1-13.
[19] A. Shirani, Q. Hu, Y. Su, T. Joy, D. Zhu, D. Berman. Combined Tribological and Bactericidal Effect of Nanodiamonds as a Potential Lubricant for Artificial Joints. *ACS App. Mat. Interfaces* **2019**, *11*, 43500–43508.
[20] A. Rehman, S. Houshyar, X. Wang. Nanodiamond in composite: Biomedical application. *J. Biomed. Mater. Res. A* **2019**, *108*, 906–922.
[21] a) X. Wu, M. Bruschi, T. Waag, S. Schweeberg, Y. Tian, T. Meinhardt, R. Stigler, K. Larsson, M. Funk, D. Steinmüller-Nethl, M. Rasse, A. Krueger. Functionalization of bone implants with nanodiamond particles and angiopoietin-1 to improve vascularization and bone regeneration. *J. Mater. Chem. B* **2017**, *5*, 6629–6636; b) S. Suliman, Y. Sun, T. O. Pedersen, Y. Xue, J. Nickel, T. Waag, A. Finne-Wistrand, D. Steinmüller-Nethl, A. Krueger, D. E. Costea, K. Mustafa. In Vivo Host Response and Degradation of Copolymer Scaffolds Functionalized with Nanodiamonds and Bone Morphogenetic Protein 2. *Advanced healthcare materials* **2016**, *5*, 730–742; c) S. Suliman, Z. Xing, X. Wu, Y. Xue, T. O. Pedersen, Y. Sun, A. P. Døskeland, J. Nickel, T. Waag, H. Lygre, A. Finne-Wistrand, D. Steinmüller-Nethl, A. Krueger, K. Mustafa. Release and bioactivity of bone morphogenetic protein-2 are affected by scaffold binding techniques in vitro and in vivo. *J. Contr. Release* **2015**, *197*, 148–157.
[22] Z. Xing, T. O. Pedersen, X. Wu, Y. Xue, Y. Sun, A. Finne-Wistrand, F. R. Kloss, T. Waag, A. Krueger, D. Steinmüller-Nethl, K. Mustafa. Biological effects of functionalizing copolymer scaffolds with nanodiamond particles. *Tissue. Eng. Part A* **2013**, *19*, 1783–1791.
[23] a) R. Aversa, R. V. V. Petrescu, A. Apicella, F. I. T. Petrescu. A nanodiamond for structural biomimetic scaffolds. *Eng. rev.* **2019**, *39*, 81–89; b) C. Shuai, Y. Li, G. Wang, W. Yang, S. Peng, P. Feng. Surface modification of nanodiamond: Toward the dispersion of reinforced phase in poly-l-lactic acid scaffolds. *Int. J. Biol. Macromol.* **2019**, *126*, 1116–1124.
[24] A. Rifai, N. Tran, P. Reineck, A. Elbourne, E. Mayes, A. Sarker, C. Dekiwadia, E. P. Ivanova, R. J. Crawford, T. Ohshima, B. C. Gibson, A. D. Greentree, E. Pirogova, K. Fox. Engineering the Interface: Nanodiamond Coating on 3D-Printed Titanium Promotes Mammalian Cell Growth and Inhibits Staphylococcus aureus Colonization. *ACS Appl. Mater. Interfaces* **2019**, *11*, 24588–24597.
[25] a) K. Vega-Figueroa, J. Santillán, C. García, J. A. González-Feliciano, S. A. Bello, Y. G. Rodríguez, E. Ortiz-Quiles, E. Nicolau. Assessing the Suitability of Cellulose-Nanodiamond Composite As a Multifunctional Biointerface Material for Bone Tissue Regeneration. *ACS Biomater. Sci. Eng.* **2017**, *3*, 960–968; b) C. Fessele, S. Wachtler, V. Chandrasekaran, C. Stiller, T. K. Lindhorst, A. Krueger. Thiourea-Bridged Nanodiamond Glycoconjugates as Inhibitors of Bacterial Adhesion. *Eur. J. Org. Chem.* **2015**, *25*, 5519–5525.
[26] F. Zhang, Q. Song, X. Huang, F. Li, K. Wang, Y. Tang, C. Hou, H. Shen. A Novel High Mechanical Property PLGA Composite Matrix Loaded with Nanodiamond-Phospholipid Compound for Bone Tissue Engineering. *ACS Appl. Mater. Interfaces* **2016**, *8*, 1087–1097.
[27] K. Fox, R. Ratwatte, M. A. Booth, H. M. Tran, P. A. Tran. High Nanodiamond Content-PCL Composite for Tissue Engineering Scaffolds. *Nanomaterials* **2020**, *10*, 948.

[28] J. Neburkova, J. Vavra, P. Cigler. Coating nanodiamonds with biocompatible shells for applications in biology and medicine. *Curr. Opin. Solid State Mater. Sci.* **2017**, *21*, 43–53.

[29] U. T. Uthappa, O. R. Arvind, G. Sriram, D. Losic, Ho-Young-Jung, M. Kigga, M. D. Kurkuri. Nanodiamonds and their surface modification strategies for drug delivery applications. *J. Drug Deliv. Sci. Technol.* **2020**, *60*, 101993.

[30] a) S. Garg, A. Garg, N. K. Sahu, A. K. Yadav. Synthesis and Characterization of Nanodiamond-Doxorubicin (Dox) Conjugate for Effective Delivery against MCF-7 Cell Lines. *J. Drug Delivery Ther.* **2019**, *9*, 589–594; b) van der Laan, Kiran, J., M. Hasani, T. Zheng, R. Schirhagl. Nanodiamonds for In Vivo Applications. *Small* **2018**, *14*, 1703838.

[31] K. Zhang, Q. Zhao, S. Qin, Y. Fu, R. Liu, J. Zhi, C. Shan. Nanodiamonds conjugated upconversion nanoparticles for bio-imaging and drug delivery. *J. Colloid Interface Sci.* **2019**, *537*, 316–324.

[32] E. Torres Sangiao, A. M. Holban, M. C. Gestal. Applications of Nanodiamonds in the Detection and Therapy of Infectious Diseases. *Materials* **2019**, *12*, 1639.

[33] E. Perevedentseva, Y.-C. Lin, C.-L. Cheng. A review of recent advances in nanodiamond-mediated drug delivery in cancer. *Expert Opin. Drug Deliv.* **2020**, *18*, 1–14.

[34] S. A. Ansari, R. Satar, M. A. Jafri, M. Rasool, W. Ahmad, S. Kashif Zaidi. Role of Nanodiamonds in Drug Delivery and Stem Cell Therapy. *Iran. J. Biotechnol.* **2016**, *14*, 130–141.

[35] G. Gao, Q. Guo, J. Zhi. Nanodiamond-Based Theranostic Platform for Drug Delivery and Bioimaging. *Small* **2019**, *15*, e1902238.

[36] a) M. Gu, T. B. Toh, L. Hooi, J. J. Lim, X. Zhang, E. K.-H. Chow. Nanodiamond-Mediated Delivery of a G9a Inhibitor for Hepatocellular Carcinoma Therapy. *ACS Appl. Mater. Interfaces* **2019**, *11*, 45427–45441; b) A. N. Bokarev, I. L. Plastun. Possibility of drug delivery due to hydrogen bonds formation in nanodiamonds and doxorubicin: molecular modeling. *Nanosystems: Phys. Chem. Math.* **2018**, *9*, 370–377; c) E. von Haartman, H. Jiang, A. A. Khomich, J. Zhang, S. A. Burikov, T. A. Dolenko, J. Ruokolainen, H. Gu, O. A. Shenderova, I. I. Vlasov, J. M. Rosenholm. Core–shell designs of photoluminescent nanodiamonds with porous silica coatings for bioimaging and drug delivery I. *J. Mater. Chem. B* **2013**, *1*, 2358.

[37] H. Huang, E. Pierstorff, E. Osawa, D. Ho. Active nanodiamond hydrogels for chemotherapeutic delivery. *Nano Lett.* **2007**, *7*, 3305–3314.

[38] L. Li, L. Tian, Y. Wang, W. Zhao, F. Cheng, Y. Li, B. Yang. Smart pH-responsive and high doxorubicin loading nanodiamond for in vivo selective targeting, imaging, and enhancement of anticancer therapy. *J. Mater. Chem. B* **2016**, *4*, 5046–5058.

[39] J. Xiao, X. Duan, Q. Yin, Z. Zhang, H. Yu, Y. Li. Nanodiamonds-mediated doxorubicin nuclear delivery to inhibit lung metastasis of breast cancer. *Biomaterials* **2013**, *34*, 9648–9656.

[40] Y. Xing, L. Dai. Nanodiamonds for nanomedicine. *Nanomedicine* **2009**, *4*, 207–218.

[41] Z. Wang, Z. Tian, Y. Dong, L. Li, L. Tian, Y. Li, B. Yang. Nanodiamond-conjugated transferrin as chemotherapeutic drug delivery. *Diam. Relat. Mater.* **2015**, *58*, 84–93.

[42] a) V. S. Madamsetty, K. Pal, S. Keshavan, T. R. Caulfield, S. K. Dutta, E. Wang, B. Fadeel, D. Mukhopadhyay. Development of multi-drug loaded PEGylated nanodiamonds to inhibit tumor growth and metastasis in genetically engineered mouse models of pancreatic cancer. *Nanoscale* **2019**, *11*, 22006–22018; b) V. S. Madamsetty, A. Sharma,

M. Toma, S. Samaniego, A. Gallud, E. Wang, K. Pal, D. Mukhopadhyay, B. Fadeel. Tumor selective uptake of drug-nanodiamond complexes improves therapeutic outcome in pancreatic cancer. *Nanomedicine* **2019**, *18*, 112–121; c) L. Zhao, Y.-H. Xu, T. Akasaka, S. Abe, N. Komatsu, F. Watari, X. Chen. Polyglycerol-coated nanodiamond as a macrophage-evading platform for selective drug delivery in cancer cells. *Biomaterials* **2014**, *35*, 5393–5406; d) T.-F. Li, K. Li, C. Wang, X. Liu, Y. Wen, Y.-H. Xu, Q. Zhang, Q.-Y. Zhao, M. Shao, Y.-Z. Li, M. Han, N. Komatsu, L. Zhao, X. Chen. Harnessing the cross-talk between tumor cells and tumor-associated macrophages with a nano-drug for modulation of glioblastoma immune microenvironment. *J. Control. Release* **2017**, *268*, 128–146; e) T.-F. Li, Y.-H. Xu, K. Li, C. Wang, X. Liu, Y. Yue, Z. Chen, S.-J. Yuan, Y. Wen, Q. Zhang, M. Han, N. Komatsu, L. Zhao, X. Chen. Doxorubicin-polyglycerol-nanodiamond composites stimulate glioblastoma cell immunogenicity through activation of autophagy. *Acta Biomater.* **2019**, *86*, 381–394; f) T.-F. Li, K. Li, Q. Zhang, C. Wang, Y. Yue, Z. Chen, S.-J. Yuan, X. Liu, Y. Wen, M. Han, N. Komatsu, Y.-H. Xu, L. Zhao, X. Chen. Dendritic cell-mediated delivery of doxorubicin-polyglycerol-nanodiamond composites elicits enhanced anti-cancer immune response in glioblastoma. *Biomaterials* **2018**, *181*, 35–52; g) S.-J. Yuan, Y.-H. Xu, C. Wang, H.-C. An, H.-Z. Xu, K. Li, N. Komatsu, L. Zhao, X. Chen. Doxorubicin-polyglycerol-nanodiamond conjugate is a cytostatic agent that evades chemoresistance and reverses cancer-induced immunosuppression in triple-negative breast cancer. *J. Nanobiotechnol.* **2019**, *17*, 110.

[43] a) A. B. Volnova, S. K. Gordeev, D. N. Lenkov. Targeted Delivery of 4-Aminopyridine Into the Rat Brain by Minicontainers from Carbon-Nanodiamonds Composite. *J. Neurosci. Neuroeng.* **2013**, *2*, 569–573; b) G. Xi, E. Robinson, B. Mania-Farnell, E. F. Vanin, K.-W. Shim, T. Takao, E. V. Allender, C. S. Mayanil, M. B. Soares, D. Ho, T. Tomita. Convection-enhanced delivery of nanodiamond drug delivery platforms for intracranial tumor treatment. *Nanomedicine* **2014**, *10*, 381–391; c) T. K. Henna, V. R. Raphey, R. Sankar, V. K. Ameena Shirin, H. V. Gangadharappa, K. Pramod. Carbon nanostructures: The drug and the delivery system for brain disorders. *Int. J. Pharm.* **2020**, *587*, 119701.

[44] P. Moscariello, M. Raabe, W. Liu, S. Bernhardt, H. Qi, U. Kaiser, Y. Wu, T. Weil, H. J. Luhmann, J. Hedrich. Unraveling In Vivo Brain Transport of Protein-Coated Fluorescent Nanodiamonds. *Small* **2019**, *15*, 1902992.

[45] Y.-A. Huang, C.-W. Kao, K.-K. Liu, H.-S. Huang, M.-H. Chiang, C.-R. Soo, H.-C. Chang, T.-W. Chiu, J.-I. Chao, E. Hwang. The effect of fluorescent nanodiamonds on neuronal survival and morphogenesis. *Sci. Rep.* **2014**, *4*, 6919.

[46] R. Namdar, S. Nafisi. Nanodiamond applications in skin preparations. *Drug Discov. Today* **2018**, *23*, 1152–1158.

[47] U. Roy, V. Drozd, A. Durygin, J. Rodriguez, P. Barber, V. Atluri, X. Liu, T. G. Voss, S. Saxena, M. Nair. Characterization of Nanodiamond-based anti-HIV drug Delivery to the Brain. *Sci. Rep.* **2018**, *8*, 1603.

[48] M. Chipaux, K. J. van der Laan, S. R. Hemelaar, M. Hasani, T. Zheng, R. Schirhagl. Nanodiamonds and Their Applications in Cells. *Small* **2018**, *14*, 1704263.

[49] V. Vaijayanthimala, P.-Y. Cheng, S.-H. Yeh, K.-K. Liu, C.-H. Hsiao, J.-I. Chao, H.-C. Chang. The long-term stability and biocompatibility of fluorescent nanodiamond as an in vivo contrast agent. *Biomaterials* **2012**, *33*, 7794–7802.

[50] L. Lu, B. Li, S. Ding, Y. Fan, S. Wang, C. Sun, M. Zhao, C.-X. Zhao, F. Zhang. NIR-II bioluminescence for in vivo high contrast imaging and in situ ATP-mediated metastases tracing. *Nat. Commun.* **2020**, *11*, 4192.
[51] N. Prabhakar, J. M. Rosenholm. Nanodiamonds for advanced optical bioimaging and beyond. *Curr. Opin. Colloid Interface Sci.* **2019**, *39*, 220–231.
[52] M. D. Torelli, N. A. Nunn, O. A. Shenderova. A Perspective on Fluorescent Nanodiamond Bioimaging. *Small* **2019**, *15*, 1902151.
[53] Y.-Y. Liu, B.-M. Chang, H.-C. Chang. Nanodiamond-enabled biomedical imaging. *Nanomedicine* **2020**, *15*, 1599–1616.
[54] a) G. Laporte, D. Psaltis. STED imaging of green fluorescent nanodiamonds containing nitrogen-vacancy-nitrogen centers. *Biomed. Opt. Express* **2016**, *7*, 34; b) K. Y. Han, K. I. Willig, E. Rittweger, F. Jelezko, C. Eggeling, S. W. Hell. Three-Dimensional Stimulated Emission Depletion Microscopy of Nitrogen-Vacancy Centers in Diamond Using Continuous-Wave Light. *Nano letters* **2009**, *9*, 3323–3329; c) Y.-K. Tzeng, O. Faklaris, B.-M. Chang, Y. Kuo, J.-H. Hsu, H.-C. Chang. Superresolution Imaging of Albumin-Conjugated Fluorescent Nanodiamonds in Cells by Stimulated Emission Depletion. *Angew. Chem. Int. Ed.* **2011**, *50*, 2262–2265; *Angew. Chem.* **2011**, *123*, 2310–2313; d) S. Arroyo-Camejo, M.-P. Adam, M. Besbes, J.-P. Hugonin, V. Jacques, J.-J. Greffet, J.-F. Roch, S. W. Hell, F. Treussart. Stimulated Emission Depletion Microscopy Resolves Individual Nitrogen Vacancy Centers in Diamond Nanocrystals. *ACS Nano* **2013**, *7*, 10912–10919.
[55] M. Pfender, N. Aslam, G. Waldherr, P. Neumann, J. Wrachtrup. Single-spin stochastic optical reconstruction microscopy. *Proc. Natl. Acad. Sci.* **2014**, *111*, 14669–14674.
[56] Bonnie O. Leung, Keng C. Chou. Review of Super-Resolution Fluorescence Microscopy for Biology. *Appl. Spectrosc.* **2011**, *65*, 967–980.
[57] T.-L. Wee, Y.-W. Mau, C.-Y. Fang, H.-L. Hsu, C.-C. Han, H.-C. Chang. Preparation and characterization of green fluorescent nanodiamonds for biological applications. *Diam. Relat. Mater.* **2009**, *18*, 567–573.
[58] L. Dei Cas, S. Zeldin, N. Nunn, M. Torelli, A. I. Shames, A. M. Zaitsev, O. Shenderova. From Fancy Blue to Red: Controlled Production of a Vibrant Color Spectrum of Fluorescent Diamond Particles. *Adv. Funct. Mater.* **2019**, *29*, 1808362.
[59] A. Magyar, W. Hu, T. Shanley, M. E. Flatté, E. Hu, I. Aharonovich. Synthesis of luminescent europium defects in diamond. *Nat. Commun.* **2014**, *5*, 3523.
[60] a) H. Zhang, I. Aharonovich, D. R. Glenn, R. Schalek, A. P. Magyar, J. W. Lichtman, E. L. Hu, R. L. Walsworth. Silicon-vacancy color centers in nanodiamonds: cathodoluminescence imaging markers in the near infrared. *Small* **2014**, *10*, 1908–1913; b) T. D. Merson, S. Castelletto, I. Aharonovich, A. Turbic, T. J. Kilpatrick, A. M. Turnley. Nanodiamonds with silicon vacancy defects for nontoxic photostable fluorescent labeling of neural precursor cells. *Opt. Lett.* **2013**, *38*, 4170–4173.
[61] a) S. Pedroso-Santana, N. Fleitas-Salazar, A. Sarabia-Sainz, E. Silva-Campa, A. Burgara-Estrella, A. Angulo-Molina, R. Melendrez, M. Pedroza-Montero, R. Riera. A nanodiamond-fluorescein conjugate for cell studies. *Adv. Nat. Sci: Nanosci. Nanotechnol.* **2018**, *9*, 15013; b) A. M. Schrand, J. B. Lin, S. C. Hens, S. M. Hussain. Temporal and mechanistic tracking of cellular uptake dynamics with novel surface fluorophore-bound nanodiamonds. *Nanoscale* **2011**, *3*, 435–445.
[62] D. Li, X. Chen, H. Wang, Y. Yu, J. Liu, Y. Wang, J. Zhang, M. Zheng, J. Zhi. Nanodiamonds as Raman probes for specifically targeted bioimaging: visualization and

mechanism study of the biorecognition between nanodiamonds-EGF and EGFR. *RSC Adv.* **2017**, *7*, 12835–12841.

[63] R. Schirhagl, K. Chang, M. Loretz, C. L. Degen. Nitrogen-vacancy centers in diamond. *Annu. Rev. Phys. Chem.* **2014**, *65*, 83–105.

[64] L. Rondin, J.-P. Tetienne, T. Hingant, J.-F. Roch, P. Maletinsky, V. Jacques. Magnetometry with nitrogen-vacancy defects in diamond. *Rep. Prog. Phys.* **2014**, *77*, 56503.

[65] M. W. Doherty, N. B. Manson, P. Delaney, F. Jelezko, J. Wrachtrup, L. C. Hollenberg. The nitrogen-vacancy colour centre in diamond. *Phys. Rep.* **2013**, *528*, 1.

[66] Y. Wu, F. Jelezko, M. B. Plenio, T. Weil. Diamond Quantum Devices in Biology. *Angew. Chem. Int. Ed.* **2016**, *55*, 6586–6598; *Angew. Chem.* **2016**, *128*, 6696–6709.

[67] K. Bray, L. Cheung, K. R. Hossain, I. Aharonovich, S. M. Valenzuela, O. Shimoni. Versatile multicolor nanodiamond probes for intracellular imaging and targeted labeling. *J. Mater. Chem. B* **2018**, *6*, 3078–3084.

[68] M. A. Zurbuchen, M. P. Lake, S. A. Kohan, B. Leung, L.-S. Bouchard. Nanodiamond landmarks for subcellular multimodal optical and electron imaging. *Sci. Rep.* **2013**, *3*, 2668.

[69] X. Chen, W. Zhang. Diamond nanostructures for drug delivery, bioimaging, and biosensing. *Chem. Soc. Rev.* **2017**, *46*, 734–760.

[70] a) E. Moreva, E. Bernardi, P. Traina, A. Sosso, S. D. Tchernij, J. Forneris, F. Picollo, G. Brida, Ž. Pastuović, I. P. Degiovanni, P. Olivero, M. Genovese. Practical Applications of Quantum Sensing: A Simple Method to Enhance the Sensitivity of Nitrogen-Vacancy-Based Temperature Sensors. *Phys. Rev. Applied* **2020**, *13*, 54057; b) M. Gulka, H. Salehi, B. Varga, E. Middendorp, O. Pall, H. Raabova, T. Cloitre, F. J. G. Cuisinier, P. Cigler, M. Nesladek, C. Gergely. Simultaneous label-free live imaging of cell nucleus and luminescent nanodiamonds. *Sci. Rep.* **2020**, *10*, 9791; c) S. Y. Ong, M. Chipaux, A. Nagl, R. Schirhagl. Shape and crystallographic orientation of nanodiamonds for quantum sensing. *Physical chemistry chemical physics : PCCP* **2017**, *19*, 10748–10752; d) T. Zhang, G.-Q. Liu, W.-H. Leong, C.-F. Liu, M.-H. Kwok, T. Ngai, R.-B. Liu, Q. Li. Hybrid nanodiamond quantum sensors enabled by volume phase transitions of hydrogels. *Nat. Commun.* **2018**, *9*, 3188; e) J. Holzgrafe, Q. Gu, J. Beitner, D. M. Kara, H. S. Knowles, M. Atatüre. Nanoscale NMR Spectroscopy Using Nanodiamond Quantum Sensors. *Phys. Rev. Applied* **2020**, *13*; f) U. Jantzen, A. B. Kurz, D. S. Rudnicki, C. Schäfermeier, K. D. Jahnke, U. L. Andersen, V. A. Davydov, V. N. Agafonov, A. Kubanek, L. J. Rogers, F. Jelezko. Nanodiamonds carrying silicon-vacancy quantum emitters with almost lifetime-limited linewidths. *New J. Phys.* **2016**, *18*, 73036.

[71] M. Radtke, E. Bernardi, A. Slablab, R. Nelz, E. Neu. Nanoscale sensing based on nitrogen vacancy centers in single crystal diamond and nanodiamonds: achievements and challenges. *Nano Futures* **2019**, *3*, 42004.

[72] N. Nunn, M. Torelli, G. McGuire, O. Shenderova. Nanodiamond: A high impact nanomaterial. *Curr. Opin. Solid State Mater. Sci.* **2017**, *21*, 1–9.

[73] a) L. Basso, M. Cazzanelli, M. Orlandi, A. Miotello. Nanodiamonds: Synthesis and Application in Sensing, Catalysis, and the Possible Connection with Some Processes Occurring in Space. *Appl. Sci.* **2020**, *10*, 4094; b) Y. V. Butenko, V. L. Kuznetsov, E. A. Paukshtis, A. I. Stadnichenko, I. N. Mazov, S. I. Moseenkov, A. I. Boronin, S. V. Kosheev. The Thermal Stability of Nanodiamond Surface Groups and Onset of

Nanodiamond Graphitization. *Fuller. Nanotub. Carbon Nanostructures* **2006**, *14*, 557–564.
[74] A. Krueger, D. Lang. Functionality is Key. *Adv. Funct. Mater.* **2012**, *22*, 890–906.
[75] H.-S. Jung, K. C. Neuman. Surface Modification of Fluorescent Nanodiamonds for Biological Applications. *Nanomaterials* **2021**, *11*, 153.
[76] Y. Liang, M. Ozawa, A. Krueger. A general procedure to functionalize agglomerating nanoparticles demonstrated on nanodiamond. *ACS Nano* **2009**, *3*, 2288–2296.
[77] O. A. Williams, J. Hees, C. Dieker, W. Jäger, L. Kirste, C. E. Nebel. Size-dependent reactivity of diamond nanoparticles. *ACS Nano* **2010**, *4*, 4824–4830.
[78] a) J. C. Arnault, H. A. Girard. Hydrogenated nanodiamonds: Synthesis and surface properties. *Curr. Opin. Solid State Mater. Sci.* **2017**, *21*, 10–16; b) A.-I. Ahmed, S. Mandal, L. Gines, O. A. Williams, C.-L. Cheng. Low temperature catalytic reactivity of nanodiamond in molecular hydrogen. *Carbon* **2016**, *110*, 438–442; c) H. A. Girard, J. C. Arnault, S. Perruchas, S. Saada, T. Gacoin, J.-P. Boilot, P. Bergonzo. Hydrogenation of nanodiamonds using MPCVD: A new route toward organic functionalization. *Diam. Relat. Mater.* **2010**, *19*, 1117–1123.
[79] J. Ackermann, A. Krueger. Efficient surface functionalization of detonation nanodiamond using ozone under ambient conditions. *Nanoscale* **2019**, *11*, 8012–8019.
[80] O. Shenderova, A. Koscheev, N. Zaripov, I. Petrov, Y. Skryabin, P. Detkov, S. Turner, G. van Tendeloo. Surface Chemistry and Properties of Ozone-Purified Detonation Nanodiamonds. *J. Phys. Chem. C* **2011**, *115*, 9827–9837.
[81] T. Jiang, K. Xu. FTIR study of ultradispersed diamond powder synthesized by explosive detonation. *Carbon* **1995**, *33*, 1663–1671.
[82] V. Pichot, M. Comet, E. Fousson, C. Baras, A. Senger, F. Le Normand, D. Spitzer. An efficient purification method for detonation nanodiamonds. *Diam. Relat. Mater.* **2008**, *17*, 13–22.
[83] a) T. Gaebel, C. Bradac, J. Chen, J. M. Say, L. Brown, P. Hemmer, J. R. Rabeau. Size-reduction of nanodiamonds via air oxidation. *Diam. Relat. Mater.* **2012**, *21*, 28–32; b) C. Bradac, S. Osswald. Effect of structure and composition of nanodiamond powders on thermal stability and oxidation kinetics. *Carbon* **2018**, *132*, 616–622; c) S. Stelmakh, K. Skrobas, S. Gierlotka, S. C. Vogel, B. Palosz. Atomic structure and grain shape evolution of nanodiamond during annealing in oxidizing atmosphere from neutron diffraction and MD simulations. *Diam. Relat. Mater.* **2021**, *111*, 108177.
[84] a) R. Martín, M. Alvaro, J. R. Herance, H. García. Fenton-treated functionalized diamond nanoparticles as gene delivery system. *ACS Nano* **2010**, *4*, 65–74; b) A. Krüger, Y. Liang, G. Jarre, J. Stegk. Surface functionalisation of detonation diamond suitable for biological applications. *J. Mater. Chem.* **2006**, *16*, 2322–2328.
[85] Y. Liu, Z. Gu, J. L. Margrave, V. N. Khabashesku. Functionalization of Nanoscale Diamond Powder: Fluoro-, Alkyl-, Amino-, and Amino Acid-Nanodiamond Derivatives. *Chem. Mater.* **2004**, *16*, 3924–3930.
[86] S. Kawai, H. Yamano, T. Sonoda, K. Kato, J. J. Buendia, T. Kageura, R. Fukuda, T. Okada, T. Tanii, T. Higuchi, M. Haruyama, K. Yamada, S. Onoda, T. Ohshima, W. Kada, O. Hanaizumi, A. Stacey, T. Teraji, S. Kono, J. Isoya, H. Kawarada. Nitrogen-Terminated Diamond Surface for Nanoscale NMR by Shallow Nitrogen-Vacancy Centers. *J. Phys. Chem. C* **2019**, *123*, 3594–3604.
[87] a) A. S. Barnard, M. Sternberg. Substitutional nitrogen in nanodiamond and bucky-diamond particles. *J. Phys. Chem. B* **2005**, *109*, 17107–17112; b) A. V. Stanishevsky, M.

J. Walock, S. A. Catledge. Surface modification and stability of detonation nanodiamonds in microwave gas discharge plasma. *Appl. Surf. Sci.* **2015**, *357*, 1403–1409; c) Ashek-I-Ahmed, L. Gines, S. Mandal, C.-Y. Song, O. A. Williams, M. N. Sarmiento, C.-L. Cheng. Facile Amine Termination of Nanodiamond Particles and Their Surface Reaction Dynamics. *ACS Omega* **2019**, *4*, 16715–16723; d) L. Lai, A. S. Barnard. Stability of Nanodiamond Surfaces Exposed to N, NH, and NH 2. *J. Phys. Chem. C* **2011**, *115*, 6218–6228.

[88] a) W. Yanhui, H. Hao, Z. Jianbing, M. Fanwei, D. Liang, S. Jing. Electrochemical Behavior of Fluorinated and Aminated Nanodiamond. *Int. J. Electrochem. Sci.* **2012**, *7*, 6807–6815; b) H. Huang, Y. H. Wang, J. B. Zang, L. Y. Bian. Improvement of suspension stability and electrophoresis of nanodiamond powder by fluorination. *Appl. Surf. Sci.* **2012**, *258*, 4079–4084.

[89] G. V. Lisichkin, I. I. Kulakova, Y. A. Gerasimov, A. V. Karpukhin, R. Y. Yakovlev. Halogenation of detonation-synthesised nanodiamond surfaces. *Mendeleev Commun.* **2009**, *19*, 309–310.

[90] B. V. Spitsyn, S. A. Denisov, N. A. Skorik, A. G. Chopurova, S. A. Parkaeva, L. D. Belyakova, O. G. Larionov. The physical–chemical study of detonation nanodiamond application in adsorption and chromatography. *Diam. Relat. Mater.* **2010**, *19*, 123–127.

[91] a) J. Zhou, C. Laube, W. Knolle, S. Naumov, A. Prager, F.-D. Kopinke, B. Abel. Efficient chlorine atom functionalization at nanodiamond surfaces by electron beam irradiation. *Diam. Relat. Mater.* **2018**, *82*, 150–159; b) I. I. Kulakova, A. Y. Pereyaslavcev, G. V. Lisichkin. Regularities of Chlorination of the Detonation NanoDiamond Surface. *Moscow Univ. Chem. Bull.* **2019**, *74*, 246–256.

[92] R. Martín, P. C. Heydorn, M. Alvaro, H. Garcia. General Strategy for High-Density Covalent Functionalization of Diamond Nanoparticles Using Fenton Chemistry. *Chem. Mater.* **2009**, *21*, 4505–4514.

[93] a) X. Duan, Z. Ao, H. Zhang, M. Saunders, H. Sun, Z. Shao, S. Wang. Nanodiamonds in sp 2 /sp 3 configuration for radical to nonradical oxidation: Core-shell layer dependence. *Appl. Catal. B* **2018**, *222*, 176–181; b) T. Petit, J.-C. Arnault, H. A. Girard, M. Sennour, P. Bergonzo. Early stages of surface graphitization on nanodiamond probed by x-ray photoelectron spectroscopy. *Phys. Rev. B* **2011**, *84*, 233407; c) M. Zeiger, N. Jäckel, D. Weingarth, V. Presser. Vacuum or flowing argon: What is the best synthesis atmosphere for nanodiamond-derived carbon onions for supercapacitor electrodes? *Carbon* **2015**, *94*, 507–517; d) A. M. Panich, A. I. Shames, N. A. Sergeev, M. Olszewski, J. K. McDonough, V. N. Mochalin, Y. Gogotsi. Nanodiamond graphitization: a magnetic resonance study. *J. Phys. Condens. Matter.* **2013**, *25*, 245303.

[94] A. A. Mohamed, Z. Salmi, S. A. Dahoumane, A. Mekki, B. Carbonnier, M. M. Chehimi. Functionalization of nanomaterials with aryldiazonium salts. *Adv. Colloid Interface Sci.* **2015**, *225*, 16–36.

[95] a) T. Meinhardt, D. Lang, H. Dill, A. Krueger. Pushing the Functionality of Diamond Nanoparticles to New Horizons: Orthogonally Functionalized Nanodiamond Using Click Chemistry. *Adv. Funct. Mater.* **2011**, *21*, 494–500; b) Y. Liang, T. Meinhardt, G. Jarre, M. Ozawa, P. Vrdoljak, A. Scholl, F. Reinert, A. Krueger. Deagglomeration and surface modification of thermally annealed nanoscale diamond. *J. Colloid Interface Sci.* **2011**, *354*, 23–30.

[96] a) L. Pilan. Tailoring the performance of electrochemical biosensors based on carbon nanomaterials via aryldiazonium electrografting. *Bioelectrochemistry* **2020**, *138*, 107697;

b) J. L. Bahr, J. Yang, D. V. Kosynkin, M. J. Bronikowski, R. E. Smalley, J. M. Tour. Functionalization of carbon nanotubes by electrochemical reduction of aryl diazonium salts: a bucky paper electrode. *J. Am. Chem. Soc.* **2001**, *123*, 6536–6542.

[97] C. Mangeney, Z. Qin, S. A. Dahoumane, A. Adenier, F. Herbst, J.-P. Boudou, J. Pinson, M. M. Chehimi. Electroless ultrasonic functionalization of diamond nanoparticles using aryl diazonium salts. *Diam. Relat. Mater.* **2008**, *17*, 1881–1887.

[98] J. Beltz, A. Pfaff, I. M. Abdullahi, A. Cristea, V. N. Mochalin, N. Ercal. Effect of Nanodiamond Surface Chemistry on Adsorption and Release of Tiopronin. *Diam. Relat. Mater.* **2019**, *100*, 107590.

[99] a) D. Wang, Y. Tong, Y. Li, Z. Tian, R. Cao, B. Yang. PEGylated nanodiamond for chemotherapeutic drug delivery. *Diam. Relat. Mater.* **2013**, *36*, 26–34; b) G. Yang, W. Long, W. Yan, H. Huang, M. Liu, H. Ouyang, Y. Feng, L. Liu, X. Zhang, Y. Wei. Surface PEGylation of nanodiamond through a facile Michael addition reaction for intracellular drug delivery. *J. Drug Deliv. Sci. Technol.* **2020**, *57*, 101644; c) X. Zhang, S. Wang, C. Fu, L. Feng, Y. Ji, L. Tao, S. Li, Y. Wei. PolyPEGylated nanodiamond for intracellular delivery of a chemotherapeutic drug. *Polym. Chem.* **2012**, *3*, 2716; d) X. Zhang, C. Fu, L. Feng, Y. Ji, L. Tao, Q. Huang, S. Li, Y. Wei. PEGylation and polyPEGylation of nanodiamond. *Polymer* **2012**, *53*, 3178–3184; e) H. Huang, M. Liu, X. Tuo, J. Chen, L. Mao, Y. Wen, J. Tian, N. Zhou, X. Zhang, Y. Wei. One-step fabrication of PEGylated fluorescent nanodiamonds through the thiol-ene click reaction and their potential for biological imaging. *Appl. Surf. Sci.* **2018**, *439*, 1143–1151.

[100] a) R. Aziz, M. I. Ul Haq, A. Raina. Effect of surface texturing on friction behaviour of 3D printed polylactic acid (PLA). *Polym. Test.* **2020**, *85*, 106434; b) Y.-Q. Zhao, K.-T. Lau, J. Kim, C.-L. Xu, D.-D. Zhao, H.-L. Li. Nanodiamond/poly (lactic acid) nanocomposites: Effect of nanodiamond on structure and properties of poly (lactic acid). *Compos. B. Eng.* **2010**, *41*, 646–653; c) S. Farah, D. G. Anderson, R. Langer. Physical and mechanical properties of PLA, and their functions in widespread applications - A comprehensive review. *Adv. Drug Deliv. Rev.* **2016**, *107*, 367–392.

[101] G. Y. Ahn, T.-K. Ryu, Y. R. Choi, J. R. Park, M. J. Lee, S.-W. Choi. Fabrication and optimization of Nanodiamonds-composited poly(ε-caprolactone) fibrous matrices for potential regeneration of hard tissues. *Biomater. Res.* **2018**, *22*, 16.

[102] M. A. Brady, A. Renzing, T. E. L. Douglas, Q. Liu, S. Wille, M. Parizek, L. Bacakova, A. Kromka, M. Jarosova, G. Godier, P. H. Warnkel. Development of Composite Poly(Lactide-co-Glycolide)- Nanodiamond Scaffolds for Bone Cell Growth. *J. Nanosci. Nanotechnol.* **2015**, *15*, 1060–1069.

[103] a) U. Maitra, K. E. Prasad, U. Ramamurty, C. Rao. Mechanical properties of nanodiamond-reinforced polymer-matrix composites. *Solid State Commun.* **2009**, *149*, 1693–1697; b) O. A. Soboleva, E. V. Porodenko, M. G. Chernysheva, V. I. Korobkov, I. Y. Myasnikov, G. A. Badun. Composite films based on polyvinyl alcohol and detonation nanodiamonds with modified surface. *Mater. Today: Proc.* **2018**, *5*, 25907–25910.

[104] M. G. Chernysheva, I. S. Chaschin, A. V. Sinolits, V. G. Vasil'ev, A. G. Popov, G. A. Badun, N. P. Bakuleva. Chitosan-nanodiamond composites for improving heart valve biological prostheses materials: preparation and mechanical trial. *Fuller. Nanotub. Carbon Nanostructures* **2020**, *28*, 256–261.

[105] S. Morimune-Moriya, T. Hashimoto, R. Haga, H. Tanahashi. Enhanced mechanical and thermal properties of nanodiamond reinforced low density polyethylene nanocomposites. *J. Appl. Polym. Sci.* **2021**, 50929.

[106] a) Q. Zhang, V. N. Mochalin, I. Neitzel, I. Y. Knoke, J. Han, C. A. Klug, J. G. Zhou, P. I. Lelkes, Y. Gogotsi. Fluorescent PLLA-nanodiamond composites for bone tissue engineering. *Biomaterials* **2011**, *32*, 87–94; b) A. Rehman, S. Houshyar, X. Wang. Nanodiamond-Based Fibrous Composites: A Review of Fabrication Methods, Properties, and Applications. *ACS Appl. Nano Mater.* **2021**, *4*, 2317–2332; c) Q. Zhang, V. N. Mochalin, I. Neitzel, K. Hazeli, J. Niu, A. Kontsos, J. G. Zhou, P. I. Lelkes, Y. Gogotsi. Mechanical properties and biomineralization of multifunctional nanodiamond-PLLA composites for bone tissue engineering. *Biomaterials* **2012**, *33*, 5067–5075; d) A. D. Salaam, M. Mishra, E. Nyairo, D. Dean. Electrospun Polyvinyl Alcohol/Nanodiamond Composite Scaffolds: Morphological, Structural, and Biological Analysis. *J. Biomater. Tissue. Eng.* **2014**, *4*, 173–180; e) C. Ribeiro, V. Sencadas, D. M. Correia, S. Lanceros-Méndez. Piezoelectric polymers as biomaterials for tissue engineering applications. *Colloids Surf. B* **2015**, *136*, 46–55; f) A. H. Rajabi, M. Jaffe, T. L. Arinzeh. Piezoelectric materials for tissue regeneration: A review. *Acta Biomater.* **2015**, *24*, 12–23; g) J. Nunes-Pereira, A. R. Silva, C. Ribeiro, S. Carabineiro, J. G. Buijnsters, S. Lanceros-Méndez. Nanodiamonds/poly(vinylidene fluoride) composites for tissue engineering applications. *Compos. B. Eng.* **2017**, *111*, 37–44.

[107] a) S. R. Hemelaar, A. Nagl, F. Bigot, M. M. Rodríguez-García, M. P. de Vries, M. Chipaux, R. Schirhagl. The interaction of fluorescent nanodiamond probes with cellular media. *Microchim. Acta* **2017**, *184*, 1001–1009; b) X. Kong, L. C. L. Huang, S.-C. V. Liau, C.-C. Han, H.-C. Chang. Polylysine-coated diamond nanocrystals for MALDI-TOF mass analysis of DNA oligonucleotides. *Anal. Chem.* **2005**, *77*, 4273–4277.

[108] T. Zheng, F. Perona Martínez, I. M. Storm, W. Rombouts, J. Sprakel, R. Schirhagl, R. de Vries. Recombinant Protein Polymers for Colloidal Stabilization and Improvement of Cellular Uptake of Diamond Nanosensors. *Anal. Chem.* **2017**, *89*, 12812–12820.

[109] A. E. Garcia-Bennett, A. Everest-Dass, I. Moroni, I. D. Rastogi, L. M. Parker, N. H. Packer, L. J. Brown. Influence of surface chemistry on the formation of a protein corona on nanodiamonds. *J. Mater. Chem. B* **2019**, *7*, 3383–3389.

[110] R. Eldawud, M. Reitzig, J. Opitz, Y. Rojansakul, W. Jiang, S. Nangia, C. Z. Dinu. Combinatorial approaches to evaluate nanodiamond uptake and induced cellular fate. *Nanotechnology* **2016**, *27*, 85107.

[111] a) S. Tenzer, D. Docter, J. Kuharev, A. Musyanovych, V. Fetz, R. Hecht, F. Schlenk, D. Fischer, K. Kiouptsi, C. Reinhardt, K. Landfester, H. Schild, M. Maskos, S. K. Knauer, R. H. Stauber. Rapid formation of plasma protein corona critically affects nanoparticle pathophysiology. *Nat. Nanotechnol.* **2013**, *8*, 772–781; b) E. Casals, T. Pfaller, A. Duschl, G. J. Oostingh, V. Puntes. Time evolution of the nanoparticle protein corona. *ACS Nano* **2010**, *4*, 3623–3632; c) M. Lundqvist, J. Stigler, T. Cedervall, T. Berggård, M. B. Flanagan, I. Lynch, G. Elia, K. Dawson. The evolution of the protein corona around nanoparticles: a test study. *ACS Nano* **2011**, *5*, 7503–7509; d) A. L. Barrán-Berdón, D. Pozzi, G. Caracciolo, A. L. Capriotti, G. Caruso, C. Cavaliere, A. Riccioli, S. Palchetti, A. Laganà. Time evolution of nanoparticle-protein corona in human plasma: relevance for targeted drug delivery. *Langmuir* **2013**, *29*, 6485–6494; e) M. Hadjidemetriou, Z. Al-Ahmady, K. Kostarelos. Time-evolution of in vivo protein corona onto blood-circulating PEGylated liposomal doxorubicin (DOXIL) nanoparticles. *Nanoscale* **2016**, *8*, 6948–6957; f) D. Khanal, Q. Lei, G. Pinget, D. A. Cheong, A. Gautam, R. Yusoff, B. Su, S. Yamaguchi, A. Kondyurin, J. C. Knowles, G. Georgiou, L. Macia, J.-H. Jang, I. Ramzan, K. W. Ng, W. Chrzanowski. The protein corona determines the cytotoxicity of

nanodiamonds: implications of corona formation and its remodelling on nanodiamond applications in biomedical imaging and drug delivery. *Nanoscale Adv.* **2020**, *2*, 4798–4812; g) A. Cox, P. Andreozzi, R. Dal Magro, F. Fiordaliso, A. Corbelli, L. Talamini, C. Chinello, F. Raimondo, F. Magni, M. Tringali, S. Krol, P. Jacob Silva, F. Stellacci, M. Masserini, F. Re. Evolution of Nanoparticle Protein Corona across the Blood-Brain Barrier. *ACS Nano* **2018**, *12*, 7292–7300.

[112] a) V. Leo. Effect of adsorbed proteins on the wettability of hydrophilic and hydrophobic solids. *Nature* **1962**, *196*, 476–477; b) M. Hadjidemetriou, K. Kostarelos. Nanomedicine: Evolution of the nanoparticle corona. *Nat. Nanotechnol.* **2017**, *12*, 288–290.

[113] C. Corbo, R. Molinaro, A. Parodi, N. E. Toledano Furman, F. Salvatore, E. Tasciotti. The impact of nanoparticle protein corona on cytotoxicity, immunotoxicity and target drug delivery. *Nanomedicine* **2016**, *11*, 81–100.

[114] L. Fusco, E. Avitabile, V. Armuzza, M. Orecchioni, A. Istif, D. Bedognetti, T. Da Ros, L. G. Delogu. Impact of the surface functionalization on nanodiamond biocompatibility: a comprehensive view on human blood immune cells. *Carbon* **2020**, *160*, 390–404.

[115] a) Y. Zhu, J. Li, W. Li, Y. Zhang, X. Yang, N. Chen, Y. Sun, Y. Zhao, C. Fan, Q. Huang. The biocompatibility of nanodiamonds and their application in drug delivery systems. *Theranostics* **2012**, *2*, 302–312; b) D. F. Moyano, K. Saha, G. Prakash, B. Yan, H. Kong, M. Yazdani, V. M. Rotello. Fabrication of corona-free nanoparticles with tunable hydrophobicity. *ACS Nano* **2014**, *8*, 6748–6755.

[116] K. Ulbrich, K. Holá, V. Šubr, A. Bakandritsos, J. Tuček, R. Zbořil. Targeted Drug Delivery with Polymers and Magnetic Nanoparticles: Covalent and Noncovalent Approaches, Release Control, and Clinical Studies. *Chem. Rev.* **2016**, *116*, 5338–5431.

[117] Y. Zou, S. Ito, F. Yoshino, Y. Suzuki, L. Zhao, N. Komatsu. Polyglycerol Grafting Shields Nanoparticles from Protein Corona Formation to Avoid Macrophage Uptake. *ACS Nano* **2020**, *14*, 7216–7226.

[118] D. F. Moyano, Y. Liu, F. Ayaz, S. Hou, P. Puangploy, B. Duncan, B. A. Osborne, V. M. Rotello. Immunomodulatory effects of coated gold nanoparticles in LPS-stimulated in vitro and in vivo murine model systems. *Chem* **2016**, *1*, 320–327.

[119] D. F. Moyano, M. Ray, V. M. Rotello. Nanoparticle–protein interactions. *MRS Bull.* **2014**, *39*, 1069–1073.

[120] a) S. Huo, Y. Jiang, A. Gupta, Z. Jiang, R. F. Landis, S. Hou, X.-J. Liang, V. M. Rotello. Fully Zwitterionic Nanoparticle Antimicrobial Agents through Tuning of Core Size and Ligand Structure. *ACS Nano* **2016**, *10*, 8732–8737; b) S. T. Kim, K. Saha, C. Kim, V. M. Rotello. The role of surface functionality in determining nanoparticle cytotoxicity. *Acc. Chem. Res.* **2013**, *46*, 681–691; c) J. B. Schlenoff. Zwitteration: coating surfaces with zwitterionic functionality to reduce nonspecific adsorption. *Langmuir* **2014**, *30*, 9625–9636; d) M. Aramesh, O. Shimoni, K. Ostrikov, S. Prawer, J. Cervenka. Surface charge effects in protein adsorption on nanodiamonds. *Nanoscale* **2015**, *7*, 5726–5736.

[121] A. S. Hoffman. Non-Fouling Surface Technologies. *J. Biomater. Sci., Polym. Ed.* **1999**, *10*, 1011–1014.

[122] a) E. Ostuni, R. G. Chapman, R. E. Holmlin, S. Takayama, G. M. Whitesides. A Survey of Structure−Property Relationships of Surfaces that Resist the Adsorption of Protein. *Langmuir* **2001**, *17*, 5605–5620; b) R. G. Chapman, E. Ostuni, S. Takayama, R. E. Holmlin, L. Yan, G. M. Whitesides. Surveying for Surfaces that Resist the Adsorption of Proteins. *J. Am. Chem. Soc.* **2000**, *122*, 8303–8304.

[123] P. Harder, M. Grunze, R. Dahint, G. M. Whitesides, P. E. Laibinis. Molecular Conformation in Oligo(ethylene glycol)-Terminated Self-Assembled Monolayers on Gold and Silver Surfaces Determines Their Ability To Resist Protein Adsorption. *J. Phys. Chem. B* **1998**, *102*, 426–436.

[124] a) K.-K. Liu, W.-W. Zheng, C.-C. Wang, Y.-C. Chiu, C.-L. Cheng, Y.-S. Lo, C. Chen, J.-I. Chao. Covalent linkage of nanodiamond-paclitaxel for drug delivery and cancer therapy. *Nanotechnology* **2010**, *21*, 315106; b) N. Prabhakar, M. H. Khan, M. Peurla, H.-C. Chang, P. E. Hänninen, J. M. Rosenholm. Intracellular Trafficking of Fluorescent Nanodiamonds and Regulation of Their Cellular Toxicity. *ACS Omega* **2017**, *2*, 2689–2693; c) I. S. Raja, S.-J. Song, M. S. Kang, Y. B. Lee, B. Kim, S. W. Hong, S. J. Jeong, J.-C. Lee, D.-W. Han. Toxicity of Zero- and One-Dimensional Carbon Nanomaterials. *Nanomaterials* **2019**, *9*, 1214.

[125] D. Khanal, H. Hau, A. Kondyurin, D. Fu, I. Ramzan, W. Chrzanowski. Nanotoxicity of nanodiamond in two and three dimensional liver models. *Int. J. Nanotechnol.* **2017**, *14*, 133.

[126] M. H. Alkahtani, F. Alghannam, L. Jiang, A. Almethen, A. A. Rampersaud, R. Brick, C. L. Gomes, M. O. Scully, P. R. Hemmer. Fluorescent nanodiamonds: past, present, and future. *Nanophotonics* **2018**, *7*, 1423–1453.

[127] J. Karpeta-Kaczmarek, A. Kędziorski, M. A. Augustyniak-Jabłokow, M. Dziewięcka, M. Augustyniak. Chronic toxicity of nanodiamonds can disturb development and reproduction of Acheta domesticus L. *Environ. Res.* **2018**, *166*, 602–609.

[128] Y.-C. Lin, K.-T. Wu, Z.-R. Lin, E. Perevedentseva, A. Karmenyan, M.-D. Lin, C.-L. Cheng. Nanodiamond for biolabelling and toxicity evaluation in the zebrafish embryo in vivo. *J. Biophotonics* **2016**, *9*, 827–836.

[129] N. Mohan, C.-S. Chen, H.-H. Hsieh, Y.-C. Wu, H.-C. Chang. In vivo imaging and toxicity assessments of fluorescent nanodiamonds in Caenorhabditis elegans. *Nano Lett.* **2010**, *10*, 3692–3699.

[130] S.-J. Yu, M.-W. Kang, H.-C. Chang, K.-M. Chen, Y.-C. Yu. Bright fluorescent nanodiamonds: no photobleaching and low cytotoxicity. *J. Am. Chem. Soc.* **2005**, *127*, 17604–17605.

[131] D.-K. Lee, S. Ha, S. Jeon, J. Jeong, D.-J. Kim, S. W. Lee, W.-S. Cho. The sp3/sp2 carbon ratio as a modulator of in vivo and in vitro toxicity of the chemically purified detonation-synthesized nanodiamond via the reactive oxygen species generation. *Nanotoxicology* **2020**, *14*, 1213–1226.

[132] L. Moore, J. Yang, T. T. H. Lan, E. Osawa, D.-K. Lee, W. D. Johnson, J. Xi, E. K.-H. Chow, D. Ho. Biocompatibility Assessment of Detonation Nanodiamond in Non-Human Primates and Rats Using Histological, Hematologic, and Urine Analysis. *ACS Nano* **2016**, *10*, 7385–7400.

[133] J. Wehling, R. Dringen, R. N. Zare, M. Maas, K. Rezwan. Bactericidal activity of partially oxidized nanodiamonds. *ACS Nano* **2014**, *8*, 6475–6483.

[134] a) A. M. Schrand, L. Dai, J. J. Schlager, S. M. Hussain, E. Osawa. Differential biocompatibility of carbon nanotubes and nanodiamonds. *Diam. Relat. Mater.* **2007**, *16*, 2118–2123; b) Y. Xing, W. Xiong, L. Zhu, E. Osawa, S. Hussin, L. Dai. DNA damage in embryonic stem cells caused by nanodiamonds. *ACS Nano* **2011**, *5*, 2376–2384; c) L. Moore, V. Grobárová, H. Shen, H. B. Man, J. Míčová, M. Ledvina, J. Štursa, M. Nesladek, A. Fišerová, D. Ho. Comprehensive interrogation of the cellular response to fluorescent, detonation and functionalized nanodiamonds. *Nanoscale* **2014**, *6*, 11712–

11721; d) T.-C. Hsu, K.-K. Liu, H.-C. Chang, E. Hwang, J.-I. Chao. Labeling of neuronal differentiation and neuron cells with biocompatible fluorescent nanodiamonds. *Sci. Rep.* **2014**, *4*, 5004; e) K.-K. Liu, C.-L. Cheng, C.-C. Chang, J.-I. Chao. Biocompatible and detectable carboxylated nanodiamond on human cell. *Nanotechnology* **2007**, *18*, 325102; f) S. P. Blaber, C. J. Hill, R. A. Webster, J. M. Say, L. J. Brown, S.-C. Wang, G. Vesey, B. R. Herbert. Effect of labeling with iron oxide particles or nanodiamonds on the functionality of adipose-derived mesenchymal stem cells. *PloS one* **2013**, *8*, e52997; g) E. K. Chow, X.-Q. Zhang, M. Chen, R. Lam, E. Robinson, H. Huang, D. Schaffer, E. Osawa, A. Goga, D. Ho. Nanodiamond therapeutic delivery agents mediate enhanced chemoresistant tumor treatment. *Sci. Transl. Med.* **2011**, *3*, 73ra21; h) L.-W. Tsai, Y.-C. Lin, E. Perevedentseva, A. Lugovtsov, A. Priezzhev, C.-L. Cheng. Nanodiamonds for Medical Applications: Interaction with Blood in Vitro and in Vivo. *Int. J. Mol. Sci.* **2016**, *17*, 1111; i) Y. Yuan, X. Wang, G. Jia, J.-H. Liu, T. Wang, Y. Gu, S.-T. Yang, S. Zhen, H. Wang, Y. Liu. Pulmonary toxicity and translocation of nanodiamonds in mice. *Diam. Relat. Mater.* **2010**, *19*, 291–299; j) Y. Yuan, Y. Chen, J.-H. Liu, H. Wang, Y. Liu. Biodistribution and fate of nanodiamonds in vivo. *Diam. Relat. Mater.* **2009**, *18*, 95–100.

[135] a) L. Marcon, F. Riquet, D. Vicogne, S. Szunerits, J.-F. Bodart, R. Boukherroub. Cellular and in vivo toxicity of functionalized nanodiamond in Xenopus embryos. *J. Mater. Chem.* **2010**, *20*, 8064; b) N. Dworak, M. Wnuk, J. Zebrowski, G. Bartosz, A. Lewinska. Genotoxic and mutagenic activity of diamond nanoparticles in human peripheral lymphocytes in vitro. *Carbon* **2014**, *68*, 763–776; c) A. P. Puzyr, D. A. Neshumayev, S. V. Tarskikh, G. V. Makarskaya, V. Dolmatov, V. S. Bondar. Destruction of human blood cells in interaction with detonation nanodiamonds in experiments in vitro. *Diam. Relat. Mater.* **2004**, *13*, 2020–2023; d) K. Solarska, A. Gajewska, W. Kaczorowski, G. Bartosz, K. Mitura. Effect of nanodiamond powders on the viability and production of reactive oxygen and nitrogen species by human endothelial cells. *Diam. Relat. Mater.* **2012**, *21*, 107–113; e) A. Cid, A. Picado, J. B. Correia, R. Chaves, H. Silva, J. Caldeira, A. P. A. de Matos, M. S. Diniz. Oxidative stress and histological changes following exposure to diamond nanoparticles in the freshwater Asian clam Corbicula fluminea (Müller, 1774). *J. Hazard. Mater.* **2015**, *284*, 27–34; f) E. Mendonça, M. Diniz, L. Silva, I. Peres, L. Castro, J. B. Correia, A. Picado. Effects of diamond nanoparticle exposure on the internal structure and reproduction of Daphnia magna. *J. Hazard. Mater.* **2011**, *186*, 265–271; g) X. Zhang, J. Yin, C. Kang, J. Li, Y. Zhu, W. Li, Q. Huang, Z. Zhu. Biodistribution and toxicity of nanodiamonds in mice after intratracheal instillation. *Toxicol. Lett.* **2010**, *198*, 237–243.

[136] M. Wang, M. Thanou. Targeting nanoparticles to cancer. *Pharmacol. Res.* **2010**, *62*, 90–99.

[137] T. S. Huang, Y. Tzeng, Y. K. Liu, Y. C. Chen, K. R. Walker, R. Guntupalli, C. Liu. Immobilization of antibodies and bacterial binding on nanodiamond and carbon nanotubes for biosensor applications. *Diam. Relat. Mater.* **2004**, *13*, 1098–1102.

[138] a) M. Mkandawire, A. Pohl, T. Gubarevich, V. Lapina, D. Appelhans, G. Rödel, W. Pompe, J. Schreiber, J. Opitz. Selective targeting of green fluorescent nanodiamond conjugates to mitochondria in HeLa cells. *J. Biophotonics* **2009**, *2*, 596–606; b) X. L. Kong, L. C. L. Huang, C.-M. Hsu, W.-H. Chen, C.-C. Han, H.-C. Chang. High-affinity capture of proteins by diamond nanoparticles for mass spectrometric analysis. *Anal. Chem.* **2005**, *77*, 259–265; c) W. Zhang, K. Patel, A. Schexnider, S. Banu, A. D. Radadia.

Nanostructuring of biosensing electrodes with nanodiamonds for antibody immobilization. *ACS Nano* **2014**, *8*, 1419–1428.

[139] a) J. Slegerova, M. Hajek, I. Rehor, F. Sedlak, J. Stursa, M. Hruby, P. Cigler. Designing the nanobiointerface of fluorescent nanodiamonds: highly selective targeting of glioma cancer cells. *Nanoscale* **2015**, *7*, 415–420; b) M. D. Torelli, A. G. Rickard, M. V. Backer, D. S. Filonov, N. A. Nunn, A. V. Kinev, J. M. Backer, G. M. Palmer, O. A. Shenderova. Targeting Fluorescent Nanodiamonds to Vascular Endothelial Growth Factor Receptors in Tumor. *Bioconjugate Chem.* **2019**, *30*, 604–613.

[140] A. Morita, T. Hamoh, A. Sigaeva, N. Norouzi, A. Nagl, K. J. van der Laan, E. P. P. Evans, R. Schirhagl. Targeting Nanodiamonds to the Nucleus in Yeast Cells. *Nanomaterials* **2020**, *10*, 1962.

[141] A. Ermakova, G. Pramanik, J.-M. Cai, G. Algara-Siller, U. Kaiser, T. Weil, Y.-K. Tzeng, H. C. Chang, L. P. McGuinness, M. B. Plenio, B. Naydenov, F. Jelezko. Detection of a few metallo-protein molecules using color centers in nanodiamonds. *Nano Lett.* **2013**, *13*, 3305–3309.

[142] F. C. Ziem, N. S. Götz, A. Zappe, S. Steinert, J. Wrachtrup. Highly sensitive detection of physiological spins in a microfluidic device. *Nano Lett.* **2013**, *13*, 4093–4098.

[143] a) S. Kaufmann, D. A. Simpson, L. T. Hall, V. Perunicic, P. Senn, S. Steinert, L. P. McGuinness, B. C. Johnson, T. Ohshima, F. Caruso, J. Wrachtrup, R. E. Scholten, P. Mulvaney, L. Hollenberg. Detection of atomic spin labels in a lipid bilayer using a single-spin nanodiamond probe. *ACS Nano* **2013**, *110*, 10894–10898; b) J.-P. Tetienne, T. Hingant, L. Rondin, A. Cavaillès, L. Mayer, G. Dantelle, T. Gacoin, J. Wrachtrup, J.-F. Roch, V. Jacques. Spin relaxometry of single nitrogen-vacancy defects in diamond nanocrystals for magnetic noise sensing. *Phys. Rev. B* **2013**, *87*, 235436; c) K. Yano, T. Matsumoto, Y. Okamoto, K. Bito, N. Kurokawa, T. Hasebe, A. Hotta. Gadolinium-Complexed Carboxylated Nanodiamond Particles for Magnetic Resonance Imaging of the Lymphatic System. *ACS Appl. Nano Mater.* **2021**, *4*, 1702–1711.

[144] A. Kuwahata, T. Kitaizumi, K. Saichi, T. Sato, R. Igarashi, T. Ohshima, Y. Masuyama, T. Iwasaki, M. Hatano, F. Jelezko, M. Kusakabe, T. Yatsui, M. Sekino. Magnetometer with nitrogen-vacancy center in a bulk diamond for detecting magnetic nanoparticles in biomedical applications. *Sci. Rep.* **2020**, *10*, 2483.

[145] a) L. T. Hall, D. A. Simpson, L. Hollenberg. Nanoscale sensing and imaging in biology using the nitrogen-vacancy center in diamond. *MRS Bull.* **2013**, *38*, 162–167; b) G. Kucsko, P. C. Maurer, N. Y. Yao, M. Kubo, H. J. Noh, P. K. Lo, H. Park, M. D. Lukin. Nanometre-scale thermometry in a living cell. *Nature* **2013**, *500*, 54–58; c) H. An, Z. Yin, C. Mitchell, A. Semnani, A. R. Hajrasouliha, M. Hosseini. Nanodiamond ensemble-based temperature measurement in living cells and its limitations. *Meas. Sci. Technol.* **2021**, *32*, 15701.

[146] D. A. Simpson, E. Morrisroe, J. M. McCoey, A. H. Lombard, D. C. Mendis, F. Treussart, L. T. Hall, S. Petrou, L. C. L. Hollenberg. Non-Neurotoxic Nanodiamond Probes for Intraneuronal Temperature Mapping. *ACS Nano* **2017**, *11*, 12077–12086.

[147] a) J. Wang, F. Feng, J. Zhang, J. Chen, Z. Zheng, L. Guo, W. Zhang, X. Song, G. Guo, L. Fan, C. Zou, L. Lou, W. Zhu, G. Wang. High-sensitivity temperature sensing using an implanted single nitrogen-vacancy center array in diamond. *Phys. Rev. B* **2015**, *91*, 155404; b) J. Cai, F. Jelezko, M. B. Plenio, A. Retzker. Diamond-based single-molecule magnetic resonance spectroscopy. *New J. Phys.* **2013**, *15*, 13020.

[148] a) K. Xia, C.-F. Liu, W.-H. Leong, M.-H. Kwok, Z.-Y. Yang, X. Feng, R.-B. Liu, Q. Li. Nanometer-precision non-local deformation reconstruction using nanodiamond sensing. *Nat. Commun.* **2019**, *10*, 3259; b) S. Castelletto, L. Rosa, A. Boretti. Micro-manipulation of nanodiamonds containing NV centers for quantum applications. *Diam. Relat. Mater.* **2020**, *106*, 107840; c) J. Teissier, A. Barfuss, P. Appel, E. Neu, P. Maletinsky. Strain coupling of a nitrogen-vacancy center spin to a diamond mechanical oscillator. *Phys. Rev. Lett.* **2014**, *113*, 20503; d) P. Ovartchaiyapong, K. W. Lee, B. A. Myers, A. C. B. Jayich. Dynamic strain-mediated coupling of a single diamond spin to a mechanical resonator. *Nat. Commun.* **2014**, *5*, 4429.

[149] P. Appel, E. Neu, M. Ganzhorn, A. Barfuss, M. Batzer, M. Gratz, A. Tschöpe, P. Maletinsky. Fabrication of all diamond scanning probes for nanoscale magnetometry. *Rev. Sci. Instrum.* **2016**, *87*, 63703.

[150] J. Tisler, R. Reuter, A. Lämmle, F. Jelezko, G. Balasubramanian, P. R. Hemmer, F. Reinhard, J. Wrachtrup. Highly efficient FRET from a single nitrogen-vacancy center in nanodiamonds to a single organic molecule. *ACS Nano* **2011**, *5*, 7893–7898.

[151] N. Mohan, Y.-K. Tzeng, L. Yang, Y.-Y. Chen, Y. Y. Hui, C.-Y. Fang, H.-C. Chang. Sub-20-nm fluorescent nanodiamonds as photostable biolabels and fluorescence resonance energy transfer donors. *Adv. Mater.* **2010**, *22*, 843–847.

[152] Y. Romach, C. Müller, T. Unden, L. J. Rogers, T. Isoda, K. M. Itoh, M. Markham, A. Stacey, J. Meijer, S. Pezzagna, B. Naydenov, L. P. McGuinness, N. Bar-Gill, F. Jelezko. Spectroscopy of surface-induced noise using shallow spins in diamond. *Phys. Rev. Lett.* **2015**, *114*, 17601.

[153] a) E. Neu, D. Steinmetz, J. Riedrich-Möller, S. Gsell, M. Fischer, M. Schreck, C. Becher. Single photon emission from silicon-vacancy colour centres in chemical vapour deposition nano-diamonds on iridium. *New J. Phys.* **2011**, *13*, 25012; b) A. Sipahigil, K. D. Jahnke, L. J. Rogers, T. Teraji, J. Isoya, A. S. Zibrov, F. Jelezko, M. D. Lukin. Indistinguishable photons from separated silicon-vacancy centers in diamond. *Phys. Rev. Lett.* **2014**, *113*, 113602.

[154] a) Di Wu, A. C. Sedgwick, T. Gunnlaugsson, E. U. Akkaya, J. Yoon, T. D. James. Fluorescent chemosensors: the past, present and future. *Chem. Soc. Rev.* **2017**, *46*, 7105–7123; b) C. K. P. Truong, T. D. D. Nguyen, I.-S. Shin. Electrochemiluminescent Chemosensors for Clinical Applications: A Review. *BioChip J.* **2019**, *13*, 203–216; c) G. Fukuhara. Analytical supramolecular chemistry: Colorimetric and fluorimetric chemosensors. *J. Photochem. Photobiol. C* **2020**, *42*, 100340; d) M. Mayer, A. J. Baeumner. A Megatrend Challenging Analytical Chemistry: Biosensor and Chemosensor Concepts Ready for the Internet of Things. *Chem. Rev.* **2019**, *119*, 7996–8027; e) L. Jiang, I. Santiago, J. Foord. Nanocarbon and nanodiamond for high performance phenolics sensing. *Commun. Chem.* **2018**, *1*, 43; f) T. A. Ivandini, Y. Einaga in *Springer Series on Chemical Sensors and Biosensors, Methods and Applications*, *Vol. 17* (Hrsg.: C. Kranz), Springer International Publishing, Cham, **2019**, S. 67–86.

[155] S. Su, L. Han, L. Gao, Q. Ren, M. Nie, Z. Zhu, H. Wan, H. Liu, N. Wu. Spark plasma sintering compaction of hybrid nanodiamond/carbon nanotubes/metal electrode and its application. *Diam. Relat. Mater.* **2020**, *104*, 107746.

[156] M. Shellaiah, T. Simon, P. Venkatesan, K. W. Sun, F.-H. Ko, S.-P. Wu. Nanodiamonds conjugated to gold nanoparticles for colorimetric detection of clenbuterol and chromium(III) in urine. *Mikrochim. Acta* **2017**, *185*, 74.

[157] N. Baghban, E. Yilmaz, M. Soylak. Nanodiamond/MoS 2 nanorod composite as a novel sorbent for fast and effective vortex-assisted micro solid phase extraction of lead(II) and copper(II) for their flame atomic absorption spectrometric detection. *J. Mol. Liq.* **2017**, *234*, 260–267.

[158] E. Demir, R. Marcos. Toxic and genotoxic effects of graphene and multi-walled carbon nanotubes. *J. Toxicol. Environ. Health, Part A* **2018**, *81*, 645–660.

[159] P. Ekaterina, R. Nikita, M. Olga, B. Alexey, B. Vladimir. A Supramolecular Indicator System for Detecting Urea Based on the Cellulose-Nanodiamond Composite Material and Urease. *Int. J. Med. Nano. Res.* **2019**, *6*, 29.

[160] a) M. Aronson, O. Medalia, L. Schori, D. Mirelman, N. Sharon, I. Ofek. Prevention of colonization of the urinary tract of mice with Escherichia coli by blocking of bacterial adherence with methyl alpha-D-mannopyranoside. *J. Infect. Dis.* **1979**, *139*, 329–332; b) M. Hartmann, P. Betz, Y. Sun, S. N. Gorb, T. K. Lindhorst, A. Krueger. Saccharide-modified nanodiamond conjugates for the efficient detection and removal of pathogenic bacteria. *Chem. Eur. J.* **2012**, *18*, 6485–6492.

[161] a) H. B. Bradl, *Heavy metals in the environment*. *Origin, interaction and remediation*, Elsevier/Acad. Press, Amsterdam, **2005**; b) Y. Cao, M. A. Skaug, O. Andersen, J. Aaseth. Chelation therapy in intoxications with mercury, lead and copper. *J. Trace Elem. Med. Biol.* **2015**, *31*, 188–192; c) J. O. Nriagu. A History of Global Metal Pollution. *Science* **1996**, *272*, 223-224; d) K. K. Kesari (Hrsg.) *Environmental science and engineering, environmental science*, Springer, Cham, Switzerland, **2019**.

[162] P. B. Tchounwou, C. G. Yedjou, A. K. Patlolla, D. J. Sutton. Heavy metal toxicity and the environment. *Experientia Suppl.* **2012**, *101*, 133–164.

[163] M. Jaishankar, T. Tseten, N. Anbalagan, B. B. Mathew, K. N. Beeregowda. Toxicity, mechanism and health effects of some heavy metals. *Interdiscip. Toxicol.* **2014**, *7*, 60–72.

[164] a) N. Fernández, R. Beiras. Combined Toxicity of Dissolved Mercury With Copper, Lead and Cadmium on Embryogenesis and Early Larval Growth of the Paracentrotus Lividus Sea-Urchin. *Ecotoxicology* **2001**, *10*, 263–271; b) B. Volesky, Z. R. Holan. Biosorption of heavy metals. *Biotech. Prog.* **1995**, *11*, 235–250.

[165] a) P. Gottesfeld. Time to ban lead in industrial paints and coatings. *Public Health Front.* **2015**, *3*, 144; b) Scientific Opinion on Lead in Food. *EFSA J.* **2010**, *8*, 1570.

[166] N. Zhang, R. Qiao, J. Su, J. Yan, Z. Xie, Y. Qiao, X. Wang, J. Zhong. Recent Advances of Electrospun Nanofibrous Membranes in the Development of Chemosensors for Heavy Metal Detection. *Small* **2017**, *13*, 1604293.

[167] Z. Kowser, U. Rayhan, T. Akther, C. Redshaw, T. Yamato. A brief review on novel pyrene based fluorometric and colorimetric chemosensors for the detection of Cu 2+. *Mater. Chem. Front.* **2021**, *5*, 2173–2200.

[168] B. Valeur, I. Leray. Design principles of fluorescent molecular sensors for cation recognition. *Coord. Chem. Rev.* **2000**, *205*, 3–40.

[169] a) W. Cho, H. J. Lee, G. Choi, S. Choi, M. Oh. Dual changes in conformation and optical properties of fluorophores within a metal-organic framework during framework construction and associated sensing event. *J. Am. Chem. Soc.* **2014**, *136*, 12201–12204; b) J. Cho, T. Pradhan, Y. M. Lee, J. S. Kim, S. Kim. A calix2triazole2arene-based fluorescent chemosensor for probing the copper trafficking pathway in Wilson's disease. *Dalton. Trans.* **2014**, *43*, 16178–16182; c) J. K. Choi, S. H. Kim, J. Yoon, K.-H. Lee, R. A. Bartsch, J. S. Kim. A PCT-based, pyrene-armed calix[4]crown fluoroionophore. *J. Org. Chem.* **2006**, *71*, 8011–8015; d) P. K. Chung, S.-R. Liu, H.-F. Wang, S.-P. Wu. A

pyrene-based highly selective turn-on fluorescent chemosensor for iron(III) ions and its application in living cell imaging. *J. Fluoresc.* **2013**, *23*, 1139–1145; e) S. Karuppannan, J.-C. Chambron. Supramolecular chemical sensors based on pyrene monomer-excimer dual luminescence. *Chem. Asian J.* **2011**, *6*, 964–984; f) H. Maeda, M. Geshi, K. Hirose, T. Furuyama, M. Segi. Synthesis, fluorescence properties, and conformational analysis of ether-linked (1,8)pyrenophanes. *Tetrahedron* **2019**, *75*, 130512; g) Y. Zhou, C.-Y. Zhu, X.-S. Gao, X.-Y. You, C. Yao. Hg2+-selective ratiometric and "off-on" chemosensor based on the azadiene-pyrene derivative. *Org. Lett.* **2010**, *12*, 2566–2569; h) Z. Xu, N. J. Singh, J. Lim, J. Pan, H. N. Kim, S. Park, K. S. Kim, J. Yoon. Unique sandwich stacking of pyrene-adenine-pyrene for selective and ratiometric fluorescent sensing of ATP at physiological pH. *J. Am. Chem. Soc.* **2009**, *131*, 15528–15533; i) S. K. Kim, J. H. Bok, R. A. Bartsch, J. Y. Lee, J. S. Kim. A fluoride-selective PCT chemosensor based on formation of a static pyrene excimer. *Org. Lett.* **2005**, *7*, 4839–4842; j) J. S. Kim, M. G. Choi, K. C. Song, K. T. No, S. Ahn, S.-K. Chang. Ratiometric determination of Hg2+ ions based on simple molecular motifs of pyrene and dioxaoctanediamide. *Org. Lett.* **2007**, *9*, 1129–1132; k) M.-H. Yang, P. Thirupathi, K.-H. Lee. Selective and sensitive ratiometric detection of Hg(II) ions using a simple amino acid based sensor. *Org. Lett.* **2011**, *13*, 5028–5031; l) A. B. Othman, J. W. Lee, J.-S. Wu, J. S. Kim, R. Abidi, P. Thuéry, J. M. Strub, A. van Dorsselaer, J. Vicens. Calix4arene-based, Hg2+ -induced intramolecular fluorescence resonance energy transfer chemosensor. *J. Org. Chem.* **2007**, *72*, 7634–7640; m) S. K. Kim, S. H. Kim, H. J. Kim, S. H. Lee, S. W. Lee, J. Ko, R. A. Bartsch, J. S. Kim. Indium(III)-induced fluorescent excimer formation and extinction in calix4arene-fluoroionophores. *Inorg. Chem.* **2005**, *44*, 7866–7875; n) H.-W. Rhee, C.-R. Lee, S.-H. Cho, M.-R. Song, M. Cashel, H. E. Choy, Y.-J. Seok, J.-I. Hong. Selective fluorescent chemosensor for the bacterial alarmone (p)ppGpp. *J. Am. Chem. Soc.* **2008**, *130*, 784–785; o) X.-L. Ni, X. Zeng, C. Redshaw, T. Yamato. Ratiometric fluorescent receptors for both Zn2+ and H2PO4(-) ions based on a pyrenyl-linked triazole-modified homooxacalix3arene: a potential molecular traffic signal with an R-S latch logic circuit. *J. Org. Chem.* **2011**, *76*, 5696–5702; p) H. S. Jung, M. Park, D. Y. Han, E. Kim, C. Lee, S. Ham, J. S. Kim. Cu2+ ion-induced self-assembly of pyrenylquinoline with a pyrenyl excimer formation. *Org. Lett.* **2009**, *11*, 3378–3381; q) J. Fernández-Lodeiro, C. Núñez, C. S. de Castro, E. Bértolo, J. S. Seixas de Melo, J. L. Capelo, C. Lodeiro. Steady-state and time-resolved investigations on pyrene-based chemosensors. *Inorg. Chem.* **2013**, *52*, 121–129; r) J. Hoche, H.-C. Schmitt, A. Humeniuk, I. Fischer, R. Mitrić, M. I. S. Röhr. The mechanism of excimer formation: an experimental and theoretical study on the pyrene dimer. *Phys. Chem. Chem. Phys.* **2017**, *19*, 25002–25015.

[170] X. Sun, Y.-W. Wang, Y. Peng. A selective and ratiometric bifunctional fluorescent probe for Al3+ ion and proton. *Org. Lett.* **2012**, *14*, 3420–3423.

[171] T. M. Figueira-Duarte, K. Müllen. Pyrene-based materials for organic electronics. *Chem. Rev.* **2011**, *111*, 7260–7314.

[172] A. Laurent. Pyrene from coal tar. *Ann. Chim. Phys* **1837**, *66*, 136–137.

[173] J. B. Birks, M. D. Lumb, I. H. Munro. 'Excimer' fluorescence V. Influence of solvent viscosity and temperature. *Proc. R. Soc. Lond. A* **1964**, *280A*, 289.

[174] a) R. H. Templer, S. J. Castle, A. R. Curran, G. Rumbles, D. R. Klug. Sensing isothermal changes in the lateral pressure in model membranes using di-pyrenyl phosphatidylcholine. *Faraday Disc.* **1998**, *111*, 41-53; b) M. R. Pokhrel, S. H. Bossmann. Synthesis, Characterization, and First Application of High Molecular Weight Polyacrylic

Acid Derivatives Possessing Perfluorinated Side Chains and Chemically Linked Pyrene Labels. *J. Phys. Chem. B.* **2000**, *104*, 2215–2223; c) Y. Fujiwara, Y. Amao. Optical oxygen sensor based on controlling the excimer formation of pyrene-1-butylic acid chemisorption layer onto nano-porous anodic oxidized aluminium plate by myristic acid. *Sens. Actuators B Chem.* **2003**, *89*, 58–61; d) Eric D. Lee, Thomas C. Werner, W. Rudolf. Seitz. Luminescence ratio indicators for oxygen. *Anal. Chem.* **1987**, *59*, 279–283; e) T. Aoyagi, H. Ikeda, A. Ueno. Fluorescence Properties, Induced-Fit Guest Binding and Molecular Recognition Abilities of Modified γ -Cyclodextrins Bearing Two Pyrene Moieties. *Bull. Chem. Soc. Jpn.* **2001**, *74*, 157–164; f) H. Ikeda, M. Nakamura, N. Ise, N. Oguma, A. Nakamura, T. Ikeda, F. Toda, A. Ueno. Fluorescent Cyclodextrins for Molecule Sensing: Fluorescent Properties, NMR Characterization, and Inclusion Phenomena of N -Dansylleucine-Modified Cyclodextrins. *J. Am. Chem. Soc.* **1996**, *118*, 10980–10988; g) A. Ueno, I. Suzuki, T. Osa. Host-guest sensory systems for detecting organic compounds by pyrene excimer fluorescence. *Anal. Chem.* **1990**, *62*, 2461–2466; h) J. S. Yang, C. S. Lin, C. Y. Hwang. Cu2+-induced blue shift of the pyrene excimer emission: a new signal transduction mode of pyrene probes. *Org. Lett.* **2001**, *3*, 889–892; i) R.-H. Yang, W.-H. Chan, A. W. M. Lee, P.-F. Xia, H.-K. Zhang, K. Li. A ratiometric fluorescent sensor for Ag(I) with high selectivity and sensitivity. *J. Am. Chem. Soc.* **2003**, *125*, 2884–2885; j) B. Bodenant, F. Fages, M.-H. Delville. Metal-Induced Self-Assembly of a Pyrene-Tethered Hydroxamate Ligand for the Generation of Multichromophoric Supramolecular Systems. The Pyrene Excimer as Switch for Iron(III)-Driven Intramolecular Fluorescence Quenching. *J. Am. Chem. Soc.* **1998**, *120*, 7511–7519.

[175] K. Kalyanasundaram, J. K. Thomas. Environmental effects on vibronic band intensities in pyrene monomer fluorescence and their application in studies of micellar systems. *J. Am. Chem. Soc.* **1977**, *99*, 2039.

[176] J. Merz, J. Fink, A. Friedrich, I. Krummenacher, H. H. Al Mamari, S. Lorenzen, M. Haehnel, A. Eichhorn, M. Moos, M. Holzapfel, H. Braunschweig, C. Lambert, A. Steffen, L. Ji, T. B. Marder. Pyrene Molecular Orbital Shuffle-Controlling Excited State and Redox Properties by Changing the Nature of the Frontier Orbitals. *Chem. Eur. J.* **2017**, *23*, 13164–13180.

[177] D. N. Coventry, A. S. Batsanov, A. E. Goeta, J. A. K. Howard, T. B. Marder, R. N. Perutz. Selective Ir-catalysed borylation of polycyclic aromatic hydrocarbons: structures of naphthalene-2,6-bis(boronate), pyrene-2,7-bis(boronate) and perylene-2,5,8,11-tetra(boronate) esters. *Chem. Commun.* **2005**, 2172–2174.

[178] A. G. Crawford, A. D. Dwyer, Z. Liu, A. Steffen, A. Beeby, L.-O. Pålsson, D. J. Tozer, T. B. Marder. Experimental and theoretical studies of the photophysical properties of 2- and 2,7-functionalized pyrene derivatives. *J. Am. Chem. Soc.* **2011**, *133*, 13349–13362.

[179] J. M. Casas-Solvas, J. D. Howgego, A. P. Davis. Synthesis of substituted pyrenes by indirect methods. *Org. Biomol. Chem.* **2014**, *12*, 212–232.

[180] X. Feng, J.-Y. Hu, C. Redshaw, T. Yamato. Functionalization of Pyrene To Prepare Luminescent Materials-Typical Examples of Synthetic Methodology. *Chem. Eur. J.* **2016**, *22*, 11898–11916.

[181] R. Kurata, A. Ito, M. Gon, K. Tanaka, Y. Chujo. Diarylamino- and Diarylboryl-Substituted Donor-Acceptor Pyrene Derivatives: Influence of Substitution Pattern on Their Photophysical Properties. *J. Org. Chem.* **2017**, *82*, 5111–5121.

[182] a) I. A. I. Mkhalid, J. H. Barnard, T. B. Marder, J. M. Murphy, J. F. Hartwig. C-H activation for the construction of C-B bonds. *Chem. Rev.* **2010**, *110*, 890–931; b) L. Ji, K.

Fucke, S. K. Bose, T. B. Marder. Iridium-catalyzed borylation of pyrene: irreversibility and the influence of ligand on selectivity. *J. Org. Chem.* **2015**, *80*, 661–665; c) A. G. Crawford, Z. Liu, I. A. I. Mkhalid, M.-H. Thibault, N. Schwarz, G. Alcaraz, A. Steffen, J. C. Collings, A. S. Batsanov, J. A. K. Howard, T. B. Marder. Synthesis of 2- and 2,7-functionalized pyrene derivatives: an application of selective C-H borylation. *Chem. Eur. J.* **2012**, *18*, 5022–5035.

[183] a) E. W. Thulstrup, J. W. Downing, J. Michl. Excited singlet states of pyrene. Polarization directions and magnetic circular dichroism of azapyrenes. *Chem. Phys.* **1977**, *23*, 307–319; b) F. W. Langkilde, E. W. Thulstrup, J. Michl. The effect of solvent environment on molecular electronic transition moment directions: Symmetry lowering in pyrene. *J. Chem. Phys.* **1983**, *78*, 3372–3381.

[184] a) L. Ji, R. M. Edkins, A. Lorbach, I. Krummenacher, C. Brückner, A. Eichhorn, H. Braunschweig, B. Engels, P. J. Low, T. B. Marder. Electron Delocalization in Reduced Forms of 2-(BMes2)pyrene and 2,7-Bis(BMes2)pyrene. *J. Am. Chem. Soc.* **2015**, *137*, 6750–6753; b) L. Ji, A. Lorbach, R. M. Edkins, T. B. Marder. Synthesis and photophysics of a 2,7-disubstituted donor-acceptor pyrene derivative: an example of the application of sequential Ir-catalyzed C-H borylation and substitution chemistry. *J. Org. Chem.* **2015**, *80*, 5658–5665.

[185] a) Y. Zhou, F. Wang, Y. Kim, S.-J. Kim, J. Yoon. Cu2+-selective ratiometric and "off-on" sensor based on the rhodamine derivative bearing pyrene group. *Org. Lett.* **2009**, *11*, 4442–4445; b) N. Zhang, J. Xu, C. Xue. Core–shell structured mesoporous silica nanoparticles equipped with pyrene-based chemosensor: Synthesis, characterization, and sensing activity towards Hg(II). *J. Lumin.* **2011**, *131*, 2021–2025; c) I. K. Astakhova, E. Samokhina, B. R. Babu, J. Wengel. Novel (phenylethynyl)pyrene-LNA constructs for fluorescence SNP sensing in polymorphic nucleic acid targets. *ChemBioChem* **2012**, *13*, 1509–1519.

[186] a) Q. Hu, S. Chen, Z. Wang, Z. Zhang. Improving selectivity of ion-sensitive membrane by polyethylene glycol doping. *Sens. Actuators B Chem.* **2021**, *328*, 128955; b) S. Zalipsky. Chemistry of polyethylene glycol conjugates with biologically active molecules. *Adv. Drug Deliv. Rev.* **1995**, *16*, 157–182; c) A. A. D'souza, R. Shegokar. Polyethylene glycol (PEG): a versatile polymer for pharmaceutical applications. *Expert Opin. Drug Deliv.* **2016**, *13*, 1257–1275; d) D. Hutanu. Recent Applications of Polyethylene Glycols (PEGs) and PEG Derivatives. *Mod. Chem. Appl.* **2014**, *2*, 1000132; e) A. Hamta, M. R. Dehghani. Application of polyethylene glycol based aqueous two-phase systems for extraction of heavy metals. *J. Mol. Liq.* **2017**, *231*, 20–24.

[187] K. P. Antonsen, A.S. Hoffmann (Hrsg.). Polyethylene Glycol Chemistry: Biotechnical and Biomedical Applications. *Water Structure of PEG Solutions by Differential Scanning Calorimetry*, Plenum Press, New York, **1992**.

[188] K. Knop, R. Hoogenboom, D. Fischer, U. S. Schubert. Poly(ethylene glycol) in drug delivery. *Angew. Chem. Int. Ed.* **2010**, *49*, 6288–6308; *Angew. Chem.* **2010**, *122*, 6430–6452.

[189] J. Fowles, M. Banton, J. Klapacz, H. Shen. A toxicological review of the ethylene glycol series. *Toxicol. Lett.* **2017**, *278*, 66–83.

[190] M. Formica, V. Fusi, L. Giorgi, M. Micheloni. New fluorescent chemosensors for metal ions in solution. *Coord. Chem. Rev.* **2012**, *256*, 170–192.

[191] B. Schulze, U. S. Schubert. Beyond click chemistry - supramolecular interactions of 1,2,3-triazoles. *Chem. Soc. Rev.* **2014**, *43*, 2522–2571.

[192] a) J. J. Bryant, U. H. F. Bunz. Click to bind: metal sensors. *Chem. Asian J.* **2013**, *8*, 1354–1367; b) E. Haldón, M. C. Nicasio, P. J. Pérez. Copper-catalysed azide-alkyne cycloadditions (CuAAC): an update. *Org. Biomol. Chem.* **2015**, *13*, 9528–9550; c) J. Cho, T. Pradhan, J. S. Kim, S. Kim. Bimodal calix2triazole2arene fluorescent ionophore. *Org. Lett.* **2013**, *15*, 4058–4061.

[193] M. S. Purdey, P. K. Capon, B. J. Pullen, P. Reineck, N. Schwarz, P. J. Psaltis, S. J. Nicholls, B. C. Gibson, A. D. Abell. An organic fluorophore-nanodiamond hybrid sensor for photostable imaging and orthogonal, on-demand biosensing. *Sci. Rep.* **2017**, *7*, 15967.

[194] C. K. Kim, P. Ghosh, C. Pagliuca, Z.-J. Zhu, S. Menichetti, V. M. Rotello. Entrapment of hydrophobic drugs in nanoparticle monolayers with efficient release into cancer cells. *J. Am. Chem. Soc.* **2009**, *131*, 1360–1361.

Chapter 2

Zwitterion-Functionalized Nanodiamond with Superior Protein Repulsion, Colloidal Stability in Physiological Media

The following section is slightly modified and reproduced from V. Merz, J. Lenhart, Y. Vonhausen, M. E. Ortiz-Soto, J Seibel, A. Krueger, Zwitterion-Functionalized Detonation Nanodiamond with Superior Protein Repulsion and Colloidal Stability in Physiological Media, *Small* **2019**, 15, 1901551, *with permission from Wiley-VCH.*

2.1 Introduction

Surface functionalization of nanodiamond (ND) is an essential tool to control the chemical, physical and physiological behavior of these materials.[1,2] Within the carbon nanoparticle family, ND is an excellent candidate for biomedical applications.[3,4,5] Due to its largely nontoxic behavior *in vivo* it can be used for biological imaging,[5,6] sensing[3,7] and drug delivery.[3,8] Additionally, the variety of functional groups on the surface of nanodiamond, which also can be adjusted, may be used in a wide range of chemical reactions.[1,9,10] When NDs are exposed to bio-fluids, such as FBS, proteins adsorb on the surface of the particles and form *in situ* a "protein corona".[11–13] The protein corona can have a positive effect on ND's colloidal stability in the presence of salts and their uptake in cells.[13,14] However, the protein corona masks all the desired functionalities on the surface and changes the interaction with the surrounding fluid. Both, the colloidal stability and the physiological properties are not controllable anymore.[3] For the intended application of labelled NDs as markers, for imaging and for drug delivery, this alteration of the original diamond properties poses a major challenge. Therefore, the control of the surface to regulate the charge and agglomeration ability have to be investigated and improve to the effect of better hydrolytic stability. For other nanoparticles, different strategies involving the covalent binding of functional moieties have been discussed in the past. Successful examples included the grafting of ethylene glycols and zwitterionic moieties resulting in non-fouling nanoparticles with high colloidal stability.[7,15–17]

For ND, several examples for the coating with biocompatible shells, typically poly(ethylene glycol) (PEG) or PEG based systems, either adsorbed or covalently bound, are applicable in medicine and biology have been reported.[18,19] Due to the interaction with water, the ND's PEG-shell and other hydrophilic shells, for instance sugar, are strongly solvated, and thereby, it is protected from interactions with biomolecules in physiological media, resulting in colloidal stability.[20] It has been known for a long time, that the dispersibility of PEG stabilized particles is due to a combination of different factors. On the one hand, the entropic repulsion based on

the tendency of the polymer to retain the freedom of a random coil leads to a steric stabilization. On the other hand, the so called osmotic repulsion, which describes the resistance of the PEG shell to release any surrounding water enhances the colloidal stability.[21] However, one negative aspect associated with PEG is the formation of toxic degradation products due to its decomposition in physiological environments caused by oxygen and metal ions.[22,23] Thus, for long circulation times, the toxicity of PEGylated nanoparticles is substantially induced by this outer shell. Another disadvantage of PEG for colloidal stabilization is the length of the chain. For best repulsing interactions between proteins and PEG, the molecular weight of PEG has to be in the range of 500 to 2000 g/mol.[24] Thereby, not only the actual size of the nanoobject is significantly increased but a defined surface chemistry is difficult to maintain since the surface would be completely covered with PEG.

With the help of surface assembled monolayers (SAMs) of lipid-oligo(ethylene glycol) it has been found that a minimum of three ethylene glycol moieties is required to observe repulsion forces between the triglycol-functionalized surface and proteins.[25] It was found that an optimal toxicity profile is obtained with chain lengths between two and six glycol moieties.[23]

However, to fully harness the properties of nanodiamond not only the surface functionalization with oligo ethylene glycols has to be ensured in a defined way, but also the head group (HG) of each moiety is of great importance. The HGs interact as an outer shell directly with the components of physiological media and water and thus directly influence the dispersibility of the nanoparticles.[15] Additionally, HGs can be used in many applications, for instance to bind drugs or labels and to incorporate the nanoparticles in composite materials.[26]

It has been reported that suitable HGs enhance colloidal stability and improve the non-fouling characteristics of organic nanoparticles or hydrogels by using them as ionic shielding.[27] When HGs are positively or negatively charged they can repulse ionic molecules or nanoparticles with the same charge, but unfortunately, they will be highly attractive for oppositely charged ions. This can result in binding certain charged amino acids or even DNA.[21,28] For the control of colloid stability and protein adsorption in a physiological environment, this property however is rather detrimental.

Based on this knowledge, zwitterionic HGs attracted much attention due to their highly repulsive interaction with proteins.[16,17,29,30] From the four “Whiteside rules”,[31] this behavior

can be rationalized: namely, zwitterionic moieties are highly hydrophilic (rule #1), possess hydrogen bond acceptors (#2) but no donors (#3) and they exhibit an overall zero net charge (#4).[16,25,32]

Combining now the beneficial properties of these zwitterionic head groups with the properties of oligo ethylene glycol functionalized nanoparticle surfaces should yield ND particles with a unique set of colloidal and non-fouling properties in physiological media. Here, we report on the synthesis and characterization of nanodiamond conjugates with a hierarchical surface architecture with zwitterionic headgroups attached to a well-defined linker structure and the behavior of these conjugates in protein containing cell culture media and buffer solutions.

2.2 Results and Discussion

In order to combine the beneficial properties of different functional elements, the nanodiamond surface has been modified in a hierarchical way. We use techniques known for the direct grafting onto detonation nanodiamond[9] and immobilize TEG chains[25,33] functionalized with zwitterionic HGs (Figure 2-1).[30,34] In order to obtain small particles, deagglomeration of the pristine DND powder is achieved using mechanical methods.[10]

To render ND applicable for cellular uptake, the pristine detonation nanodiamond has to be deaggregated. Usually, the size of aggregates is larger when the samples are stored as dry powder. Thus, in the past, some of us reported a method to deaggregate and deagglomerate the individual particles while dispersing them in water without the addition of surface-active agents. (Figure 1 (A)).[35] The latter should be avoided by all means for biological applications as detergents strongly interact e.g. with cell membranes.[36] Another issue related to agglomerated nanoparticles arises from buried, uncontrolled surface that could be liberated in the course of subsequent steps or in contact with bio-fluids. Therefore, such surfaces need to be accessible also for the initial steps of the functionalization in order to ensure a homogeneous coverage. The mechanochemical deagglomeration has proven to be highly effective to ensure homogeneous functionalization of the individual nanoparticles (Figure 1 (B), step 2).[10] Here, benzoic acid groups have been chosen as the initial short linker as this modification also results in an inversion of the zeta potential from positive (ca. 38 mV) to negative (ca. -30 mV). The change in zeta potential not only allows the monitoring of the reaction progress but also

provides highly charged, water-dispersible ND particles with very low particle size. Using the carboxylic groups as anchor points, the selected chain system can be grafted in a subsequent step (Figure 1B, step 3). Figure 2-2 shows the series of prepared ND conjugates carrying different types of linker chains and headgroups.

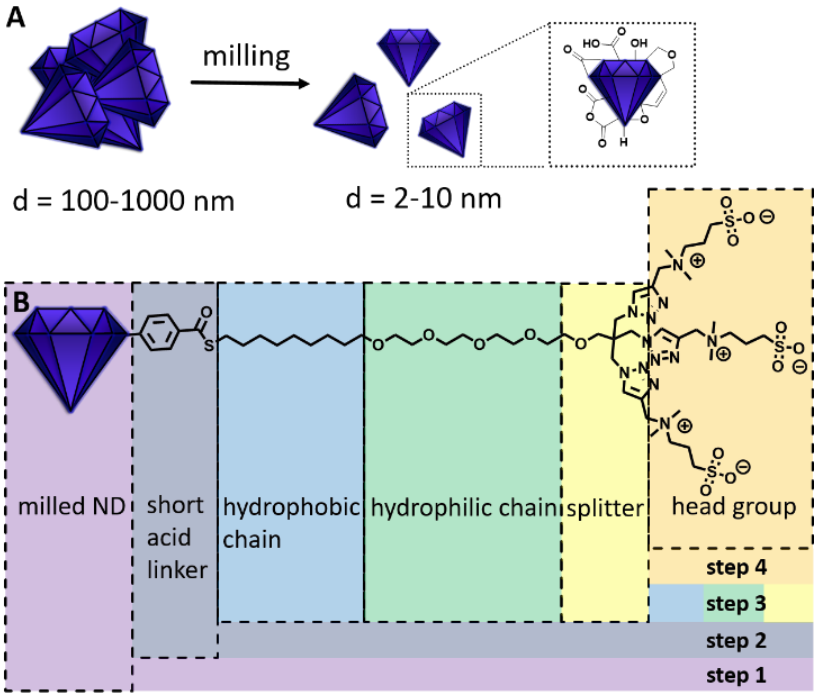

Figure 2-1. Overview of (A) the preparation of individual ND particles prior to their functionalization by milling in aqueous suspension and (B) hierarchical structure of the ND surface architecture achieved in four general steps: preparation of milled ND (step 1), grafting of short linker (step 2), grafting of a structural element chosen from hydrophobic chain, hydrophilic chain and splitter (step 3), choice of HG (step 4).

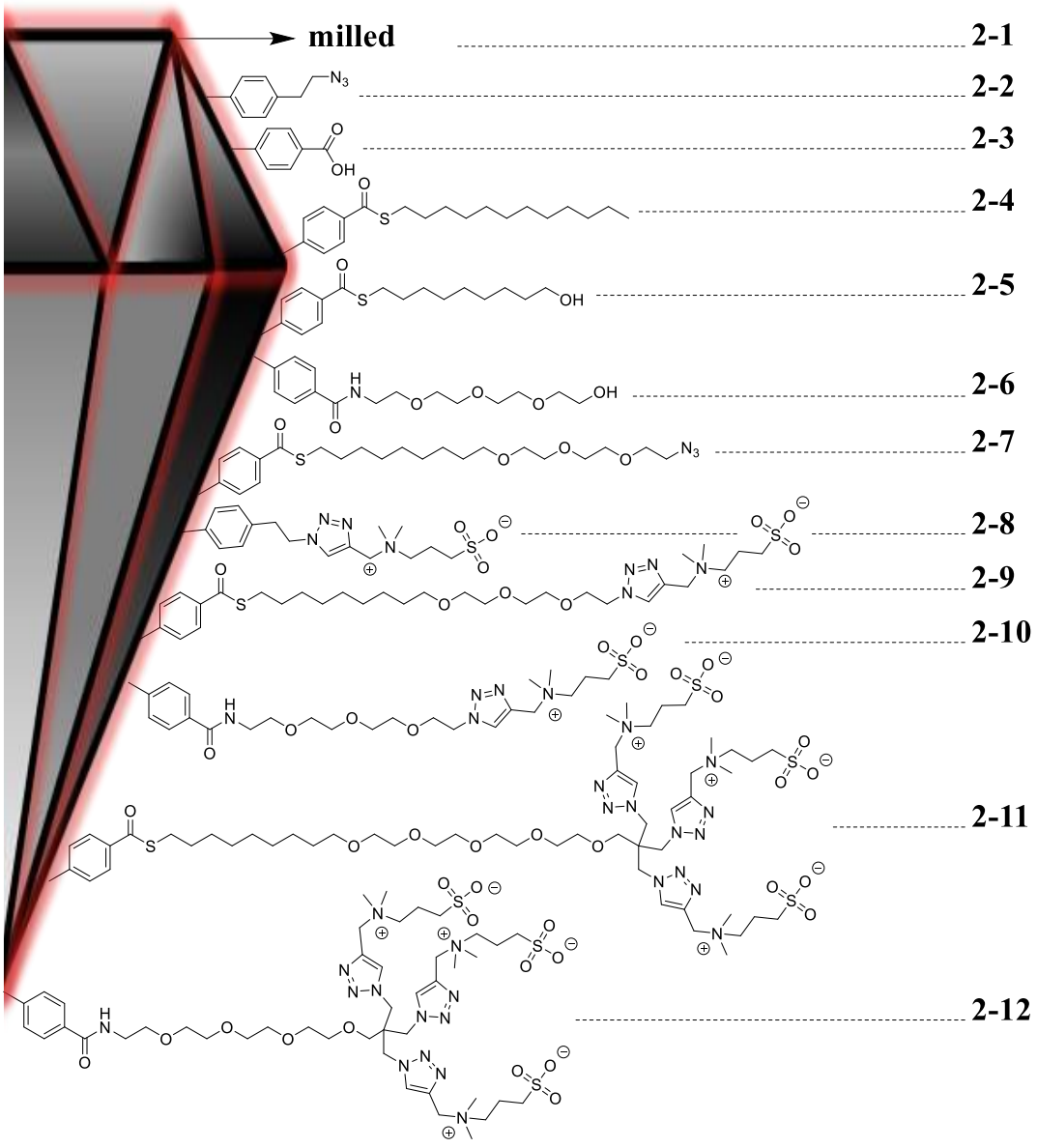

Figure 2-2. Nanodiamond conjugates with different surface functionalization synthetized in this work.

The grafting onto the benzoic acid was performed by the formation of amide and thioester bonds with two different types of chains based on a variety of the three parts of step 3 (Figure 1 (B)). In order to study how the hydrophobic, hydrophilic part and the splitter group would influence the interaction of the ND surface with bio-fluids, several test systems were grafted on ND **2-3**. Comparative data was obtained from ND **2-4**, **2-5** and **2-6** which are designed for investigating only one chain section, either the hydrophilic or hydrophobic chain, whereas ND **2-7** carries a

combined chain with the hydrophobic and hydrophilic section. This conjugate was also used for the further functionalization with zwitterions (ND **2-9**). A system without a linker chain was used to investigate the influence of the zwitterionic headgroup onto the colloidal stability (ND **2-8**). ND **2-9** is based on a combination of a hydrophobic and a hydrophilic moiety (Figure 1 (B), step 3) in analogy to Harder *et al*.[25] and Kim *et al*.[30] where such moieties have been introduced as a pocket for hydrophobic drugs. While the alkane thiolate is used as a hydrophobic moiety stretching out from the nanoparticle surface, the hydrophilic TEG interacts with water to stabilize the ND solvation. For comparison, ND conjugates carrying solely the hydrophilic moiety (**2-10**, **2-12**) have been synthetized as well. Here, the lack of additional stabilizing effects of an inner, hydrophobic shell is excluded.

As described in the introduction, the HGs play a highly important role for colloidal stability but also for protein repulsion. It can be expected, that a higher number of headgroups should have a beneficial effect on these two properties. Therefore, a so-called splitter group was attached to some of the ND conjugates (ND **2-11** and **2-12**) to enable the grafting of multiple headgroups to each linker moiety. In the chosen example, the number of HGs is increased three times provided that the grafting reaction proceeds to completion. The latter can be efficiently monitored by the observation of the exceptionally strong azide peak in FT-IR spectrum before the click reaction (Figure 1 (B), step 4). Figure 2-3 shows an exemplary series of FTIR spectra for the different synthetic steps to the final zwitterionic ND conjugate **2-12** (see Supporting information for reaction schemes, detailed experimental procedures and analytical data).

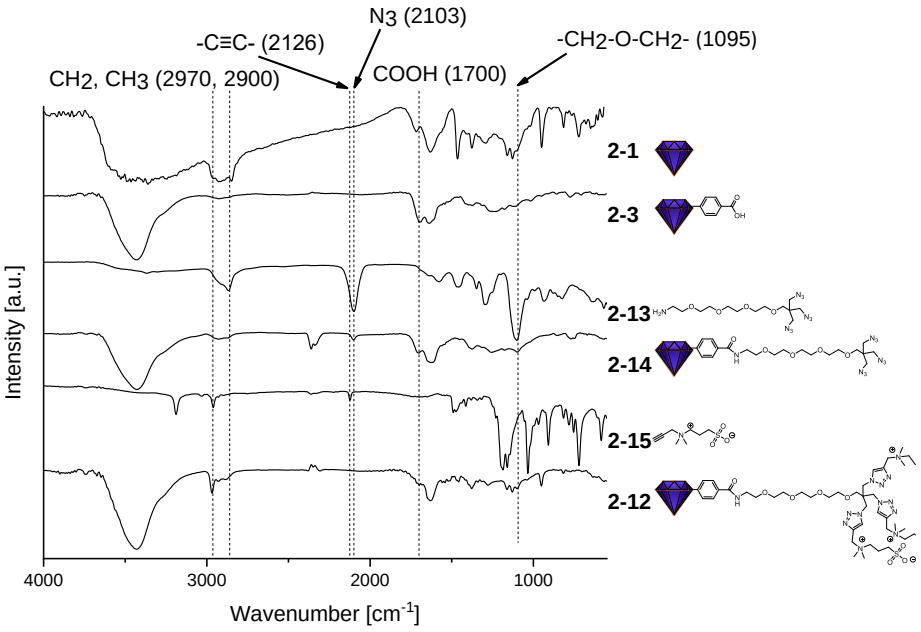

Figure 2-3. Series of FT-IR spectra (ATR for organic molecules and KBr pellet for ND samples) of an exemplary reaction from milled ND (**2-1**) via benzoic acid functionalized ND **2-3**, subsequently reacting with amine **2-13** to ND **2-14**, which then reacts with the zwitterionic alkyne **2-15** to the final conjugate **2-12** (Detailed FT-IR spectra of all synthetized ND conjugates and precursors are given in the Supporting information).

During the reaction of ND **2-1** to ND **2-3**, the zeta potential dropped from positive to negative due to grafting of the benzoic acid, which is indicated by the carboxylic band at 1700 cm^{-1} in the IR spectrum. Upon reaction with amine **2-13** the corresponding azide-functionalized ND **2-14** is formed. Correspondingly, the bands at 2900-3000 cm^{-1} for aliphatic CH_2-groups increased and the azide band at 2103 cm^{-1} appeared while the band at 1700 cm^{-1} decreased. In the following step, the vanishing of the azide band at 2103 cm^{-1} and the appearance of the strong CH_3 band from the zwitterion at 2970 cm^{-1} indicate the completion of the reaction to ND **2-12**. It is noteworthy, that the band at 2103 cm^{-1} vanishes completely in the reported cases. Typically, residual azides e.g. included in agglomerates are not accessible for the click reaction and thus prevent the completion of the subsequent surface functionalization step leading to a residual azide peak in the IR spectra. However, in our approach the surface-bound glycol chains are highly solvated by water molecules and the particles have a low tendency to agglomerate. Thus, the azide groups are easily accessible for the click reaction. Surface loadings of organic

moieties have been measured by thermogravimetric analysis and show an efficient binding of the groups (see Experimental section and Supporting information for details).

After the grafting of the zwitterion, the nanoparticles are easily solvated at their entire surface and therefore an increased stability in water or physiological media like FBS/DMEM is achieved. To determine the colloidal stability of the different moieties, DLS measurements were performed. Upon addition of 0.07 mg/mL ND to the respective medium, the size and count rate of the particles in the dynamic light scattering were monitored. It has to be noted that FBS contains proteins with sizes detectable by DLS. They thus appear in the size distributions (see DLS measurement of FBS in the Supporting Information). In order to clearly distinguish protein-related peaks and ND related peaks the intensity based distribution of the particle size is shown here. For comparison, the size distribution of FBS, ND **2-3** and ND **2-12** in separate colloidal solution is also shown in Figure 4C. It was observed that over different period of times the agglomeration of the ND conjugates sets in as indicated by a broadening of the ND-related peak in the size distribution. This is due to the initial flocculation followed by a complete precipitation of the ND agglomerates, resulting in the disappearance of the ND peak. Figure 2-4 A and B show exemplary size distribution evolutions for ND **2-3** (not stable in cell culture media) and ND **2-12** (highly stable in cell culture media) over the course of 3 days. Whereas after 3 days the ND related peak has vanished for ND **2-3** (and the ND particles have precipitated), it remains largely unchanged for ND **2-12**. The time-points for the agglomeration of each ND conjugate at room temperature have been determined using consecutive DLS measurements of the colloidal solutions at daily intervals (after monitoring at shorter intervals on the first day). The peaks at ~200 nm are representing ND, although the actual particle size is much smaller. The particle size measurement in serum media is known to be complex due to the polydispersity of the mixture, which leads to apparent higher particle sizes in DLS profiles (% Intensity), For 5 nm gold particles, the sizes in FBS measured by DLS are in the same range of diameters as in our case.[37,38] Long-term monitoring of the stable zwitterionic colloids was in some cases at the end limited by a deterioration of the serum proteins by the flocculation of the latter. The most stable conjugates, carrying both the oligoethylene glycol chains as well as the zwitterionic moieties, have thus reached the situation, where the ND material itself is not limiting its applicability in physiological media anymore and rather the stability of the serum

at room temperature becomes the relevant factor. Figure 4 D shows the time-points for the onset of agglomeration for the different types of nanodiamond materials prepared for this study.

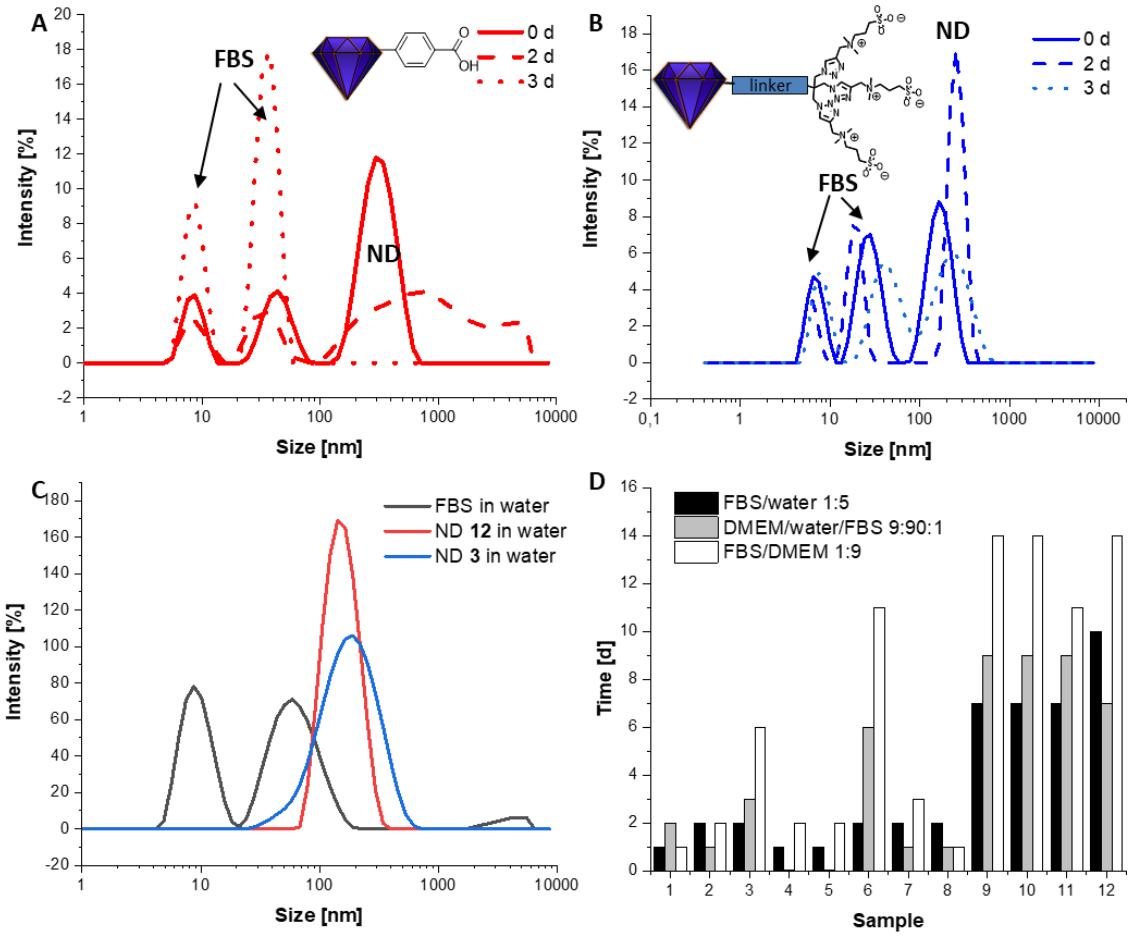

Figure 2-4. Colloidal stability of ND conjugates in protein containing media. (A) Time dependent evolution of size distribution in a colloid containing ND **2-3** and (B) ND **2-12** in FBS/DD-water 1:5 v/v. While the two peaks at ~10 nm and ~30 nm represent the FBS proteins, the peak at 200 nm represents the ND particles; (C) size distribution of FBS and ND in separate colloidal solutions; (D) Measurement of colloid stability (in days) for ND conjugates with an without stabilizing moieties. For all ND samples the time before the onset of agglomeration is shown in different media: FBS and water in a ratio of 1:5 v/v (black), DMEM and water in a ratio 1:9 and additional 1 % FBS v/v (gray), FBS and DMEM in a ratio of 1:9 v/v (white).

Comparing systems with surface functionalization and without, it can be concluded that any kind of modifications already provokes a positive effect on the colloidal stability except for ND **2-8** (see below). The milled ND (**2-1**) although very stable in aqueous colloidal solution possesses only a very limited colloidal stability in the chosen physiological media, as had been

reported previously by us and others for DND and other nanodiamond materials.[10,11,19,39] As can be seen in Figure 4D, the time until the onset of agglomeration is significantly enhanced for all systems functionalized with different types of chains and zwitterions except for ND **2-8**. While all other ND conjugates are prepared from ND **2-3** with a highly negative ionic surface, ND **2-8** is built up from a highly positive surface without ionic surface groups, thus the initial stability during functionalization is already limited. By clicking the zwitterion on the surface, the zetapotential is getting neutral and thus the stability of the conjugate very poor. Even the highly ionic nature of the zwitterions is not able to prevent colloid collapse for more than two days. A reason for this inferior performance could be the short distance of the headgroups to the ND surface inducing a steric solvation hindrance with the result of poor colloidal stability. Additionally, the beneficial glycol chain is missing in this conjugate (see below). From these findings, the following conclusions can be drawn:

The comparison of systems ND **2-1** and **2-3**, especially for the FBS/DMEM-media, shows that the higher the number of ionic surface groups, i.e. of benzoic acid moieties, the higher is the colloidal stability of the ND dispersion. This stability can be improved further by the addition of TEG (ND **2-6**), whereas the addition of non-polar alkyl chains does not improve stability (ND **2-4** and **2-5**) as they cannot easily be solvated by water molecules. In combination with residual benzoic acid moieties, which lead to an overall negative zeta potential, the TEG significantly improves the colloidal stability from 6 to 13 days in FBS/DMEM media. Comparing ND **2-6** with the systems carrying zwitterionic headgroups in addition to the TEG chain, the stability of the systems (ND **2-9**–**2-12**) against agglomeration is already in the same range. in FBS/DMEM. The fact, that ND **2-8** does not show this improved colloidal stability clearly shows that the TEG-chain is required to ensure superior colloidal stability.

However, besides the stability of a NDs in physiological media, it is also crucial to prevent the non-specific adsorption of proteins on the surface of NDs. It is well known, that the protein corona is built up within the first minutes after nanoparticles are exposed to bio-fluids, such as FBS.[37,38] Whereas the soft corona can be simply washed away with water, the hard corona however cannot be easily removed by washing and thus is covering the surface of the nanoparticles even after extended cleaning procedures. In this approach we incubated NDs one hour in FBS-water-mixture (1:5 ratio) at 37 °C to complete the formation of both soft and hard

protein corona and subsequently washed the ND with water to remove the soft corona (Figure 2-5). The samples were then dried and a thermogravimetric measurement was performed with both unincubated and incubated NDs. Thus, the difference of mass loss between the ND that was in contact with the serum and the one that was only functionalized with the respective organic groups (in TGA these groups also give a mass loss upon heating) gives the amount of proteins that are adsorbed on the surface as a hard corona.

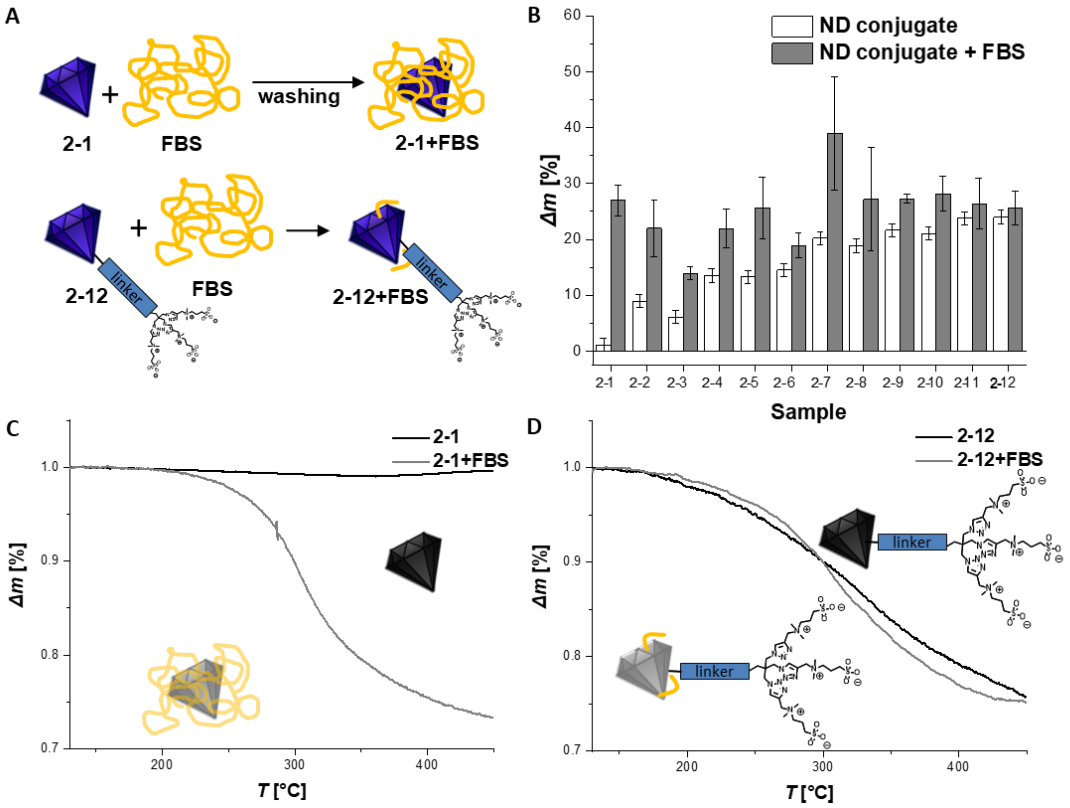

Figure 2-5. Prevention of non-specific protein adsorption on zwitterion-functionalized nanodiamond. A) Schematic representation of the different surface loadings with serum proteins after incubation of ND **2-1** and **2-12** in FBS media for 1 h and subsequent removal of non-adsorbed serum and soft corona by washing; B) thermogravimetric analysis of serum protein adsorption on functionalized ND conjugates (ND conjugate + FBS, grey) and the same ND without FBS treatment (ND conjugate, white) as reference. The difference between the grey and white columns give the amount of adsorbed proteins for each material; C) (detailed thermogravimetric profile of milled ND **2-1** and D) zwitterion functionalized ND **2-12**.

In case of milled ND (**2-1**) the amount of adsorbed protein on the surface is extremely high. A rise from around 1 % surface loading stemming from surface functional groups to over 27 % of the total mass shows the very fast and non-specific adsorption of proteins on detonation

nanodiamond and the formation of a large hard corona. Already the functionalization with small linker systems as in ND **2-2** and **2-3**, reduces the amount of adsorbed proteins, which remains nevertheless very high and accounting for more than 50% of the organic matter present on the surface of the particles. The functionalization with TEG-based chains, such as in ND **2-6**, further reduces the amount of protein corona to a value of less than 50 %. The best result was however achieved when a zwitterionic headgroup was attached to the ND conjugate as in ND **2-8**–**2-12**. All these systems exhibit an outstanding performance for prevention of protein adsorption with results close to the non-existence of a hard protein corona. Large error bars are observed for the short zwitterionic system **2-8** which has remarkably low stability in FBS (see Figure 4 (D)), which renders the experiment difficult due to uncontrollable agglomeration within the incubation time of one hour. A significant change in protein adsorption was observed after click reaction from ND **2-7** to monozwitterionic ND **2-9** which differ only in the presence of the zwitterionic moiety in ND **2-9**. The surface loading with serum proteins dropped from 25 % to less than 5 %, clearly showing the importance of the zwitterionic moiety for the repulsion of the proteins. Further improvement to a complete inhibition of hard protein corona formation was achieved by immobilizing not only one but three zwitterionic moieties on every linker chain. In doing so, the surface is completely covered with zwitterionic moieties and thus does not leave room for non-specific interaction, e.g. with hydrophilic or hydrophobic parts of the linkers. It can be concluded that zwitterionic surface groups efficiently prevent the formation of a hard protein corona. However, they do not ensure a stable colloidal dispersion of the ND conjugates as was drastically shown by ND **2-8**. Only the combination of the oligoethylene glycol moieties with the zwitterionic headgroups gives rise to both colloidal stability in aqueous systems with strong ion background (such as cell culture media) and simultaneously avoiding the formation of a hard protein corona that is detrimental for a variety of intended applications of functionalized nanodiamond.

However, it had been shown in the literature, that zwitterionic moieties have sometimes adverse effects e.g. on bacteria that are treated with such nanomaterials.[40] We therefore conducted a first test with an ubiquitous strain of bacteria, i.e. E. coli, to ensure that in general the ND conjugates are usable even with such biological systems. Figure 2-6 shows the results of an incubation test with and without the different nanodiamond materials.

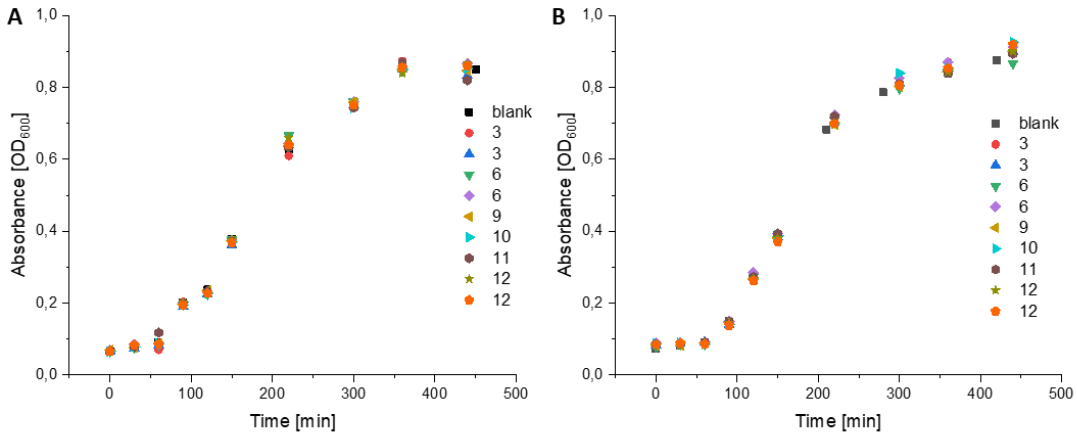

Figure 2-6. *E. Coli* growth curves with 0.1 mg mL^{-1} (A) and 0.5 mg mL^{-1} (B) of each ND (sample numbers given for each individual curve).

It can be seen that none of the tested ND functionalized with benzoic acid (**2-3**), glycol linker (**2-6**) or zwitterionic systems (**2-9**–**2-12**) inhibited bacterial growth at rather high concentrations of 0.1 and 0.5 mg mL^{-1}. Details of the assay are described in the Supporting Information. Although this first test with a common bacterium is promising, further experiments will be needed to fully assess the interaction with different types of bacteria, the overall biocompatibility and toxicity of the zwitterion functionalized ND conjugates and to explore their full potential in biomedical applications of nanodiamond.

2.3 Conclusion

In conclusion, we have developed a highly versatile toolbox for the tailored functionalization of nanodiamond. It allows to simultaneously control the colloidal stability in different environments and the prevention of non-specific protein binding by using a combination of hydrophilic oligoethylene glycol chains, hydrophobic alkyl moieties and zwitterionic headgroups. The linkage between the diamond surface and the organic surface groups can be chosen from different anchor groups to address the specific needs for stability e.g. against hydrolysis or enzymatic cleavage. Additionally, the use of azide-alkyne click chemistry also allows to efficiently immobilize other functional moieties on the surface of the stabilized ND conjugates and to monitor the reaction progress by IR spectroscopy.

Based on our investigations it can be concluded that the surface modification of ND by a combination of TEG chains and zwitterionic headgroups leads to an efficient colloidal stabilization and the avoidance of hard protein corona formation or non-specific adsorption of serum proteins.

This could enhance the circulation times of such NDs in vivo and opens the way for a multitude of biomedical applications of these systems as they can be further functionalized by well-established methods.

2.4 Experimental Section

General Methods: All solvents were freshly distilled and dried using standard procedures. For the purification of the ND, Millipore grade water (MQ-water, 18.2 MΩ cm) at a pH of 5.5 and T = 20 °C) was used. For further experiments (e.g. colloidal stability/formation of protein corona) all NDs were washed and redispersed in bidistilled water (DD-water, pH at 6-7). Acid purified detonation nanodiamond was purchased from Gansu Lingyun Corp. (China) and milled in an attrition mill using 50 µm zirconia beads to a colloidal aqueous solution according to a previously reported protocol.[35] Nuclear magnetic resonance spectra (^{1}H and ^{13}C) were measured with a Bruker AVANCE 400 FT-NMR spectrometer at 27 °C. For the calibration of spectra, the chemical shift of the deuterated solvents were used as internal reference. Mass spectrometry (ESI) was performed using a Bruker Daltonics micOTOF focus. The characterization with FT-IR was carried out in a Jasco FT/IR-430 using ~1 mg ND in a 200 mg KBr pellet dried in vacuo. ATR spectra were recorded using the same spectrometer equipped with an ATR unit MIRacle^{TM} from PIKE Technologies. IR spectra of ND samples were additionally measured using a DRIFTS spectrometer Nicolet iS5. Thermogravimetric analysis was performed in a Perkin–Elmer STA 6000 with 60 mL min^{-1} N_2 flowrate and a heating rate of 10 K min^{-1} from 50 °C to 130 °C, a plateau time of 60 min at 130 °C and a heating phase from 130 °C to 700/900 °C at 5 K min^{-1}. The particle size and zeta potential were measured in bidistilled water at the intrinsic pH of the sample colloid using a Malvern Zetasizer Nanoseries Nano-ZS (dynamic light scattering, backscattering mode). The size distribution is given as volume distribution (Dv(10), Dv(50) and Dv(90)) (or intensity distribution for observation of the agglomeration onset) and was obtained using the Marquardt method. The reaction with milled ND and diazonium salts was carried out under sonication with a Branson Sonifier 450

102C (max. 400 W, 19850–20050 Hz) with conical 5 mm titanium-microtip using it for 3-4 h at level 2 of 10 in a 50 % pulse and 50 % pause period. For washing the samples, the sonication was carried out in a Bandelin Sonorex Digitec Typ DT52 (max. 80 W, 35 kHz) and for centrifugation Thermo Scientific Sorvall MTX 150 was used at 52.000 RPM.

Organic Synthesis:

The synthesis of the organic precursors is reported in the Supporting information. See Scheme Figure S1 and Figure S26 for sample numbers and experimental details.

Nanodiamond functionalization:

Milled ND (**2-1**) was initially functionalized in analogy to previously published work of our group.[41] Experimental details for preparation of ND **2-2** and ND **2-3** can be found in the Supporting information.

General procedure for the preparation of ND 4, 5, 7 by thioester formation

ND 2-3 (72 mg) was washed two times in THF (10 mL) and two times in dry THF (10 mL) and dispersed in 30 mL of dry THF. *N*,*N*-Dimethylpyridin-4-amine (4-DMAP, 12.0 mg, 100 µmol, 1.00 eq), *N,N'*-dicyclohexylcarbodiimide (DCC, 103 mg, 500 µmol, 5.00 eq) and the respective thiol (100 µmol, 1.00 eq) were added at 0 °C. The reaction mixture was stirred under nitrogen for 1 h at 0 °C and after sonication at r.t. in a sonication bath (Bandelin, 30 W), the suspension was stirred 6 days. After the reaction the dispersion was washed with 12 mL of each acetone (3x, 10k RPM), MQ-H_2O (1x, 15k RPM), acetone (1x, 10k RPM), acetone/MQ-H_2O (1:1, 3x, 30k RPM), MQ-H_2O (3x, 15k RPM). Following, 1.5 mL (1/8) of a total dispersion of 12 mL was dried at 80 °C in vacuum to obtain material for the characterization.

ND 2-4 (78 mg, dark grey powder): **Zeta potential:** -23.7 mV (DD-water, intrinsic pH=5.5), **Particle size** (DLS, DD-water): 10 % ≤ 83 nm, 50 % ≤ 151 nm, 90 % ≤ 409 nm, **Surface loading (TGA):** 13.5 % (150-450 °C), **FT-IR (KBr):** 3400 (br), 2930 (s), 2845 (m), 1712 (s), 1644 (s), 1537 (s), 1383 (m), 1220 (s), 1152 (s), 771 (s) cm^{-1}.

ND 2-5 (65 mg, grey powder)**: Zeta potential:** -19.1 mV (DD-water, pH=5.1), **Particle size:** (DLS, DD-water): 10 % ≤ 40 nm, 50 % ≤ 68 nm, 90 % ≤ 204 nm, **Surface loading (TGA):**

13.3 % (150-450 °C), **FT-IR (KBr):** 3440 (br), 2926 (s), 2862 (m), 1709 (m), 1632 (s), 1379 (m), 1315 (w), 1251 (m), 1148 (m), 1084 (m), 1037 (m) cm^{-1}.

ND 2-7 (70mg, brownish-grey powder)**: Zeta potential:** 5 mV (DD-water, intrinsic pH=5.6), **Particle size:** (DLS, DD-water): 10 % ≤ 128 nm, 50 % ≤ 224 nm, 90 % ≤ 423 nm, **Surface loading (TGA):** 20.2 % (150-450 °C), **FT-IR (KBr):** 3324 (s), 2926 (vs), 2848 (s), 2103 (w), 1700 (m), 1624 (vs), 1568 (vs), 1452 (m), 1310 (s), 1247 (s), 1084 (w) cm^{-1}.

ND 2-6*:* ND **2-3** (72 mg) was washed with 12 mL DMF and 12 mL dry DMF (2x) under nitrogen and dispersed in 20 mL of dry DMF and 2-(1H-Benzotriazole-1-yl)-1,1,3,3-tetramethylaminium tetrafluoroborate (TBTU, 209 mg, 652 µmol, 3.00 eq), Hünig's base (DIPEA, 0.38 mL, 2.17 mmol, 10.0 eq) and respective amine (0.22 mmol, 1.00 eq) were added to the suspension and the reaction was stirred at 35 °C for 6 days. After the reaction mixture was cooled to r.t. the dispersion was washed with 12 mL of each solvent: acetone (3x, 10k RPM), MQ-H_2O (1x 52k RPM), acetone (1x 10k RPM), acetone/MQ-H_2O (1:1, 3x, 30k RPM), MQ-H_2O (3x, 52K RPM). Following, 1.5 mL (1/8) of a total dispersion of 12 mL was dried at 80 °C in vacuum.

ND 2-6 (63 mg, grey powder): **Zeta potential:** 6 mV (DD-water, intrinsic pH=6.3), **Particle size:** (DLS, DD-water): 10 % ≤ 57 nm, 50 % ≤ 90 nm, 90 % ≤ 170 nm, **Surface loading (TGA):** 14.5 % (150-450 °C), **FT-IR (KBr):** 3339 (br), 2973 (s), 2923 (s), 2872 (s), 1724 (m), 1648 (s), 1603 (s), 1544 (m), 1465 (m), 1370 (s), 1300 (s), 1149 (vs), 1127 (vs), 954 (vs), 821 (m) cm^{-1}.

General procedure for the preparation of ND 8, 9, 10, 11, 12 by Click chemistry

Azide functionalized ND **2-2**, **2-7**, **2-41**, **2-42**, **2-43** (30 mg, see SI for the preparation of **2-41**–**2-43**) was dispersed in a 1:1 (v/v) mixture of water and THF (10 mL) and the suspension was degassed in an ultra-sonic bath under nitrogen atmosphere. After adding the zwitterionic alkyne 3-(dimethyl(prop-2-yn-1-yl)ammonio)propane-1-sulfonate (**2-15**, 205 mg, 1.00 mmol, 1.00 eq), sodium ascorbate (158 mg, 0.80 mmol, 0.80 eq) and $CuSO_4$ (63.8 mg, 0.40 mmol, 0.40 eq) the reaction mixture was sonicated for 5 min under nitrogen. The suspension was stirred at r.t. for typically 5 days. After the reaction control by DRIFT spectroscopy showed no

azide band at 2100 cm^{-1} the mixture was washed with 9 mL of each solvent: MQ-H_2O (2x, 52k RPM), acetone (3x, 30k RPM), EDTA (2x, 15k RPM), MQ-H_2O (3x, 30k RPM).

ND 2-8 (28 mg, light grey powder)**: Zeta potential:** -6 mV (MQ-water, intrinsic pH=5.8), **Particle size:** (DLS, MQ-water): 10 % ≤ 49 nm, 50 % ≤ 58 nm, 90 % ≤ 70 nm, **Surface loading (TGA):** 18.8 % (150-450 °C), **FT-IR (KBr):** 3434 (br), 2961 (m), 2917 (m), 2879 (w), 2058 (br), 1635 (vs), 1456 (w), 1364 (m), 1313 (m), 1212 (s), 1124 (m), 1048 (s), 852 (vw), 821 (w), 733 (vw), 675 (w) cm^{-1}.

ND 2-9 (28 mg, light grey powder)**: Zeta potential:** 7 mV (MQ-water, intrinsic pH = 5.9) **Particle size:** (DLS, MQ-water): 10 % ≤ 65 nm, 50 % ≤ 102 nm, 90 % ≤ 199 nm. **Surface loading (TGA):** 21.7 % (150-450 °C). **FT-IR (KBr):** 3440 (br), 2927 (m), 2859 (m), 1692 (s), 1635 (vs), 1382 (s), 1073 (s) cm^{-1}.

ND 2-10 (26 mg, light grey powder)**: Zeta potential:** 13 mV (MQ-water, intrinsic pH=6.0), **Particle size:** (DLS, MQ-water): 10 % ≤ 72 nm, 50 % ≤ 110 nm, 90 % ≤ 191 nm, **Surface loading (TGA):** 21.1 % (150-450 °C), **FT-IR (KBr):** 3440 (br), 2935 (m), 2847 (m), 1698 (m), 1635 (vs), 1395 (s), 1067 (vs) cm^{-1}.

ND 2-11 (32 mg, light grey powder): **Zeta potential:** 15 mV (MQ-water, intrinsic pH = 5.8), **Particle size:** (DLS, MQ-water): 10 % ≤ 52 nm, 50 % ≤ 77 nm, 90 % ≤ 135 nm, **Surface loading (TGA):** 23.8 % (150-450 °C), **FT-IR (KBr):** 3503 (br), 2961 (s), 2923 (vs), 2853 (s), 1704 (s), 1629 (vs), 1515 (w), 1446 (m), 1376 (s), 1313 (m), 1256 (m), 1137 (s), 1073 (s) cm^{-1}.

ND 2-12 (24 mg, light grey powder)**: Zeta potential:** 25 mV (MQ-water, intrinsic pH=6.3)

Particle size: (DLS, MQ-water): 10 % ≤ 78 nm, 50 % ≤ 120 nm, 90 % ≤ 199 nm, **Surface loading (TGA):** 24.0 % (150-450 °C), **FT-IR (KBr):** 3453 (br), 2954 (m), 2927 (s), 2875 (m), 1698 (m), 1635 (vs), 1541 (w), 1477 (w), 1389 (s), 1306 (m), 1200 (vs), 1099 (s), 1039 (vs) cm^{-1}.

2.5 References

[1] A. Krueger, D. Lang, *Adv. Funct. Mater.* **2012**, *22*, 890.
[2] V. N. Mochalin, O. Shenderova, D. Ho, Y. Gogotsi, *Nat. Nanotechnol.* **2011**, *7*, 11.
[3] Y. Zhu, J. Li, W. Li, Y. Zhang, X. Yang, N. Chen, Y. Sun, Y. Zhao, C. Fan, Q. Huang, *Theranostics* **2012**, *2*, 302.
[4] a) K. Turcheniuk, V. N. Mochalin, *Nanotechnol.* **2017**, *28*, 252001; b) A. M. Schrand, S. A. C. Hens, O. A. Shenderova, *Crit. Rev. Solid. State Mater. Sci.* **2009**, *34*, 18.
[5] Y.-C. Lin, L.-W. Tsai, E. Perevedentseva, H.-H. Chang, C.-H. Lin, D.-S. Sun, A. E. Lugovtsov, A. Priezzhev, J. Mona, C.-L. Cheng, *J. Biomed. Opt.* **2012**, *17*, 101512.
[6] P. Happel, T. Waag, M. Schimke, S. Schweeberg, A. Muzha, K. Fortak, D. Heesch, L. Klask, M. Pilscheur, F. Hoppe et al., *Adv. Funct. Mater.* **2018**, *28*, 1802873.
[7] S. Huo, Y. Jiang, A. Gupta, Z. Jiang, R. F. Landis, S. Hou, X.-J. Liang, V. M. Rotello, *ACS Nano* **2016**, *10*, 8732.
[8] a) X. Zhang, S. Wang, M. Liu, J. Hui, B. Yang, L. Tao, Y. Wei, *Toxicol. Res.* **2013**, *2*, 335; b) Y. Xing, L. Dai, *Nanomedicine* **2009**, *4*, 207.
[9] Y. Liang, T. Meinhardt, G. Jarre, M. Ozawa, P. Vrdoljak, A. Scholl, F. Reinert, A. Krueger, *J. Colloid Interface Sci.* **2011**, *354*, 23.
[10] Y. Liang, M. Ozawa, A. Krueger, *ACS Nano* **2009**, *3*, 2288.
[11] S. R. Hemelaar, A. Nagl, F. Bigot, M. M. Rodríguez-García, M. P. de Vries, M. Chipaux, R. Schirhagl, *Microchim. Acta* **2017**, *184*, 1001.
[12] X. Kong, L. C. L. Huang, S.-C. V. Liau, C.-C. Han, H.-C. Chang, *Anal. Chem.* **2005**, *77*, 4273.
[13] T. Zheng, F. Perona Martínez, I. M. Storm, W. Rombouts, J. Sprakel, R. Schirhagl, R. de Vries, *Anal. Chem.* **2017**, *89*, 12812.
[14] R. Eldawud, M. Reitzig, J. Opitz, Y. Rojansakul, W. Jiang, S. Nangia, C. Z. Dinu, *Nanotechnol.* **2016**, *27*, 85107.
[15] S. T. Kim, K. Saha, C. Kim, V. M. Rotello, *Acc. Chem. Res.* **2013**, *46*, 681.
[16] D. F. Moyano, M. Ray, V. M. Rotello, *MRS Bull.* **2014**, *39*, 1069.
[17] J. B. Schlenoff, *Langmuir* **2014**, *30*, 9625.
[18] a) M. C. Lukowiak, B. Ziem, K. Achazi, G. Gunkel-Grabole, C. S. Popeney, B. N. S. Thota, C. Böttcher, A. Krueger, Z. Guan, R. Haag, *J. Mater. Chem. B* **2015**, *3*, 719; b) A. Bumb, S. K. Sarkar, N. Billington, M. W. Brechbiel, K. C. Neuman, *J. Am. Chem. Soc.* **2013**, *135*, 7815; c) T.-F. Li, K. Li, Q. Zhang, C. Wang, Y. Yue, Z. Chen, S.-J. Yuan, X. Liu, Y. Wen, M. Han et al., *Biomaterials* **2018**, *181*, 35.
[19] J. Neburkova, J. Vavra, P. Cigler, *Curr. Opin. Solid State Mater. Sci.* **2017**, *21*, 43.
[20] a) X. Zhang, C. Fu, L. Feng, Y. Ji, L. Tao, Q. Huang, S. Li, Y. Wei, *Polymer* **2012**, *53*, 3178; b) M. Hartmann, P. Betz, Y. Sun, S. N. Gorb, T. K. Lindhorst, A. Krueger, *Chem. Eur. J.* **2012**, *18*, 6485; c) C. Fessele, S. Wachtler, V. Chandrasekaran, C. Stiller, T. K. Lindhorst, A. Krueger, *Eur. J. Org. Chem.* **2015**, *2015*, 5519.
[21] A. S. Hoffman, *J. Biomater. Sci., Polym. Ed.* **1999**, *10*, 1011.
[22] K. Knop, R. Hoogenboom, D. Fischer, U. S. Schubert, *Angew. Chem., Int. Ed.* **2010**, *49*, 6288.
[23] J. Fowles, M. Banton, J. Klapacz, H. Shen, *Toxicol. Lett.* **2017**, *278*, 66.

[24] K. P. Antonsen, A.S. Hoffmann (Ed.) *Polyethylene Glycol Chemistry: Biotechnical and Biomedical Applications*. *Water Structure of PEG Solutions by Differential Scanning Calorimetry*, Plenum Press, New York, **1992**.
[25] P. Harder, M. Grunze, R. Dahint, G. M. Whitesides, P. E. Laibinis, *J. Phys. Chem. B* **1998**, *102*, 426.
[26] K. Ulbrich, K. Holá, V. Šubr, A. Bakandritsos, J. Tuček, R. Zbořil, *Chem. Rev.* **2016**, *116*, 5338.
[27] a) T. A. Horbett, A. S. Hoffmann in *Adv. Chem. Ser.*, *Vol. 145* (Ed.: R. E. Baier), A. Chem. Soc., Washington, DC, **1975**, pp. 230–254; b) R. A. Alvarez-Puebla, E. Arceo, P. J. Goulet, J. J. Garrido, R. F. Aroca, *J. Phys. Chem. B* **2005**, *109*, 3787.
[28] M. Aramesh, O. Shimoni, K. Ostrikov, S. Prawer, J. Cervenka, *Nanoscale* **2015**, *7*, 5726.
[29] a) S. Mondini, M. Leonzino, C. Drago, A. M. Ferretti, S. Usseglio, D. Maggioni, P. Tornese, B. Chini, A. Ponti, *Langmuir* **2015**, *31*, 7381; b) S. Jiang, Z. Cao, *Adv. Mat.* **2010**, *22*, 920; c) H. Wei, N. Insin, J. Lee, H.-S. Han, J. M. Cordero, W. Liu, M. G. Bawendi, *Nano lett.* **2012**, *12*, 22; d) W. Lin, G. Ma, N. Kampf, Z. Yuan, S. Chen, *Biomacromolecules* **2016**; e) W. Zheng, H. Li, W. Chen, J. Ji, X. Jiang, *Anal. Chem.* **2016**, *88*, 4140; f) I. Izquierdo-Barba, M. Colilla, M. Vallet-Regi, *Acta Biomater.* **2016**; g) T. Mizuhara, K. Saha, D. F. Moyano, C. S. Kim, B. Yan, Y. K. Kim, V. M. Rotello, *Angew. Chem., Int. Ed. Engl.* **2015**, *54*, 6567.
[30] C. K. Kim, P. Ghosh, C. Pagliuca, Z.-J. Zhu, S. Menichetti, V. M. Rotello, *J. Am. Chem. Soc.* **2009**, *131*, 1360.
[31] a) Q. Wei, T. Becherer, S. Angioletti-Uberti, J. Dzubiella, C. Wischke, A. T. Neffe, A. Lendlein, M. Ballauff, R. Haag, *Angew. Chem., Int. Ed. Engl.* **2014**, *53*, 8004; b) E. van Andel, S. C. Lange, S. P. Pujari, E. J. Tijhaar, M. M. J. Smulders, H. F. J. Savelkoul, H. Zuilhof, *Langmuir* **2018**.
[32] a) E. Ostuni, R. G. Chapman, R. E. Holmlin, S. Takayama, G. M. Whitesides, *Langmuir* **2001**, *17*, 5605; b) R. G. Chapman, E. Ostuni, S. Takayama, R. E. Holmlin, L. Yan, G. M. Whitesides, *J. Am. Chem. Soc.* **2000**, *122*, 8303.
[33] K. Brunner, J. Harder, T. Halbach, J. Willibald, F. Spada, F. Gnerlich, K. Sparrer, A. Beil, L. Möckl, C. Bräuchle et al., *Angew. Chem. Int. Ed.* **2015**, *54*, 1946.
[34] S.-L. Niu, G. Ulrich, P. Retailleau, J. Harrowfield, R. Ziessel, *Tetrahedron Lett.* **2009**, *50*, 3840.
[35] A. Krüger, F. Kataoka, M. Ozawa, T. Fujino, Y. Suzuki, A. E. Aleksenskii, A. Y. Vul', E. Ōsawa, *Carbon* **2005**, *43*, 1722.
[36] D. K. Miller, *J. Cell Biol.* **1983**, *97*, 1841.
[37] D. F. Moyano, K. Saha, G. Prakash, B. Yan, H. Kong, M. Yazdani, V. M. Rotello, *ACS Nano* **2014**, *8*, 6748.
[38] R. F. Landis, A. Gupta, Y.-W. Lee, L.-S. Wang, B. Golba, B. Couillaud, R. Ridolfo, R. Das, V. M. Rotello, *ACS Nano* **2017**, *11*, 946.
[39] A. Krueger, *Chem. Eur. J.* **2008**, *14*, 1382.
[40] a) S. Guo, D. Jańczewski, X. Zhu, R. Quintana, T. He, K. G. Neoh, *J. Colloid Interface Sci.* **2015**, *452*, 43; b) L. Huang, L. Zhang, S. Xiao, Y. Yang, F. Chen, P. Fan, Z. Zhao, M. Zhong, J. Yang, *Chem. Eng. J.* **2018**, *333*, 1; c) N. Encinas, M. Angulo, C. Astorga, M. Colilla, I. Izquierdo-Barba, M. Vallet-Regí, *Acta Biomater.* **2019**, *84*, 317; d) B. R. Knowles, D. Yang, P. Wagner, S. Maclaughlin, M. J. Higgins, P. J. Molino, *Langmuir* **2019**, *35*, 1335.

[41] T. Meinhardt, D. Lang, H. Dill, A. Krueger, *Adv. Funct. Mater.* **2011**, *21*, 494.

Chapter 3

Zwitterion- and Antibody-Functionalized Fluorescent Nanodiamond for Targeting Application

The following section is slightly modified and reproduced from the manuscript of A. Sigaeva‡, V. Merz‡, R. Sharmin, S. R. Hemelaar, R. Schirhagl*, A. Krueger*.

3.1 Introduction

The versatile surface of ND, which purposefully can be modified, has a high potential for a wide range of applications in tribology, drug delivery, tissue engineering, nanocomposite core material and additive for polymers.[1,2] But in addition to surface group modifications, diamond can have a variety of active defects in its sp^3 matrix that are sensitive to changes in physical parameters in the environment, for example, magnetic fields, electric fields, temperature, or crystal strain.[3,4] Using defect structures, such as nitrogen-vacancy (NV) centers, diamond particles can be used as fluorescent nanodiamonds (fNDs) for photostable labeling, bioimaging and nanoscale sensing in living cells and organisms.[2,3,5]

One prerequisite for using fNDs as bioprobes is the physical proximity of the fNDs to the target site. A very effective way to achieve this in cells is to attach antibodies to the fND surface, which specifically form stable antibody-antigen formation at the nucleus.[6]

In order to immobilize antibodies on nanoparticles or surfaces two approaches can be envisaged: the physisorption of the protein structure or the covalent attachment using the reaction of functional groups of the surface with groups from the antibody.[7]

In general, there are three essential functional groups on antibodies that can further be functionalized: the amino, carboxyl and thiol moieties. Specific reactions can be used to address these groups in a selective manner.[8] With the help of *N*-hydroxysuccinimide (NHS) esters, amino groups of biomolecules can be functionalized within minutes.[9] In combination with another functional group, the diarylcyclooctyne (DBCO), a linker can be created between an antibody and an azide. The use of the so-called DBCO-NHS ester not only offers a very fast and almost quantitative functionalization of labile biomolecules, such as antibodies, but also a very fast and also almost quantitative click reaction with the alkyne of DBCO and an azide to a stable triazole without toxic copper catalysts.[10,11]

An important aspect when ND are given in the biofluids is the formation of a protein corona.[12] To enable targeting by antibodies, it is important to prevent masking by a corona. Strategies

such as coating the particles with polymers[13] or certain proteins[14], for example, protect against the formation of a protein corona but could also mask the antibodies in some circumstances. In a recent study, we demonstrate that short chains with terminal zwitterionic moieties protect against non-specific adsorption of proteins in serum and additionally stabilize them colloidally in biofluids.[15]

Here, we report on the combined functionalization of fluorescent nanodiamond with a nucleus targeting antibody ([Mab414] ab24609), which is required for the assembly of peripheral proteins into the nuclear pore complex, and moieties for the control of surface interactions. These zwitterionic moieties in combination with tetraethylene glycol (TEG) improve the colloidal dispersion in physiological media with strong ion background and the prevent non-specific interactions with proteins, as some of us have recently reported for a different type of nanodiamond.[15] The covalent attachment of the antibodies is enabled by the click chemistry with DBCO using a terminal azide group on the linker architecture of the pre-functionalized nanodiamond, (**Scheme 3-1**). To ensure the accessibility of the clickable groups the azide unit is presented on a linker architecture with the same length and polarity as the zwitterions.

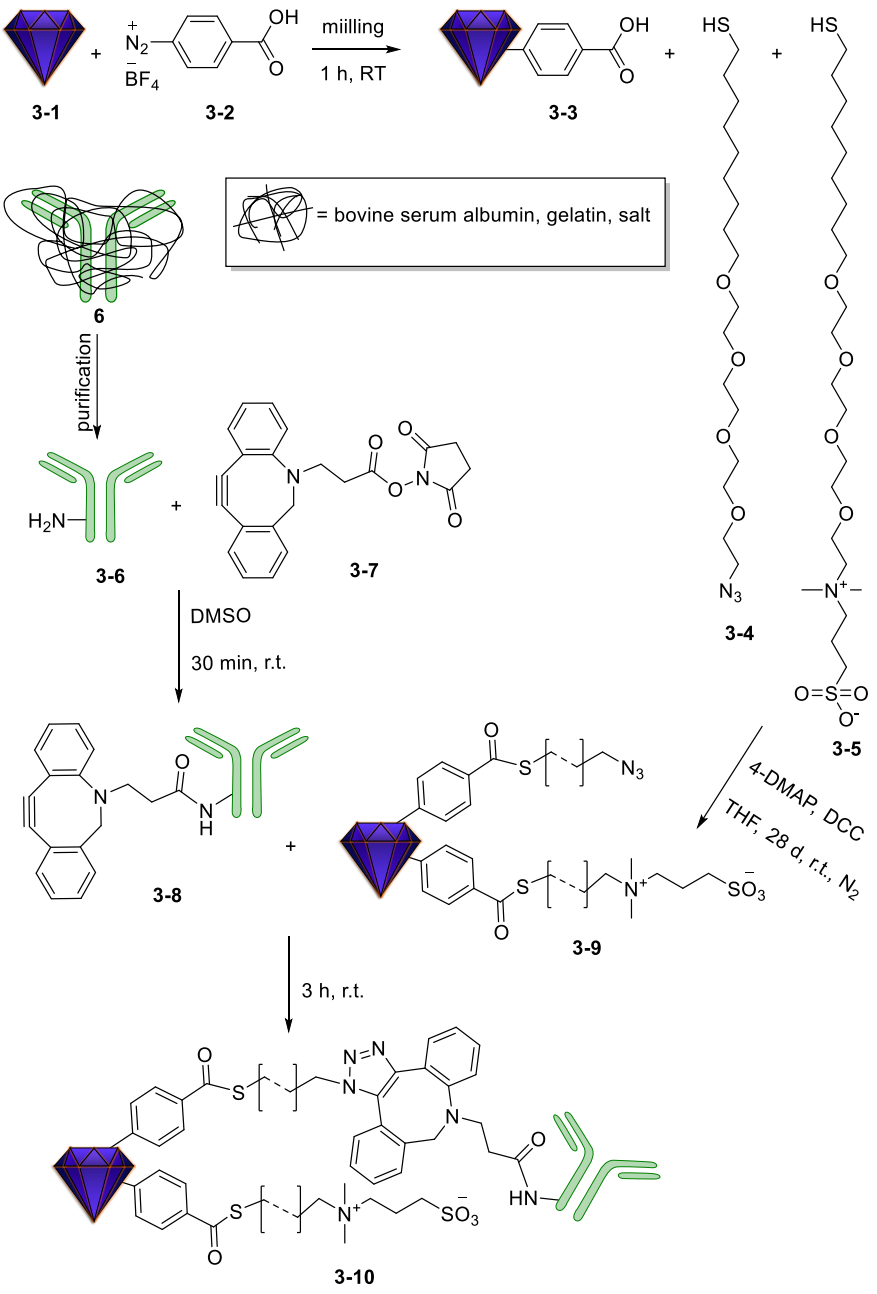

Scheme 3-1. Functionalization of fluorescent nanodiamond (fND) **3-1** with acid groups **3-3**, a mixture of chains with azides **3-4** and zwitterions **3-5** as the head group to yield ND **9** and subsequent click reaction with the DBCO-NHS ester functionalized and purified antibody **3-8** to the final fND **3-10**.

3.2 Results and Discussion

The fND was functionalized using an adapted procedure reported in.[15] However, in that work the functionalization was carried out on detonation nanodiamond (DND).[15] These contain far less NV centers and are thus not suitable for imaging applications. As HPHT fND, are less reactive, the reaction procedures have to be adapted. Thus, harsher conditions were required leading to the replacement of ultrasonic treatment by mechanochemical reaction of the HPHT nanodiamond **3-1** and diazonium compound **3-2** using a mini mill at 50 Hz with steel beads. The successful functionalization is shown in the FT-IR spectra in Figure 3-1 by strong signals of the surface groups, e.g. the aromatic bands at 788 and 710 cm^{-1}. The subsequent functionalization with the two chains **3-4** and **3-5** is simultaneously performed leading to a stoichiometric distribution of the two moieties when assuming comparable reactivity. The IR spectrum shows changes at 2102 cm^{-1} due to the azide band and the sulfonic acid at 1040 and 1207 cm^{-1}. The surface loading for product fND **3-9**, obtained from the TGA data (see supporting information), shows that about 50 % acid moieties were converted to thioesters, which also explains the still present signal for the carboxylic groups.

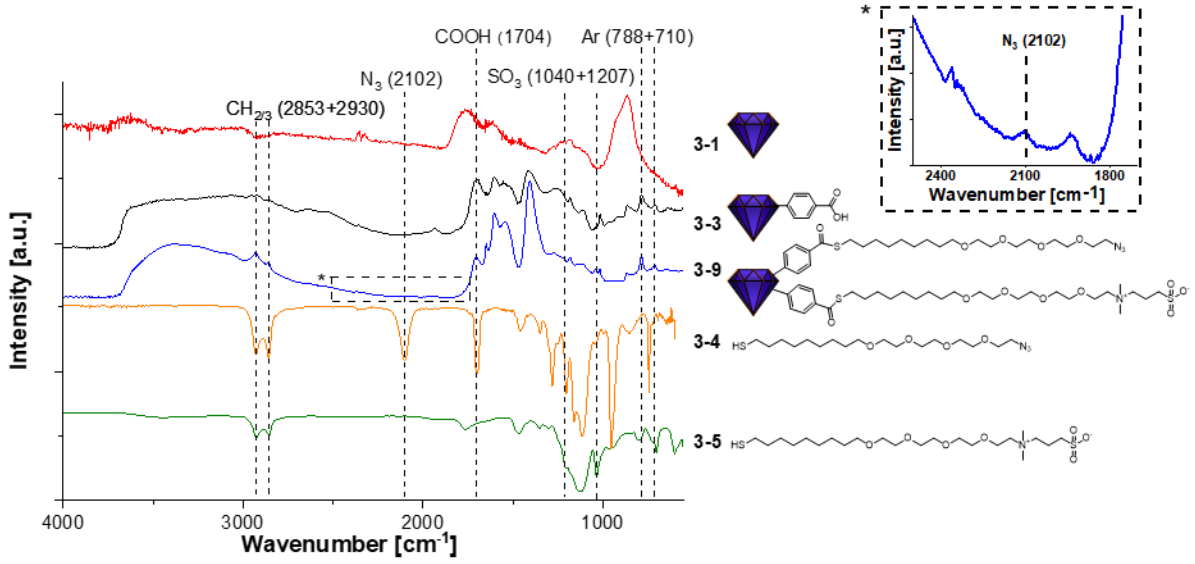

Figure 3-1. Series of DRIFT (red, black and blue) spectra of the functionalization of the ND **3-1** to ND **3-9** using the chains **3-4** and **3-5** (for which FT-IR ATR orange and green are shown) on a pre-functionalized ND **3** (significant wavenumbers pointed out in dotted lines with the respective moieties and wavenumbers in brackets), insert: zoomed IR-spectra of ND **3-9** indicating the presence of the azide band.

The functionalization of the fND with the chains containing TEG not only increases the colloidal stability but also the dispersibility. Drying the functionalized samples for the recording of IR spectra and subsequent redispersion was possible and let to again fully deagglomerated nanoparticles. This is of great importance for the generation of a homogeneous material with a fully controlled surface with as many primary particles as possible for subsequent reactions. Functionalization with long chains, as already shown in our recently published work, lead to a significant increase of the hydrodynamic diameter of the nanoparticles measured by DLS, while the particles show their actual, only slightly increased diameter in AFM measurements.[15] Here, the successful functionalization, did not lead to increased particle sizes and no agglomeration was observed. For fNDs **3-1** to **3-9** the hydrodynamic diameter (D(50) = 287(**3-1**) → 266(**3-9**) nm) remained largely the same. In addition, the mechanochemical functionalization to ND **3-3** using a mill (see SI in the appendix ND **3-3**) not only made the reaction possible, but also achieved a small particle size (D (50) = 287(**3-1**) → 184(**3-3**) nm). The typically observed increasing particle size in the DLS (but not in the AFM) during the functionalization of detonation NDs was not observed here when using the same functionalization of fNDs, since the aggregate size was continuously controlled due to the *in-situ* milling, which counteracts the increasing hydrodynamic radius due to the functionalization.

To achieve stabilization in physiological media, the ND was functionalized with a zwitterion chain. The zwitterionic betaine derivative provides effective protection against ions on the surface thanks to an overall neutral surface charge, which not only stabilizes the ND physiologically but also leads to protein repulsion. The entire zwitterionic chain system follows the so called “Whiteside rules” and is therefore suitable for forming a protective layer against a protein corona.[16] Without this protective layer, a protein corona or other molecules would attach onto the surface of the particle and disrupt the functionality of the antibodies. Thus, the additional zwitterion chains, in addition to the azide chains, are important for the functionality of the targeting because the ND does not adsorb other molecules before it reaches the target.[15]

The DBCO grafted antibody, which has previously reacted with an NHS ester through the amino group, was attached to the azide groups on the ND surface using a copper free click

reaction. The successful application of this method had been reproted for a similar system by Simon *et al.* for proteins.[10]

To verify the targeting ability, the different fND dispersions were added to HeLa cells, which were then examined microscopically for the position of the particles in the cell. The fND without any treatment, with adsorbed antibody, and with antibody and zwitterion functionalized surface were compared. To simulate the influence of biofluids, the different fNDs were additionally incubated with fetal bovine serum (FBS) and added to cells (see Scheme 3-2).

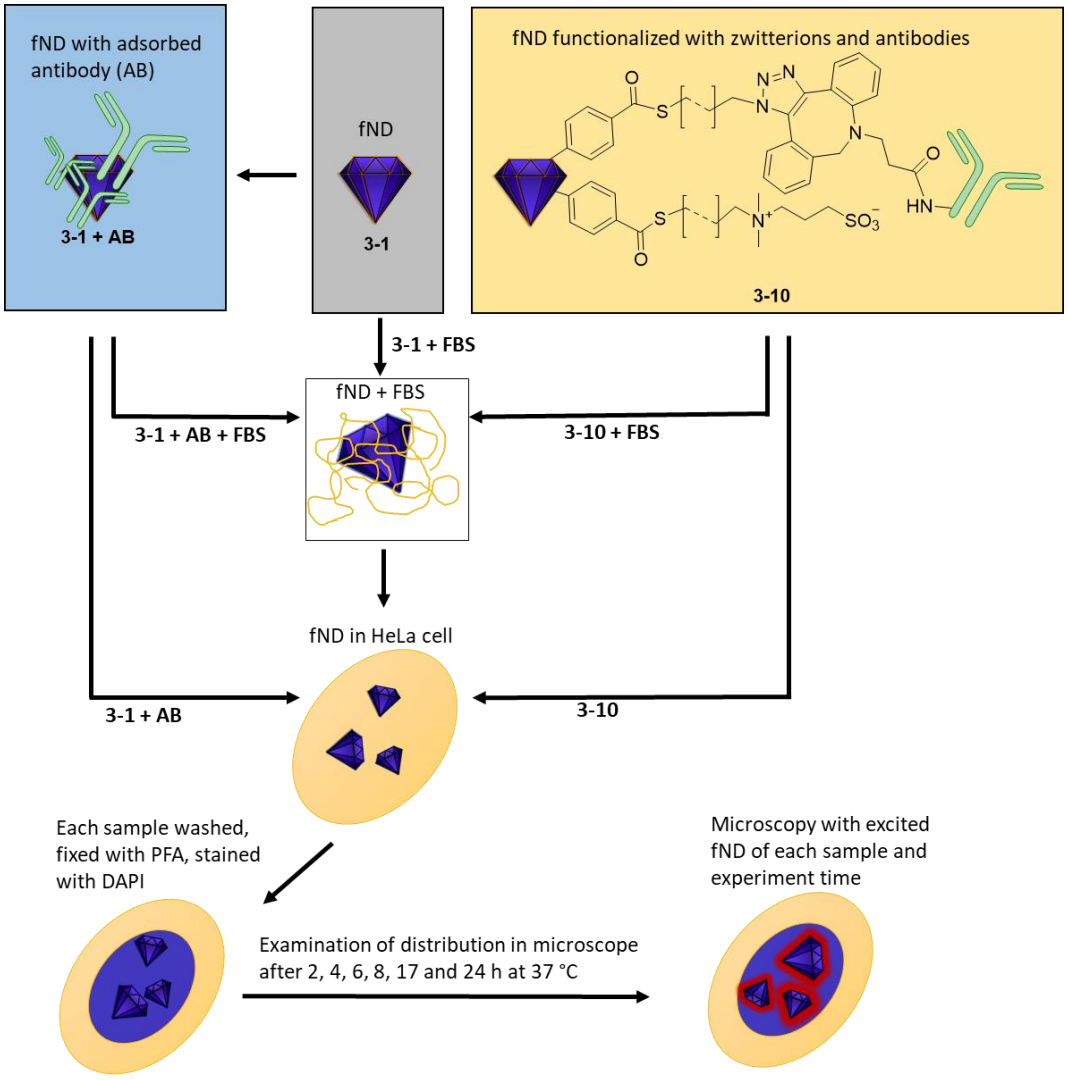

Scheme 3-2: Schematic illustration of the experiment procedure of each of the five fND dispersion **3-1**, **3-1+AB**, **3-10**, **3-1+AB+FBS** and **3-10+FBS** respectively investigated regarding their targeting distribution with and without FBS in HeLa cells.

The distances between each particle and the closest cell nucleus were measured, using the 3D Euclidean Distance Maps method reported by A. Sigaeva *et al*., and shown in Figure 3-2.[17]

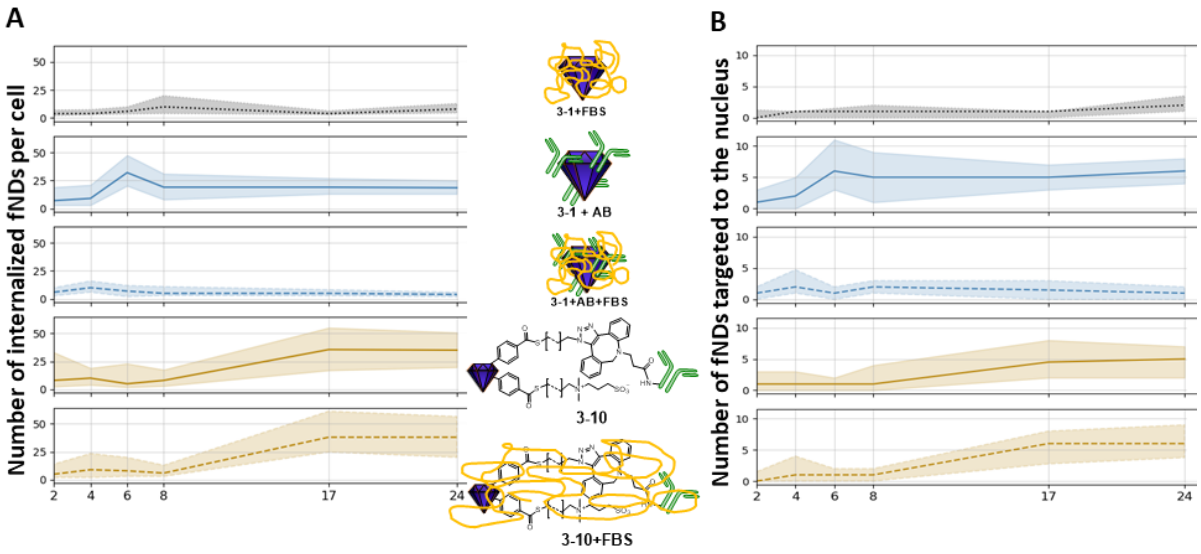

Figure 3-2: Number of A; internalized fNDs per cell and B; targeted fNDs to the nucleus in a 24 h experiment in HeLa cells of each dispersion **3-1+FBS**, **3-1+AB**, **3-10**, **3-1+AB+FBS** and **3-10+FBS** (dotted lines with FBS incubation, solid lines without FBS and the shaded areas represent the interquartile ranges of 50 samples for each data point).

In comparison, internalization numbers of the fND systems in the cells are in some cases very different (Figure 3-1, A). On the one hand, only some small numbers of fND **3-1+FBS** and **3-1+AB+FBS** entered the cells. On the other hand, there is hardly any difference between the first measurement of the two fNDs after two hours and after 24 hours. The reason for this could be the formation of a protein corona, which prevents penetration due to the increase in size of the particles. Without incubation with FBS, there is no change in the number of fNDs in cells after six hours for **3-1+AB**, but it is significantly higher than those treated with FBS. The best values are reached by both fNDs with TEG-zwitterion chain, **3-10** and **3-10+FBS**, where here the uptake stagnates in the first 8 hours but takes the highest value after 17 hours. Interestingly, in the two samples with zwitterion, not only the uptake after 17 hours is best, but also the difference between with FBS and without FBS is statistically insignificant. One possible explanation is that the zwitterions promote repulsion from the protein corona, ensuring not only that the particles are unmasked and colloidally stabilized, but also that the antibody is not prevented from binding to the cell nucleus. In addition, the late penetration into the cell could

be due to the colloidal stabilization of the particles by the TEG zwitterion chains. Even in complex media, the particles are colloidally stabilized, so that even after a long residence time (17 h), small, non-agglomerated, fNDs can still enter the cell, which for all other samples is not the case.

Once inside the cell, the number of particles bound to the nucleus can be similarly explained (Figure 3-1, B). By masking the surface, **3-1**+**AB**+**FBS** is no longer able to perform targeting and cannot bind significantly to the nucleus compared to fND **3-1**+**AB** not treated with FBS. The situation is different for the colloidally stabilized particles **3-10** and **3-10**+**FBS**. Not only can these partially successfully perform targeting, but again show no difference between FBS-treated and non-FBS-treated samples, indicating successful shielding by the zwitterions.

3.3 Experimental Section

Methods: fND was purchased Adámas Nanotechnologies (fND Carboxylated 70 nm Red, in DI water, ≤ 3ppm NV 1 mg/mL) as aqueous suspension. Chemicals were purchased from *Thermo Fisher Scientifics* (*Acros Organics, Fluka*), *Merck* (*Sigma Aldrich*) and *Grüssing* and used without further purification unless noted. All solvents were freshly distilled and dried using standard procedures. For the purification of the fND, bidistilled water (DD-water, 18.2 MΩ cm) at a pH of 5.5 and T = 20 °C) was used. Nuclear magnetic resonance spectra (^{1}H and ^{13}C) were measured with a *Bruker* AVANCE 400 FT-NMR spectrometer at 27 °C. The chemical shift of the deuterated solvents was used as internal reference for the calibration of spectra. Electrospray ionization (ESI) was performed using a *Bruker Daltonics* micOTOF focus. The FT-IR spectroscopy was carried out in a *Jasco* FT/IR-430 using ~1 mg ND. ATR spectra were recorded using the same spectrometer equipped with an ATR unit MIRacleTM from *PIKE Technologies*. Diffuse reflectance IR spectra (DRIFT) of ND samples were additionally measured using a DRIFT spectrometer *Nicolet* iS5. Thermogravimetric analysis (TGA) was performed on a *Perkin-Elmer* STA 6000 with 60 mL min^{-1} nitrogen flow rate and a heating rate of 10 K min^{-1} from 50 °C to 130 °C, a plateau time of 60 min at 130 °C and a heating phase from 130 °C to 700 °C at 5 K min^{-1}. The particle size and zeta potential were measured in bidistilled water at the intrinsic pH of the sample colloid using a *Malvern* Zetasizer Nanoseries Nano-ZS (dynamic light scattering, backscattering mode). The size distribution is given as volume distribution (Dv(10), Dv(50) and Dv(90)) and was obtained using the Marquardt method. The reaction with HPHT ND and diazonium compounds was carried out in a mini mill Pulverisette 23 (*Fritsch*) for 1 h at 50 Hz vibration mode with 10 pieces of 2 mm stainless steel beads. The sonication for washing of the samples was carried out in a *Bandelin* Sonorex Digitec Typ DT52 (max. 80 W, 35 kHz). Centrifugation was performed in a *Hettich* Mikro 220 R at 15 °C and a maximum of 31 514 RCF (18 000 RPM) using 2 mL Eppendorf safelock-cap tubes PP. The purifications of the antibody before and after reaction were carried out using a *Thermo Scientific* Pierce Antibody Clean-up Kit (detailed use in the supporting information). The anti-Nuclear Pore Complex Proteins (aNPC) ChIP Grade (ab24609) were purchased from *abcam* and were cleaned as described in the supporting information in the appendix.

Synthesis of organic linkers and the prefunctionalized nanodiamond are shown together with the respective spectra in the supporting information in the appendix.

The following part was executed by Alina Sigaeva in a cooperation with Romana Schirhagl's group at the University of Groningen. The cell culture (HeLa) was prepared under standard culturing conditions in Eagle's Minimal Essential Medium (DMEM) with 4500 mg/L glucose supplemented with 10 % Fetal Bovine Serum (FBS), 1 % Penicillin/streptomycin and 1 % Glutamax (Gibco, ThermoFisher Scientific) at 37°C, 5% CO_2 in glass bottom CELLview™ cell culture dishes (Greiner Bio-One B.V.) until approximately 60-90% confluency on the day of the experiment.

The cells were exposed to various fND dispersion in the cell culture medium in the final concentration of 1 μg/mL (see Scheme 3-2) for 2, 4, 6, 8, 17 or 24 hours at +37 °C and 5 % CO_2. After the incubation the cells were rinsed with phosphate buffered saline (PBS, pH = 7.4) and fixed in 3.7% paraformaldehyde (PFA) for 15 minutes. The fixed cells were washed with PBS, stained with 4′,6-diamidin-2-phenylindol (DAPI) and stored in 1% paraformaldehyde (PFA) until the microscopic imaging and analysis.

The visual recording of the cells and nanodiamonds was obtained using a LSM780 laser scanning confocal microscope (ZEISS), using a 405 nm laser for a DIC image and DAPI, and a 561 nm laser to excite the fNDs, which was detected between 653–758 nm.

All confocal images were processed in FIJI 2.0.0 (https://fiji.sc), using *Diffraction PSF 3D*, *Iterative Deconvolve 3D* and *3D Objects Counter* plugin. All fNDs that were not internalized were excluded from the analysis.

3.4 References

[1] V. N. Mochalin, O. Shenderova, D. Ho, Y. Gogotsi. The properties and applications of nanodiamonds. *Nat. Nanotechnol.* **2012**, *7*, 11–23.

[2] O. A. Shenderova, G. E. McGuire. Science and engineering of nanodiamond particle surfaces for biological applications (Review). *Biointerphases* **2015**, *10*, 30802.

[3] M. Radtke, E. Bernardi, A. Slablab, R. Nelz, E. Neu. Nanoscale sensing based on nitrogen vacancy centers in single crystal diamond and nanodiamonds: achievements and challenges. *Nano Futures* **2019**, *3*, 42004.

[4] a) L. Rondin, J.-P. Tetienne, T. Hingant, J.-F. Roch, P. Maletinsky, V. Jacques. Magnetometry with nitrogen-vacancy defects in diamond. *Rep. Prog. Phys.* **2014**, *77*, 56503; b) M. H. Alkahtani, F. Alghannam, L. Jiang, A. Almethen, A. A. Rampersaud, R. Brick, C. L. Gomes, M. O. Scully, P. R. Hemmer. Fluorescent nanodiamonds: past, present, and future. *Nanophotonics* **2018**, *7*, 1423–1453.

[5] a) E. Moreva, E. Bernardi, P. Traina, A. Sosso, S. D. Tchernij, J. Forneris, F. Picollo, G. Brida, Ž. Pastuović, I. P. Degiovanni, P. Olivero, M. Genovese. Practical Applications of Quantum Sensing: A Simple Method to Enhance the Sensitivity of Nitrogen-Vacancy-Based Temperature Sensors. *Phys. Rev. Applied* **2020**, *13*, 54057; b) M. Gulka, H. Salehi, B. Varga, E. Middendorp, O. Pall, H. Raabova, T. Cloitre, F. J. G. Cuisinier, P. Cigler, M. Nesladek, C. Gergely. Simultaneous label-free live imaging of cell nucleus and luminescent nanodiamonds. *Sci. Rep.* **2020**, *10*, 9791; c) S. Y. Ong, M. Chipaux, A. Nagl, R. Schirhagl. Shape and crystallographic orientation of nanodiamonds for quantum sensing. *Physical chemistry chemical physics : PCCP* **2017**, *19*, 10748–10752; d) T. Zhang, G.-Q. Liu, W.-H. Leong, C.-F. Liu, M.-H. Kwok, T. Ngai, R.-B. Liu, Q. Li. Hybrid nanodiamond quantum sensors enabled by volume phase transitions of hydrogels. *Nat. Commun.* **2018**, *9*, 3188; e) J. Holzgrafe, Q. Gu, J. Beitner, D. M. Kara, H. S. Knowles, M. Atatüre. Nanoscale NMR Spectroscopy Using Nanodiamond Quantum Sensors. *Phys. Rev. Applied* **2020**, *13*; f) U. Jantzen, A. B. Kurz, D. S. Rudnicki, C. Schäfermeier, K. D. Jahnke, U. L. Andersen, V. A. Davydov, V. N. Agafonov, A. Kubanek, L. J. Rogers, F. Jelezko. Nanodiamonds carrying silicon-vacancy quantum emitters with almost lifetime-limited linewidths. *New J. Phys.* **2016**, *18*, 73036.

[6] M. P. Lake, L.-S. Bouchard. Targeted nanodiamonds for identification of subcellular protein assemblies in mammalian cells. *PloS one* **2017**, *12*, e0179295.

[7] A. Morita, T. Hamoh, A. Sigaeva, N. Norouzi, A. Nagl, K. J. van der Laan, E. P. P. Evans, R. Schirhagl. Targeting Nanodiamonds to the Nucleus in Yeast Cells. *Nanomaterials* **2020**, *10*, 1962.

[8] N. G. Welch, J. A. Scoble, B. W. Muir, P. J. Pigram. Orientation and characterization of immobilized antibodies for improved immunoassays (Review). *Biointerphases* **2017**, *12*, 02D301.

[9] O. Koniev, A. Wagner. Developments and recent advancements in the field of endogenous amino acid selective bond forming reactions for bioconjugation. *Chem. Soc. Rev.* **2015**, *44*, 5495–5551.

[10] M. Simon, U. Zangemeister-Wittke, A. Plückthun. Facile double-functionalization of designed ankyrin repeat proteins using click and thiol chemistries. *Bioconjugate Chem.* **2012**, *23*, 279–286.

[11] S. Arumugam, J. Chin, R. Schirrmacher, V. V. Popik, A. P. Kostikov. 18Fazadibenzocyclooctyne (18FADIBO): a biocompatible radioactive labeling synthon for peptides using catalyst free 3+2 cycloaddition. *Bioorg. Med. Chem.* **2011**, *21*, 6987–6991.

[12] a) S. R. Hemelaar, A. Nagl, F. Bigot, M. M. Rodríguez-García, M. P. de Vries, M. Chipaux, R. Schirhagl. The interaction of fluorescent nanodiamond probes with cellular media. *Microchim. Acta* **2017**, *184*, 1001–1009; b) A. E. Garcia-Bennett, A. Everest-Dass, I. Moroni, I. D. Rastogi, L. M. Parker, N. H. Packer, L. J. Brown. Influence of surface chemistry on the formation of a protein corona on nanodiamonds. *J. Mater. Chem. B* **2019**, *7*, 3383–3389; c) I. Machova, M. Hubalek, T. Belinova, A. Fucikova, S. Stehlik, B. Rezek, M. H. Kalbacova. The bio-chemically selective interaction of hydrogenated and oxidized ultra-small nanodiamonds with proteins and cells. *Carbon* **2020**, *162*, 650–661; d) D. Khanal, Q. Lei, G. Pinget, D. A. Cheong, A. Gautam, R. Yusoff, B. Su, S. Yamaguchi, A. Kondyurin, J. C. Knowles, G. Georgiou, L. Macia, J.-H. Jang, I. Ramzan, K. W. Ng, W. Chrzanowski. The protein corona determines the cytotoxicity of nanodiamonds: implications of corona formation and its remodelling on nanodiamond applications in biomedical imaging and drug delivery. *Nanoscale Adv.* **2020**, *2*, 4798–4812.

[13] a) Y. Zou, S. Ito, F. Yoshino, Y. Suzuki, L. Zhao, N. Komatsu. Polyglycerol Grafting Shields Nanoparticles from Protein Corona Formation to Avoid Macrophage Uptake. *ACS Nano* **2020**, *14*, 7216–7226; b) D. Terada, S. Sotoma, Y. Harada, R. Igarashi, M. Shirakawa. One-Pot Synthesis of Highly Dispersible Fluorescent Nanodiamonds for Bioconjugation. *Bioconjugate Chem.* **2018**, *29*, 2786–2792; c) M. C. Lukowiak, B. Ziem, K. Achazi, G. Gunkel-Grabole, C. S. Popeney, B. N. S. Thota, C. Böttcher, A. Krueger, Z. Guan, R. Haag. Carbon-based cores with polyglycerol shells – the importance of core flexibility for encapsulation of hydrophobic guests. *J. Mater. Chem. B* **2015**, *3*, 719–722; d) I. Rehor, H. Mackova, S. K. Filippov, J. Kucka, V. Proks, J. Slegerova, S. Turner, G. van Tendeloo, M. Ledvina, M. Hruby, P. Cigler. Fluorescent Nanodiamonds with Bioorthogonally Reactive Protein-Resistant Polymeric Coatings. *ChemPlusChem* **2014**, *79*, 21–24.

[14] B.-M. Chang, H.-H. Lin, L.-J. Su, W.-D. Lin, R.-J. Lin, Y.-K. Tzeng, R. T. Lee, Y. C. Lee, A. L. Yu, H.-C. Chang. Highly Fluorescent Nanodiamonds Protein-Functionalized for Cell Labeling and Targeting. *Advanced functional materials* **2013**, *23*, 5737–5745.

[15] V. Merz, J. Lenhart, Y. Vonhausen, M. E. Ortiz-Soto, J. Seibel, A. Krueger. Zwitterion-Functionalized Detonation Nanodiamond with Superior Protein Repulsion and Colloidal Stability in Physiological Media. *Small* **2019**, *15*, 1901551.

[16] Q. Wei, T. Becherer, S. Angioletti-Uberti, J. Dzubiella, C. Wischke, A. T. Neffe, A. Lendlein, M. Ballauff, R. Haag. Protein interactions with polymer coatings and biomaterials. *Angew. Chem. Int. Ed.* **2014**, *53*, 8004–8031.

[17] A. Sigaeva, A. Morita, S. R. Hemelaar, R. Schirhagl. Nanodiamond uptake in colon cancer cells: the influence of direction and trypsin-EDTA treatment. *Nanoscale* **2019**, *11*, 17357–17367.

[18] C. Kim, G. Y. Tonga, B. Yan, C. S. Kim, S. T. Kim, M.-H. Park, Z. Zhu, B. Duncan, B. Creran, V. M. Rotello. Regulating exocytosis of nanoparticles via host-guest chemistry. *Org. Biomol. Chem.* **2015**, *13*, 2474–2479.

[19] C. K. Kim, P. Ghosh, C. Pagliuca, Z.-J. Zhu, S. Menichetti, V. M. Rotello. Entrapment of hydrophobic drugs in nanoparticle monolayers with efficient release into cancer cells. *J. Am. Chem. Soc.* **2009**, *131*, 1360–1361.

Chapter 4

Pyrene-Based "Turn-Off" Probe with Broad Detection Range for Cu^{2+}, Pb^{2+} and Hg^{2+} Ions

The following section is slightly modified and reproduced from V. Merz, J. Merz, M. Kirchner, J. Lenhart, T. B. Marder, A. Krueger, Pyrene-Based "Turn-Off" Probe with Broad Detection Range for Cu^{2+}, Pb^{2+} and Hg^{2+} Ions, *Chem. Eur. J.* **2021**, *27*, 8118., *with permission from Wiley-VCH.*

4.1 Introduction

The use of heavy metals in industry, agriculture, household and technology is among others one of the main sources for environmental pollution and detrimental effects on plants and the health of animals and humans.[1–7] Metals such as copper, lead and mercury are among the most common in waste water.[8] Copper is very common, not only in industry, but also in the home (copper pipes, etc.) and as a pesticide that is released directly into the environment. It causes diseases such as Wilson's disease and the so-called "vineyard sprayer's lung".[9–11] Sources of lead pollution in the environment are manifold. The majority originate from the melting and processing of ores, but industrial and car exhaust gases, lead batteries, additives in paints and varnishes, and petrol additives that were used until the 2000's are also sources.[6b,12] Consequential damage from prolonged exposure to these pollutants include reduced intelligence, delayed or impaired neurobehavioral development, reduced hearing acuity, speech impairment, and growth disorders, even at very low exposure.[6] Mercury had its peak in industrial demand when numerous measuring instruments, such as thermometers, barometers, etc., as well as lighting tubes were manufactured using this metal. When it is released into the environment, mercury is broken down by microorganisms into toxic methyl mercury compounds and it accumulates in the food chain which causes the so-called Minamata disease.[6,7,13,14]

Once heavy metals are ingested, their ability to be reduced or oxidized enables them to bind to biomolecules in various oxidation states and then alter or even block important functions of vital metal complexes, thereby circumventing control mechanisms of the organism and leading to toxic effects.[5,7,15,16]

In order to prevent the release of heavy metals into the environment as early as possible, control mechanisms must be implemented whenever these metals are used.[6,17,18] As heavy metals in industry are not only applied in an aqueous environment, whereas it is crucial to have water

soluble sensors, there is a need for sensors applicable in different solvents. It is therefore important to manufacture specific sensors for applications in different media. In order to address the diverse range of uses of heavy metals, and to detect and eliminate them quickly in the event of uncontrolled release into the environment, tailored sensors are required.

In this work, we present a pyrene- and tetraethylene glycol (TEG)-based molecular sensor for selectively detecting Cu(II), Pb(II) and Hg(II) in health-relevant concentrations via quenching of the monomer fluorescence of pyrene in organic solvents.

4.2 Results and Discussion

The reported sensor combines a previously reported glycol precursor[19] with a rigid arrangement of pyrene moieties. Due to its versatile and extensively investigated properties, pyrene is well suited as a chemical sensor.[20–29] Pyrene derivatives functionalized at the 2-position via a one-step iridium-catalyzed reaction with B_2pin_2 offers a significantly longer fluorescence lifetime in contrast to pyrene derivatives that are functionalized at the 1-position.[30,31] As a chemosensor, in most cases, reports on the analyte in its excited state, the response is enhanced for sensors with longer excited state lifetimes, leading to improved sensistivity.[32] However, until now, only a few chemosensors based on pyrenes functionalized at their 2-position have been reported.[27,28,33,34] These sensors were designed to enter into targeted interactions with metals through functional groups or crown ethers on the pyrene. In our work, we combine pyrene functionalized at its 2-position with a tailored glycol chain, which has two decisive advantages. First, the molecule is soluble and can be purified via solution-phase methods such as chromatography and applied in a variety of solvents. Second, TEG provides crown ether-like properties which improve coordination to metal ions.[35] Therefore, the sensor was constructed using a TEG chain carrying a branching moiety that bears three binding sites for pyrenyl groups bound at their 2-position.

4.2.1 Synthesis and Characterization of a Rigid tris-Pyrenyl Sensor

The TEG chain **4-1** is used as the scaffold for the attachment of three pyrenes via the formation of triazole linkers in a click reaction of **4-1** with three molecules of 2-ethynylpyrene **4-2** (Scheme 4-1). The resulting tris-pyrenyl conjugate not only possesses the ability to complex metal ions, but the opposite terminus is designed to allow for subsequent immobilization of the

sensor using the amino function for coupling to, e.g., nanoparticles, chip surfaces or biomolecules.

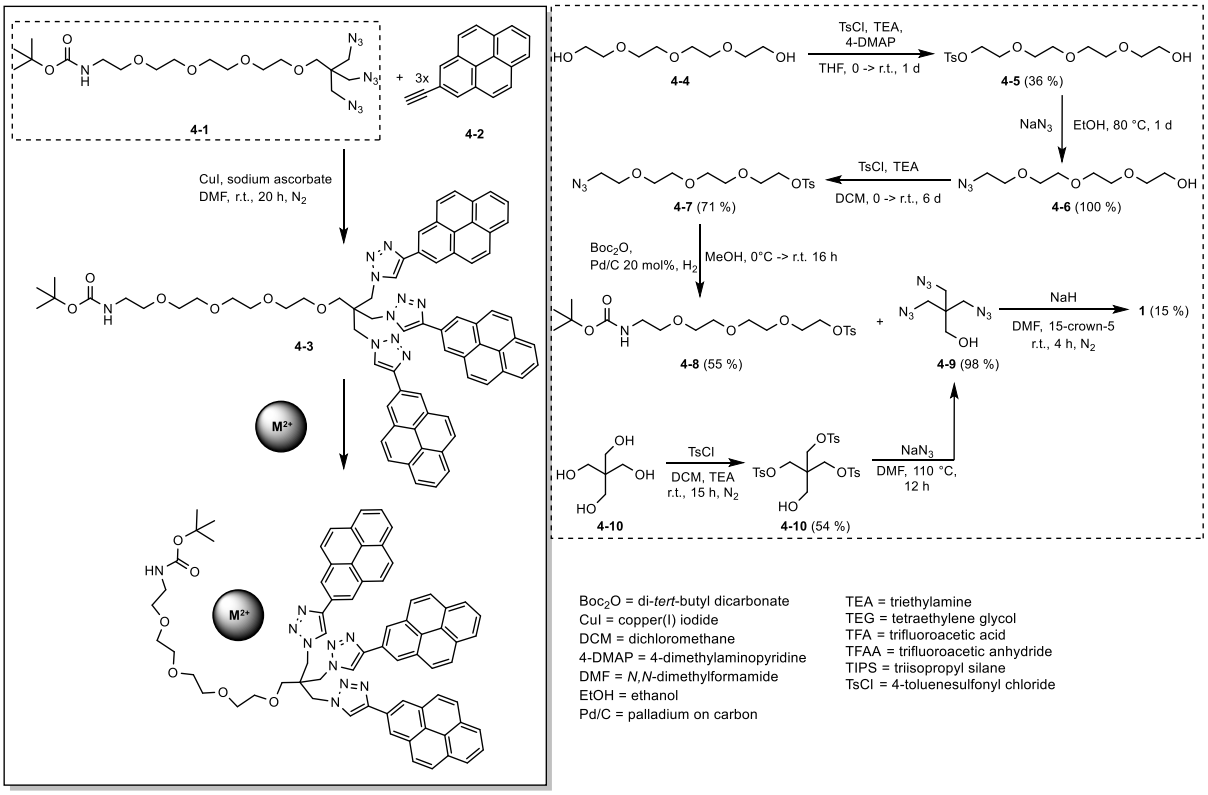

Scheme 4-1. Synthesis of the glycol chain (dashed rectangle) and of probe **4-3** using click chemistry and its mode of action when complexing a divalent M^{2+} cation in acetonitrile.

A very important feature for the functionality of this probe is the reduced spacing and the ensuing low steric flexibility at the focal point of the molecule's branching unit, preventing **4-3** from forming *intra*molecular dimers of the pyrene head groups. The interaction between two molecule head groups to form an *inter*molecular dimer is also suppressed by the limited flexibility of the branching unit. These structural features allowed us to apply this sensor in a very broad concentration range (see below). Previously, Seela and Ingale reported a pyrene-based sensor for the detection of Zn^{2+}, which shows very efficient excimer formation due to the flexibility of the different pyrene moieties.[36] However, due to its structural design, our probe does not show excimer emission that could mask possible signals in the longer-wavelength range in solvents such as MeOH, MeCN, CH_2Cl_2 and toluene from low to even very high concentrations (Supporting Information Figure S4-4 and Figure 4-1). However, for applications such as fluorescent ratiometric detection pyrene's excimer emission can be of interest.[36]

Pyrene excimer formation is usually observed in the wavelength range between 400–600 nm, with a maximum at about 500 nm, and is used in many applications for sensing due to its fluorescence signal strength and sensitivity.[25–27,37–41] However, when sensing depends on longer lifetimes of the excited state, a chemical sensor relying on monomer fluorescence is superior to a sensor based on excimer formation. Depending on the system, the lifetime of an excimer of pyrene is typically about one order of magnitude shorter than that of the excited monomer state.[42]

The absorption and emission spectra of **4-3** are shown in Figure 4-1. The spectral features of pyrenes are clearly visible.

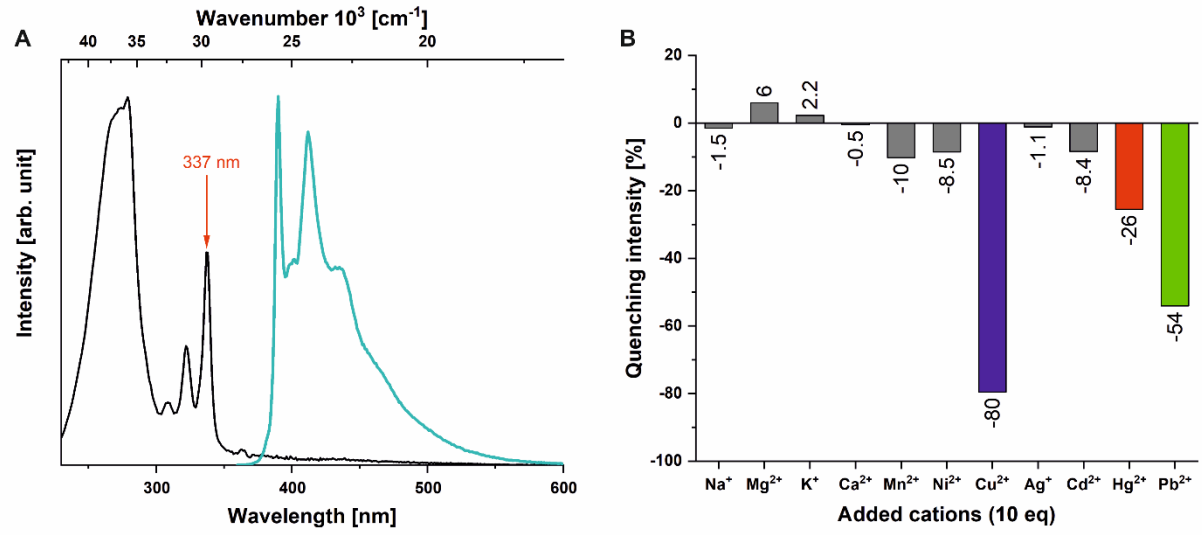

Figure 4-1. A) Normalized absorption and emission (excited at 337 nm) spectra of probe **4-3** in acetonitrile (concentration: 3.17 x 10^{-6} mol L^{-1}) and B) fluorescence responses of **4-3** (concentration: 1.02 x 10^{-6} mol L^{-1}) to a selection of monovalent and divalent metal ions (used in the form of perchlorate salts) at 10 eq excess (see SI for a complete set of tested cations).

The absorption spectrum of unsubstituted pyrene consists of four bands,[43] one forbidden band ($S_1 \leftarrow S_0$) at 372 nm (ε = 510 mol^{-1} cm^{-1} L) with vibrational fine structure, two bands ($S_2 \leftarrow S_0$ and $S_3 \leftarrow S_0$) at 334 and 272 nm, and a strongly allowed band ($S_4 \leftarrow S_0$) at 243 nm (ε = 88000 mol^{-1} cm^{-1} L).[30,43] In this work, the absorption of the probe is very similar to that of unsubstituted pyrene due to the functionalization at 2-position of pyrene, which is situated on nodal planes in both the HOMO and LUMO, previously studied in detail by Marder and co-

workers.[30,44] Thus, the $S_1 \leftarrow S_0$ transition is still forbidden (372 nm) and the $S_2 \leftarrow S_0$ transition is slightly bathochromically shifted with a maximum at 337 nm.

In a screening experiment, the effect of a large number of cations on the fluorescence of **4-3** was investigated (Figure S4-12). The metal ions leading to significant changes and the most typical background ions were again measured as perchlorate salts, as these offer good solubility in acetonitrile and do not absorb light in the region of the sensor's fluorescence, avoiding reabsorption of emitted light. Strong fluorescence quenching was observed in the presence of Cu^{2+}, Pb^{2+} and Hg^{2+} while the emission wavelength was not influenced. Moreover, no quenching effects were observed upon addition of Ca^{2+}, Mg^{2+}, Na^{+} and K^{+}, which makes the sensor interesting for applications in which solvents come into contact with ions that are typically present in aqueous environments.

4.2.2 Fluorescence Titrations

Titrations of the three analyte cations (Figure 4-2) show strong, concentration-dependent quenching until a plateau of -83 (Pb^{2+}), -90 (Hg^{2+}) and -99 (Cu^{2+}) %, of their initial luminescence intensity is reached.

The detection limit (LOD) describes the lower limit at which the sensor can reliably measure the ions. According to the definition, this is achieved if the measurement signal is at least 3.3 times higher than the standard deviation of the measurement.[45] Here, the LOD was determined for a sensor concentration of 1.02×10^{-6} mol L^{-1} leading to an optical density of 0.1. The strongest effect on the fluorescence of **4-3** (at a concentration of 1.02×10^{-6} mol L^{-1}, 1 eq) is observed upon addition of Cu^{2+} translating to an LOD of 7.7×10^{-7} mol L^{-1} (0.7 eq), Pb^{2+} can be measured at concentrations from 6×10^{-7} mol L^{-1} (0.6 eq) and Hg^{2+} from 2.1×10^{-6} mol L^{-1} (2 eq) equivalents with confidence, which allows the sensing of all these ions in the health-relevant concentration range. However, as can be seen in the titrations carried out for the determination of the complex' stoichiometry (see below), the system delivers precise values also in the single-digit nM range, when the concentration of sensor **4-3** is reduced to 1.06×10^{-10} mol L^{-1}.

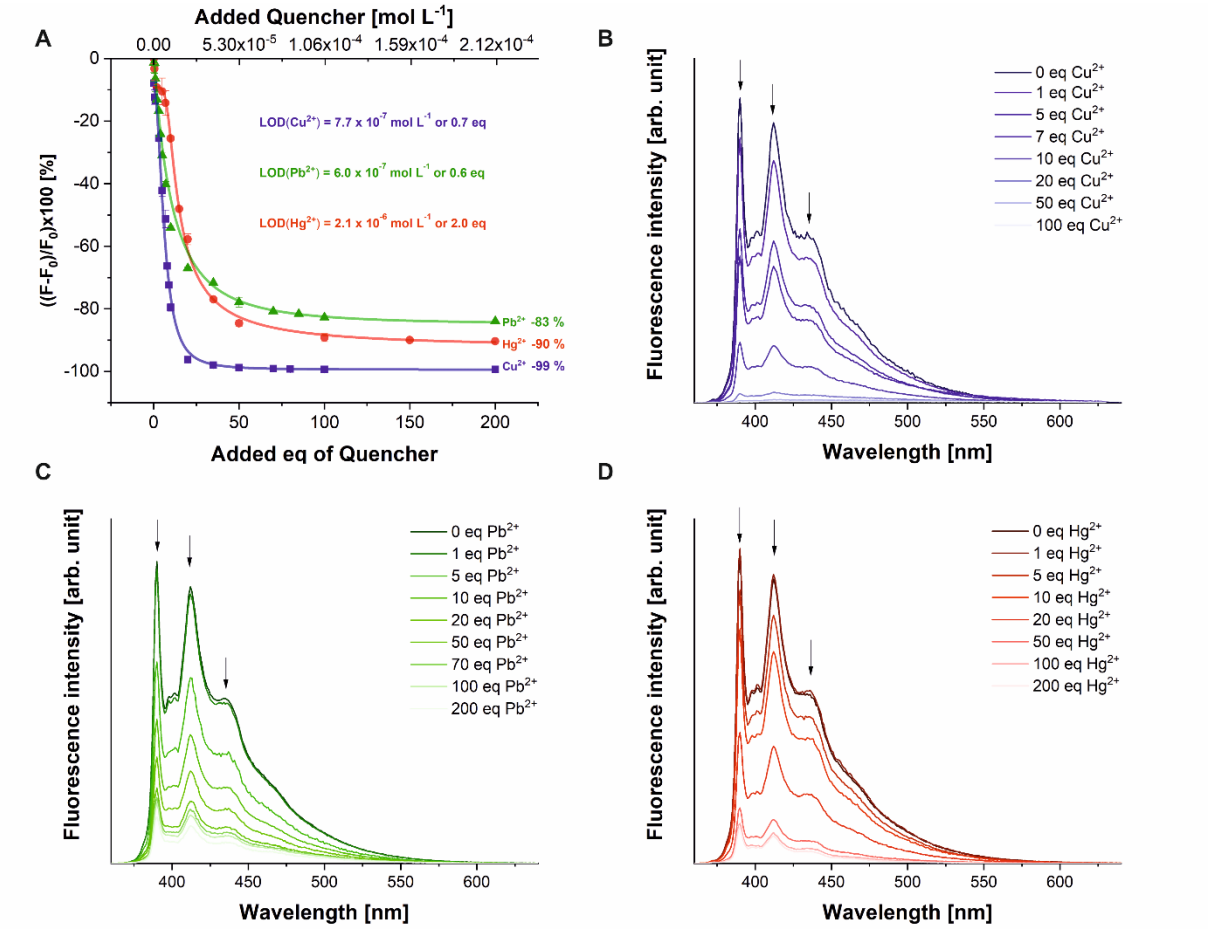

Figure 4-2. A) Fluorescence titration spectra of sensor **4-3** at 1.02 x 10^{-6} mol L^{-1} with the quencher ions Cu^{2+}(blue squares), Pb^{2+} (green triangles) and Hg^{2+} (red dots), error bars are given for all data points (see Figure S4-13 for magnification); individual spectra for the titration of B) copper, C) lead, D) mercury. All cations were used in the form of their perchlorate salts

For all sensor concentrations, quantitative statements can be made in a range of up to 50 eq. of the quencher ions, thus defining the upper limit of quantification (ULOQ). As can be seen in Fig. 2A, the linear part of the dynamic range of the sensor covers the ratio of 0 to 10 eq. of quencher (see below for a detailed discussion of the non-linear behaviour). Therefore, the ULOQ has to be determined by visual inspection of the titration curves, leading to ULOQ values of 20 eq. for Cu^{2+} (2.1 x 10^{-5} mol L^{-1}) and for Pb^{2+} and Hg^{2+} of 50 eq (5.3 x 10^{-5} mol L^{-1}) for a sensor concentration of 1.02 x 10^{-6} mol L^{-1}.

As the spectroscopic characteristics of the sensor fluorescence are identical for concentrations from 1.06 x 10^{-10} mol L^{-1} to 3.17 x 10^{-6} mol L^{-1} due to the absence of excimer formation, the concentration of **4-3** can be adjusted to the amount of quencher ions in the analyte solution. The

saturation plateau for the three ions Pb^{2+}, Hg^{2+} and Cu^{2+} is reached at -83 %, -90 % and -99 % of the initial fluorescence intensity, respectively.

The observed sensor properties are related to its mode of action. The system is based on dynamic quenching, which is the interaction of a quencher with a molecule in an excited state. Therefore, the sensitivity of the sensors strongly depends on the lifetime of the excited state from which the observed emission originates.[46] Thus, the observed very long fluorescence lifetime of **3** (165 nm) is beneficial for an efficient sensing process if dynamic quenching is the mode of action.

4.2.3 Fluorescence Lifetime Measurement

As shown in Figure 4-3, the fluorescence lifetime of sensor **4-3** is strongly dependent on the ion concentration. This can be used to confirm the type of fluorescence quenching process.

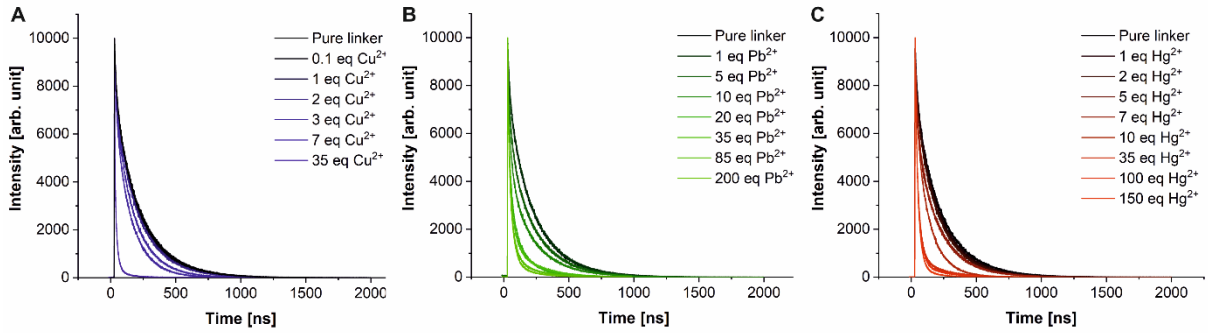

Figure 4-3. Lifetime titration spectra of sensor **4-3** upon addition of A) Cu^{2+}, B) Pb^{2+} and C) Hg^{2+}.

If dynamic quenching is involved, the decrease in lifetime is proportional to the concentration of the quencher.[46] After reaching the ULOQ, the lifetimes decrease for **4-3** to 5 ns quenched by Cu^{2+}, to 47 ns by Pb^{2+} and to 36 ns by Hg^{2+}. Additionally, the characteristics of the dynamic quenching process, like the mode and rate of interaction between host and quencher, need to be investigated.

4.2.4 Job Plots

A commonly used method to determine the interaction stoichiometry of the host sensor with a guest ion, is the Job plot, which is shown in Figure 4.[47,48] However, this plot cannot be used to

display systems with stoichiometries other than 1:1. In 1:2 or 2:1 complexes the maximum of the plot does not necessarily show the actual binding stoichiometry. In cases where the quotient of $K_{1:1}/K_{1:2}$ (or $K_{1:1}/K_{2:1}$) is larger than 1, the Job plot cannot be applied. Here, the maximum at 0.5 indicates a 1:1 ratio, which has only one binding constant, thus the application of the Job plot is justified.[49] This result has been confirmed using the free *bindfit* software, where a 1:1 stoichiometry gave highly satisfactory results (http://supramolecular.org). The fit for hypothetical 1:2 and 2:1 complexes resulted in negative values for binding constants and/or unrealistically high error values, while the unconstrained fit for a 1:1 system coincided with the results of the linear fits (see Figure S4-5 and S4-6).

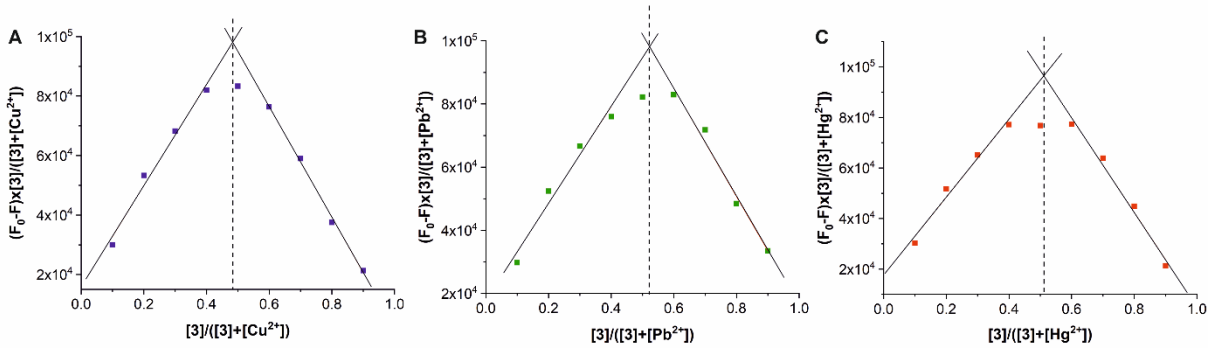

Figure 4-4. Job plot for each metal ion A) Cu^{2+}, B) Pb^{2+} and C) Hg^{2+} for a titration with a constant total host and guest concentration of 1.06 x 10^{-9} mol L^{-1} in the concentration ratio 9:1 to 1:9 in integer steps.

In addition to binding constants, the total concentration of the sensor is also a crucial factor for this type of analysis. The more concentrated the system, the more reliable values can be read from the Job plot.[47] However, for fluorescence measurements, the concentration range is usually determined by two factors: the detection window is limited on one side by the fluorescence detection limit and on the other side by the prevention of self-quenching of the fluorophores. In the case of pyrene derivatives, excimer formation is also observed in concentrated solutions.[29] By design, the system presented here has no possibilities to form an excimer, as already discussed. However, an unforeseen aspect of the molecular structure has been elucidated using Stern-Volmer plots (Figure 4-5).

4.2.5 Stern-Volmer Plots

An important prerequisite for the validity of the Stern-Volmer equation is the equal accessibility of all molecules of the fluorophore by the quencher, i.e. the same Stern-Volmer constant must apply to all molecules of the fluorophore.[50] If this precondition is not applicable due to the presence of differently accessible fluorophores, the Stern-Volmer equation cannot be used in its usual form. In the system presented here, all titrations can be linearly fit in the Stern-Volmer plot for the range of 0–7 eq (0–7 x 10^{-6} mol L^{-1}) of quencher.

The quenching constant, the Stern-Volmer constant (K_{SV}), can be read from the slope of the straight line. The slope for Cu^{2+} is 1.3 x 10^5 M^{-1}, for Pb^{2+} 8.1 x 10^4 M^{-1} and for Hg^{2+} 2.9 x 10^4 M^{-1}. For concentrations above 7 eq, however, the slope of the curve increases. Values for $F_0/F - 1$ in the Stern-Volmer plot deviating from linearity to higher values indicate the presence of processes that lead to a more efficient quenching of the fluorescence at higher quencher concentrations.

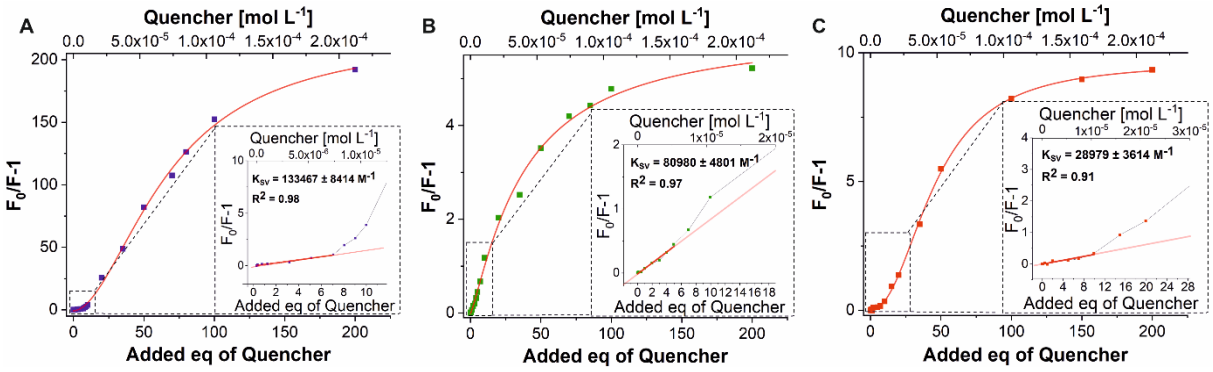

Figure 4-5. Stern-Volmer plots of A) Cu^{2+}, B) Pb^{2+} and C) Hg^{2+} titrated to a constant host **4-3** concentration (1.02 x 10^{-6} mol L^{-1}, 1 eq) from 0–200 eq of analyte. The insets show the linear regions at low quencher concentration.

These results suggest that a further quenching effect comes into play at higher ratios of guest ions to host sensor **4-3**. As the formation of excimers can be excluded from concentration-dependent measurement of **4-3**, we hypothesized that larger aggregates are formed. In fact, with the help of dynamic light scattering (DLS) experiments (Figure 4-6), metal ion-induced aggregate formation was confirmed that is not observed for solutions of sensor molecule **4-3** in

the absence of metal ions. The formation of flocculates upon the generation of an iron complex of a pyrene sensor that led to fluorescence quenching has been reported.[51]

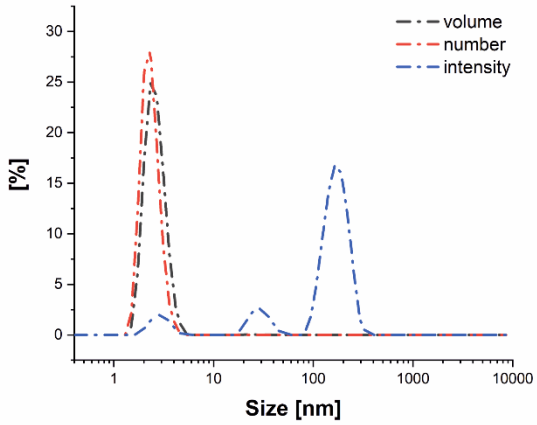

Figure 4-6. DLS size measurement (diameter) in acetonitrile of probe **4-3** (5 x 10^{-6} mol L^{-1}, 1 eq) in the presence of 200 eq of Cu^{2+}. To identify the different size classes of aggregates, different presentation modes of the scattering signal are shown. Note: Large objects are overrepresented in the intensity plot due to their higher scattering cross section (scaling with r^6) whereas in the number plot, larger objects are not visible due to their low concentration.

The aggregation process was found to be reversible as shown by the disappearance of the agglomerates upon addition of an equally concentrated solution of **4-3** until the concentration of Cu^{2+} is reduced to 60 eq, and their slow reformation after about 30 min as shown by DLS (see Figure S9 for details). As can be deduced from the volume distribution determined by DLS, 90 % of the agglomerates are smaller than 3.5 nm in diameter. The simultaneous presence of larger objects in the size range of 30 and 200 nm is evidenced by the scattering peaks in the intensity distribution. This confirms the suspected complex agglomeration behaviour of the sensor molecule. In previous agglomeration studies similar observations have been reported for titrations and the associated Stern-Volmer plots.[50,52–54]

4.2.6 Comparison with Benesi-Hildebrand Plots

Another frequently applied method to characterize the binding between host and analyte is the Benesi-Hildebrand method, where the binding constant (K_a) can be determined from the double reciprocal plot of the fluorescence ratio over the quencher concentration (see Figure S10).[55]

As for the Stern-Volmer plot, the Benesi-Hildebrand plots of **4-3** exhibits the different interaction regimes at low and high analyte concentrations. For Cu^{2+} and Pb^{2+}, the linearity is preserved in the low concentration range, the results for Hg^{2+} are not fully congruent. However, it turns out that in the sensitive area of the sensor (0-10 eq), the linearity is not sufficiently accurate to use the results of the Benesi-Hildebrand method to determine the binding constants. At higher concentrations (>20 eq), all three systems show linearity. However, the binding constants calculated from these slopes differ greatly from the results obtained with the *bindfit* method for the region of >10 eq (Table 4-1).

Table 4-1. Quenching constants K_{SV} obtained from Stern-Volmer-plots and binding constants K_a obtained from Benesi-Hildebrand (BH) plot and the software *bindfit* for low and high quencher concentrations.

Quencher	eq	K_{SV} [M^{-1}]	$K_{a(BH)}$[M^{-1}]	$K_{a(bindfit)}$ [M^{-1}]
Cu^{2+}	<10	1.3×10^5	1.26×10^5	1.54×10^5
Cu^{2+}	>10		1.21×10^6	3.96×10^4
Pb^{2+}	<10	8.1×10^4	2.25×10^4	1.10×10^4
Pb^{2+}	>10		1.55×10^5	2.18×10^4
Hg^{2+}	<10	2.9×10^4	2.02×10^5	9.16×10^5
Hg^{2+}	>10		5.69×10^4	2.99×10^4

The results for the respective binding constants, determined via the Benesi-Hildebrand-plot and *bindfit*, suggest that the Benesi-Hildebrand plot fails to adequately describe a quenching method that consists of dynamic quenching and agglomeration, which has also been discussed previously.[48]

4.2.7 NMR Titration

In order to obtain more information about the binding constants in addition to the fluorescence titration experiments, we performed NMR titration experiments in DMSO-d_6 to investigate the ^{1}H-NMR shifts upon addition of the three quenchers. The results are presented in the SI (Figure S4-11). They suggest that the interaction of the metal ions is not limited to the pyrene moiety and the triazole unit, but also involves the TEG chain, as indicated by the concomitant strong ^{1}H NMR shift. The NMR experiments also confirm an identical binding mode for all three

analyte ions (see details in SI). In the concentration range that was observable by NMR spectroscopy (0–50 eq), no saturation effect was found, thus confirming the assumed dynamic interaction between the ions and the sensor.

4.3 Conclusion

A highly specific, pyrene-based turn-off probe for the detection and quantification of the environmentally important metals Cu^{2+}, Pb^{2+} and Hg^{2+} was developed. The substitution of pyrene at its 2-position instead of the usual 1-position led to a rare probe with long fluorescence lifetimes enabling investigation of the dynamic quenching mechanism. Furthermore, the rigidity of the sensor architecture prevents the otherwise prominent excimer formation of the pyrenes and thereby allows the study of the monomer emission. A 1:1 complex stoichiometry was confirmed using *bindfit* and Job plots, whereas the Stern-Volmer plots revealed a complex set of interactions involving not only the formation of the stoichiometric complex, but also the reversible, metal-induced formation of nanosized aggregates at higher quencher concentrations. Binding constants in the range of $1.10 \times 10^4 – 9.16 \times 10^5\ M^{-1}$ allow for the sensitive quantification of the ions over a broad concentration range in organic solvents. In the future, the system could be immobilized on a solid support to prevent aggregate formation and moreover, make the system applicable in aqueous environments. Such applications are already underway in our laboratory.

4.4 Experimental Section

Synthetic and Spectroscopic Procedures

General methods. Azide **4-1** and alkyne **4-2** were prepared according to literature procedures.[19,44] All other starting materials were purchased from commercial sources and used as received. The solvents were freshly distilled and dried using standard procedures. Nuclear magnetic resonance spectra (^{1}H and ^{13}C) were measured with a Bruker AVANCE 400 FT-NMR spectrometer at 27 °C. For the calibration of spectra, the chemical shift of the deuterated solvents was used as internal reference. HRMS were recorded using a Thermo Scientific Exactive PlusOrbitrap MS system with either an Atmospheric Sample Analysis Probe (ASAP) or by Electrospray Ionization. The characterization by Fourier-transform infrared spectroscopy (FTIR) was carried out using a Jasco FT/IR-430 spectrometer fitted with an attenuated total reflection (ATR) MIRacle unit from PIKE Technologies. The particle size was measured using a Malvern Zetasizer Nanoseries Nano-ZS (dynamic light scattering, backscattering mode). The size distribution is given as volume, number and intensity distribution and was obtained using the Marquardt method. Degassing of solutions was performed by sonication using a Bandelin Sonorex Digitec Typ DT52 sonicator bath (max. 80 W, 35 kHz). All photophysical measurements were carried out under an argon atmosphere by preparing the samples in an argon-filled glovebox. The solution state measurements were performed in standard quartz cuvettes (1 cm x 1 cm cross section). The UV/Vis absorption spectra were measured using an Agilent 1100 diode array UV/Vis spectrophotometer. Excitation, emission, lifetime and quantum yield measurements were recorded using an Edinburgh Instruments FLSP920 spectrometer equipped with a 450 W Xenon arc lamp, double monochromators for the excitation and emission pathways, and a red-sensitive photomultiplier (PMT-R928P) as the detector. The measurements were performed in right-angle (90°) geometry mode and all spectra were fully corrected for the spectral response of the instrument.

Fluorescence quantum yields of the samples were measured using a calibrated integrating sphere (150 mm inner diameter) from Edinburgh Instruments attached to the FLSP920 spectrometer described above. For solution-state measurements, the longest wavelength absorption maximum of the compound in the respective solvent was chosen for the excitation.

In order to exclude self-absorption, the emission spectra were measured with dilute samples (approx. 0.1 optical density at the excitation wavelength).

Fluorescence lifetime measurements were conducted using the time-correlated single-photon counting method (TCSPC) on the FLSP920 spectrometer equipped with a high-speed photomultiplier tube positioned after a single emission monochromator. Measurements were made in right-angle (90°) geometry mode, and the emission was collected through a polarizer set to the magic angle. Solutions were excited with a 315 nm (pulse width 932.5 ps) pulsed diode laser at repetition rates of 1–5 MHz and were recorded at the emission maxima. Decays were recorded to 10,000 counts in the peak channel with a record length of at least 4,000 channels. The band-pass of the monochromator was adjusted to give a signal count rate of <20 kHz. Iterative reconvolution of the instrument response function (IRF) with one decay function and nonlinear least-squares analysis were used to analyze the data. The quality of all decay fits was judged to be satisfactory, based on the calculated values of the reduced χ^2 and Durbin-Watson parameters and visual inspection of the weighted and autocorrelated residuals.

The titration experiments for the Job plot were carried out in a 0:10–10:0 ratio (c/c), the total concentration of all components always being 1.06 x 10^{-9} mol L^{-1}. For all other titrations, the concentration of the host was kept constant at 1.02 x 10^{-6} mol L^{-1} and 0–200 eq of the quencher was added. All titrations were carried out at least in triplicate to obtain a standard deviation.

Synthesis of 4-3. Under an N_2 atmosphere, azide **4-1** (0.80 g, 1.6 mmol, 1.0 eq) and alkyne **4-2** (1.50 g, 6.6 mmol, 4.1 eq) were dissolved in DMF (20 mL) and degassed under a stream of nitrogen in an ultrasonic bath for 15 min. Sodium ascorbate (1.31 g, 6.6 mmol, 4.1 eq) and CuI (0.42 g, 1.6 mmol, 1.0 eq) were then added and the mixture was stirred at room temperature for 20 h. The solvent was removed, and the residue was dissolved in CH_2Cl_2 and water. The organic phase was washed with brine and the combined aqueous solutions extracted with CH_2Cl_2. The combined organic phases were dried over magnesium sulphate and concentrated under reduced pressure. The crude product was purified by column chromatography (eluent CyH / EtOAc, 1:1 → 0:1, v/v). After evaporation of the solvent, product **4-3** was obtained as a yellowish solid. **Yield**: 0.6 g (0.51 mmol, 32 %). M.p.: 180-220 °C. $\mathbf{R_f}$ (cyclohexane/EtOAc, 1:1): 0.05. **^{1}H NMR** (400 MHz, $CDCl_3$): δ = 8.94 (s, 3H, H-12), 8.73 (s, 6H, H-7), 8.16 (d, $^3J_{2,1}$ = 7.6 Hz, 6H, H-2), 8.13-8.03 (m, 12H, H-4+5), 7.99 (dd, $^3J_{1,2}$ = 7.6 Hz, 3H, H-1), 4.81 (br, 1H, H-24), 4.69

(s, 6H, H-13), 3.90-3.81 (m, 4H, H-18/19/20/21), 3.79-3.74 (m, 2H, H-18/19/20/21), 3.74-3.64 (m, 2H, H-18/19/20/21), 3.42-3.33 (m, 2H, H-16), 3.32-3.27 (m, 2H, H-17), 3.27 3.19 (m, 2H, H-22), 3.18-3.01 (m, 4H, H-15+23), 1.36 (s, 9H, H-27) ppm. **^{13}C NMR** (100 MHz, $CDCl_3$): δ = 156.0 (C_q, C-25), 148.2 (C_q, C-11), 131.8 (C_q, C-8), 131.2 (C_q, C-6), 128.1 (CH, C-4), 127.9 (C_q, C-3), 127.5 (CH, C-5), 126.2 (CH, C-1), 125.4 (CH, C-2), 124.7 (C_q, C 9/10), 124.6 (C_q, C 9/10), 124.2 (CH, C-12), 122.1 (CH, C 7), 79.3 (C_q, C 26), 77.4 (CH, C-16), 70.8 (CH_2, C 17-22), 70.7 (CH_2, C 17-22), 70.6 (CH_2, C 17-22), 70.5 (CH_2, C-17-22), 70.1 (CH_2, C 17-22), 70.0 (CH_2, C 17-22), 68.3 (CH_2, C-15), 49.7 (CH_2, C-13), 46.5 (C_q, C-14), 40.2 (CH_2, C-23), 28. 5 (CH_3, C-27) ppm. **FT-IR** (ATR): $\tilde{\nu}$ = 3127 (w), 3039 (w), 2966 (w), 2868 (m), 1704 (vs), 1608 (m), 1504 (s), 1437 (s), 1365 (s), 1275 (m), 1245 (vs), 1170 (vs), 1137 (vs), 1095 (vs), 1040 (vs), 1006 (w), 962 (vw), 879 (vs), 839 (vs), 819 (vs), 759 (m), 727 (s), 706 (vs), 660 (m), 608 (w) cm^{-1}. **HRMS** (ESI,+): found: 1164.5000 $[M]^+$; calc. for $[M]^+$: 1164.5010.

4.5 References

[1] H. B. Bradl, *Heavy metals in the environment: Origin, interaction and remediation*; Interface science and technology 6; Elsevier/Acad. Press, Amsterdam, **2005**.

[2] Y. Cao, M. A. Skaug, O. Andersen, J. Aaseth, *J. Trace Elem. Med. Biol.* **2015**, *31*, 188-192.

[3] J. O. Nriagu, *Science* **1996**, *272*, 223-224.

[4] K. K. Kesari, Ed., *Networking of mutagens in environmental toxicology*; Environmental science and engineering, environmental science; Springer, Cham 2019

[5] F. Pietrucci, M. Boero, W. Andreoni, *Chem Sci.* **2021**, DOI: 10.1039/d0sc06204a.

[6] (a) L. Ma, Q. Wang, S. M. Islam, Y. Liu, S. Ma, M. G. Kanatzidis, *J. Amer. Chem. Soc.* **2016**, *138*, 2858-2866; (b) P. B. Tchounwou, C: G. Yedjou, A. K. Patlolla, D. J. Sutton, in *Molecular, Clinical and Environmental Toxicology. Experientia Suppl. Vol. 101 (Ed.: A Luch)*, Springer, Basel **2012**, pp.133-164, https://doi.org/10.1007/978-3-7643-8340-4_6.

[7] M. Jaishankar, T. Tseten, N. Anbalagan, B. B. Mathew, K. N. Beeregowda, *Interdiscip. Toxicol.* **2014**, *7*, 60-72.

[8] A. Członkowska, T. Litwin, P. Dusek, P. Ferenci, S. Lutsenko, V. Medici, J. K. Rybakowski, K. H. Weiss, M. L. Schilsky, *Nat. Rev., Dis. Primers* **2018**, *4*, 21, DOI: 10.1038/s41572-018-0018-3.

[9] P. P. Leal, C. L. Hurd, S. G. Sander, E. Armstrong, P. A. Fernández, T. J. Suhrhoff, M. Y. Roleda, *Sci. Rep.* **2018**, *8*, 14763.

[10] J. C. Pimentel, F. Marques, *Thorax* **1959**, 678-688.

[11] T. G. Villar, *Amer. Rev. Respir. Dis.* **1974**, *110*, 545-555.

[12] H. Küpper in *Lead: Its Effects on Environment and Health, Metal Ions in Life Sciences Vol. 17* (Eds.: A. Sigel, H. Sigel, R.K.O. Sigel), Walter de Gruyter, Berlin, **2017**, pp. 491-500, DOI: 10.1515/9783110434330-015.

[13] M. Harada, *Teratol.* **1978**, 285-288.

[14] M. Sakamoto, T. Itai, K. Marumoto, M. Marumoto, H. Kodamatani, T. Tomiyasu, H. Nagasaka, K. Mori, A. J. Poulain, J. L. Domingo, M. Horvat, A. Matsuyama, *Environ. Res.* **2020**, *180*, 108668.

[15] N. Fernández, R. Beiras, *Ecotoxicol.* **2001**, *10*, 263-271.

[16] B. Volesky, Z. R. Holan, *Biotech. Prog.* **1995**, *11*, 235-250.

[17] P. Gottesfeld, *Public Health Front.* **2015**, *3*, 144.

[18] European Food Safety Authority, *Scientific Opinion on Lead in Food*. *EFSA J.* **2010**, *8*, 1570.

[19] V. Merz, J. Lenhart, Y. Vonhausen, M. E. Ortiz-Soto, J. Seibel, A. Krueger, *Small* **2019**, *15*, 1901551.

[20] (a) A. Gładysiak, T. N. Nguyen, R. Bounds, A. Zacharia, G. Itskos, J. A. Reimer, K. C. Stylianou, *Chem Sci.* **2019**, *10*, 6140-6148; (b) A. Ruiu, M. Vonlanthen, E. G. Morales-Espinoza, S. M. Rojas-Montoya, I. González-Méndez, E. Rivera, *J. Mol. Struct.* **2019**, *1196*, 1-7.

[21] (a) T. Delgado, M. Meneses-Sánchez, L. Piñeiro-López, C. Bartual-Murgui, M. C. Muñoz, J. A. Real, *Chem. Sci.* **2018**, *9*, 8446-8452.; (b) A. Saravanan, S. Shyamsivappan, T. Suresh, G. Subashini, K. Kadirvelu, N. Bhuvanesh, R. Nandhakumar, P. S. Mohan, *Talanta* **2019**, *198*, 249-256.

[22] C. S. de Castro, T. F. G. G. Cova, A. C. C. Pais, D. Pinheiro, C. Nuñez, C. Lodeiro, J. S. Seixas de Melo, *Dyes Pigm.* **2016**, *134*, 601-612.
[23] H.-F. Wang, S.-P. Wu, *Sens. Actuators, B,* **2013**, *181*, 743-748.
[24] C.-B. Bai, P. Xu, J. Zhang, R. Qiao, M.-Y. Chen, M.-Y. Mei, B. Wei, C. Wang, L. Zhang, S.-S. Chen, *ACS Omega* **2019**, *4*, 14621-14625.
[25] W. Cho, H. J. Lee, G. Choi, S. Choi, M. Oh, *J. Am. Chem. Soc.* **2014**, *136*, 12201-12204.
[26] J. K. Choi, S. H. Kim, J. Yoon, K.-H. Lee, R. A. Bartsch, J. S. Kim, *J. Org. Chem.* **2006**, *71*, 8011-8015.
[27] X. Sun, Y.-W. Wang, Y. Peng, *Org. Lett.* **2012**, *14*, 3420-3423.
[28] Y. Zhou, F. Wang, Y. Kim, S.-Y. Kim, J. Yoon, *Org. Lett.* **2009**, *11*, 4442-4445.
[29] J. J. Bryant, U. H. F. Bunz, *Chem. Asian J.* **2013**, *8*, 1354-1367.
[30] A. G. Crawford, A. D. Dwyer, Z. Liu, A. Steffen, A. Beeby, L.-O. Pålsson, D. J Tozer, T. B. Marder, *J. Am. Chem. Soc.* **2011**, *133*, 13349-13362.
[31] D. N. Coventry, A. S. Batsanov, A. E. Goeta, J. A. K. Howard, T. B. Marder, R. N. Perutz, *Chem. Commun.* **2005**, 2172-2174.
[32] B. Valeur, *Molecular Fluorescence*, 1st ed.; Wiley-VCH, Weinheim, **2001**.
[33] N.-b. Zhang, J.-j. Xu and C.-g. Xue, *J. Lumin.* **2011**, *131*, 2021-2025.
[34] I. K. Astakhova, E. Samokhina, B. R. Babu, J. Wengel, *ChemBioChem* **2012**, *13*, 1509-1519.
[35] M. Formica, V. Fusi, L. Giorgi, M. Micheloni, *Coord. Chem. Rev.* **2012**, *256*, 170-192.
[36] S. A. Ingale and F. Seela, *J. Org. Chem* **2012**, *77*, 9352-9356.
[37] (a) J. Rodríguez-Lavado; A. Lorente, E. Flores, A. Ochoa, F. Godoy, P. Jaque, C. Saitz, *RSC Adv.*, **2020**, 10, 21963-21973, (b) J. Cho, T. Pradhan, Y. M. Lee, J. S. Kim and S. A. Kim, *Dalton. Trans.* **2014**, *43*, 16178-16182.
[38] P. K. Chung, S.-R. Liu, H.-F. Wang, S.-P. Wu, *J. Fluoresc.* **2013**, *23*, 1139-1145.
[39] H. Maeda, M. Geshi, K. Hirose, T. Furuyama, M. Segi, *Tetrahedron* **2019**, *75*, 130512.
[40] Y. Zhou, C.-Y. Zhu, X.-S. Gao, X.-Y. You, C. Yao, *Org. Lett.* **2010**, *12*, 2566-2569.
[41] J. S: Kim, M. G. Choi, K. C. Song, K. T. No, S. Ahn, S.-K. Chang, *Org. Lett.* **2007**, *9*, 1129-1132.
[42] J. B. Birks, D. J. Dyson, I. H. Munro, *Proc. R. Soc. Lond. A* **1963**, *275*, 575-588.
[43] N. P. E. Barry, B. Therrien, in *Organic nanoreactors: From molecular to supramolecular organic compounds* (Ed.: S. Sadjadi) Academic Press (Elsevier), London, **2016**, pp. 421-461.
[44] A. G. Crawford, Z. Liu, I. A. I. Mkhalid, M.-H. Thibault, N. Schwarz, G. Alcaraz, A. Steffen, J. C. Collings, A. S. Batsanov, J. A. K. Howard, T. B. Marder, *Chem. Eur. J.* **2012**, *18*, 5022-5035.
[45] A. Shrivastava, V. Gupta, *Chron. Young Sci.* **2011**, *2*, 21.
[46] J. R. Lakowicz, *Principles of fluorescence spectroscopy*, 3rd ed.; Springer: New York, **2006**.
[47] D. Brynn Hibbert, P. Thordarson, *Chem. Commun.* **2016**, *52*, 12792-12805.
[48] P. Thordarson, *Chem. Soc. Rev.* **2011**, *40*, 1305-1323.
[49] E. J. Olson, P. Bühlmann, *J. Org. Chem.* **2011**, *76*, 8406-8412.
[50] D. T. Cramb, S. C. Beck, *J. Photochem. Photobiol. A* **2000**, *134*, 87-95.
[51] M. Zhao, X. Zhou, J. Tang, Z. Deng, X. Xu, Z. Chen, X. Li, L. Yang, L.-J. Ma, *Spectrochim. Acta A* **2017**, *173*, 235-240.
[52] E. Blatt, R. C. Chatelier, W. H. Sawyer, *Biophys. J.* **1986**, *50*, 349-356.
[53] S. E. Webber, *Photochem. Photobiol.* **1996**, *65*, 33-38.

[54] A. Bettoschi, A. Ceglie, F. Lopez, V. Meli, S. Murgia, M. Tamburro, C. Caltagirone, F. Cuomo, *J. Colloid Interface Sci.* **2016**, *477*, 8-15.
[55] T. Hayashita, S. Taniguchi, Y. Tanamura, T. Uchida, S. Nishizawa, N. Teramae, Y. S. Jin, J. C. Lee, R. A. Bartsch, *J. Chem. Soc., Perkin Trans. 2* **2000**, 1003-1006.

Chapter 5

Pyrene-functionalized Nanodiamond for Sensing of Cu(II), Pb(II) and Hg(II) in Aqueous Environments.

The following section is slightly modified and reproduced from the manuscript of V. Merz, J. Merz, T. B. Marder, A. Krueger.

5.1 Introduction

In recent years, the number of applications for nanodiamonds (NDs) has increased.[1,2] An important reason for this is, besides the chemical diversity, its non-toxic properties in *in vivo* experiments. Good colloidal stability in aqueous media as well as organic solvents make ND a promising candidate for sensor applications in, for example, wastewater or even physiological media.[3] The potential applications of defect structures in diamonds, in particular nanodiamonds, were recognized early on, giving single crystal diamonds several hundred different colors. These defect centers, such as NV centers, can be changed by chemical and physical influences and thus serve as sensors as well.[4] If defect centers in NDs are to be used, they are usually layered on electrodes to obtain information. When it comes to the detection of metal ions in solutions, classical sensor molecules, for instance by static and dynamic quenching, are important to obtain quantitative results.[1,5,6] Thus, both quenching types are relevant when it comes to the sensitivity of chemical sensors to heavy metal ions in wastewater.

This is particularly important when the use of heavy metals in industry, agriculture, households and technology leads to environmental pollution that can be found in wastewater and groundwater. Such pollution leads to enormous toxic influence on the health of plants, animals and humans due to the accumulation in food chains.[7,8,9] Metals such as copper, lead and mercury are among the most common contaminations found in waste water.[10] When these metals are ingested in a living being, their reduction and oxidation ability, in the form of metal complexes, enables them to block vital metal complexes or even replace important metal ions, bypassing control mechanisms of the organism and making it complex toxic.[8,9,11]

Here, we combine the advantage of in water colloidal stability of widely non-toxic ND-particles and classic chemical sensors to be able to detect metal ions in wastewater.[5] Due to the versatile surface of nanodiamonds, a broad range of reactions can be carried out and thus the properties of the NDs are significantly changed depending on the immobilized moieties. For instance, by functionalizing the surface, colloidally stable dispersions of NDs in a wide variety of media can be achieved.[12,13] Hence, the potentially large surface area of NDs are permanently accessible.

In our recently published work, we have shown that a modular system consisting of a tetraethylene glycol chain in combination with an azide head group for click reactions has a positive effect on the stabilization of the NDs in complex media.[12] The click reaction enables a variety of possible applications, such as the connection of dyes, which are equipped with heteroatoms with the help of the triazoles formed by the reaction. Triazoles are known to bind well to metal ions and, for example, dyes that are functionalized with triazoles by a click reaction can act as a chemosensor.[14] Here, we use pyrene that has been functionalized at its 2-position which has been realized via a very convenient one-step iridium-catalyzed C-H borylation. This offers, in contrast to pyrene derivatives that are functionalized at the 1-position, a significantly longer fluorescence lifetime.[15] The asset of this property is an enhanced sensitivity of the sensor as the quenching mechanism of most chemosensors is based on an interaction with an analyte in its excited state.[16] In this work, we present a new pyrene-functionalized nanodiamond chemosensor, shown in Scheme 5-1, for detection of Cu^{2+}, Pb^{2+} and Hg^{2+} ions.

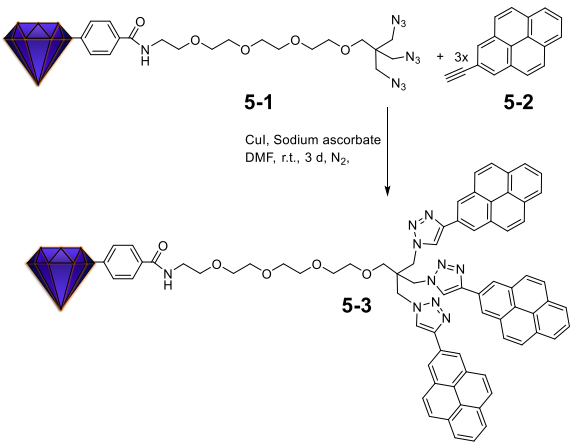

Scheme 5-1. Reaction of ND derivative **5-1** and 2-ethynyl pyrene **5-2** to the final chemosensor **5-3**.

During the click creation, a 1,2,3-triazole is generated via cyclization of the alkyne moieties in **2** and the azide groups in **1** using CuI as the catalyst, which was completely removed in chelated form after the reaction was completed. Thus, our sensor **3** has an expanded conjugated π-system and a distinguished metal ligand is inserted. The fact that the triazole-functionalized pyrene skeleton is kept close together by the head group of the chain leads to the following advantages: firstly, the three-triazole- moieties can intramolecularly form a complex with one

metal ion and secondly, not only intramolecularly, but also intermolecularly, excimer formation is prevented by the sterically hindered arrangement of the individual chromophores. This has been extensively tested on the molecular sensor beforehand and analyzed in our recently published work.[17]

The novel combination of the sensor on the ND allows to unite the advantage of the long lifetime of pyrene and the colloidal stabilizing effect of the ethylene glycol chain on the nanoparticle. Analogous to the previously published sensor, this sensor is also sensitive only to Cu^{2+}, Pb^{2+} and Hg^{2+} ions among all the tested metal ions, which is why only these three ions will be discussed further.[17]

5.2 Results and Discussion

The grafting on the nanodiamond's surface was carried out using a modified version of the recently published functionalization method.[12] The course of the reaction can be followed observing the aromatic bands (600–800 cm^{-1}) of the pyrene headgroups and the two bands of azide (2103 cm^{-1}) and alkyne (2100 and 3126 cm^{-1}) in the FT-IR spectrum (see Figure 5-1).

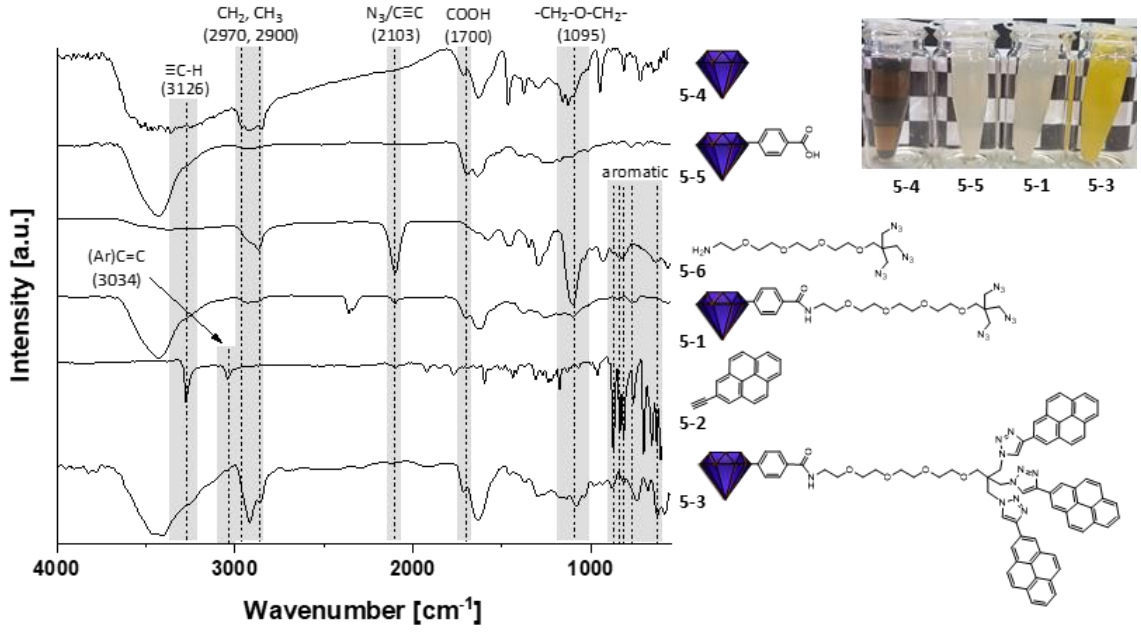

Figure 5-1. FT-IR (KBr) spectra of the reaction cascade of the milled ND **5-4** to an acid grafted ND **5-5,** which undergoes a reaction with azide-chain **5-6** to a precursor-ND **5-1** and in a final click-reaction with pyrene **5-4** to the chemosensor **5-3**, with respected images of the dispersion in water (~10 mg mL^{-1}): from left to right the dark dispersion **5-4**, the gray dispersion **5-5**, the second gray dispersion **5-1** and the yellow dispersion **5-3**.

After the click reaction of ND **5-1** with pyrene **5-2** the hydrodynamic diameter of the particles represented by the $D_v(50)$ value changed from 133 nm to 194 nm which indicates the growth of the particle's shell. The zeta potential remains largely unchanged (from 24 to 27 mV), which is expected for a reaction without changing the charge of the surface. Also, the color of the dispersion changed from bright greyish to yellowish due to the yellow pyrene derivative used for the reaction. However, dried samples remain dark grey after the reaction.

An important point for sensor preparation is that the sensor molecule is freely accessible to the analyte, *i.e.,* it must not be adsorbed on the ND surface, for example. As reported earlier, the organic moiety of **5-3** functions as a dynamically quenched sensor, thus the sensor needs to be freely accessible for collusion interactions with the metal ion.[17] However, the flexibility of the covalently attached linker moiety enables adsorption of pyrene head groups at the ND. To ensure the functionality of the sensor, this adsorption needs to be minimized.

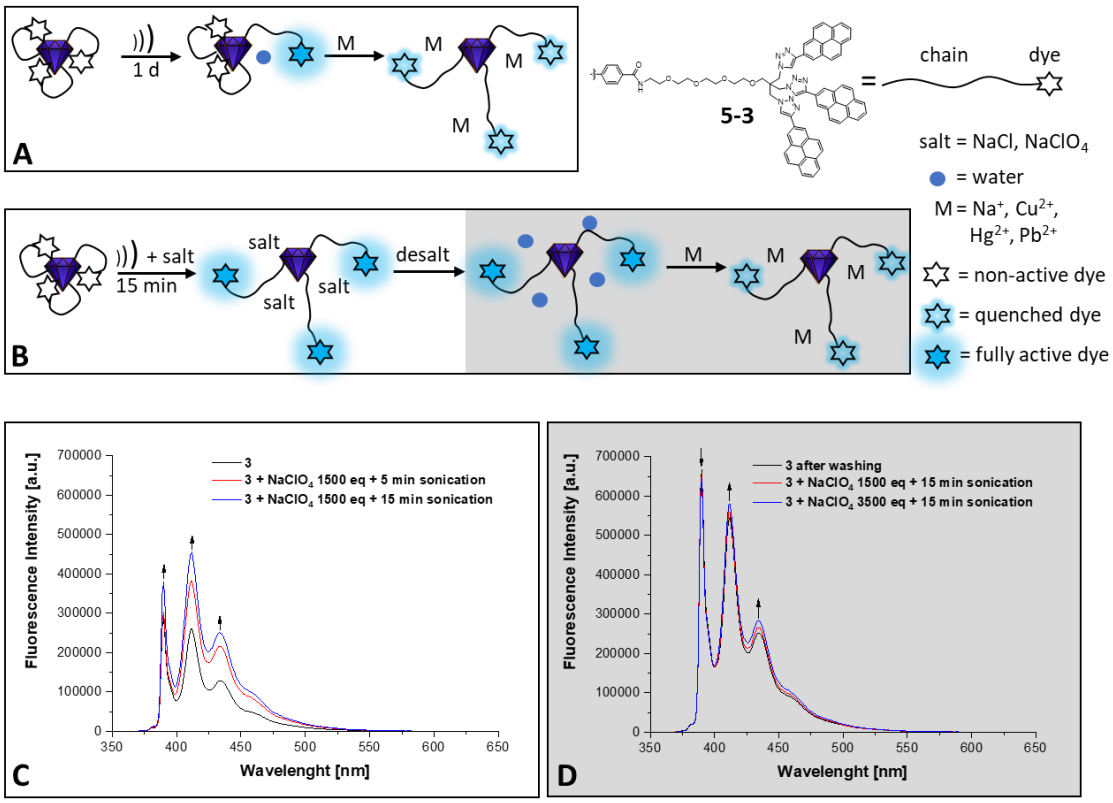

Figure 5-2. Schematic illustration of the A) preparation of ND in an ultrasonic bath, B) preparation of ND in an ultrasonic bath and addition of $NaClO_4$, C) fluorescence spectra of ND **5-3** (0.5 mg, sensor conc.: 1.4×10^{-5} M) in dry and degassed MeCN, D) fluorescence spectra of the finished procedure of B and addition of $NaClO_4$ in a high concentration.

In general, NDs can almost always be purified after a chemical reaction via washing processes with various solvents or acids/alkalis, complexing reagents or by dialysis. However, in our case this procedure was not sufficient as the fluorescence of our sensor **5-3** is not quenched in the presence of Cu^{2+}, Hg^{2+} and Pb^{2+}(see Figure 2). Thus, a competing process must take place that increases the intensity of the fluorescence. As it is known that ND can easily adsorb dyes on its surface, due to the versatile surface groups of NDs[18], we have come to the conclusion that the salts, which according to our previous studies quench the fluorescence of our sensor, have contributed to desorb more inactive dyes from the surface and thus a fluctuation in the intensity takes place between the quenched sensor and the freshly released sensor (see Figure 5-2. A). To complete the desorbtion of the chemosensor head groups prior to the actual sensor application, the ND was washed with a salt solution that does not quench with the sensor. As a result, the intensity signal after 5–15 min sonication already improves in 40–50% (see Figure 5-2. B (left part) and **C**). After the ND is washed with sodium perchlorate until no fluorescence intensity rise is visible anymore the dispersion is desalted by extensive washing and sodium perchlorate was again added in an extremely high concentration in order to observe the influence of high salt concentration (see Figure 5-2. B (right part) and D**)**. Two decisive advantages were found by observing the fluorescence spectra: On the one hand, the ND dispersions are colloidally stable for a few minutes, although the salt concentration was up to 9 mg mL^{-1} (3500 eq) at a maximum. On the other hand, as soon as the maximum intensity is reached by washing, the sodium perchlorate in extreme excess has almost no influence (± 3 %) on the spectrum, which can probably be explained by interactions in the highly concentrated salt medium between the particles, since ND tend to agglomerate slightly in saline solutions. In the following, the ND, which has been washed with sodium perchlorate and then desalted, is used as the starting material for all measurements. Titration with Cu, Hg and Pb, which was measured with high and without sodium perchlorate content in MeCN, shows that the sensing of Cu^{2+}, Hg^{2+} and Pb^{2+} is not affected by the presence of sodium ions. (see Figure 5-3).

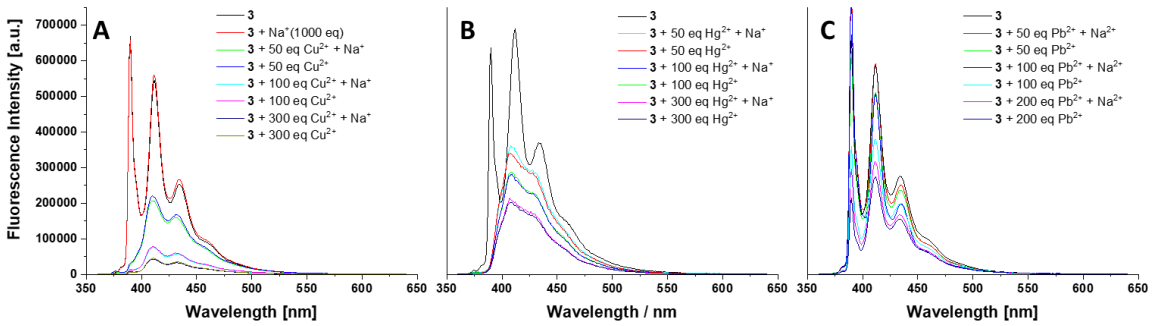

Figure 5-3. Titration of ND **5-3** (0.5 mg, sensor conc.: 1.4×10^{-5} M) in MeCN with Cu^{2+} (A), Hg^{2+} (B) and Pb^{2+} (C) in presence of sodium perchlorate and without.

The titration in acetonitrile is very similar to the titration of the organic chemosensor, which is almost completely quenched with Cu^{2+} at relatively low concentrations (100 eq, 1.4×10^{-4} M) already, while the quenching with the two other metal ions takes place much more slowly even if overall higher concentrations are detected here (> 300 eq). The chemosensor without ND has already reached its limit at 20–50 eq, while with the ND as carrier, the sensor is quenched more slowly. This is expected since the sensor interacts not only with itself and the surrounding metal ions, but also with the ND surface. If the sensor chains are attached to the nanodiamond surface, the interaction with the metal ion may be prevented (see Figure 5-2). By desorbing the sensor from the ND surface, it can be assumed that almost all sensor molecules can interact with the metal ions during the titration. Consequently, only desorbed sensor headgroups can interact with the analyte. If all sensor functions interact with the analyte Cu^{2+}, then the fluorescence intensity should be quenched to well above 90%, as with the organic sensor molecule. This is the case for the given system. To allow the availability of desorbing chemosensor head groups to interact with the analyte, the ND is washed with Na^{+}. However, these due not influence the quenching behavior. By titrating with and without the addition of Na+ ions, it was found that no significant influence on the quenching behavior of all three analytes was detected. The quantum yield of the sensor without ND is 94 % in MeCN.[17] Compared to this the quantum yield of chemosensor ND **5-3** decreases to 52 % in MeCN. It should be noted that the previously purely organic chemosensor was not water soluble, and by binding to the ND, it not only forms colloidally stable dispersions, but also can be used as a chemosensor with good quantum yield. Furthermore, working under an oxygen-free atmosphere in dry and freshly cleaned solvents is

usually important for chemosensors. Here we present a dispersion that not only enables the measurement in water, but even allows practicality in contaminated tap water under an oxygen (95 %) atmosphere.

In order to characterize the sensor properties under relevant application conditions, we subsequently contaminated water with the three analytes and determined their concentration with 0.5 mg of a dispersion of **5-3** without protective gas during the fluorescence titrations (see Figure 5-3). It was found that the sensor's quantum yield amounts to 3.5% under optimal aqueous conditions (double-distilled water, degassed and under an argon atmosphere). The measurement in tap water (27 dH) and saturation with 95% pure oxygen gives a quantum yield of 2.1%, which corresponds to 60% of the best possible value. The real value lies between the two quantum yields depending on the hardness of the water and the oxygen content in the air and in the water.

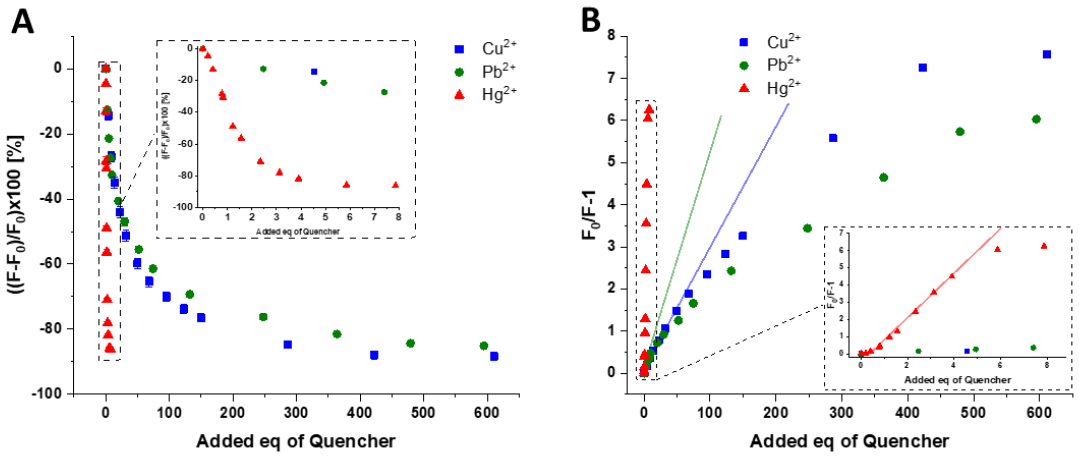

Figure 5-4. Titration experiments in tab water under air conditions A) Fluorescence titration curve and B) Stern Volmer (SV) Plot of ND **5-3** (0.5 mg, sensor conc.: $1.4x10^{-5}$ M) with each of the following three analyte ions in blue (Cu^{2+}) green (Pb^{2+}) and red (Hg^{2+}) and a zoomed part as an inset for the area of 0–8 eq.

All three ions quench the fluorescence of the sensor in water. The maximum quenching is reached for copper at -88%, for lead at -85% and for mercury at -85% of the initial fluorescence intensity. Although this corresponds to the trend of the sensor without ND, there is a clear difference in the quench constant. Mercury is a hundred times more effective than the other two metal ions when quenching in water. While for lead and copper the saturation of quenching

only occurs after the addition of 300-600 eq, with mercury after 6 eq there is no longer any effect due to the addition of further salt. Mercury exhibits the highest binding constant based on the fluorescence titration curves (Figure 5-3 A). A comparison of the binding constants K_a obtained using the bindfit algorithm for the organic sensor molecule and the sensor bound to ND is shown in Table 5-1.

Table 5-1. Comparison of the binding constant K_a of the organic sensor and the sensor attached on ND's surface using the software bindfit limit of detection (LOD), lower limit auf quantification (LLOQ) and upper limit of quantification (ULOQ) of the ND-sensor.

Analyte	**$K_{a(bindfit)}$ [M^{-1}]**	**$K_{a(bindfit)}$ [M^{-1}] (ND)**	**LOD [M]**	**LLOQ [M]**	**ULOQ [M]***
Cu^{2+}	$1.73x10^{+5}$	$3.09x10^{+3}$	$1.11x10^{-5}$	$3.35x10^{-5}$	$2.10x10^{-3}$
Pb^{2+}	$1.12x10^{+5}$	$3.64x10^{+3}$	$1.43x10^{-5}$	$4.29x10^{-5}$	$2.10x10^{-3}$
Hg^{2+}	$4.62x10^{+4}$	$6.39x10^{+4}$	$1.74x10^{-6}$	$5.23x10^{-6}$	$4.20x10^{-5}$
*estimated from the curve for Cu^{2+}/Pb^{2+}: 150 eq and Hg^{2+}: 4 eq					

While the binding constant for the titration of Hg^{2+} are almost identical for the free and the immobilized sensor, the binding constants for Cu^{2+} and Pb^{2+} are 55 and 30 times smaller for the ND-bound sensor, respectively. It is known that ND's surface moieties can also be coordinated through versatile mechanisms to ions. Such an attachment can strongly influence the balance of a dynamically quenched chemosensor. [20] The binding constant of the chemosensor with Hg^{2+} is approximately the same for both systems, on the nanoparticle and as a molecule without a carrier. This can mean that the analyte interacts only with the chemosensor without further interactions, e.g., with the ND surface.

The limit of detection (LOD) is determined by the 3.3 times of the error bar on the ordinate of the SV-plot.[21] The analyte which is detected with the highest sensitivity by ND **5-3** is Hg^{2+} which is detected 6-8 times more effectively than the Cu^{2+} and Pb^{2+}. The lower limit of quantification (LLOQ) can be found by multiplying the LOD by 3, but for a complex system without a linear course of the SV-plot (see Figure 5-3 B) this is not possible.

A realistic value for the ULOQ can be set for Cu^{2+}/Pb^{2+} as 150 eq and for Hg^{2+} at 4 eq. As a result, the values can be summarized so that Hg^{2+} is detected more sensitive (LOD / LLOQ) but Cu^{2+} and Pb^{2+} have an approximately 35 times wider detection range (LLOQ–ULOQ).

5.3 Conclusion

A new nanodiamond sensor system containing TEG chains linked to triazoles carrying pyrene moieties is reported. The TEG linker ensures the colloidal stability in salt solutions and thus renders the sensor applicability in relevant sensing environments. Moreover, new insight into the often-overlooked interactions of the nanoparticle surface with the solvent and the organic and inorganic compounds are given. The interaction between ND surface, solvent, ions and aromatic compounds, which is otherwise very difficult to classify, could be presented in a measurable way. It was uniquely demonstrated that washing with a wide variety of solvents does not sufficiently uncover the surface of NDs. Rather, it is important to also establish the accessibility of the functional groups, which only then, as in this work, can act as a sensor, or can also undergo further reactions. This is achieved by reversible saturation of the ND surface with Na ions, which provide for desorption of the sensor head group. Due to the generally good colloidal stability of NDs in water, it is possible to use a previously completely water-insoluble chemosensor for sensing in water, which, due to the modular architecture of the chemosensor, can also be transferred to a variety of different water-insoluble molecules. The functionalization of the sensor linker to NDs still bears the ability of detecting Cu^{2+}, Pb^{2+} and Hg^{2+} without being influenced by other metal ions with detecting ranges of $1.4x10^{-5}$–$1.4x10^{-3}$ M. This study clearly shows the versatility of our linker system and more chromophores can be linked to ND for further studies. Due to its non-toxic properties, the ND based sensor could also be used for applications such as bioimaging. This method can also be extended to fluorescent ND for imaging applications, which is especially interesting for systems where the sensor is completely quenched.

5.4 Experimental Part

General Methods: All solvents were freshly distilled and dried using standard procedures. For washing the samples, the sonication was carried out in a Bandelin Sonorex Digitec Typ DT52 (max. 80 W, 35 kHz) and for centrifugation a Thermo Scientific Sorvall MTX 150 was used at 52.000 RPM. The characterization with FTIR was carried using a Jasco FT/IR-430 using ≈1 mg ND in a 200 mg KBr pellet dried *in vacuo*. Attenuated total reflection (ATR) infrared spectra were recorded using the same spectrometer equipped with an ATR unit MIRacle from PIKE Technologies. IR spectra of ND samples were additionally measured for reaction control using diffuse reflectance infrared Fourier transform spectroscopy (DRIFTS) with a Nicolet iS5 spectrometer. The particle size and zeta potential were measured in doubly distilled water (DD water) at the intrinsic pH of the sample colloid using a Malvern Zetasizer Nanoseries Nano-ZS (dynamic light scattering, backscattering mode). The size distribution is given as volume distribution and was obtained using the Marquardt method. Degassing the samples was performed by sonication in a bath type Bandelin Sonorex Digitec Typ DT52 (max. 80 W, 35 kHz) while purging the dispersion with argon. Thermogravimetric analysis (TGA) was performed with a Perkin-Elmer STA 6000 with 60 mL min^{-1} N_2 flowrate and a heating rate of 10 K min^{-1} from 50 to 130 °C, a plateau time of 60 min at 120 °C, and a heating phase from 120 to 650 °C at 5 K min^{-1}. All photophysical measurements were carried out under an argon atmosphere unless stated otherwise and solution state measurements were performed in standard quartz cuvettes (1 cm x 1 cm cross section). The UV/Vis absorption spectra were measured using an Agilent 1100 diode array UV/Vis spectrophotometer. Excitation, emission, lifetime and quantum yield measurements were recorded using an Edinburgh Instruments FLSP920 spectrometer equipped with a 450 W Xenon arc lamp, double monochromators for the excitation and emission pathways, and a red-sensitive photomultiplier (PMT-R928P) and a near-IR PMT as detectors. The measurements were made in right-angle geometry mode and all spectra were fully corrected for the spectral response of the instrument.

Fluorescence quantum yields of the samples were measured using a calibrated integrating sphere (150 mm inner diameter) from Edinburgh Instruments combined with the FLSP920 spectrometer described above. For solution-state measurements, the longest wavelength absorption maximum of the compound in the respective solvent was chosen for the excitation.

In order to exclude self-absorption, the emission spectra were measured with dilute samples (ca. 0.1 OD at the excitation wavelength).

The titration experiments the concentration of the host (**5-3**) was kept constant at (0.5 mg), $1.4x10^{-5}$ M and 0–3500 eq of the analyte was added. All titrations were carried out at least five times to obtain a standard deviation.

*Synthesis of chemosensor **5-3***

The initial functionalization of pristine ND **5-4** was described in detail in our recently published work.[12]

The azide **5-1** (30 mg) dispersed in 1:1 DD-water/DMF and the alkyne **5-2** (30 mg, 0.13 mmol, 1.00 eq) were degassed under a stream of nitrogen in an ultrasonic bath for 15 min. Sodium ascorbate (105 mg, 0.53 mmol, 4.00 eq) and CuI (34 mg, 0.13 mmol, 1.00 eq) were then added and the mixture was stirred at room temperature for 72 h. During the day it was put in ultrasonic bath at intervals of 2–2.5 h for 8–10 h. After the reaction control by DRIFT spectroscopy showed no azide band at 2100 cm^{-1}, the mixture was washed with 20 mL of each solvent acetone (5x, 16k RPM), DMSO (5x, 52k RPM), ethylenediamine tetraacetic acid (EDTA) solution (0.1 M in ethanol, 3x, 16k RPM), dichloromethane (DCM, 5x, 12k RPM), acetone (3x 16k RPM), DD-water (3x, 16k RPM). For the removal of unreacted pyrene **5-2**, the ND was washed again in consecute dipserion-centrifugation steps with acetone (3x 16k RPM) acetonitrile (MeCN, 20x, 16k RPM), DCM (20x, 12k RPM), (3x 16k RPM) and DD-water (5x, 16k RPM). Before the titration experiments the chemosensor **5-3** was washed with water/MeCN (5x, 3000 eq of NaCl, 16k RPM) and DD-water/MeCN (5x, 16k RPM). yield 42 mg of **5-3** (yellowish dispersion in water, grayish powder). Zeta potential: 27 mV (DD-water, intrinsic pH = 6.3), particle size: (DLS, DD-water): 10% ≤ 120 nm, 50% ≤ 194 nm, 90% ≤ 305 nm, surface loading (TGA): 10 % (130–450 °C), FT-IR (KBr): $\tilde{\nu}$ = 3405 (w), 3034 (vw), 2915 (s), 2855 (m), 1711 (m), 1628 (s), 1454 (w), 1370 (w), 1298 (m), 1253 (m), 1178 (m), 1140 (m), 1180 (vs), 1095 (s), 1038 (m), 983 (w), 931 (w), 882 (m), 833 (vw), 811 (m), 764 (m), 745 (s), 779 (m), 628 (s), 583 (s) cm^{-1}.

5.5 References

[1] L. Basso, M. Cazzanelli, M. Orlandi, A. Miotello. Nanodiamonds: Synthesis and Application in Sensing, Catalysis, and the Possible Connection with Some Processes Occurring in Space. *Appl. Sci.* **2020**, *10*, 4094.

[2] a) S. Kumar, M. Nehra, D. Kedia, N. Dilbaghi, K. Tankeshwar, K.-H. Kim. Nanodiamonds: Emerging face of future nanotechnology. *Carbon* **2019**, *143*, 678–699; b) A. V. Shvidchenko, E. D. Eidelman, A. Y. Vul', N. M. Kuznetsov, D. Y. Stolyarova, S. I. Belousov, S. N. Chvalun. Colloids of detonation nanodiamond particles for advanced applications. *Adv. Colloid Interface Sci.* **2019**, *268*, 64–81.

[3] a) K. Turcheniuk, V. N. Mochalin. Biomedical applications of nanodiamond (Review). *Nanotechnology* **2017**, *28*, 252001; b) V. D. N. Bezzon, T. L. A. Montanheiro, B. R. C. de Menezes, R. G. Ribas, V. A. N. Righetti, K. F. Rodrigues, G. P. Thim. Carbon Nanostructure-based Sensors: A Brief Review on Recent Advances. *Advances in Materials Science and Engineering* **2019**, *2019*, 1–21; c) J. Zhang, F. Cheng, J. Li, J.-J. Zhu, Y. Lu. Fluorescent nanoprobes for sensing and imaging of metal ions: recent advances and future perspectives. *Nano today* **2016**, *11*, 309–329.

[4] a) T. Fujisaku, R. Tanabe, S. Onoda, R. Kubota, T. F. Segawa, F. T.-K. So, T. Ohshima, I. Hamachi, M. Shirakawa, R. Igarashi. pH Nanosensor Using Electronic Spins in Diamond. *ACS Nano* **2019**, *13*, 11726–11732; b) R. A. Almotiri, K. J. Ham, V. M. Vijayan, S. A. Catledge. Molecularly Imprinted Polyacrylamide with Fluorescent Nanodiamond for Creatinine Detection. *Materials* **2019**, *12*; c) R. Schirhagl, K. Chang, M. Loretz, C. L. Degen. Nitrogen-vacancy centers in diamond. *Annu. Rev. Phys. Chem.* **2014**, *65*, 83–105.

[5] L. Baù, P. Tecilla, F. Mancin. Sensing with fluorescent nanoparticles. *Nanoscale* **2011**, *3*, 121–133.

[6] E. Nurhayati, Y. Juang, M. Rajkumar, C. Huang, C.-C. Hu. Effects of dynamic polarization on boron-doped NCD properties and on its performance for electrochemical-analysis of Pb (II), Cu (II) and Hg (II) in aqueous solution via direct LSV. *Separation and Purification Technology* **2015**, *156*, 1047–1056.

[7] a) H. B. Bradl, *Heavy metals in the environment*. *Origin, interaction and remediation*, Elsevier/Acad. Press, Amsterdam, **2005**; b) Y. Cao, M. A. Skaug, O. Andersen, J. Aaseth. Chelation therapy in intoxications with mercury, lead and copper. *J. Trace Elem. Med. Biol.* **2015**, *31*, 188–192; c) J. O. Nriagu. A History of Global Metal Pollution. *Science* **1996**, *272*, 223-224; d) K. K. Kesari (Hrsg.) *Environmental science and engineering, environmental science*, Springer, Cham, Switzerland, **2019**; e) P. B. Tchounwou, C. G. Yedjou, A. K. Patlolla, D. J. Sutton. Heavy metal toxicity and the environment. *Experientia Suppl.* **2012**, *101*, 133–164.

[8] G. Azeh Engwa, P. Udoka Ferdinand, F. Nweke Nwalo, M. N. Unachukwu.

[9] M. Jaishankar, T. Tseten, N. Anbalagan, B. B. Mathew, K. N. Beeregowda. Toxicity, mechanism and health effects of some heavy metals. *Interdiscip. Toxicol.* **2014**, *7*, 60–72.

[10] R. Singh, N. Gautam, A. Mishra, R. Gupta. Heavy metals and living systems: An overview. *Indian J. Pharmacol.* **2011**, *43*, 246–253.

[11] a) N. Fernández, R. Beiras. Combined Toxicity of Dissolved Mercury With Copper, Lead and Cadmium on Embryogenesis and Early Larval Growth of the Paracentrotus Lividus Sea-Urchin. *Ecotoxicology* **2001**, *10*, 263–271; b) B. Volesky, Z. R. Holan. Biosorption of heavy metals. *Biotech. Prog.* **1995**, *11*, 235–250.

[12] V. Merz, J. Lenhart, Y. Vonhausen, M. E. Ortiz-Soto, J. Seibel, A. Krueger. Zwitterion-Functionalized Detonation Nanodiamond with Superior Protein Repulsion and Colloidal Stability in Physiological Media. *Small* **2019**, *15*, 1901551.

[13] a) G. Reina, L. Zhao, A. Bianco, N. Komatsu. Chemical Functionalization of Nanodiamonds: Opportunities and Challenges Ahead. *Angew. Chem. Int. Ed.* **2019**, *58*, 17918–17929; *Angew. Chem.* **2019**, *131*, 18084–18095; b) N. Bondon, L. Raehm, C. Charnay, R. Boukherroub, J.-O. Durand. Nanodiamonds for bioapplications, recent developments. *J. Mater. Chem. B* **2020**, *8*, 10878–10896.

[14] a) J. J. Bryant, U. H. F. Bunz. Click to bind: metal sensors. *Chem. Asian J.* **2013**, *8*, 1354–1367; b) B. Schulze, U. S. Schubert. Beyond click chemistry - supramolecular interactions of 1,2,3-triazoles. *Chem. Soc. Rev.* **2014**, *43*, 2522–2571; c) E. Haldón, M. C. Nicasio, P. J. Pérez. Copper-catalysed azide-alkyne cycloadditions (CuAAC): an update. *Org. Biomol. Chem.* **2015**, *13*, 9528–9550.

[15] a) A. G. Crawford, A. D. Dwyer, Z. Liu, A. Steffen, A. Beeby, L.-O. Pålsson, D. J. Tozer, T. B. Marder. Experimental and theoretical studies of the photophysical properties of 2- and 2,7-functionalized pyrene derivatives. *J. Am. Chem. Soc.* **2011**, *133*, 13349–13362; b) D. N. Coventry, A. S. Batsanov, A. E. Goeta, J. A. K. Howard, T. B. Marder, R. N. Perutz. Selective Ir-catalysed borylation of polycyclic aromatic hydrocarbons: structures of naphthalene-2,6-bis(boronate), pyrene-2,7-bis(boronate) and perylene-2,5,8,11-tetra(boronate) esters. *Chem. Commun.* **2005**, 2172–2174.

[16] B. Valeur, *Molecular Fluorescence,* 1. Aufl., Wiley, Weinheim, **2001**.

[17] V. Merz, J. Merz, M. Kirchner, J. Lenhart, T. B. Marder, A. Krueger. Pyrene-Based "Turn-Off" Probe with Broad Detection Range for Cu^{2+}, Pb^{2+} and Hg^{2+} Ions. *Chem. Eur. J.* **2021**, *27*, 8118–8126.

[18] J. B. Birks, D. J. Dyson, I. H. Munro. 'Excimer' fluorescence II. Lifetime studies of pyrene solutions. *Proc. R. Soc. Lond. A* **1963**, *275*, 575–588.

[19] a) H.-D. Wang, Q. Yang, C. Hui Niu, I. Badea. Adsorption of azo dye onto nanodiamond surface. *Diam. Relat. Mater.* **2012**, *26*, 1–6; b) H. Molavi, A. Shojaei, A. Pourghaderi. Rapid and tunable selective adsorption of dyes using thermally oxidized nanodiamond. *J. Colloid Interface Sci.* **2018**, *524*, 52–64.

[20] a) J. Gong, N. Steinsultz, M. Ouyang. Nanodiamond-based nanostructures for coupling nitrogen-vacancy centres to metal nanoparticles and semiconductor quantum dots. *Nat. Commun.* **2016**, *7*, 11820; b) E. B. Yudina, A. E. Aleksenskii, I. G. Fomina, A. V. Shvidchenko, D. P. Danilovich, I. L. Eremenko, A. Y. Vul. Interaction of Carboxyl Groups with Rare Metal Ions on the Surface of Detonation Nanodiamonds. *Eur. J. Inorg. Chem.* **2019**, *2019*, 4345–4349.

[21] A. Shrivastava, V. Gupta. Methods for the determination of limit of detection and limit of quantitation of the analytical methods. *Chron. Young. Sci.* **2011**, *2*, 21–25.

Chapter 6

Summary

&

Zusammenfassung

6.1 Summary

Nanodiamond (ND) is a versatile and promising material for bio-applications. Despite many efforts, agglomeration of nanodiamond and the non-specific adsorption of proteins on the ND surface when exposed to bio-fluids remains a major obstacle for biomedical applications. An assortment of branched and linear molecules with superior ability to colloidally stabilize nanoparticles in salt and cell media environment, for up to 30 days, was attached to the ND's surface.

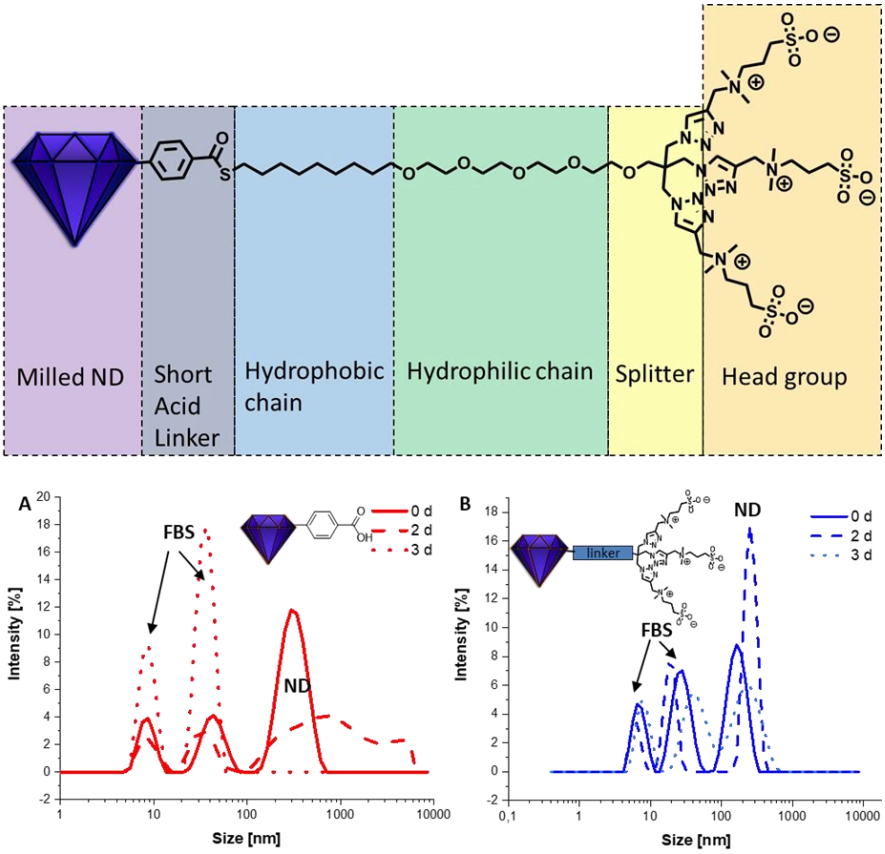

Figure 6-1: Schematic illustration of an exemplary molecule on nanodiamond (top) and its ability to colloidally stabilize the particle in FBS over three days, shown in dynamic light scattering experiments (bottom).

The building box system with azide as external groups offers a huge variety of binding with many molecules, such as drugs, dyes or targeting molecules, is possible. Clicking, for instance, zwitterions moieties to the chain protects ND surface from protein corona forming when the particles get in contact with biofluids containing proteins.

Thermogravimetric analysis results of the ND surface loading show a significant prevention of up to 98 % of the protein adsorption compared with NDs without zwitterionic headgroups and long colloidal stability when tetraethylene glycol (TEG) are attached to the surface.

The versatility of the modular system to bind not only zwitterionic chains but also clickable functional molecules to fluorescent nanodiamonds (fNDs) demonstrates the potential of the system at the nanodiamond. Using defect structures, such as nitrogen-vacancy (NV) centers, diamond particles, due to their widely non-toxic behavior, can be used as fNDs for photostable labeling, bioimaging and nanoscale sensing in living cells and organisms. To functionalize the fND surface a novel milling technique with diazonium salts was established to perform grafting on poorly reactive HPHT fNDs yielding in high surface loading and high negative zeta potential.

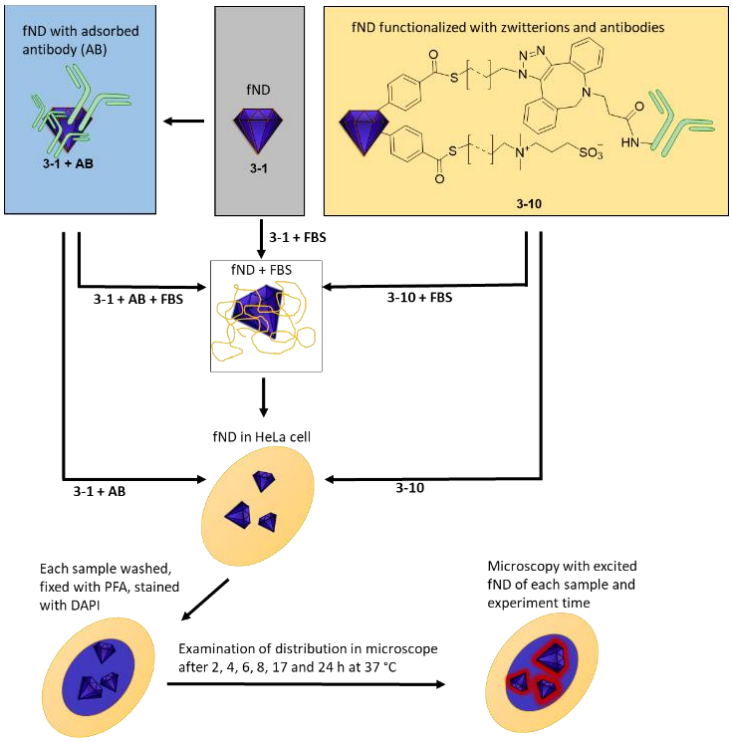

Figure 6-2: Schematic illustration of the experiment procedure of each of the five fND dispersion **3-1**, **3-1+AB**, **3-10**, **3-1+AB+FBS** and **3-10+FBS** respectively investigated regarding their targeting distribution with and without FBS in HeLa cells.

Combining the benefits of TEG and zwitterion containing groups with antibody enabled nucleus targeting ability on fND confirms the enhanced colloidal stability in living cells

experiments for the first time. Furthermore, the results indicate an improved corona repulsion compared with fND without zwitterion containing headgroups. As a result, the circulation times were enlarged from 4 (fND without zwitterion chain but with antibody) to 17 (with antibody and zwitterion chains) hours.

In non-biomedical applications, the modular system can be used as a probe for heavy metals by binding it to dyes. Detection of metals in different environments with high selectivity and specificity is one of the prerequisites of the fight against environmental pollution with these elements. Pyrenes are well suited and known for fluorescence sensing in different media.

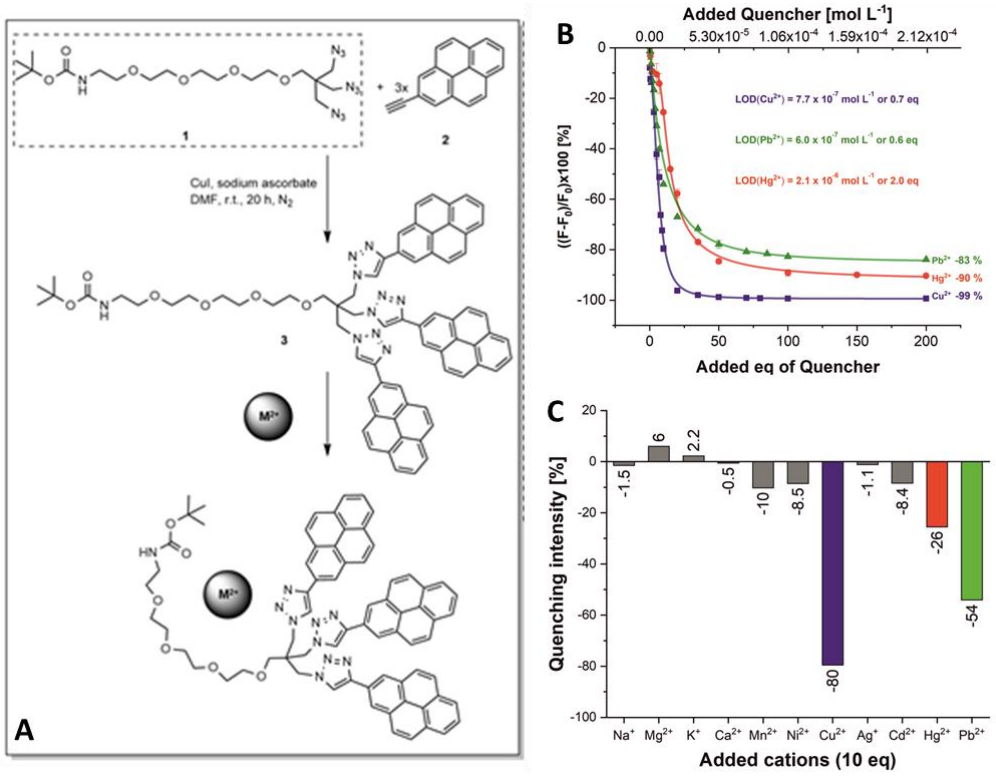

Figure 6-3. A) Synthesis of the glycol chain (dashed rectangle) and of probe **4-3** using click chemistry and its mode of action when complexing a divalent M^{2+} cation in acetonitrile, B) Fluorescence titration spectra of sensor **4-3** at 1.02 x 10^{-6} mol L^{-1} with the quencher ions Cu^{2+}(blue squares), Pb^{2+} (green triangles) and Hg^{2+} (red dots), error bars are given for all data points and C) fluorescence responses of **4-3** (concentration: 1.02 x 10^{-6} mol L^{-1}) to a selection of monovalent and divalent metal ions (used in the form of perchlorate salts) at 10 eq excess.

The applied sensing principle typically relies on the formation of intra- and intermolecular excimers, which is however limiting the sensitivity range due to masking of e.g. quenching

effects by the excimer emission. This study shows a highly selective, structurally rigid chemical sensor based on the monomer fluorescence of pyrene moieties bearing triazole groups.

This probe can quantitatively detect Cu^{2+}, Pb^{2+} and Hg^{2+} in organic solvents over a broad concentration range, even in the presence of ubiquitous ions such as Na^{+}, K^{+}, Ca^{2+} and Mg^{2+}. The strongly emissive sensor's fluorescence with a long lifetime of 165 ns is quenched by a 1:1 complex formation upon addition of metal ions in acetonitrile. Upon addition of a tenfold excess of the metal ion to the sensor, agglomerates with a diameter of about 3 nm are formed. Due to complex interactions in the system, conventional linear correlations are not observed for all concentrations. Therefore, a critical comparison between the conventional Job plot interpretation, the method of Benesi-Hildebrand, and a non-linear fit is presented. The reported system enables the specific and robust sensing of medically and environmentally relevant ions in the health-relevant nM range and could be used e.g. for the monitoring of the respective ions in waste streams.

Nonetheless, often these waste streams end up in sensitive aquacultures, where such sensor technology only works if the probe is water-soluble to monitor the spread and formation of environmental damage from heavy metals. Many chemosensors only work quantitatively in specific solvents and under highly pure conditions. In this thesis a method to stabilize water-insoluble chemosensors on nanodiamonds in saline water while maintaining the sensor efficacy and specificityas as well as colloidal stability is presented. Additionally, the sensor capability is retained in organic solvents. This study provides insight into the absorptivity of pyrene derivatives to the nanodiamond surface and a way to reversibly desorb them.

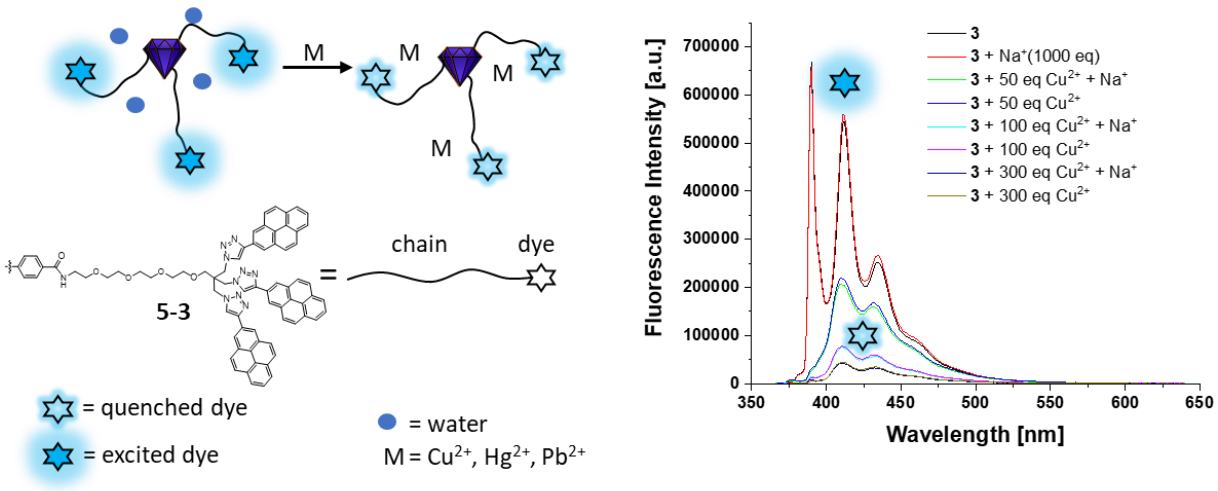

Figure 6-4. Schematic illustration of ND **5-3** interaction with metal ions (left) and fluorescence spectrum results of titration of ND **5-3** (0.5 mg, sensor conc.: 1.4×10^{-5} M) in MeCN with Cu^{2+} in presence of sodium perchlorate and without (right).

Moreover, the system proves that in presence of 95 % oxygen atmosphere while the fluoresce measurement the results of the do not vary from the one in argon atmosphere. Furthermore, the presence of common ions in water do not disturb the colloidal stability of the NDs and also no influence the sensor functionality and thus is highly promising candidate for measurement without cumbersome preparation steps.

6.2 Zusammenfassung

Nanodiamant (ND) ist ein vielseitiges und vielversprechendes Material für Bio-Anwendungen. Trotz vieler Bemühungen bleibt die Agglomeration von Nanodiamant und die unspezifische Adsorption von Proteinen an der ND-Oberfläche bei Kontakt mit Bioflüssigkeiten ein großes Hindernis für biomedizinische Anwendungen. Eine Auswahl verzweigter und linearer Moleküle mit überlegener Fähigkeit zur kolloidalen Stabilisierung von Nanopartikeln in Salz- und Zellmedienumgebung, für bis zu 30 Tage, wurde an die ND-Oberfläche angebracht.

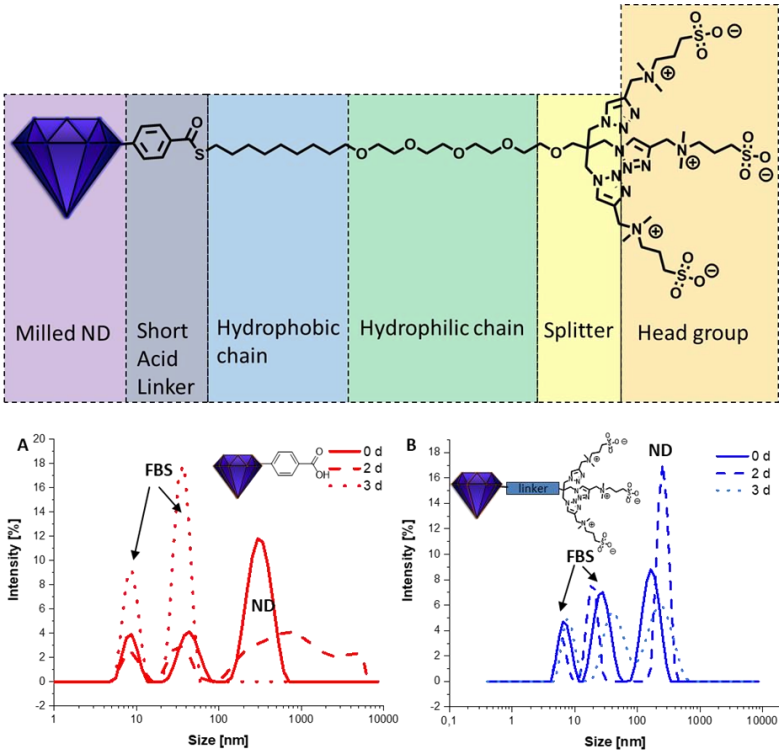

Abbildung 6-1: Schematische Darstellung eines exemplarischen Moleküls auf Nanodiamant (oben) und seine Fähigkeit, das Partikel in FBS über drei Tage kolloidal zu stabilisieren, dargestellt in dynamischen Lichtstreuungsexperimenten (unten).

Das Baukastensystem mit Azid als Außengruppen bietet eine große Vielfalt an Bindungen mit vielen Molekülen, wie z. B. Medikamenten, Farbstoffen oder Targeting-Molekülen. Das Anhängen von z. B. Zwitterionen an die Kette schützt die ND-Oberfläche vor der Bildung einer Proteinkorona, wenn die Partikel mit proteinhaltigen Bioflüssigkeiten in Kontakt kommen.

Die Ergebnisse der thermogravimetrischen Analyse der Beladung der ND-Oberfläche zeigen eine signifikante Verhinderung der Proteinadsorption von bis zu 98 % im Vergleich zu NDs

ohne zwitterionische Kopfgruppen und eine lange kolloidale Stabilität, wenn Tetraethylenglykol (TEG) an die Oberfläche gebunden wird.

Die Vielseitigkeit des modularen Systems, um nicht nur zwitterionische Ketten, sondern auch klickbare funktionelle Moleküle an fluoreszierende Nanodiamanten (fNDs) zu binden, zeigt das Potenzial des Systems am Nanodiamanten. Unter Verwendung von Defektstrukturen, wie Stickstoff-Vakanz-Zentren (NV), können Diamantpartikel aufgrund ihres weitgehend ungiftigen Verhaltens als fluoreszierende Nanodiamanten (fNDs) für photostabile Markierung, Bioimaging und nanoskalige Sensorik in lebenden Zellen und Organismen verwendet werden. Um die fND-Oberfläche zu funktionalisieren, wurde eine neuartige Mahltechnik mit Diazoniumsalzen etabliert, um ein Pfropfen auf wenig reaktive HPHT-fNDs durchzuführen, was zu einer hohen Oberflächenbeladung und einem hohen negativen Zetapotenzial führt.

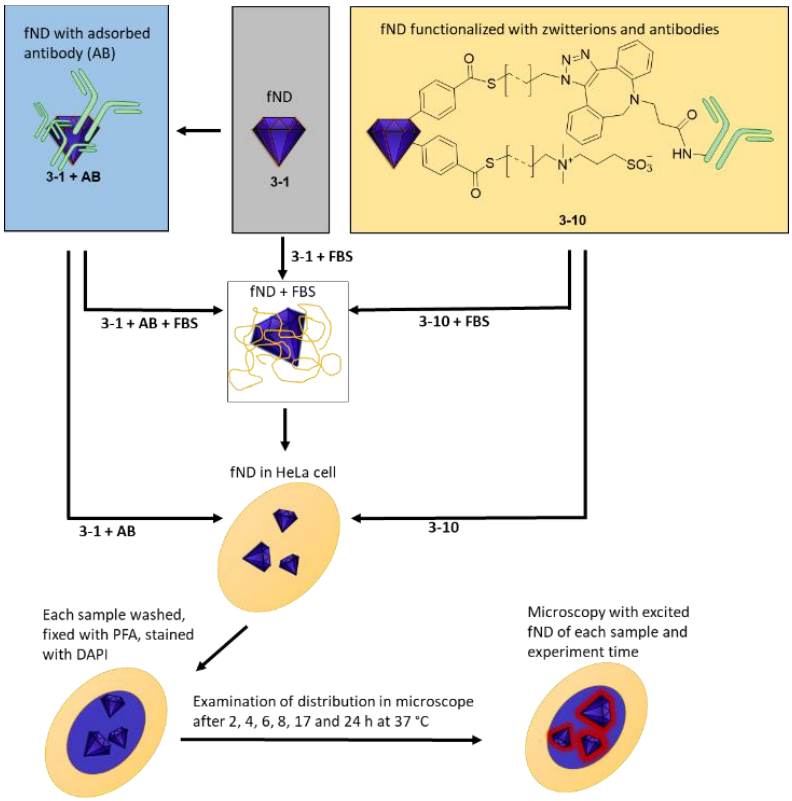

Abbildung 6-2: Schematische Darstellung des Versuchsablaufs jeder der fünf fND-Dispersionen **3-1**, **3-1+AB**, **3-10**, **3-1+AB+FBS** und **3-10+FBS**, die jeweils auf ihre Targeting-Verteilung mit und ohne FBS in HeLa-Zellen untersucht wurden.

Die Kombination der Vorteile von TEG und zwitterionhaltigen Gruppen mit der Fähigkeit zum Targeting von Antikörpern auf fND bestätigt zum ersten Mal die verbesserte kolloidale Stabilität in Experimenten mit lebenden Zellen. Darüber hinaus deuten die Ergebnisse auf eine verbesserte Corona-Abstoßung im Vergleich zu fND ohne zwitterionhaltige Kopfgruppen hin. Infolgedessen wurden die Zirkulationszeiten von 4 (fND ohne Zwitterionenkette, aber mit Antikörper) auf 17 (mit Antikörper und Zwitterionenketten) Stunden vergrößert.

In nicht-biomedizinischen Anwendungen kann das modulare System als Sonde für Schwermetalle durch die Anbindung von Farbstoffen verwendet werden. Die Detektion von Metallen in verschiedenen Umgebungen mit hoher Selektivität und Spezifität ist eine der Voraussetzungen für den Kampf gegen die Umweltverschmutzung mit diesen Elementen. Pyrene sind gut geeignet und weit bekannt für die Fluoreszenzsensorik in verschiedenen Medien. Das angewandte Sensorprinzip beruht typischerweise auf der Bildung von intra- und intermolekularen Excimeren, was jedoch den Empfindlichkeitsbereich aufgrund der Maskierung von z.B. Quenching-Effekten durch die Excimer-Emission einschränkt. Diese Studie zeigt einen hochselektiven, strukturstabilen chemischen Sensor, der auf der monomeren Fluoreszenz von Pyrenanteilen mit Triazolgruppen basiert.

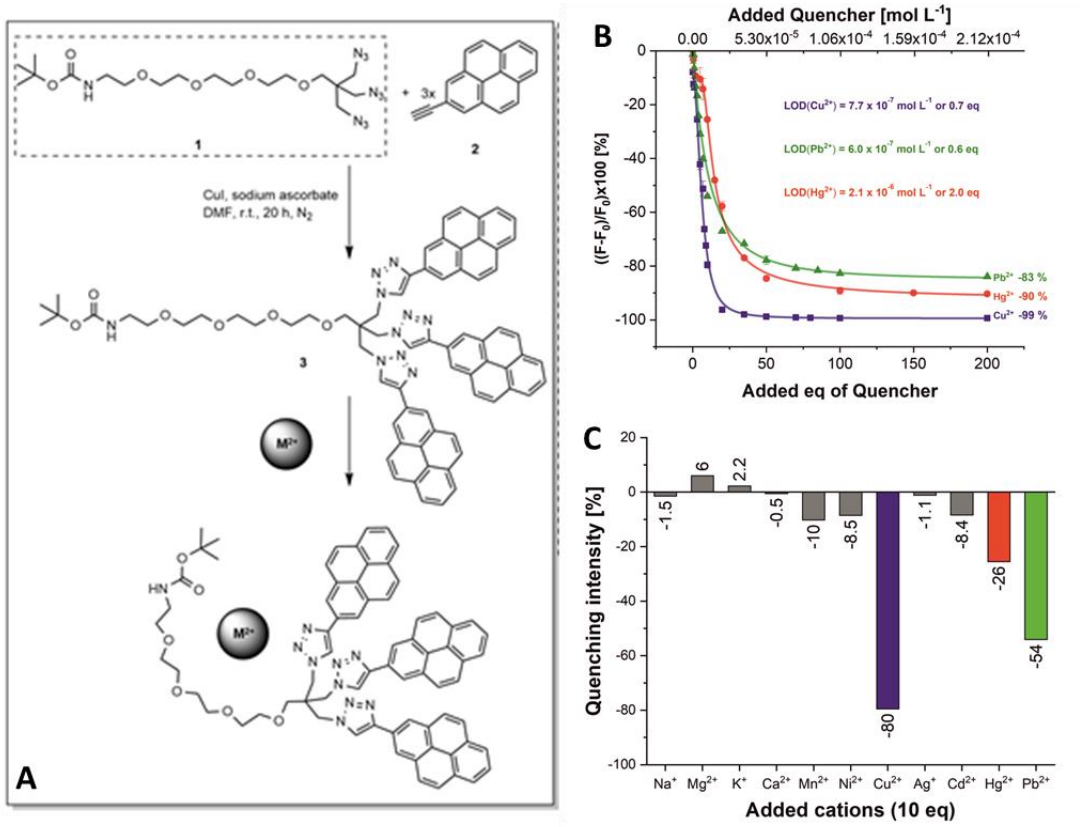

Abbildung 6-3. A) Synthese der Glykolkette (gestricheltes Rechteck) und der Sonde **4-3** mittels Click-Chemie und deren Wirkungsweise bei der Komplexierung eines zweiwertigen M^{2+}-Kations in Acetonitril, B) Fluoreszenztitrationsspektren der Sonde **4-3** bei 1.02 x 10^{-6} mol L^{-1} mit den Quencher-Ionen Cu^{2+} (blaue Quadrate), Pb^{2+} (grüne Dreiecke) und Hg^{2+} (rote Punkte), Fehlerbalken sind für alle Datenpunkte angegeben und C) Fluoreszenzspektren von **4-3** (Konzentration: 1.02 x 10^{-6} mol L^{-1}) auf eine Auswahl ein- und zweiwertiger Metallionen (verwendet in Form von Perchlorat-Salzen) bei 10 eq Überschuss.

Dieser Sensor kann Cu^{2+}, Pb^{2+} und Hg^{2+} in organischen Lösungsmitteln über einen weiten Konzentrationsbereich quantitativ nachweisen, auch in Gegenwart von ubiquitären Ionen wie Na^{+}, K^{+}, Ca^{2+} und Mg^{2+}. Die stark emittierende Fluoreszenz des Sensors mit einer langen Lebensdauer von 165 ns wird durch eine 1:1-Komplexbildung bei Zugabe von Metallionen in Acetonitril gelöscht. Bei Zugabe eines zehnfachen Überschusses des Metallions zum Sensor bilden sich Agglomerate mit einem Durchmesser von etwa 3 nm. Aufgrund der komplexen Wechselwirkungen im System werden konventionelle lineare Korrelationen nicht für alle Konzentrationen beobachtet. Daher wird ein kritischer Vergleich zwischen der konventionellen Job-Plot-Interpretation, der Methode von Benesi-Hildebrand und einem nicht-linearen Fit vorgestellt. Das vorgestellte System ermöglicht die spezifische und robuste Erfassung von

medizinisch und ökologisch relevanten Ionen im gesundheitsrelevanten nM-Bereich und könnte z. B. zur Überwachung der entsprechenden Ionen in Abfallströmen eingesetzt werden.

Doch häufig landen diese Abfallströme in empfindlichen Aquakulturen, wo eine solche Sensortechnik nur funktioniert, wenn die Sonde wasserlöslich ist, um die Ausbreitung und Bildung von Umweltschäden durch Schwermetalle zu überwachen. Viele Chemosensoren arbeiten nur in bestimmten Lösungsmitteln und unter hochreinen Bedingungen quantitativ. In dieser Arbeit wird eine Methode zur Stabilisierung von wasserunlöslichen Chemosensoren auf Nanodiamanten in salzhaltigem Wasser unter Beibehaltung der Sensoreffektivität und -spezifität sowie der kolloidalen Stabilität vorgestellt. Zusätzlich wird die Sensorfähigkeit in organischen Lösungsmitteln beibehalten. Diese Studie gibt Einblick in die Absorptionsfähigkeit von Pyren-Derivaten an der Nanodiamant-Oberfläche und einen Weg, diese reversibel zu desorbieren.

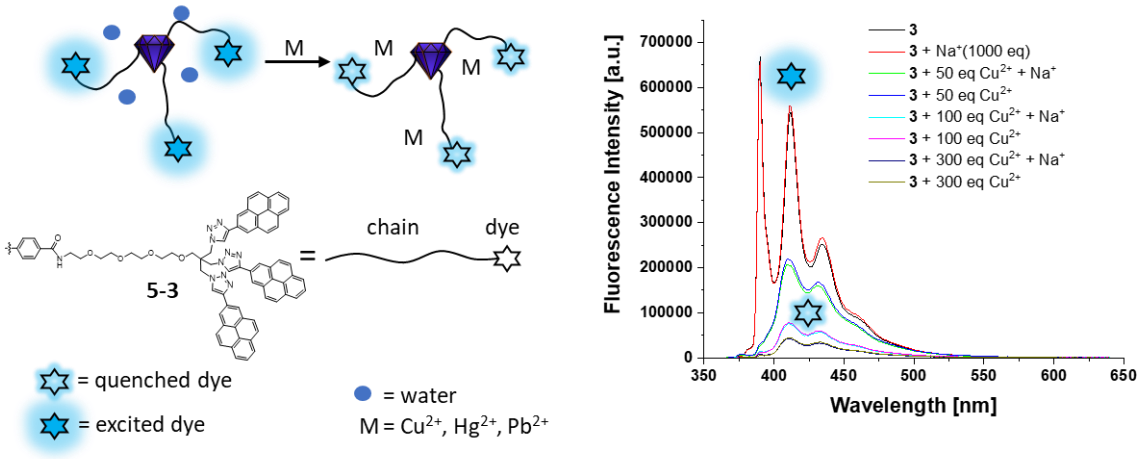

Abbildung 6-4. Schematische Darstellung der Wechselwirkung von ND **5-3** mit Metallionen (links) und Fluoreszenzspektren der Titration von ND **5-3** (0.5 mg, Sensorkonz.: 1.4×10^{-5} M) in MeCN mit Cu^{2+} in Gegenwart von Natriumperchlorat und ohne (rechts).

Außerdem beweist das System, dass in Anwesenheit von 95 % Sauerstoffatmosphäre bei der Fluoreszenzmessung die Ergebnisse nicht von denen in Argonatmosphäre abweichen. Darüber hinaus stört das Vorhandensein gängiger Ionen im Wasser die kolloidale Stabilität der NDs nicht und hat auch keinen Einfluss auf die Sensorfunktionalität und ist somit ein vielversprechender Kandidat für Messungen ohne aufwändige Präparationsschritte.

Chapter 7

Appendix

7.1 Chapter 2 - Supporting Information

The following section is slightly modified and reproduced from V. Merz, J. Lenhart, Y. Vonhausen, M. E. Ortiz-Soto, J Seibel, A. Krueger, Zwitterion-Functionalized Detonation Nanodiamond with Superior Protein Repulsion and Colloidal Stability in Physiological Media, *Small* **2019**, 15, 1901551, *with permission from Wiley-VCH.*

7.1.1 Synthesis of organic linker molecules

7.1.1.1 Synthesis of long linkers 2-26 and 2-28

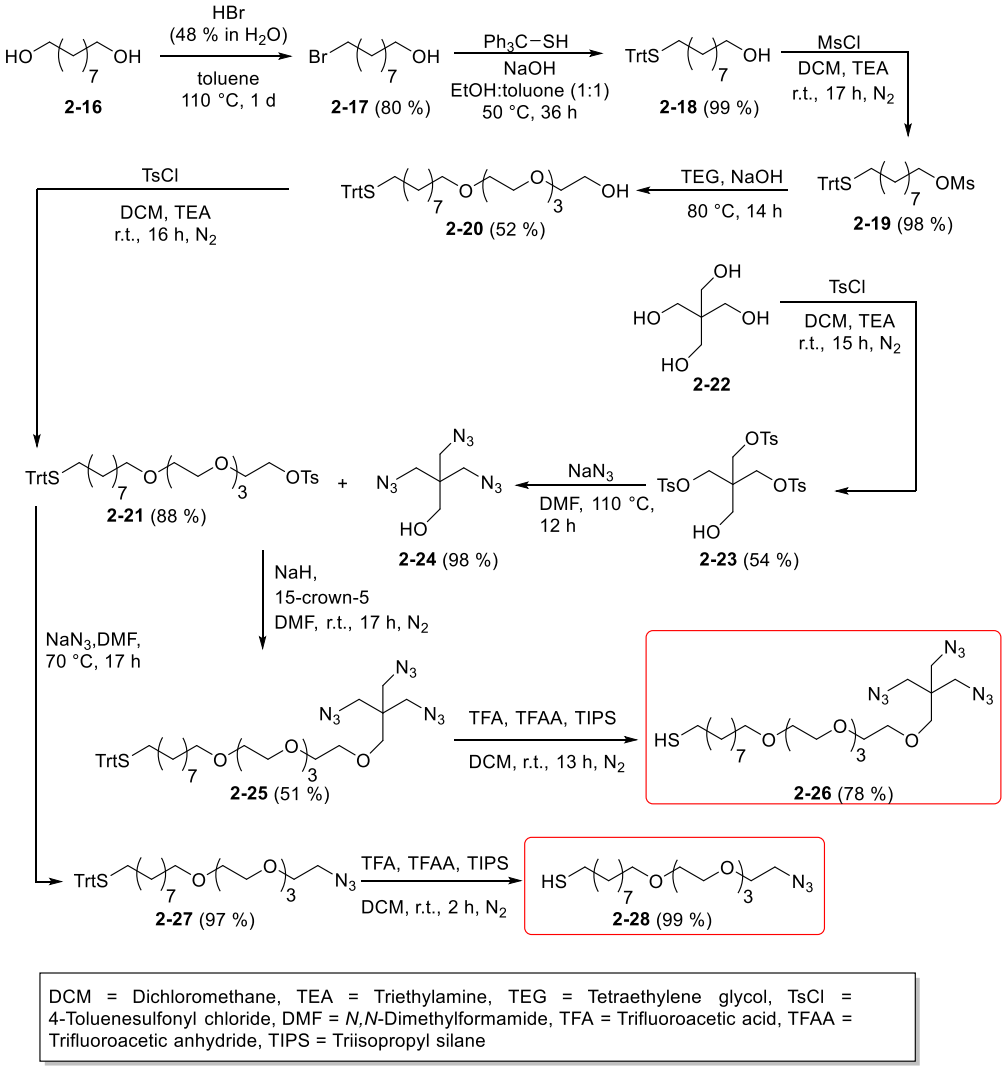

DCM = Dichloromethane, TEA = Triethylamine, TEG = Tetraethylene glycol, TsCl = 4-Toluenesulfonyl chloride, DMF = *N,N*-Dimethylformamide, TFA = Trifluoroacetic acid, TFAA = Trifluoroacetic anhydride, TIPS = Triisopropyl silane

Figure S2-1: Synthesis of long azide-ligands **2-26** and **2-28** for the preparation of ND **2-11** and ND **2-10**.

9-Bromononan-1-ol (2-17)[1]

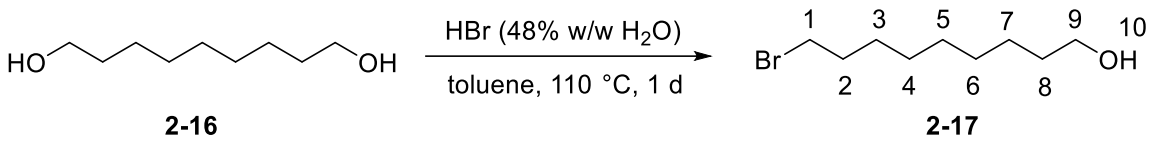

2-16 **2-17**

To a stirred solution of nonane-1,9-diol (**2-16**, 12.8 g, 80.3 mmol, 1.00 eq) in 200 mL toluene HBr (48 % w/w in H_2O, 18.2 mL, 160 mmol, 2.00 eq) was added. The reaction was stirred 1 d at 110 °C. Afterwards the solvent was removed under reduced pressure. The crude product was purified by column chromatography (silica, cyclohexane/EtOAc, 4:1, v/v) to obtain a colorless solid.

R_f (cyclohexane/EtOAc, 4/1): 0.23, **Yield**: 14.3 g (64 mmol, 80 %), **^{1}H-NMR** (400 MHz, $CDCl_3$): δ = 3.64 (t, $^3J_{9,8}$ = 6.6 Hz, 2H, H-9), 3.41 (t, $^3J_{1,2}$ = 6.8 Hz, 2H, H-1),1.88-1.81 (m, 2H, H-2), 1.63-1.26 (m, 12H, H-3 - H-8) ppm. **^{13}C-NMR** (100 MHz, $CDCl_3$): δ = 63.2 (CH_2, C-9), 34.2, 32.9, 32.9, 29.5, 29.4, 28.8, 28.3, 25.8 ((CH_2)$_8$, C-1 – C-8) ppm.

9-[(Triphenylmethyl)thio]-nonan-1-ol (2-18)[2]

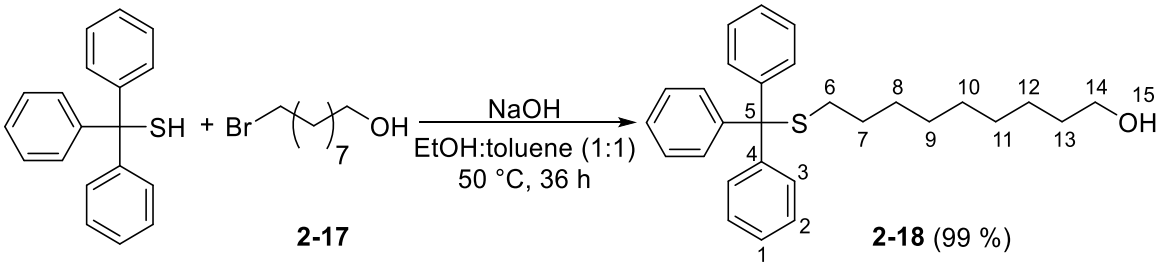

2-17 **2-18** (99 %)

9-bromo-1-nonanol (**2-17**, 6.70 g, 30.0 mmol, 1.00 eq) and triphenylmethanethiol (9.67 g, 35.0 mmol, 1.20 eq) were each dissolved in ethanol/toluene (70 mL, 1:1, v/v) and then both solutions were mixed. A concentrated solution of potassium hydroxide in deionized-water (1.90 g NaOH in 2.00 mL H_2O, 47.5 mmol, 1.60 eq) was added and the reaction mixture was stirred for 36 h at 50 °C. After the reaction was completed (TLC control), the reaction mixture was washed two times with saturated $NaHCO_3$ solution, and the organic layer was dried with Na_2SO_4 and concentrated in vacuo. The crude product was purified by column chromatography (silica, cyclohexane/EtOAc, 5:1, v/v). After removing the solvent, the product was obtained as a slightly yellow oil.

Yield: 12.42 g (29.7 mmol, 99 %). **R_f** (cyclohexane/EtOAc, 5:1): 0.13. **^{1}H-NMR** (400 MHz, $CDCl_3$): δ = 7.45-7.39 (m, 6H, H-3), 7.32-7.24 (m, 6H, H-2), 7.24-7.16 (m, 3H, H-1), 3.62 (t, $^3J_{13,14}$ = 6.6 Hz, 2H, H-14), 2.14 (t, $^3J_{6,7}$ = 7.4 Hz, 2H, H-6), 1.61-1.49 (m, 2H, H-13), 1.47-1.06 (m, 12H, H-7 - H-12) ppm. **^{13}C-NMR** (100 MHz, $CDCl_3$): δ = 145.1 (C_q, C-4), 129.9 (CH, C-3), 128.1 (CH, C-2), 126.8 (CH, C-1), 66.7 (C_q, C-5), 63.3 (CH_2, C-14), 33.1 (CH_2, C-13), 32.3 (CH_2, C-6), 29.7, 29.6, 29.4, 29.3, 28.9, 26.0 ((CH_2)$_6$, C-7 – C-12) ppm. **HRMS** (ESI,+): Found: 441.22129 [M]+; calc. for [M]+: 441.22226 **FT-IR (ATR):** $\tilde{\nu}$ = 3332 (br), 3054 (w), 3028 (w), 2924 (s), 2852 (m), 1595 (m), 1489 (m), 1443 (m), 1184 (w), 1076 (w), 1057 (m), 1034 (m), 885 (w), 850 (w), 742 (s), 696 (s), 619 (m) cm^{-1}. **UV/Vis** (acetonitrile): λ_{max} (log ε) = 256 (5.40) (c = $1.20 \cdot 10^{-4}$ mol L^{-1}).

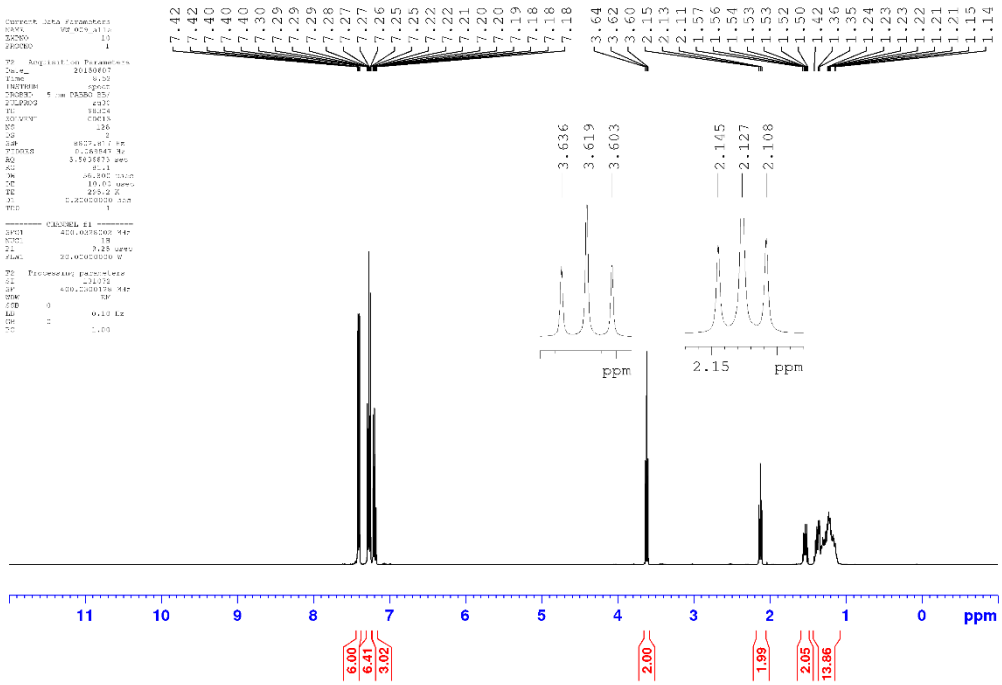

Figure S2-2: ^{1}H-NMR spectrum of 9-[(triphenylmethyl)thio]-nonan-1-ol (**2-18**).

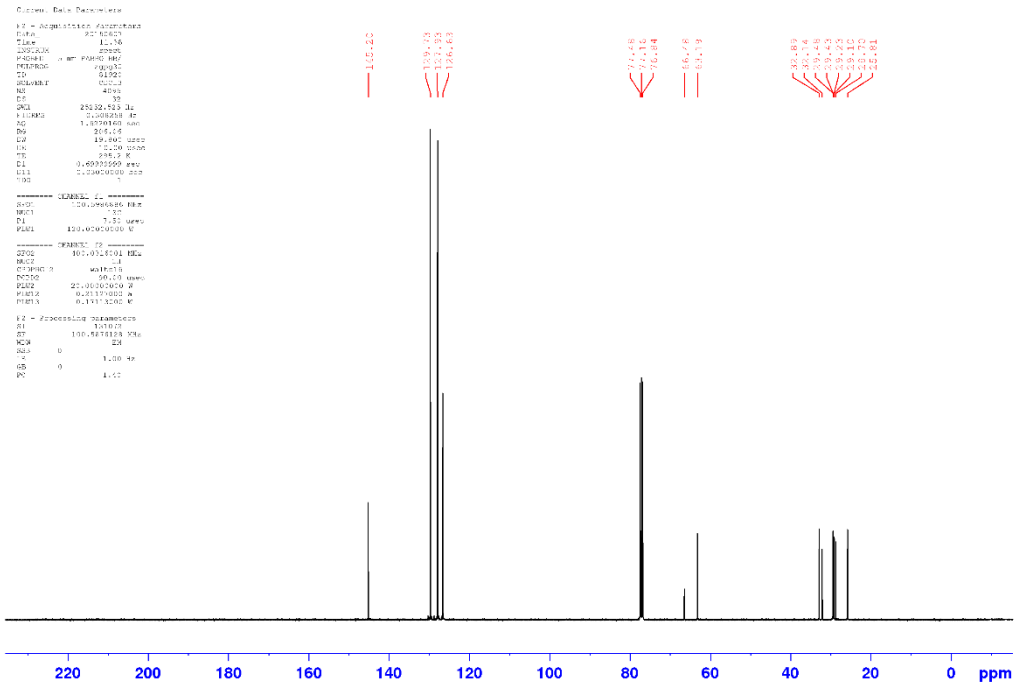

Figure S2-3: ^{13}C-NMR spectrum of 9-[(triphenylmethyl)thio]-nonan-1-ol (**2-18**).

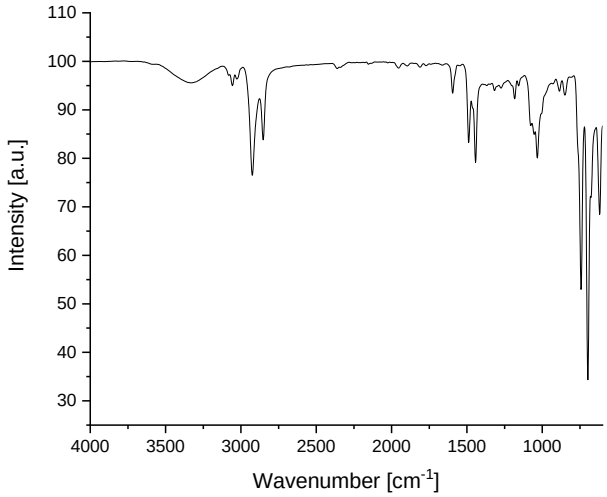

Figure S2-4: FT-IR ATR spectrum of 9-[(triphenylmethyl)thio]-nonan-1-ol (**2-18**).

9-[(Triphenylmethyl)thio]-nonyl methanesulfonate (2-19)[2]

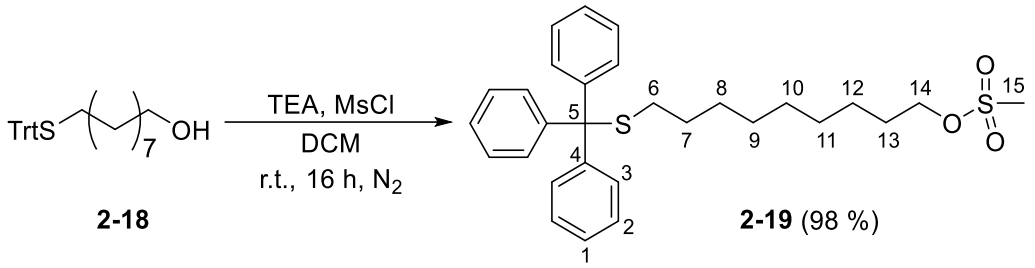

2-19 (98 %)

The nonanol **2-18** (12.0 g, 28.6 mmol, 1.00 eq) was dissolved in dry DCM (150 mL) and TEA (4.39 g, 6 mL, 43.4 mmol, 1,50 eq) was added. After cooling the mixture in an ice bath, methanesulfonyl choride (3.70 g, 2.50 mL, 32.3 mmol, 1.10 eq) was added dropwise. After 60 min at 0 °C the reaction mixture was warmed to room temperature and stirred overnight (16 h). Upon completion, the reaction mixture was concentrated in vacuo. The crude product mixture was dissolved in DCM (100 mL) and washed two times with 0.1 M HCl (100 mL), neutralized with saturated $NaHCO_3$-solution and washed twice with deionized. The organic layer was dried with Na_2SO_4 and concentrated with vacuo. The crude product was purified by column chromatography (silica, cyclohexane/EtOAc, 4:1, v/v). After removing the solvent, the product was obtained as a slightly yellow oil.

Yield: 13.94 g (28.05 mmol, 98 %). $\mathbf{R_f}$ (cyclohexane/EtOAc, 4:1): 0.37. **^{1}H-NMR** (400 MHz, $CDCl_3$): δ = 7.44-7.38 (m, 6H, H-3), 7.33-7.24 (m, 6H, H-2), 7.24-7.16 (m, 3H, H-1), 4.21 (t, $^3J_{14,13}$ = 6.7 Hz, 2H, H-14), 2.99 (s, 3H, H-15) 2.13 (t, $^3J_{6,7}$ = 7.3 Hz, 2H, H-6), 1.78-1.68 (m, 2H, H-13), 1.47-1.06 (m, 12H, H-7 - H-12) ppm. **^{13}C-NMR** (100 MHz, $CDCl_3$): δ = 145.2 (C_q, C-4), 129.7 (CH, C-2), 127.9 (CH, C-3), 126.6 (CH, C-1), 70.3 (CH_2, C-14) 66.5 (C_q, C-5), 37.5 (CH_3, C-15), 32.1 (CH_2, C-6), 29.3, 29.2, 29.2, 29.0, 28.7, 27.1, 25.5 ((CH_2)$_7$, C-7-13) ppm. **HRMS** (ESI,+): found: 519.19847 [M]+; calc. for [M]+: 519.19981. **FT-IR (ATR):** $\tilde{\nu}$ = 3056 (w), 3029 (w), 2925 (s), 2854 (m), 1595 (m), 1489 (m), 1442 (m), 1353 (vs), 1173 (vs), 1080 (w), 1034 (w), 970 (m), 943 (br), 822 (w), 742 (m), 698 (m), 619 (w) cm^{-1}. **UV/Vis** (acetonitrile): λ_{max}(log ε) = 256 (5.27) (c = $1.20 \cdot 10^{-4}$ mol L^{-1}) nm.

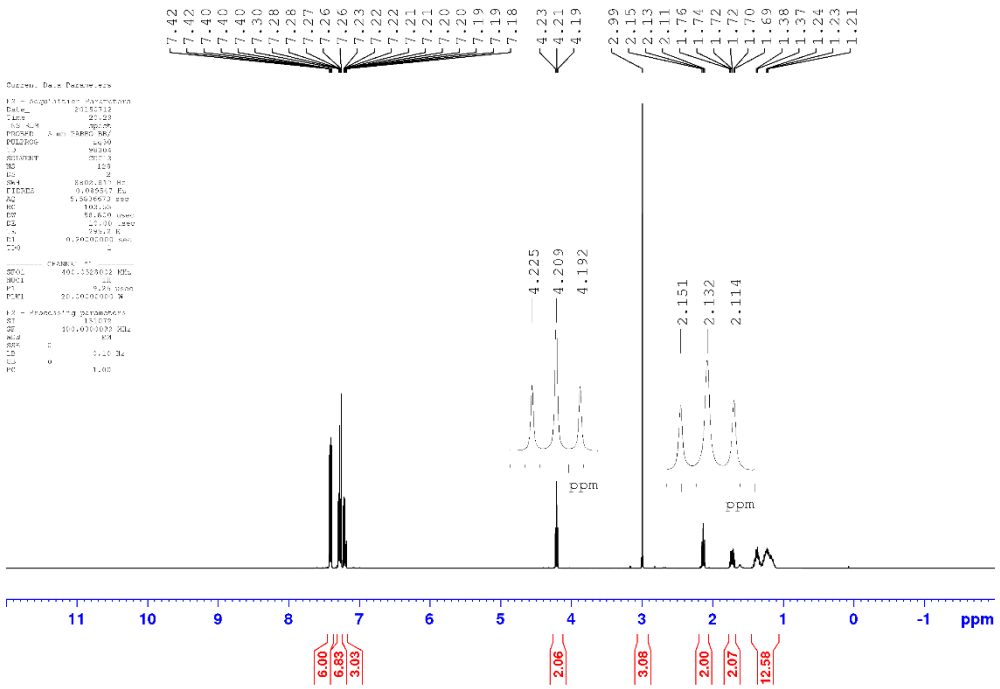

Figure S2-5: ^{1}H-NMR spectrum of 9-[(triphenylmethyl)thio]-nonyl methanesulfonate (**2-19**).

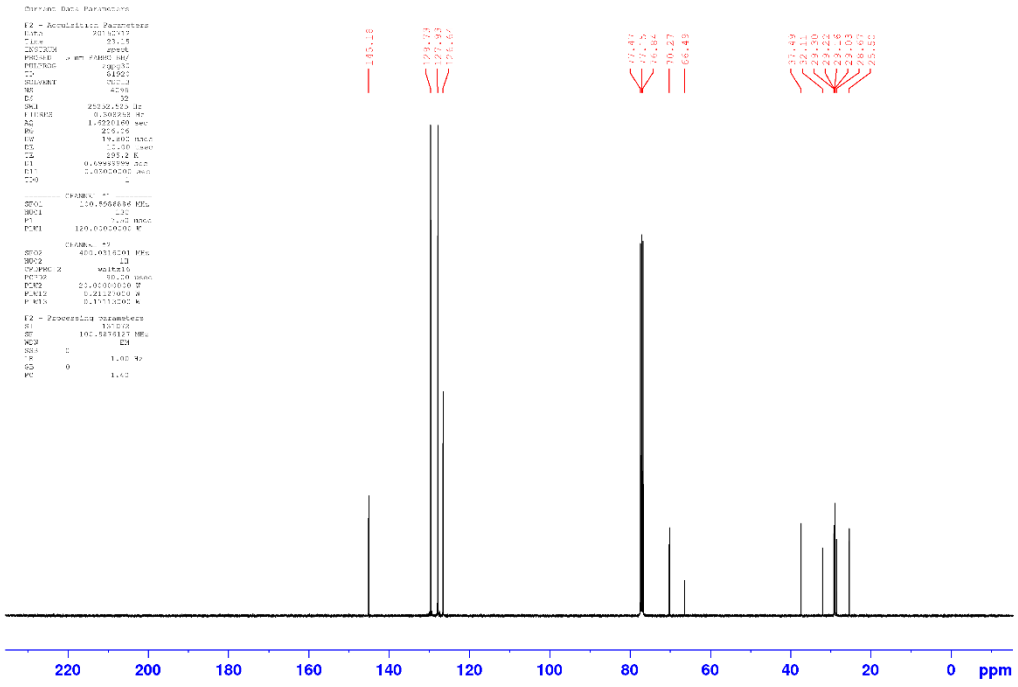

Figure S2-6: ^{13}C-NMR spectrum of 9-[(triphenylmethyl)thio]-nonyl methanesulfonate (**2-19**).

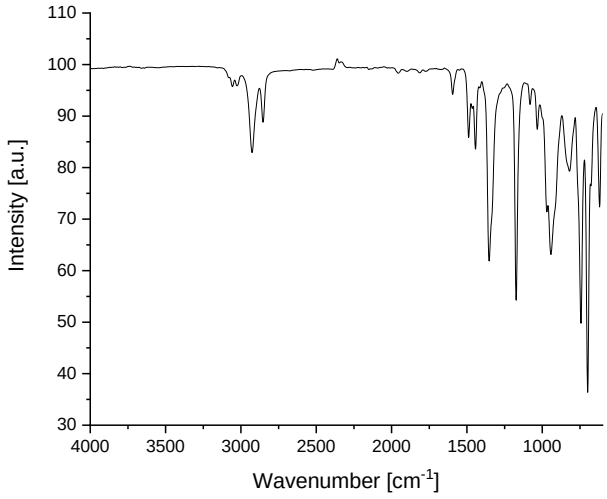

Figure S2-7: FT-IR ATR spectrum of 9-[(triphenylmethyl)thio]-nonyl methanesulfonate (**2-19**)

1,1,1-Triphenyl-12,15,18,21-tetraoxa-2-nonyl-23-ol (2-20)[2]

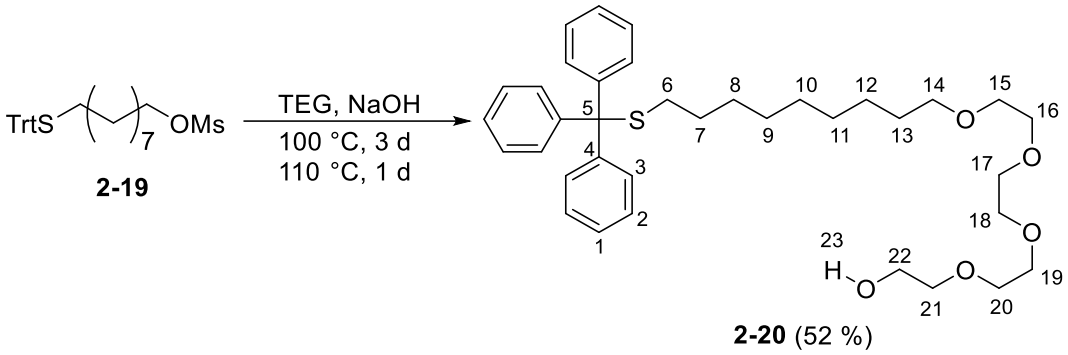

2-20 (52 %)

NaOH (1.31 g, 32.9 mmol) was dissolved in deionized water (2 mL) and mixed with tetraethylene glycol (TEG) (100 mL, 0.57 mol). The reaction mixture was stirred at 85 °C for 1.5 h. The mixture was subsequently added to 9-(tritylthio)nonyl methanesulfonate (**2-19**, 13.6 g, 27.4 mmol) and stirred for three days at 100 °C and one day at 110 °C. After four days the mixture was cooled down to room temperature and extracted ten times with EtOAc/cyclohexane (100 mL, 1:4, v/v). The organic layer was concentrated in vacuo and the crude product was purified by column chromatography (silica, cyclohexane/EtOAc, 4:1 -> 0:1 v/v). After removing the solvent, the product was obtained as a slightly yellow oil.

Yield: 8.67 g (14.6 mmol, 52 %). **R_f** (EtOAc): 0.30. **^{1}H-NMR** (400 MHz, $CDCl_3$): δ = 7.44-7.38 (m, 6H, H-3), 7.34-7.24 (m, 6H, H-2), 7.24-7.17 (m, 3H, H-1), 3.75 (m, 16H, H-15 – H-22) 3.44 (t, $^3J_{14,13}$ = 6.8 Hz, 2H, H-14), 2.47 (br, 1H,H-23), 2.12 (t, $^3J_{6,7}$ = 7.3 Hz, 4H, H-6), 1.64-1.47 (m, 2H, H-13), 1.47-1.33 (m, 2H, H-7) 1.33-1.04 (m, 10H, H-8 – H-12) ppm. **^{13}C-NMR** (100 MHz, $CDCl_3$): δ = 145.2 (C_q, C-4), 129.7 (CH, C-2), 127.9 (CH, C-3), 126.6 (CH, C-1), 72.7, 71.8, 7.8, 70.7, 70.7, 70.5, 70.2 ($(CH_2)_8$, C-14-21), 66.5 (C_q, C-5), 61.9 (CH_2, C-22), 32.1 (CH_2, C-6), 29.7, 29.5, 29.5, 29.3, 29.1, 28.7, 26.2 ($(CH_2)_7$, C-7-13) ppm. **HRMS** (ESI,+): found: 617.32679 [M]+; calc. for [M]+: 617.32712. **FT-IR (ATR):** $\tilde{\nu}$ = 3460 (br), 3056 (vw), 3024 (vw), 2924 (s), 2858 (s), 1738 (s), 1597 (w), 1489 (w), 1444 (m), 1238 (s), 1105 (s), 1055 (s), 943 (w), 885 (w), 847 (w), 744 (s), 700 (s), 619 (m) cm^{-1}. **UV/Vis** (acetonitrile): λ_{max}(log ε) = 256 (5.29), 262 (5.30) (c = $2.02 \cdot 10^{-5}$ mol L^{-1}) nm.

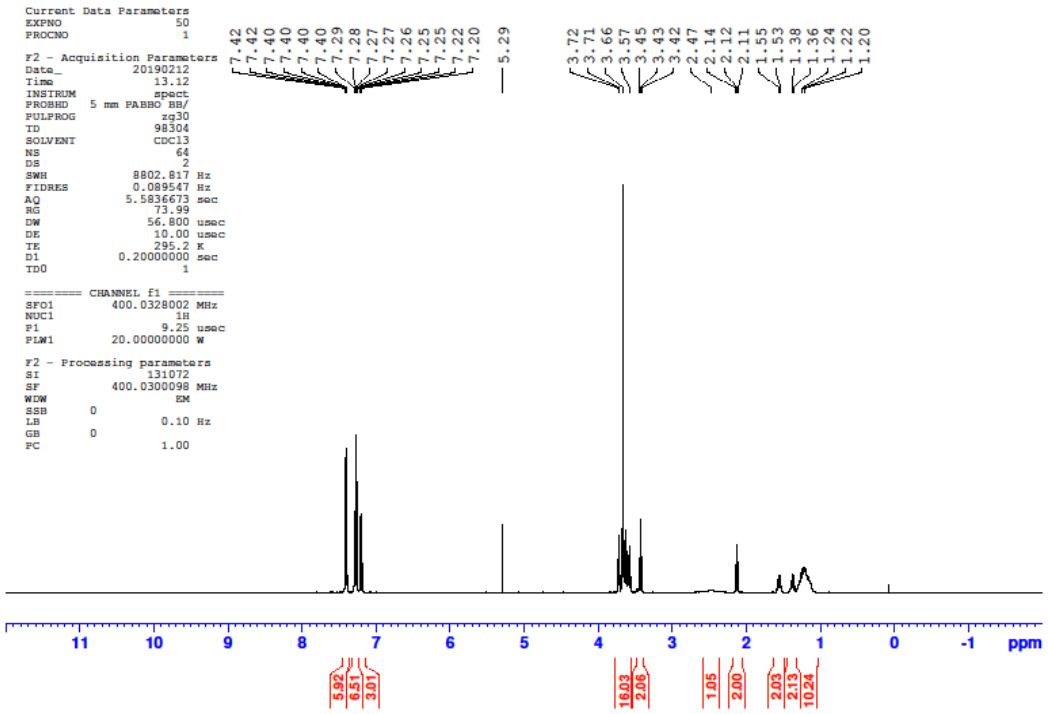

Figure S2-8: ^{1}H-NMR spectrum of 1,1,1-triphenyl-12,15,18,21-tetraoxa-2-nonyl-23-ol (**2-20**)

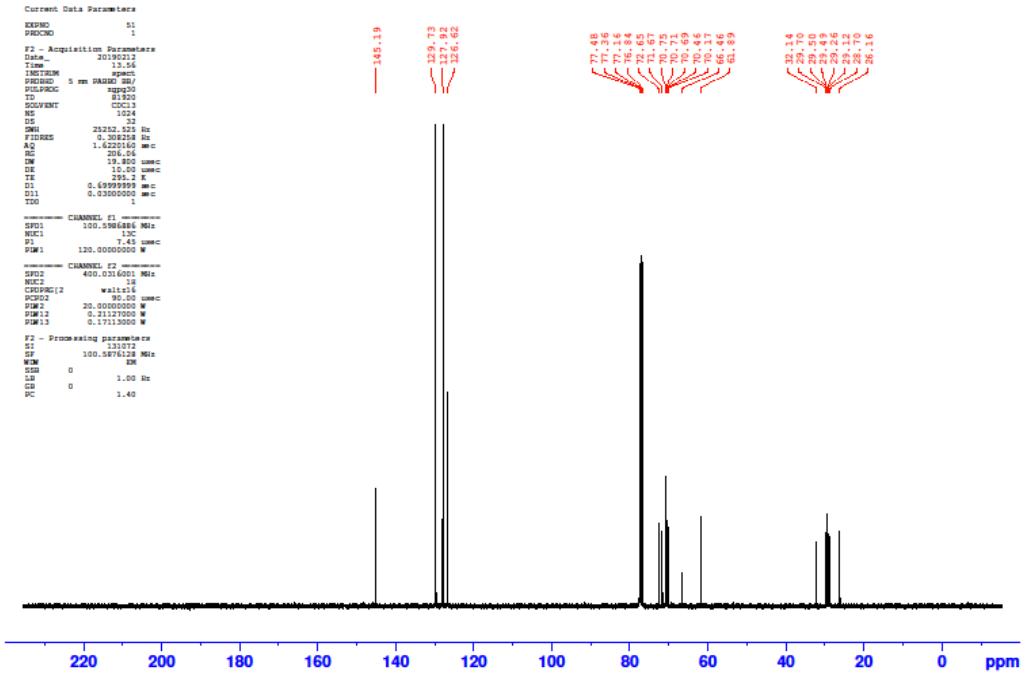

Figure S2-9: ^{13}C-NMR spectrum of 1,1,1-triphenyl-12,15,18,21-tetraoxa-2-nonyl-23-ol (**2-20**)

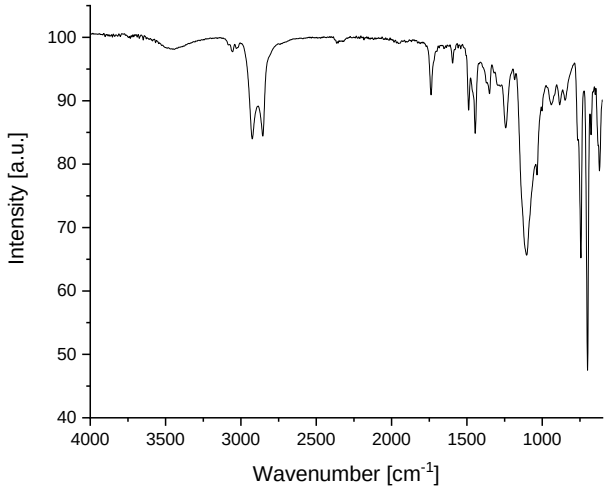

Figure S2-10: FT-IR ATR spectrum of 1,1,1-triphenyl-12,15,18,21-tetraoxa-2-nonyl-23-ol (**2-20**)

1,1,1-Triphenyl-12,15,18,21-tetraoxa-2-nonyl-23-yl 4-methyl-benzenesulfonate (2-21)

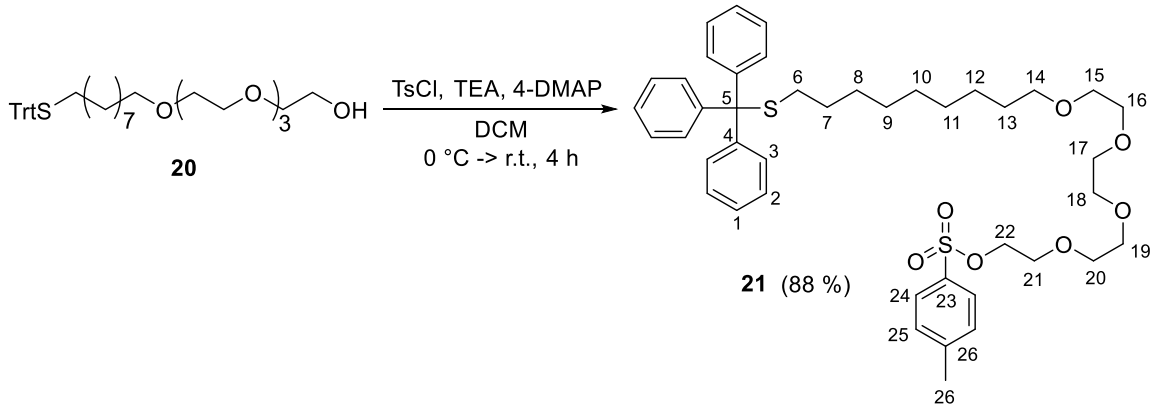

The glycol precursor **2-20** (19.9 g, 33.9 mmol, 1.00 eq) was dissolved in dry DCM (200 mL) and TEA (14.1 mL, 101 mmol, 3.00 eq) was added. After cooling the mixture in an ice bath, 4-methylbenzenesulfonyl chloride (12.9 mL, 67.8 mmol, 2.00 eq) was added. The reaction mixture was warmed to room temperature and stirred for 4 h. Upon completion, the reaction mixture was washed three times with deionized water. The organic layer was dried with $MgSO_4$ and the solvent removed in vacuo. The crude product was purified by column chromatography (silica, cyclohexane/EtOAc, 3:1, v/v). After removing the solvent, the product was obtained as a slightly yellow oil.

Yield: 22.4 g (29.9 mmol, 88 %). **R_f** (EtOAc/cyclohexane, 1:3): 0.18. **^{1}H-NMR** (400 MHz, $CDCl_3$): δ = 7.81-7.78 (m, 2H, H-24), 7.42-7.39 (m, 6H, H-3), 7.35-7.32 (m, 2H, H-25), 7.30-7.25 (m, 6H, H-2), 7.22-7.18 (m, 3H, H 1), 4.17-4.14 (m, 2H, H 22), 3.69-3.55 (m, 14H, H-15 – H-21), 3.43 (t, $^3J_{14,13}$ = 6.9 Hz, 2H, H-14), 2.44 (s, 3H, H-27), 2.13 (t, $^3J_{6,7}$ = 7.4 Hz, 2H, H-6), 1.60-1.51 (m, 2H, H-13), 1.41-1.34 (m, 2H, H-7), 1.29-1.13 (m, 10H, H-8 – H-12) ppm. **^{13}C-NMR** (100 MHz, $CDCl_3$): δ = 145.2 (C_q, C-4), 144.9 (C_q, C-23), 133.1 (C_q, C-26), 129.9 (CH, C-25), 129.7 (CH, C-2), 128.1 (CH, C-24), 127.9 (CH, C-3), 126.6 (CH, C-1), 71.6, 70.9, 70.7, 70.7, 70.6, 70.2, 69.4, 68.8 ($(CH_2)_9$, C-14-22), 66.5 (C_q, C-5), 32.1 (CH_2, C-6), 29.7, 29.5, 29.5, 29.2, 29.1, 28.7, 26.2 ($(CH_2)_8$, C-6-13) 21.8 (CH_3, C-26) ppm. **HRMS** (ESI,+): found: 771.3371 [M]+; calc. for [M]+: 771.3365. **FTIR (ATR):** $\tilde{\nu}$ = 3054 (vw) 2934 (s), 2856 (s), 1738 (w), 1594 (m), 1494 (m), 1438 (s), 1355 (vs), 1292 (w), 1244 (w), 1188 (s), 1178 (vs), 1102 (vs), 1036 (m), 1019 (s), 921 (vs), 815 (s), 768 (s), 745 (vs), 698 (vs), 658 (vs), 618 (m) cm^{-1}.

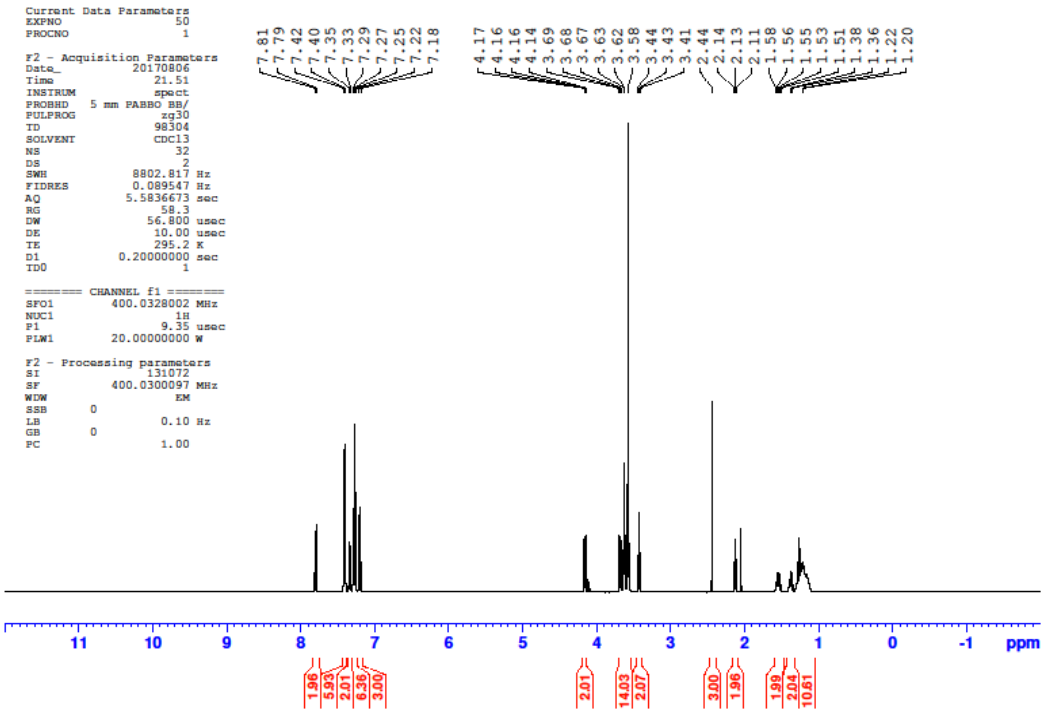

Figure S2-11: ^{1}H-NMR spectrum of 1,1,1-triphenyl-12,15,18,21-tetraoxa-2-nonyl-23-yl 4-methyl-benzenesulfonate (**2-21**).

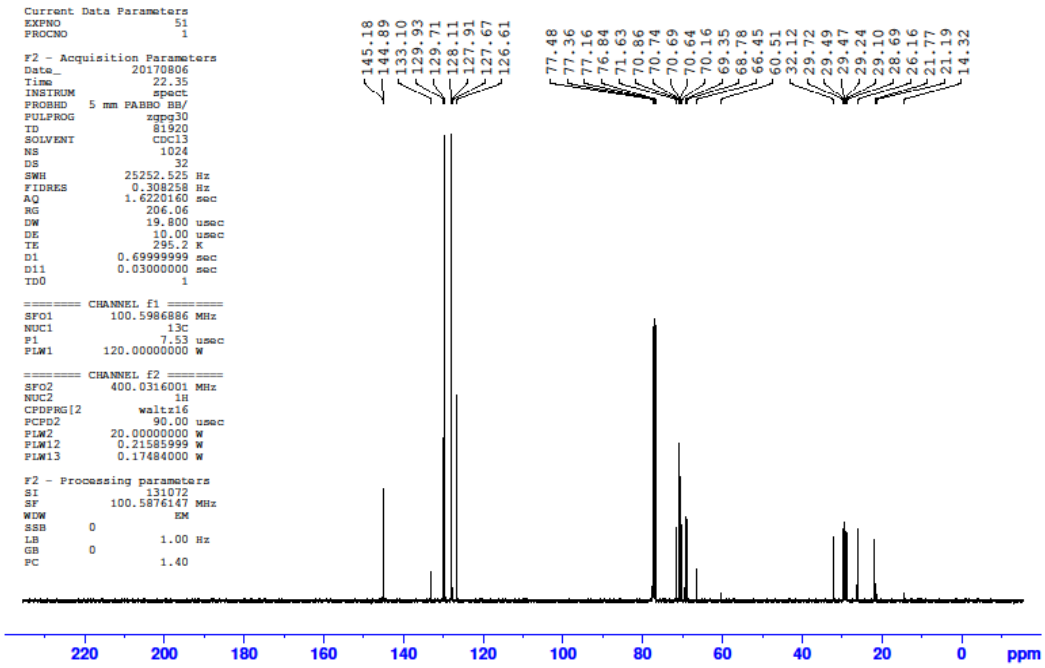

Figure S2-12: ^{13}C-NMR spectrum of 1,1,1-triphenyl-12,15,18,21-tetraoxa-2-nonyl-23-yl 4-methyl-benzenesulfonate (**2-21**).

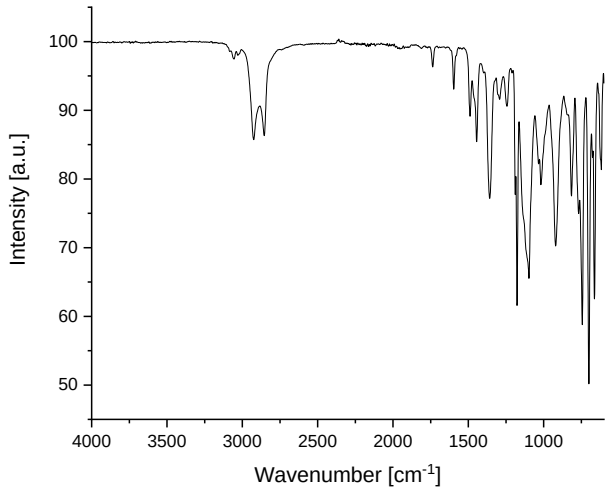

Figure S2-13: FT-IR ATR spectrum of 1,1,1-triphenyl-12,15,18,21-tetraoxa-2-thiatricosan-23-yl 4-methyl-benzenesulfonate (**2-21**)

2-(Hydroxymethyl)-2-((tosyloxy)methyl)propane-1,3-diyl bis(4-methylbenzene sulfonate) (2-23)[3]

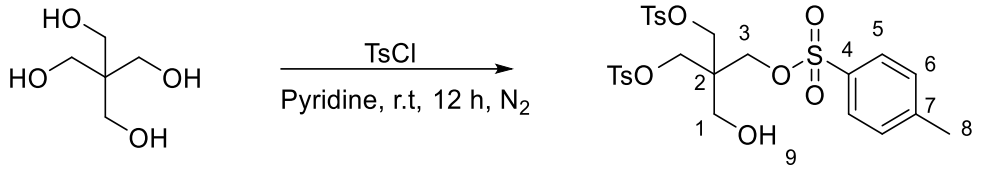

2-22 **2-23** (54 %)

2,2-Bis(hydroxymethyl)propane-1,3-diol (10.0 g, 73.5 mmol, 1.00 eq) was dissolved in dry pyridine (70 mL) and cooled to 0 °C. 4-Methylbenzenesulfonyl chloride (42.0 g, 220 mmol, 3.00 eq) was dissolved in dry pyridine (100 mL) and added dropwise to the starting material. The reaction mixture was warmed to room temperature and stirred overnight (12 h). The solvent was removed in vacuo. The solid residue was dissolved in 100 mL DCM and washed with HCl (2 N, 100 mL) und dried with $MgSO_4$. The solvent was removed in vacuo and the crude product purified by column chromatography (silica, cyclohexane/EtOAc, 4:1 -> 1:1, v/v). After removing the solvent and recrystallization in DCM, the product was obtained as a colorless crystals.

Yield: 19.9 g (33.0 mmol, 45 %) **R_f** (cyclohexane:EtOAc, 1:1): 0.42 **^{1}H-NMR** (400 MHz, $CDCl_3$): δ = 7.73.14-7.68 (m, 6H, H-5), 7.37-7.33 (m, 6H, H-6), 3.92 (s, 6H, H-3), 3.51 (d, $^3J_{5,6}$ = 6.1 Hz, 2H, H-1), 2.46 (s, 9H, H-9) ppm. **^{13}C-NMR** (100 MHz, $CDCl_3$): δ = 145.7 (C_q, C-4), 131.9 (C_q, C-7), 130.3 (CH, C-5), 128.1 (CH, C-6), 66.8 (CH_2, C-3), 59.5 (CH_2, C-1), 44.9 (C_q, C-2), 21.9 (CH_3, C-8) ppm. **FT-IR** (ATR): $\tilde{\nu}$ = 3539 (m), 3059 (vw), 2900 (vw), 1597 (m), 1466 (w), 1356 (s), 1308 (w), 1173 (vs), 1097 (m), 1063 (m), 1018 (m), 987 (s), 966 (vs), 928 (w), 858 (s), 833 (vs), 808 (vs), 706 (w), 667 (vs), 627 (m) cm^{-1}.

3-Azido-2,2-bis(azidomethyl)propan-1-ol (2-24)[3]

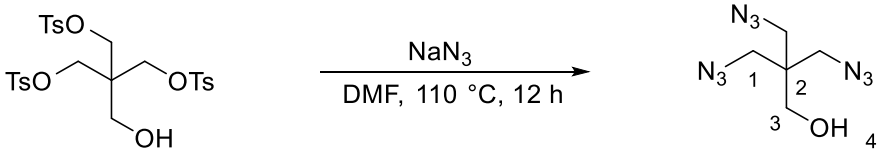

2-23 **2-24** (98 %)

A solution of tosylate **2-23** (10.0 g, 16.7 mmol, 1.00 eq) and DMF (200 mL) was prepared. NaN_3 (6.50 g, 100 mmol, 6.00 eq) was added and the mixture stirred at 110 °C overnight. Upon

completion (TLC), the reaction mixture was concentrated in vacuo and the residue suspended in water and extracted with EtOAc (6x, 100 mL). The organic layers were combined and washed with saturated Na_2CO_3 solution. The organic layer was then dried with $MgSO_4$ and the solvent removed in vacuo. The product was obtained as a yellow oil which was used without further purification

Yield: 3.46 g (16.4 mmol, 98 %). **^{1}H-NMR** (400 MHz, $CDCl_3$): δ = 3.37 (s, 6H, H-1), 2,95 (s, 2H, H-3) ppm. **^{13}C-NMR** (100 MHz, $CDCl_3$): δ = 62.1 (CH_2, C-3), 51.1 (CH_2, C-1), 44.6 (C_q, C-2) ppm. **FT-IR** (ATR): $\tilde{\nu}$ = 3374 (br), 2935 (w), 2877 (w), 2530 (vw), 2091 (vs), 1660 (s), 1448 (m), 1360 (w), 1286 (s), 1101 (w), 1047 (s), 889 (m), 660 (m) cm^{-1}.

27-Azido-26,26-bis(azidomethyl)-1,1,1-triphenyl-12,15,18,21,24-pentaoxa-2-nonyl (2-25)[3]

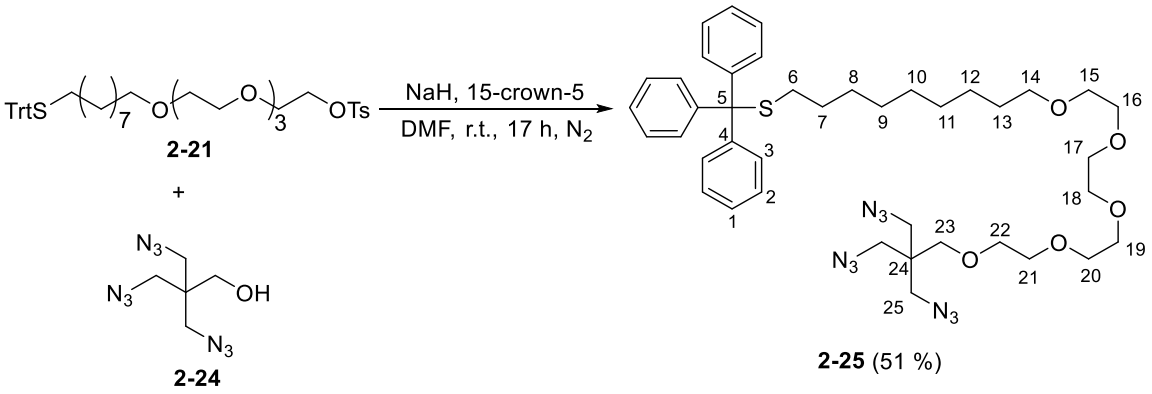

Sodium hydride (60 % dispersion in mineral oil, 0.05 g, 2.00 mmol, 2.00 eq) and 15-crown-5 (1 mg) was added to a solution of 3-azido-2,2-bis(azidomethyl)propan-1-ol (**2-24**, 0.32 g, 1.50 mmol, 1.50 eq) in dry DMF (10 mL). The reaction mixture was stirred at room temperature for 5 min. The tosylate **2-21** (0.75 g, 1.00 mmol, 1.00 eq) was dissolved in dry DMF (10 mL) and added to the reaction mixture which was stirred at room temperature overnight (17 h). Upon completion (TLC), the reaction was quenched by adding methanol dropwise. The solvent was removed in vacuo. After dissolving the brownish solid in deionized water, the mixture was extracted with EtOAc (2x) and DCM (2x). The organic layers were combined and washed with concentrated NaCl-solution, dried over $MgSO_4$ and the solvent removed in vacuo. The crude product was purified by column chromatography (silica, cyclohexane/EtOAc, 3:2, v/v). After removing the solvent, the product was obtained as a slightly yellow oil.

Yield: 0.62 g (0.51 mmol, 51 %). **R**$_f$ (cyclohexane:EtOAc, 3:2): 0.43. **^{1}H-NMR** (400 MHz, $CDCl_3$): δ = 7.42-7.38 (m, 6H, H-3), 7.30-7.25 (m, 6H, H-2), 7.22-7.17 (m, 3H, H-1), 3.66-3.55 (m, 16H, H-15 – H-22), 3.43 (t, $^3J_{14,13}$ = 6.8 Hz, 2H, H-14), 3.35-3.32 (m, 8H, H-23), 2.12 (t, $^3J_{6,7}$ = 7.5 Hz, 2H, H-6), 1.58-1.51 (m, 2H, H-13), 1.41-1.32 (m, 2H, H-7) 1.32-1.08 (m, 10H, H-8 – H-12) ppm. **^{13}C-NMR** (100 MHz, $CDCl_3$): δ = 145.2 (C_q, C-4), 129.7 (CH, C-2), 127.9 (CH, C-3), 126.6 (CH, C-1), 71.7, 70.9, 70.8, 70.7, 70.7 70.7 70.7, 70.5, 70.2, 69.6 ($(CH_2)_{10}$, C-14-23), 66.5 (C_q, C-5), 51.6 ($(CH_2)_3$, C-25), 44.8 (C_q, C-24), 32.1 (CH_2, C-6), 29.7, 29.5, 29.5, 29.3, 29.1, 28.7, 26.2 ($(CH_2)_7$, C-7-13) ppm. **HRMS** (ESI,+): found: 810.4092 [M]+; calc. for [M]+: 810.4101. **FT-IR** (ATR): $\tilde{\nu}$ = 3057 (w), 3024 (vw), 2925 (s), 2856 (s), 2096 (vs), 1595 (w), 1487 (m), 1444 (s), 1352 (m), 1292 (s), 1252 (s), 1105 (vs), 1036 (m), 943 (m), 881 (m), 744 (s), 700 (s), 675 (m), 621 (m) cm^{-1}.

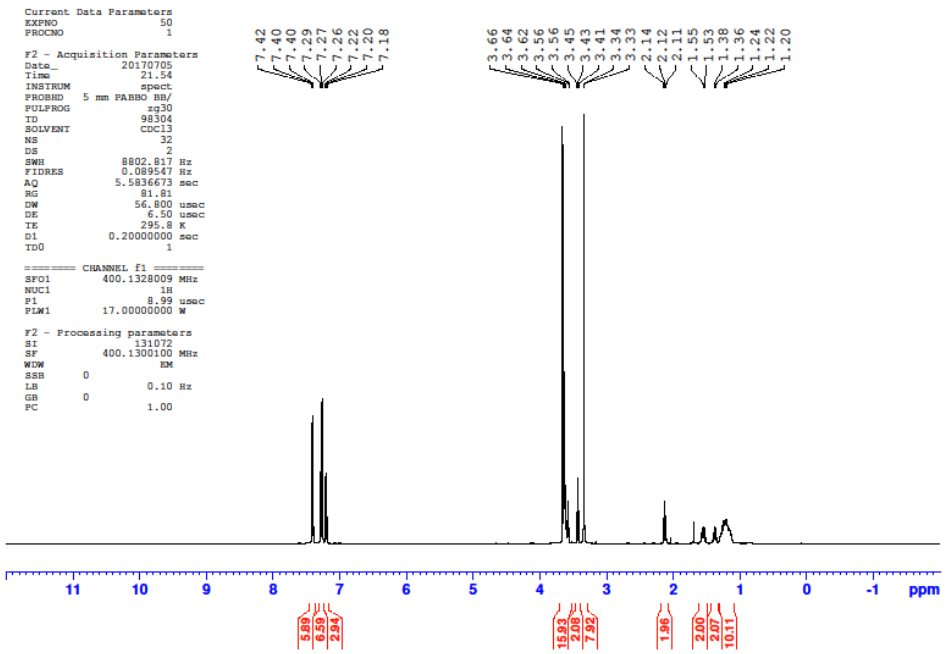

Figure S2-14: ^{1}H-NMR spectrum of 27-azido-26,26-bis(azidomethyl)-1,1,1-triphenyl-12,15,18,21,24-pentaoxa-2-nonyl (**2-25**).

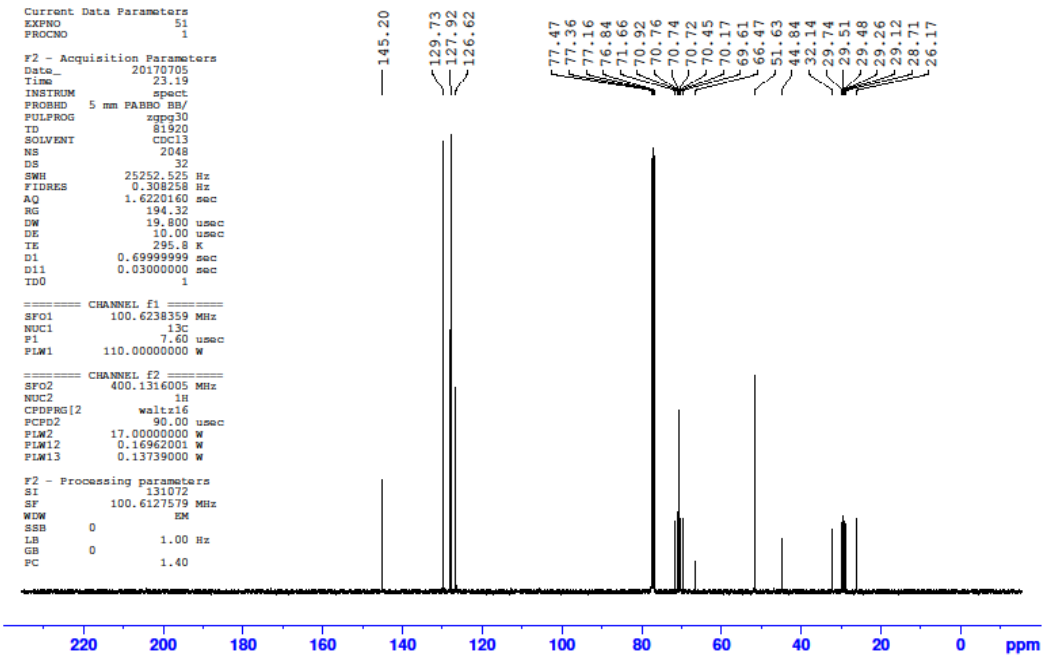

Figure S2-15: ^{13}C-NMR spectrum of 27-azido-26,26-bis(azidomethyl)-1,1,1-triphenyl-12,15,18,21,24-pentaoxa-2-nonyl (**2-25**).

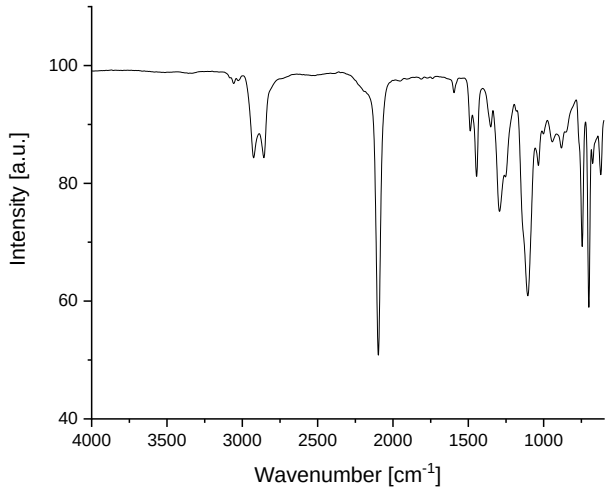

Figure S2-16: FT-IR ATR spectrum of 27-azido-26,26-bis(azidomethyl)-1,1,1-triphenyl-12,15,18,21,24-pentaoxa-2-nonyl (**2-25**).

1-Azido-2,2-bis(azidomethyl)-4,7,10,13,16-pentaoxapentacosane-25-thiol (26)[4]

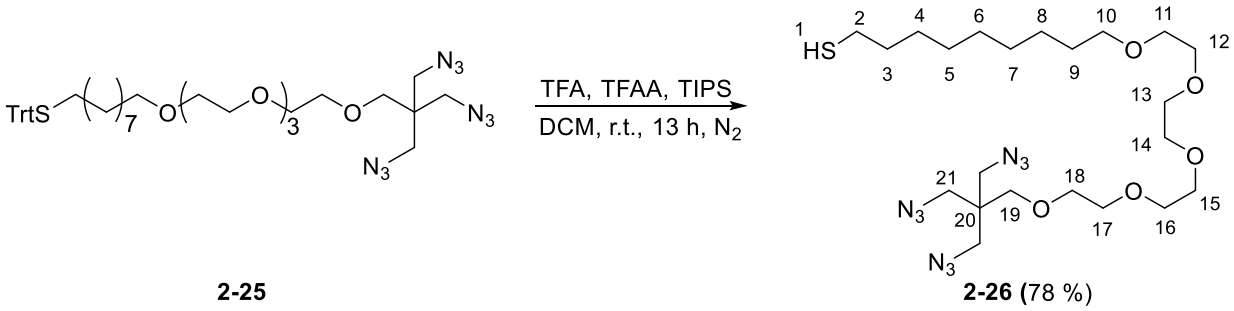

2-25 **2-26** (78 %)

The triazide **2-25** (100 mg, 130 µmol, 1.00 eq) was dissolved in dry DCM (1 mL). TFA (0.20 mL, 2.54 mmol, 20.00 eq), TFAA (0.05 mL, 0.38 mmol, 3.00 eq) and TIPS (0.08 mL, 0.38 mmol, 3.00 eq) were added to the solution. The mixture was stirred at room temperature overnight (13 h). After the reaction was finished (TLC), the solvent was removed in vacuo. The crude product was purified by column chromatography (silica, cyclohexane/EtOAc, 2:1, v/v + 5% Et_3N). After removing the solvent, the product was obtained as a slightly yellow oil.

Yield: 54.0 mg (0.10 mmol, 78 %). **R_f** (cyclohexane:EtOAc, 2:1): 0.55. **^{1}H-NMR** (400 MHz, $CDCl_3$): δ = 3.59-3.50 (m, 16H, H-11 – H 18), 3.38 (t, $^3J_{10,9}$ = 6.8 Hz, 2H, H 10), 3.28 (s, 6H, H 21), 3.27 (s, 2H, H 19), 2.98 (t, $^3J_{2,3}$ = 7.4 Hz, 2H, H 2), 1.62-1.55 (m, 2H, H 9), 1.53-1.47 (m, 2H, H 3) 1.36-1.17 (m, 10H, H 4 – H 8) ppm. **^{13}C-NMR** (100 MHz, $CDCl_3$): 71.6, 70.9, 70.8, 70.7, 70.7 70.7 70.7, 70.5, 70.2, 69.6 ((CH2)10, C 10/15/16/17/18/19/20/21/22/19), 51.6 ((CH2)3, C 21), 44.9 (Cq, C 20), 29.7, 29.5, 29.4, 29.4, 29.0, 28.8, 28.7, 26.2 ($(CH2)_8$, C 2/3/4/5/6/7/8/9) ppm. **HRMS** (ESI,+): found: 568.2990 [M]+; calc. for [M]+: 568.3006. **FT-IR (ATR)**: $\tilde{\nu}$ = 2927 (s), 2860 (s), 2360 (w), 2098 (vs), 1701 (m), 1450 (s), 1352 (m), 1282 (s), 1203 (s), 1155 (m), 1107 (vs), 952 (m), 881 (m), 742 (m), 650 (m) cm^{-1}.

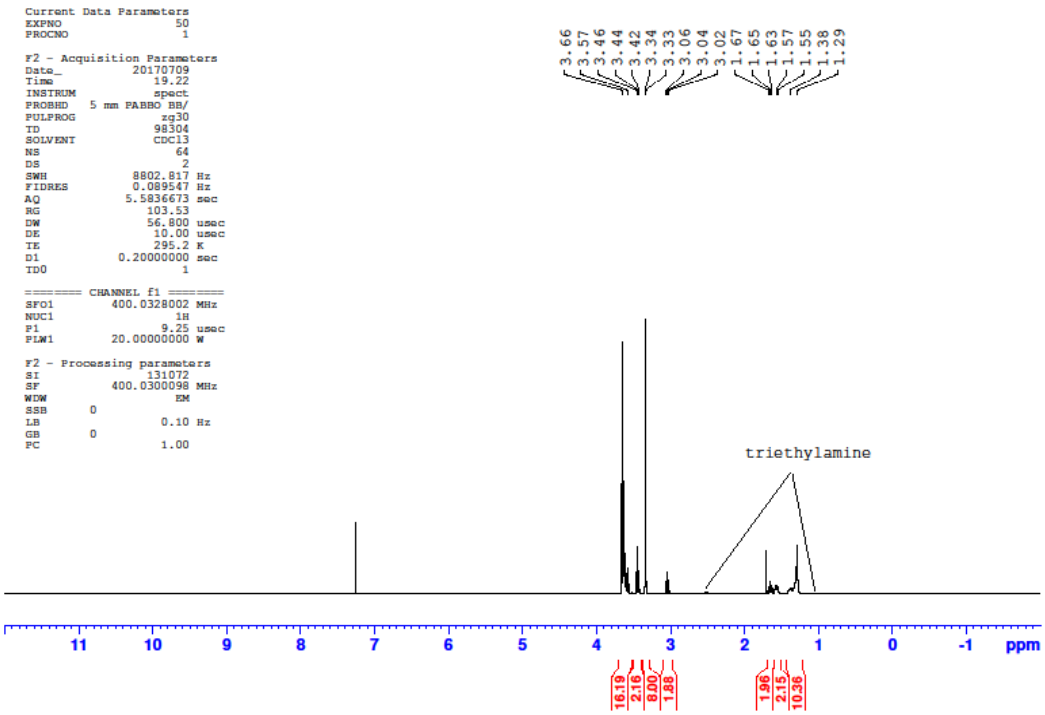

Figure S2-17: ^{1}H-NMR spectrum of 1-azido-2,2-bis(azidomethyl)-4,7,10,13,16-pentaoxa-pentacosane-25-thiol (**2-26**).

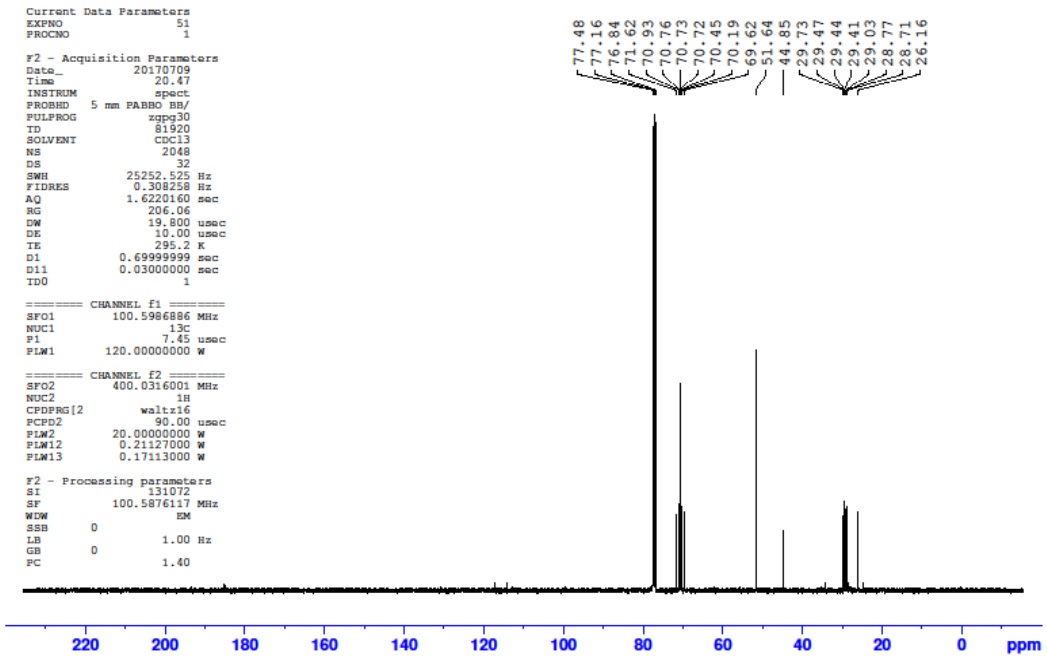

Figure S2-18: ^{13}C-NMR spectrum of 1-azido-2,2-bis(azidomethyl)-4,7,10,13,16-pentaoxa-pentacosane-25-thiol (**2-26**).

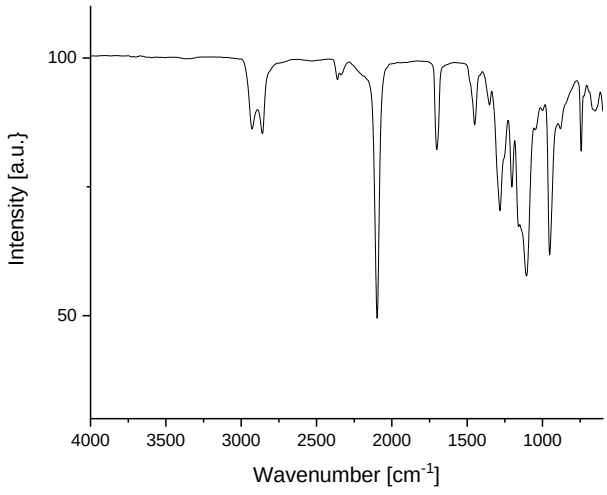

Figure S2-19: FT-IR ATR spectrum of 1-azido-2,2-bis(azidomethyl)-4,7,10,13,16-penta-oxapentacosane-25-thiol (**2-26**).

23-Azido-1,1,1-triphenyl-12,15,18,21-tetraoxa-2-thiatricosane (2-27)

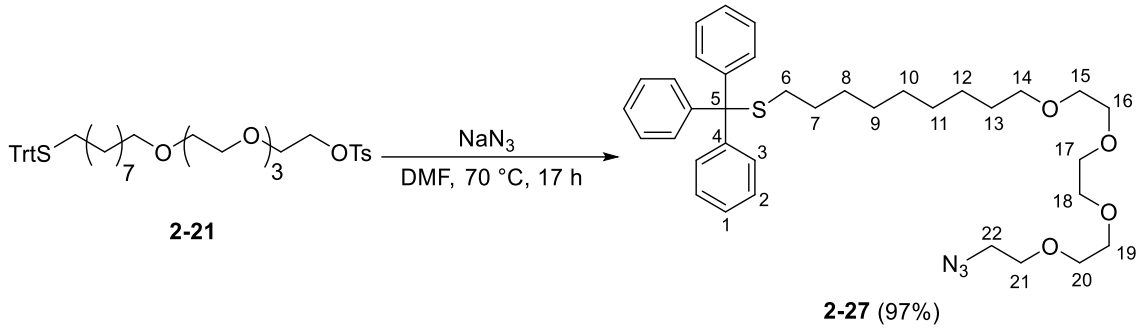

The tosylate **2-21** (1.00 g, 1.34 mmol, 1.00 eq) was dissolved in 8 mL DMF and sodium azide (0.43 g, 6.67 mmol, 5.00 eq) was added. The reaction mixture was stirred for 17 h at 70 °C. After the reaction was finished, the solvent was removed in vacuo and the residue was dissolved in DCM and deionized water (50 mL, 1:1). After extracting the mixture with DCM, the organic layers were combined and dried with $MgSO_4$. The solvent was removed in vacuo. The crude product was obtained as a colorless oil and was used without further purification.

Yield: 0.82 g (1.32 mmol, 99 %). **R_f** (CyH/EtOAc, 3:2): 0.43. **^{1}H-NMR** (400 MHz, CDCl3): δ = 7.42-7.39 (m, 6H, H-3), 7.29-7.26 (m, 6H, H-2), 7.22-7.18 (m, 3H, H-1), 3.68-3.63 (m, 12H, H-15 – H-20), 3.58-3.56 (m, 2H, H-21), 3.43 (t, $^3J_{14,13}$ = 6.9 Hz, 2H, H-14), 3.38 (t, $^3J_{22,21}$ = 5.3 Hz, 2H, H-22), 2.12 (t, $^3J_{6,7}$ = 7.3 Hz, 2H, H-6), 1.58-1.51 (m, 2H, H-13), 1.41-1.34 (m, 2H, H-7) 1.29-1.13 (m, 10H, H-8 – H-12) ppm. **^{13}C-NMR** (100 MHz, $CDCl_3$): δ = 145.2 (C_q, C-4), 129.7 (CH, C-2), 127.9 (CH, C-3), 126.6 (CH, C-1), 71.7, 70.8, 70.8, 70.8, 70.8, 70.5, 70.2, 70.2 ((CH_2)$_8$, C-14-21), 66.5 (C_q, C-5), 50.8 (CH_2, C-22), 32.2 (CH_2, C-6), 29.8, 29.5, 29.5, 29.3, 29.1, 28.7, 26.2 ((CH_2), C-7-13) ppm. **HRMS** (ESI,+): found: 642.3323 [M]+; calc. for [M]+: 642.3341. **FT-IR** (ATR): $\tilde{\nu}$ = 3057 (w), 3019 (vw), 2924 (s), 2856 (s), 2100 (vs), 1678 (w), 1595 (w), 1489 (m), 1443 (s), 1348 (m), 1286 (s), 1111 (vs), 1034 (m), 937 (m), 850 (m), 744 (s), 700 (s), 677 (m), 619 (m) cm^{-1}.

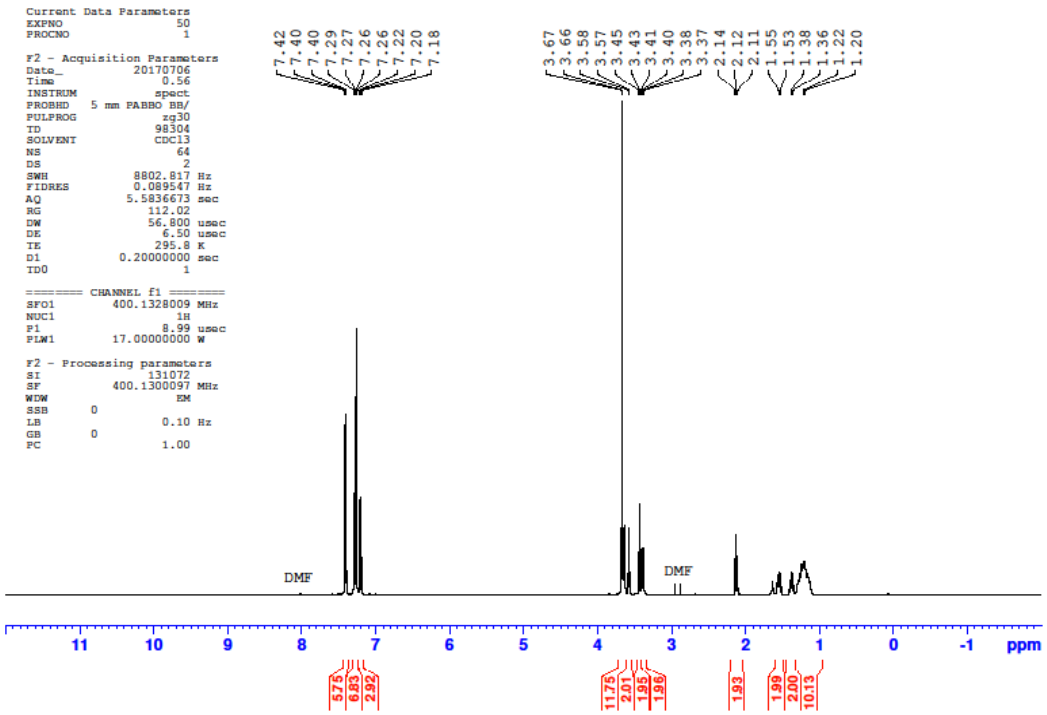

Figure S2-20: ^{1}H-NMR spectrum of 23-azido-1,1,1-triphenyl-12,15,18,21-tetraoxa-2-thiatricosane (**2-27**).

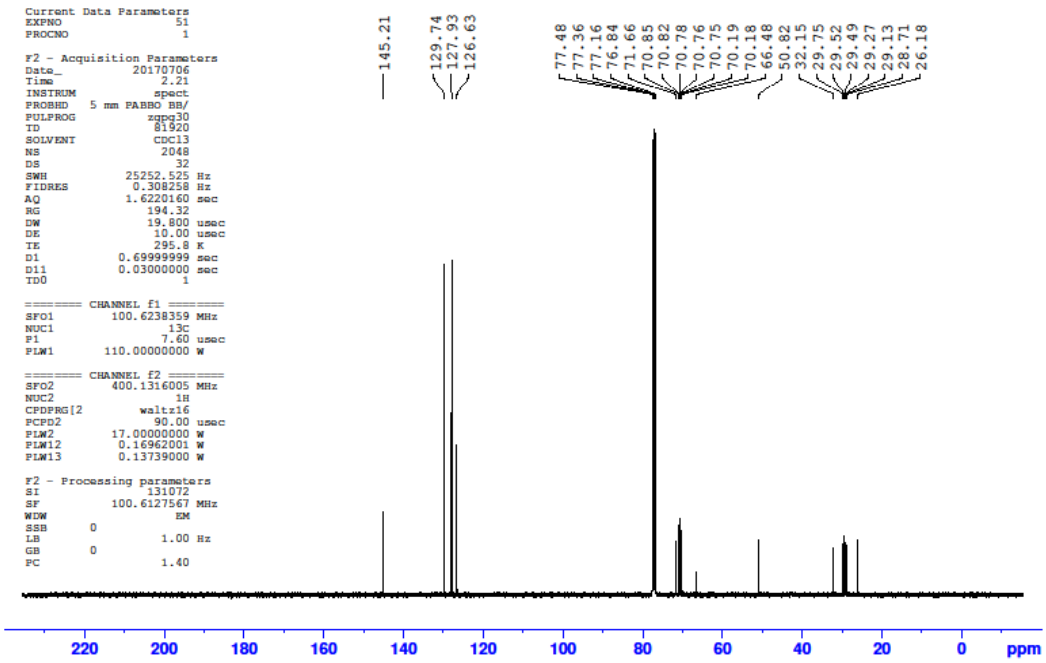

Figure S2-21: ^{13}C-NMR spectrum of 23-Azido-1,1,1-triphenyl-12,15,18,21-tetraoxa-2-thiatricosane (**2-27**).

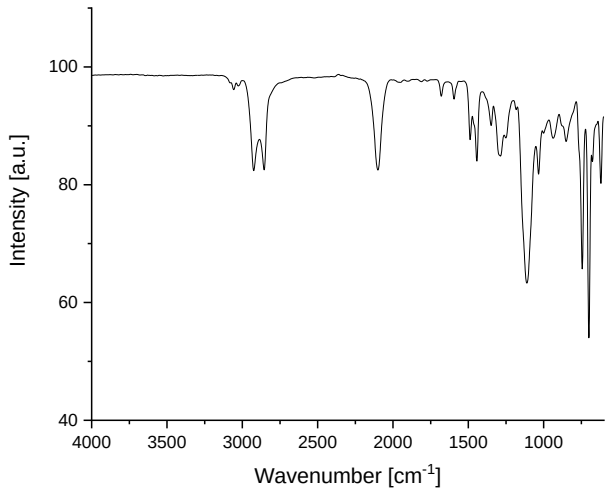

Figure S2-22: FT-IR ATR spectrum of 23-Azido-1,1,1-triphenyl-12,15,18,21-tetraoxa-2-thiatricosane (**2-27**).

1-Azido-3,6,9,12-tetraoxahenicosane-21-thiol (2-28)

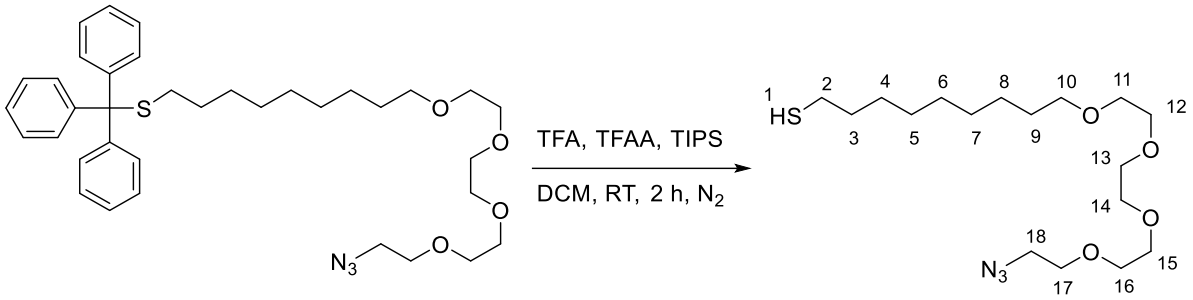

2-27 **2-28** (99 %)

The azide **2-27** (1.65 g, 2.66 mmol, 1.0 eq) was dissolved in dry DCM (16 mL). TFA (4.10 mL, 53 mmol, 20.0 eq), TFAA (1.13 mL, 7.98 mmol, 3.0 eq) and TIPS (1.64 mL, 7.98 mmol, 3.0 eq) were added to the solution. The mixture was stirred at room temperature for 2 h under nitrogen atmosphere. After the reaction was finished (TLC), the solvent was removed in vacuo. The crude product was purified by column chromatography (silica, cyclohexane/EtOAc, 2:1, v/v). After removing the solvent, the product was obtained as a slightly yellow oil.

Yield: 1 g (2.64 mmol, 99 %). **R_f** (cyclohexane:EtOAc, 2:1): 0.38. **^{1}H-NMR** (400 MHz, CDCl3): δ = 3.73-3.60 (m, 12H, H-11 – H-16), 3.62-3.54 (m, 2H, H-17), 3.44 (t, $^3J_{10,9}$ = 6.9 Hz, 2H, H-10), 3.38 (t, $^3J_{18,17}$ = 5.3 Hz, 2H, H-18), 3.03 (t, $^3J_{6,7}$ = 7.4 Hz, 2H, H-2), 1.71-1.60 (m, 2H, H-3), 1.60-1.51 (m, 2H, H-9) 1.41-1.22 (m, 10H, H-4 – H-8) ppm. **^{13}C-NMR** (100 MHz, $CDCl_3$): δ = 71.6, 70.8, 70.8, 70.8, 70.8, 70.4, 70.2, 70.2 ($(CH_2)_8$, C-10-17), 50.8 (CH_2, C-18), 29.7, 29.5, 29.4, 29.4, 29.0, 28.8, 28.7, 26.2 ($(CH_2)_8$, C-2-9) ppm. **HRMS** (ESI,+): found: 400.2230 [M]+; calc. for [M]+: 400.2246. **FT-IR** (ATR): $\tilde{\nu}$ = 2927 (s), 2862 (s), 298 (vs), 1700 (s), 1454 (m), 1353 (m), 1279 (s), 1243 (m), 1203 (vs), 115 (vs), 1116 (vs), 1046 (m), 998 (w), 949 (vs), 875 (m), 848 (m), 748 (s), 721 (w) cm^{-1}.

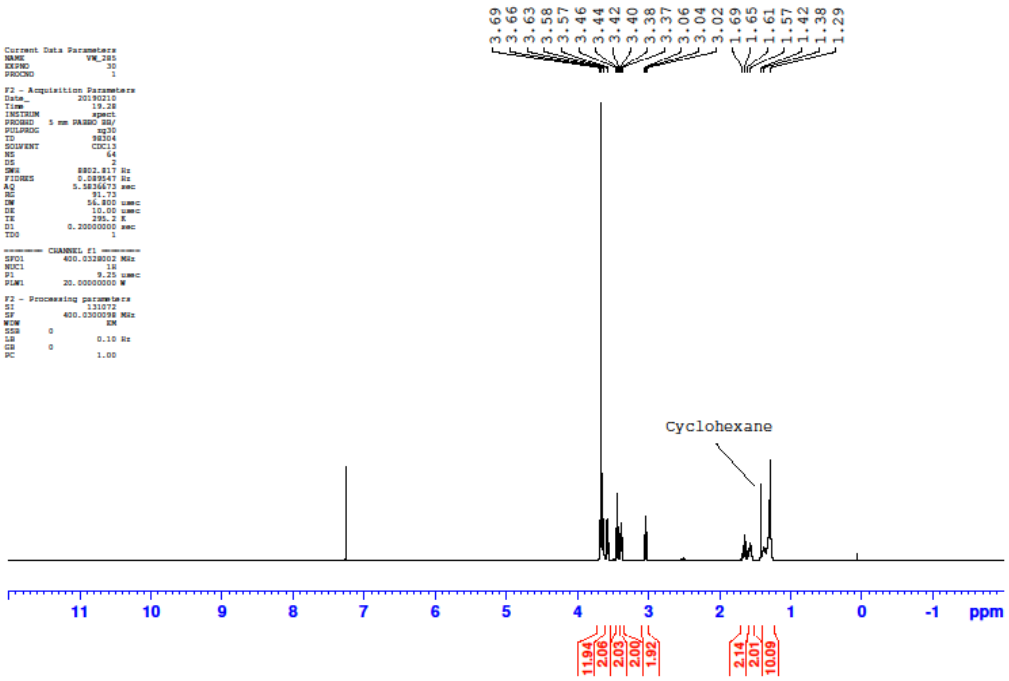

Figure S2-23: ^{1}H-NMR spectrum of 1-azido-3,6,9,12-tetraoxahenicosane-21-thiol (**2-28**).

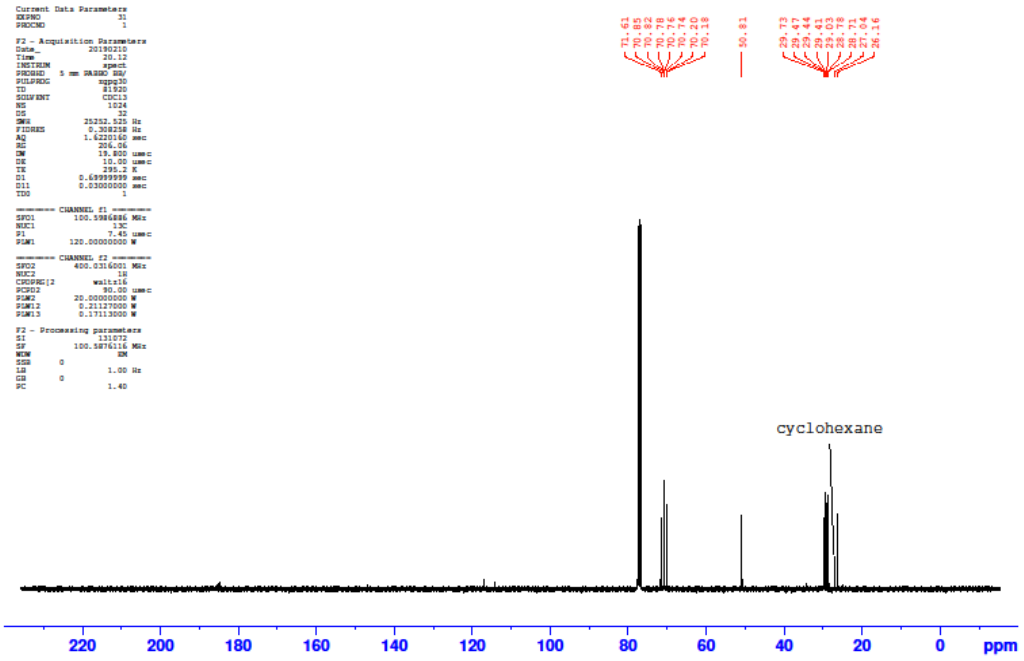

Figure S2-24: ^{13}C-NMR spectrum of 1-azido-3,6,9,12-tetraoxahenicosane-21-thiol (**2-28**).

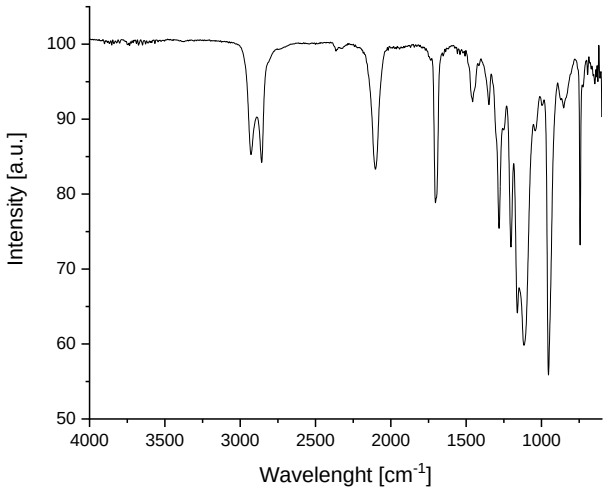

Figure S2-25: FT-IR ATR spectrum of 1-azido-3,6,9,12-tetraoxahenicosane-21-thiol (**2-28**).

3-(Dimethyl(prop-2-yn-1-yl)ammonio)propane-1-sulfonate (2-15)[5]

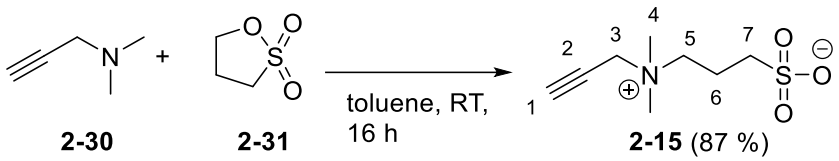

2-30 **2-31** **2-15** (87 %)

1,2-Oxathiolane-2,2-dioxide (3.23 g, 2.30 mL, 26.5 mmol, 2.20 eq) was added to a solution of *N,N*-dimethylprop-2-yn-1-amine (1.00 g, 1.30 mL, 12.0 mmol, 1.00 eq) in toluene (50 mL). The reaction mixture was stirred overnight (16 h) at room temperature. The precipitated colorless solid was separated by centrifugation (5k RPM, 2 min) and washed with toluene and pentane. The colorless powder was dried in vacuo at room temperature.

Yield: 2.14 g (10.4 mmol, 87 %)**.** **^{1}H-NMR** (400 MHz, D_2O): δ = δ4.27 (d, $^{4}J_{3,1}$ = 2.5 Hz, 2H, H-3), 3.59 (m, 2H, H-5), 3.25 (t, $^{4}J_{1,3}$ = 2.5 Hz, 1H, H-1), 3.19 (s, 6H, H-4), 2.98 (t, $^{3}J_{7,6}$ = 7.2 Hz 2H), 2.29-2.17 (m, 2H, H-6) ppm. **^{13}C-NMR** (100 MHz, D_2O): δ = 81.6, 70.6, 62.3, 54.3, 50.3, 47.1, 18.2 ppm. **IR** (ATR): $\tilde{\nu}$ = 3187 (s), 3028 (vw), 2955 (s), 2120 (m), 1700 (br), 1491 (s), 1469 (m), 1413 (m), 1383 (w), 1341 (w), 1315 (w), 1229 (s), 1191 (vs), 1161 (vs), 1028 (vs), 969 (s), 913 (vs), 818 (s), 779 (s), 754 (s), 720 (vs).

7.1.1.2 Synthesis of short linkers 2-13, 2-34 and 2-37

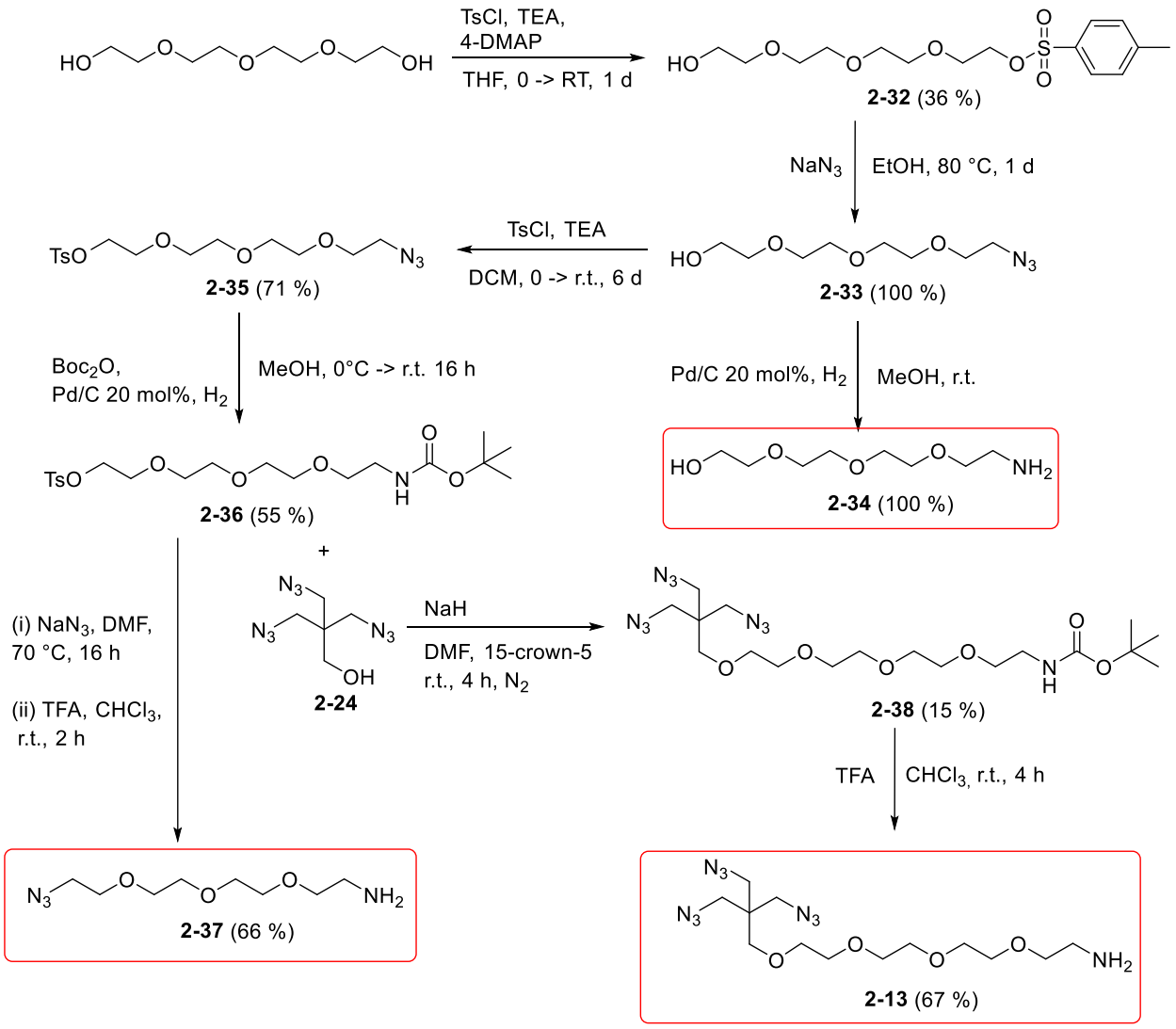

DCM = Dichloromethane, $CHCl_3$ = Chloroform, 4-DMAP = 4-Dimethylaminopyridine, TEA = Triethylamine, TsCl = 4-Toluenesulfonyl chloride, Boc2O = Di-*tert*-butyl dicarbonate, DMF = *N,N*-Dimethylformamide, TFA = Trifluoroacetic acid

Figure S2-26: Synthesis of short TEG-ligands **2-13**, **2-34** and **2-37** for the preparation of ND **2-6**, **2-10** and **2-12**.

2-(2-(2-(2-Hydroxyethoxy)ethoxy)ethoxy)ethyl 4-methylbenzenesulfonate (2-32)[3]

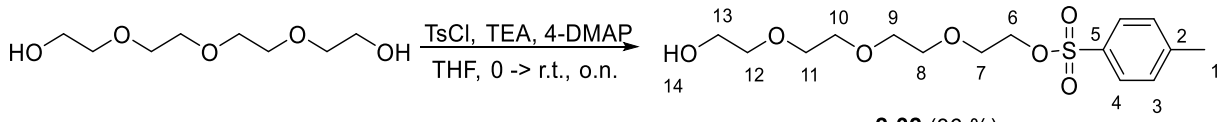

2-32 (36 %)

TEG (20.0 mL, 22.4 g, 115 mmol, 1.00 eq), TEA (24.0 mL, 17.5 g, 173 mmol, 1.50 eq) and 4-DMAP (2.82 g, 23.1 mmol, 0.20 eq) were dissolved in THF (100 mL) and cooled to 0 °C with an ice bath. TsCl (24.2 g, 127 mmol, 1.10 mmol) in THF (50 mL) was added dropwise. The reaction mixture was stirred at room temperature for 1 d. The solvent was removed in vacuo and the residue dispersed in HCl (2 N, 100 mL). The aqueous layer was extracted with DCM (4x, 100 mL) and the organic layers were combined, dried with $MgSO_4$ and filtered. The solvent was removed in vacuo and the crude product purified by column chromatography (silica, cyclohexane/EtOAc, 1:1 -> 1:10 -> 0:1, v/v). After removing the solvent, the product was obtained as a colorless oil.

Yield: 14.5 g (41.6 mmol, 36 %). $\mathbf{R_f}$ (cyclohexane:EtOAc, 1:1): 0.2. **^{1}H-NMR** (400 MHz, $CDCl_3$): δ = 7.80 (m, 2H, H-4), 7.34 (m, 2H, H-3), 4.16 (t, $^3J_{6,7}$ = 8 Hz, 2H, H-6) 3.72-3.60 (m, 16H, H-7-13), 2.45 (s, 3H, H-1) ppm. **^{13}C-NMR** (100 MHz, $CDCl_3$): δ = 144.9 (C_q, C-5), 132.9 (C_q, C-2), 129.9 (CH, C-4), 128.0 (CH, C-3), 72.5, 70.7, 70.6, 70.3, 69.3, 68.7 (CH_2, C-7/8/9/10/11/12), 61.7 (CH_2, C-13), 21.7 (CH_3, C-1) ppm. **IR** (ATR): $\tilde{\nu}$ = 3080 (vw), 3054 (w), 3028 (vw), 2926 (s), 2853 (s), 1739 (w), 1602 (m), 1482 (m), 1448 (s), 1358 (vs), 1289 (m), 1238 (m), 1174 (vs), 1096 (vs), 1032 (s), 1013 (s), 921 (vs), 810 (s), 772 (s), 740 (vs), 698 (vs), 660 (vs) cm^{-1}.

2-(2-(2-(2-Azidoethoxy)ethoxy)ethoxy)ethan-1-ol (33)[3]

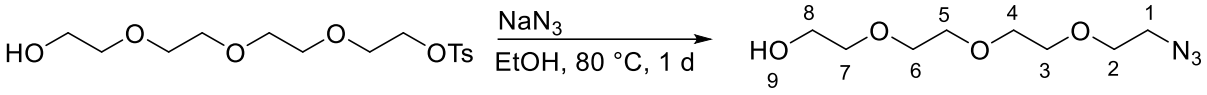

2-32 **2-33** (100 %)

The tosylate **2-32** (7.00 g, 20.1 mmol, 1.00 eq) was dissolved in EtOH (150 mL) and NaN_3 (10.5 g, 161 mmol, 8.00 eq) was added. The reaction mixture was stirred at 80 °C (1 d). Upon completion, the reaction mixture was diluted with saturated NaCl solution (100 mL) and the EtOH was removed in vacuo. The remaining aqueous solution was extracted twice with $CHCl_3$ (200 mL). The combined organic layers were washed with saturated NaCl solution. The organic layer was dried with Na_2SO_4. After removing the solvent, the product was obtained as a slightly yellow oil that was used without further purification.

Yield: 4.40 g (20.1 mmol, 100 %). **^{1}H-NMR** (400 MHz, $CDCl_3$): δ = 3.76 (m, 12H, H-2-7), 3.38 (m, 2H, H-1), 3.28 (m, 2H, H-8) 2.99 (m, 1H, H-9) ppm. **^{13}C-NMR** (100 MHz, $CDCl_3$): δ = 72.4, 70.5, 70.5, 70.4, 70.2, 69.9 (CH_2, C-2-7), 61.4 (CH_2, C-8), 50.5 (CH_2, C-1) ppm. **IR** (ATR): $\tilde{\nu}$ = 3431 (br), 2865 (s), 2099 (vs), 1744 (vw), 1662 (s), 1456 (m), 1388 (m), 1345 (s), 1281 (s), 1259 (s), 1096 (vs), 1062 (vs), 998 (m), 930 (s), 882 (s), 852 (s), 827 (s) cm^{-1}.

2-(2-(2-(2-Aminoethoxy)ethoxy)ethoxy)ethan-1-ol (34)[3]

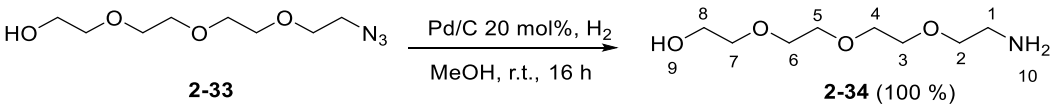

2-33 **2-34** (100 %)

The azide **2-33** (2.46 g, 7.49 mmol, 1.0 eq) was dissolved in dry MeOH (10 mL) and 10 %-Pd/C (0.55 g, 0.20 eq) was added. The reaction mixture was stirred under H_2-atmosphere overnight (16 h). Upon completion, the reaction mixture was filtered and the solvent removed in vacuo. The product was obtained as a colorless oil and used without further purification.

Yield: 1.45 g (7.49 mmol, 100 %). **^{1}H-NMR** (400 MHz, $CDCl_3$): δ = 3.76-3.64 (m, 12H, H-2-7), 3.60-3.50 (m, 2H, H-1), 3.84 (m, 2H, H-8), 2.28 (br. 2H, H-10) ppm. **^{13}C-NMR** (100 MHz, $CDCl_3$): δ = 73.4, 73.2, 70.8, 70.7, 70.4, 70.2 (CH_2, C-2-7), 61.7 (CH_2, C-8), 41.6 (CH_2, C-1) ppm. **IR** (ATR): $\tilde{\nu}$ = 3450 (br), 2870 (s), 1739 (w), 1662 (s), 1593 (m), 1537 (w), 1456 (s), 1349 (s), 1293 (m), 1251 (m), 1093 (vs), 1062 (vs), 930 (s), 891 (s), 827 (m) cm^{-1}.

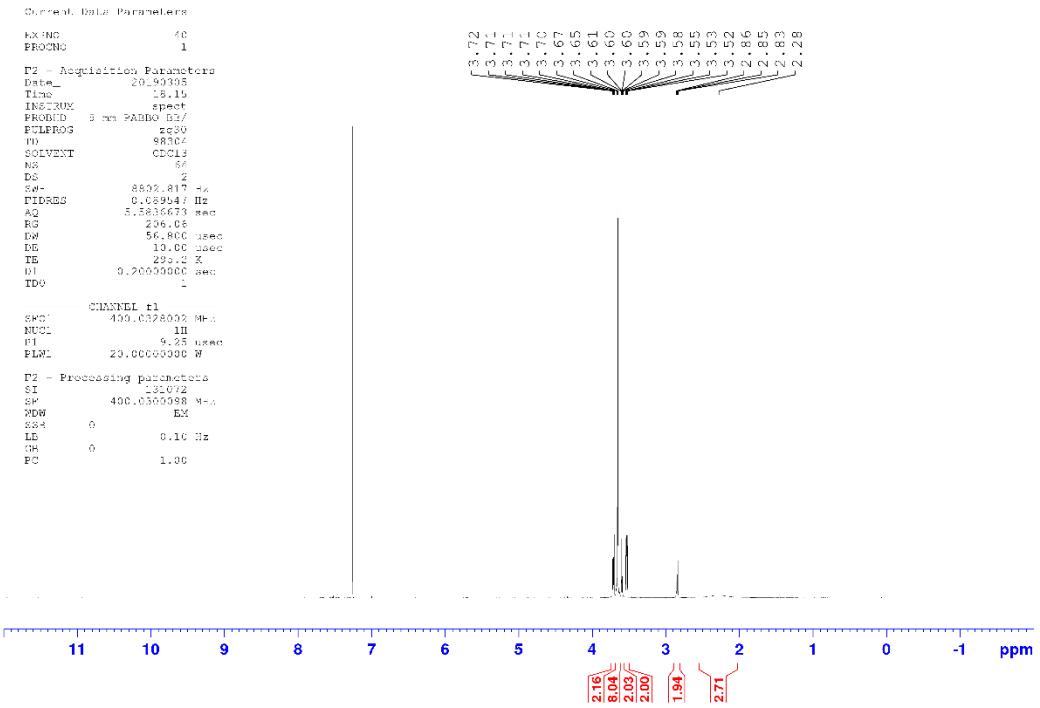

Figure S2-27: ^{1}H-NMR spectrum of 2-(2-(2-(2-aminoethoxy)ethoxy)ethoxy)ethan-1-ol (**2-34**).

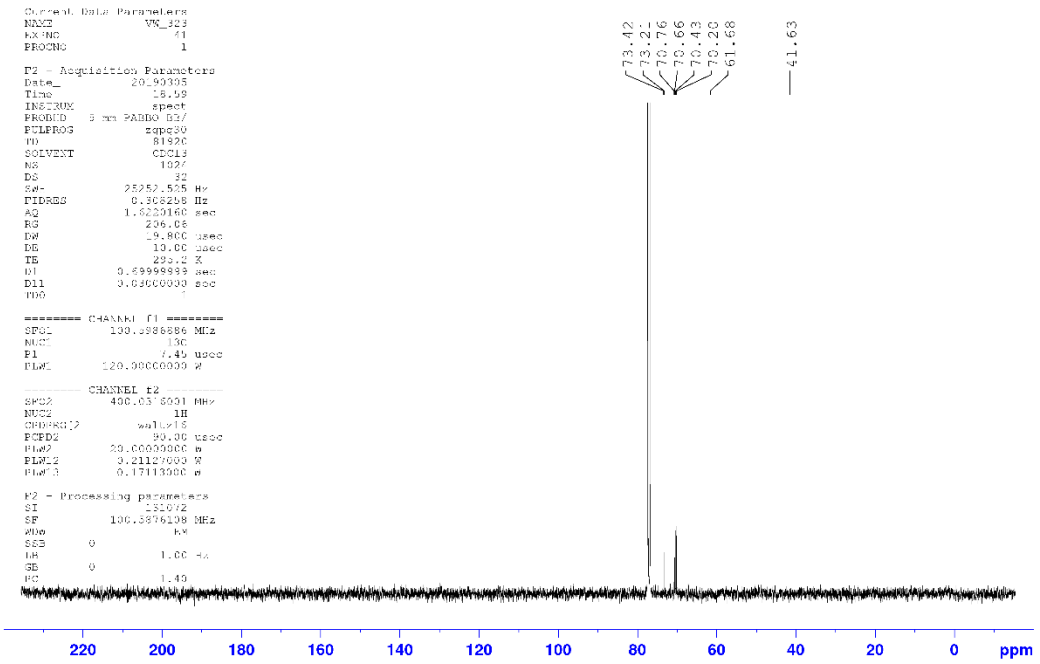

Figure S2-28: ^{13}C-NMR spectrum of 2-(2-(2-(2-azidoethoxy)ethoxy)ethoxy)ethan-1-ol (**2-34**).

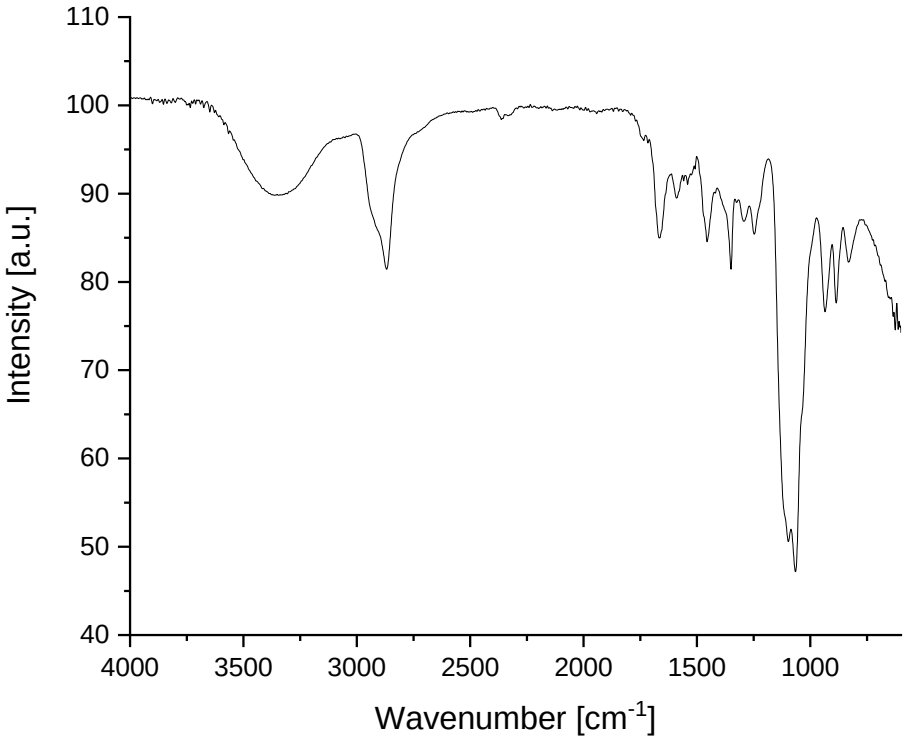

Figure S2-29: FT-IR ATR spectrum of 2-(2-(2-(2-aminoethoxy)ethoxy)ethoxy)ethan-1-ol (**2-34**).

2-(2-(2-(2-Hydroxyethoxy)ethoxy)ethoxy)ethyl 4-methylbenzenesulfonate (2-35)[4]

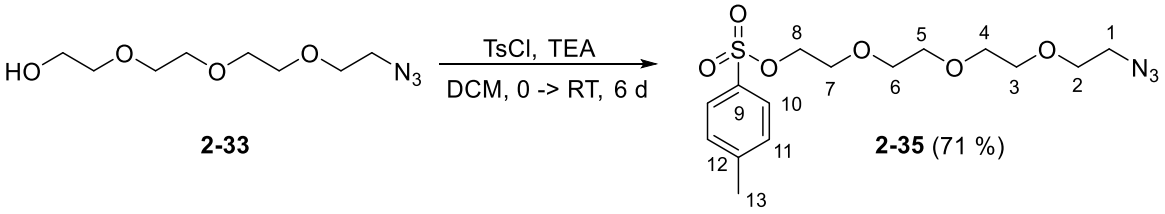

2-33 **2-35** (71 %)

The alcohol **2-33** (4.40 g 20.1 mmol, 1.00 eq) was dissolved in dry DCM (200 mL) and Et_3N (22.3 mL, 161 mmol, 8.00 eq) was added. The reaction mixture was cooled with an ice bath to 0 °C. TsCl (30.6 g, 160 mmol, 8.00 eq) was added in portions. The mixture was stirred for 6 d at room temperature. The solution was then concentrated in vacuo and the residue dispersed in HCl (2 N, 100 mL). The aqueous suspension was then extracted with DCM (4x 100 mL) and the combined organic layers were dried with $MgSO_4$. The solvent was removed in vacuo and

the crude product purified by column chromatography (silica, cyclohexane/EtOAc, 1:4 -> 0:1, v/v). After removing the solvent, the product was obtained as a yellowish oil.

Yield: 5.30 g, (14.2 mmol, 71%). **^{1}H-NMR** (400 MHz, $CDCl_3$): δ = 7.79 (m, 2H, H-10), 7.34 (m, 2H, H-11), 4.14 (m, 2H, H-8) 3.72-3.69-3.54 (m, 12H, H-2-7), 3.37 (m, 3H, H-1), 2.37 (s, 3H, H-13) ppm. **^{13}C-NMR** (100 MHz, $CDCl_3$): δ = 144.8 (C_q, C-9), 132.8 (C_q, C-12), 129.8 (CH, C-10), 127.9 (CH, C-11), 70.6, 70.6, 70.5, 70.5, 70.0, 69.3, 68.6 (CH_2, C-2/3/4/5/6/7/8), 50.6 (CH_2, C-1), 21.6 (CH_3, C-13) ppm. **IR** (ATR): $\tilde{\nu}$ = 2865 (s), 2095 (vs), 1752 (w), 1602 (m), 1452 (s), 1354 (vs), 1293 (s), 1255 (s), 1172 (vs), 1093 (vs), 1013 (s), 917 (s), 813 (vs), 771 (vs), 660 (vs) cm^{-1}.

2,2-Dimethyl-4-oxo-3,8,11,14-tetraoxa-5-azahexadecan-16-yl 4-methyl-benzene-sulfonate (2-36)[4]

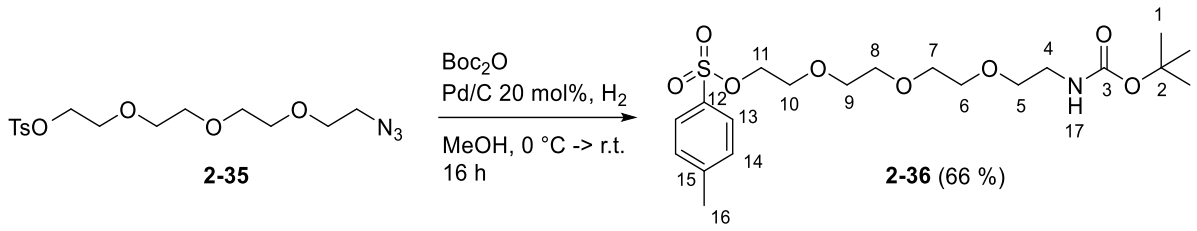

The azide **2-35** (4.55 g, 12.2 mmol, 1.00 eq) was dissolved in dry MeOH (10 mL) and 10 %-Pd/C (0.90 g, 0.20 eq) was added. The black dispersion was cooled to 0 °C and Boc_2O (7.19 g, 32.9 mmol, 2.7 eq.) was added. The reaction mixture was stirred under H_2-atmosphere overnight (16 h). Upon completion, the reaction mixture was filtered and the solvent removed in vacuo. The crude product was purified by column chromatography (silica, cyclohexane/EtOAc, 2:1 -> 1:1, v/v). After removing the solvent, the product was obtained as a slightly yellow oil.

Yield: 3.49 g, (7.79 mmol, 63 %). **^{1}H-NMR** (400 MHz, $CDCl_3$): δ = 7.79-7.74 (m, 2H, H-13), 7.35-7.33 (m, 2H, H-14), 5.00 (br, 1H, H-17), 4.17-4.09 (m, 2H, H-11) 3.70-3.64 (m, 2H, H-10), 3.64-3.53 (m, 8H, H-6-9), 3.53-3.46 (m, 2H, H-5), 3.32-3.19 (m, 2H, H-4), 2.42 (s, 3H, H-16), 1.40 (s, 9H, H-1) ppm. **^{13}C-NMR** (100 MHz, $CDCl_3$): δ = 156.1 (C_q, C-3) 144.9 (C_q, C-12), 133.0 (C_q, C-15), 129.9 (CH, C-13), 120.0 (CH, C-14), 79.2 (C_q, C-2), 70.8, 70.6, 70.6, 70.2, 70.2, 69.3, 68.7 (CH_2, C-5/6/7/8/9/10/11), 40.4 (CH_2, C-4), 28.5 (CH_3, C-1), 21.7 (CH_3, C-16) ppm. **IR** (ATR): $\tilde{\nu}$ = 3345 (br), 2972 (m), 2926 (m), 2865 (s), 1700 (s), 1598 (w), 1520 (s) 1452

(s), 1392 (s), 1366 (vs), 1281 (s), 1242 (s), 1178 (vs), 1096 (vs), 1011 (vs), 913 (vs), 865 (w), 813 (s), 767 (s), 660 (vs) cm^{-1}

2-(2-(2-(2-Azidoethoxy)ethoxy)ethoxy)ethan-1-amine (2-37)[3,6]

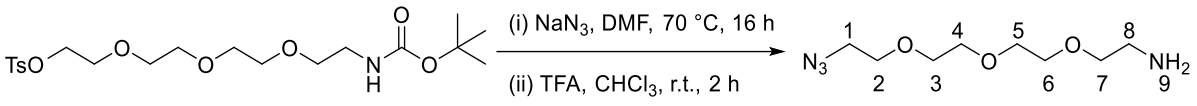

2-36 **2-37** (66 %)

The tosylate **2-36** (2.00 g, 4.46 mmol, 1.00 eq) was dissolved in dry DMF (12 mL) and NaN_3 (1.45 g, 22.3 mmol, 5.00 eq) was added. The reaction mixture was stirred at 70 °C overnight (16 h). Upon completion, the solvent was removed in vacuo. The oily mixture was dissolved in water (50 mL) and extracted three times with DCM (50 mL). The combined organic layers were dried with $MgSO_4$. After removing the solvent, the product was obtained as a slightly yellow oil. The crude product was filtered through a silica column with cyclohexane/EtOAc 2:1 and the product was collected in the filtrate and concentrated in vacuo. After dissolving the intermediate (0.87 g, 2.73 mmol. 1.00 eq) in $CHCl_3$ (67 mL) and adding TFA (33.7 mL, 437 mmol, 160 eq), the reaction mixture was stirred for 2 h at room temperature. After 2 h, TFA and $CHCl_3$ were removed in vacuo and dissolved again in $CHCl_3$. The organic layer was washed with sat. $NaHCO_3$ and NaCl solution and dried with $MgSO_4$. The solvent was removed in vacuo and the product was obtained as slightly yellowish oil and used without further purification.

Yield: 0,39 g (1,80 mmol, 66 %). **^{1}H-NMR** (400 MHz, $CDCl_3$): δ = 3.72-3.57 (m, 10H, H-2-6), 3.51 (t, 2H, H-7), 3.39 (t, 2H, H-1), 2.86 (t, 1H, H-8), 1.58 (br. 2H, H-9) ppm. **^{13}C-NMR** (100 MHz, $CDCl_3$): δ = 73.3 (CH_2, C-7), 70.8, 70.8, 70.7, 70.4, 70.2 (CH_2, C-2/3/4/5/6), 50.8 (CH_2, C-1), 41.8 (CH_2, C-8) ppm. **IR** (ATR): $\tilde{\nu}$ = 3367 (br), 2865 (s), 2097 (s), 1731 (w), 1662 (s), 1561 (m), 1458 (s), 1345 (s), 1290 (s), 1251 (s), 1205 (w), 1101 (vs), 1047 (s), 989 (w), 938 (s), 878 (w), 848 (m), 823 (s) cm^{-1}.

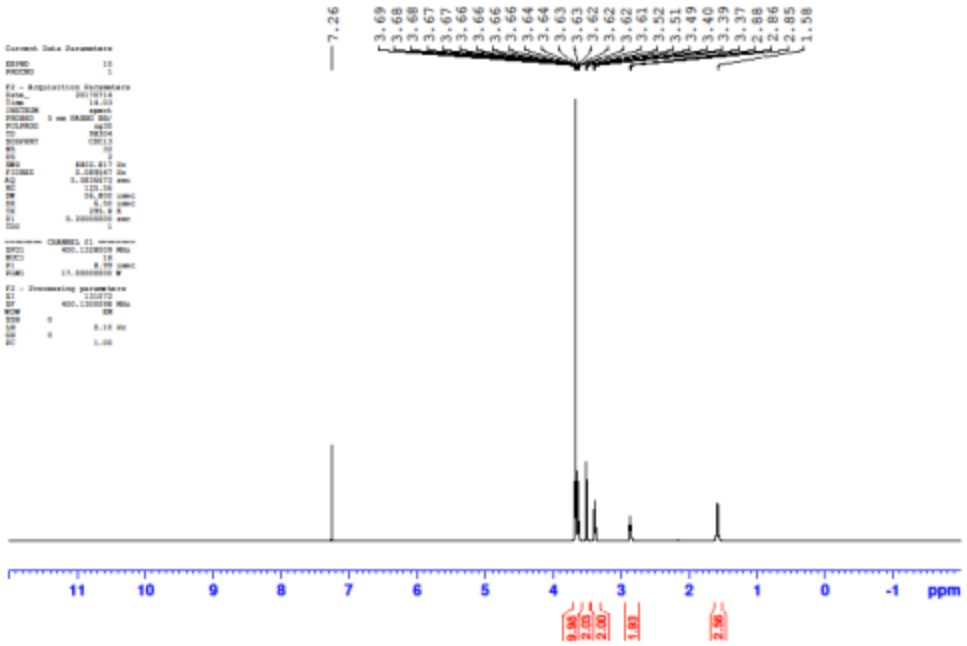

Figure S2-30: ^{1}H-NMR spectrum of 2-(2-(2-(2-azidoethoxy)ethoxy)ethoxy)ethan-1-amine (**2-37**).

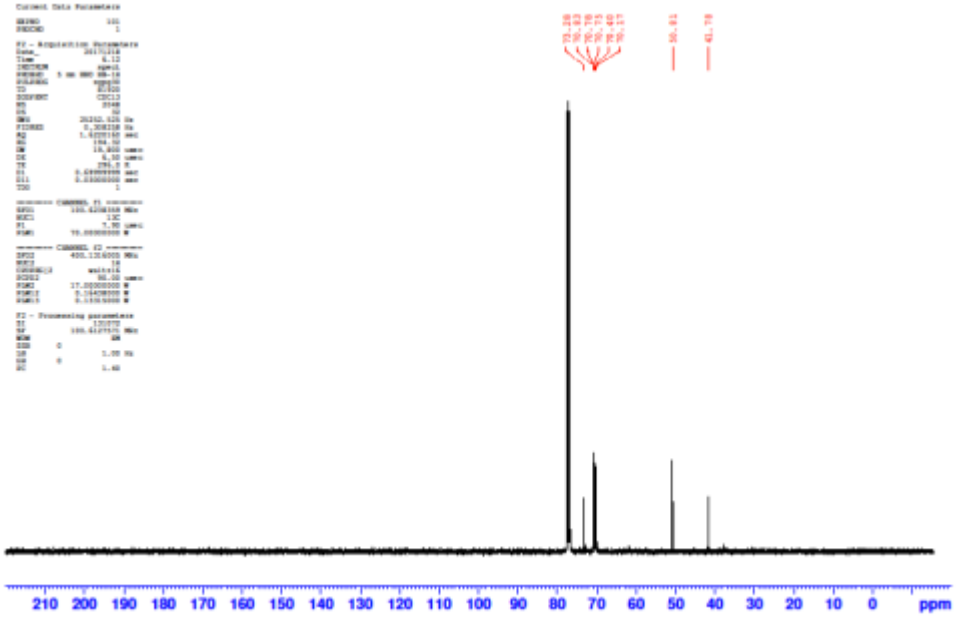

Figure S2-31: ^{13}C-NMR spectrum of 2-(2-(2-(2-azidoethoxy)ethoxy)ethoxy)ethan-1-amine (**2-37**).

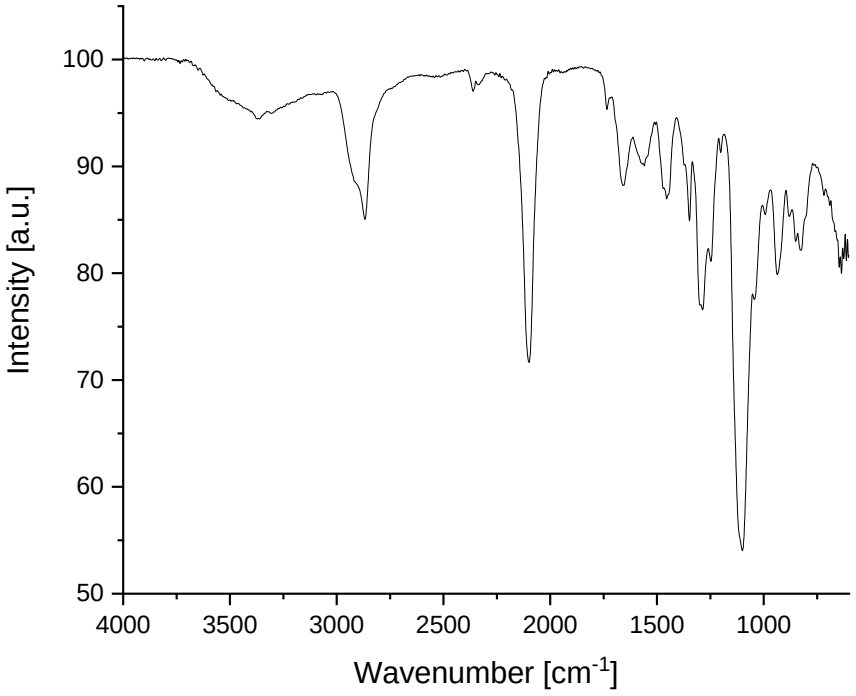

Figure S2-32: FT-IR ATR spectrum of 2-(2-(2-(2-azidoethoxy)ethoxy)ethoxy)ethan-1-amine (**2-37**).

tert-Butyl (15-azido-14,14-bis(azidomethyl)-3,6,9,12-tetraoxapentadecyl)-carbamate (2-38)[4]

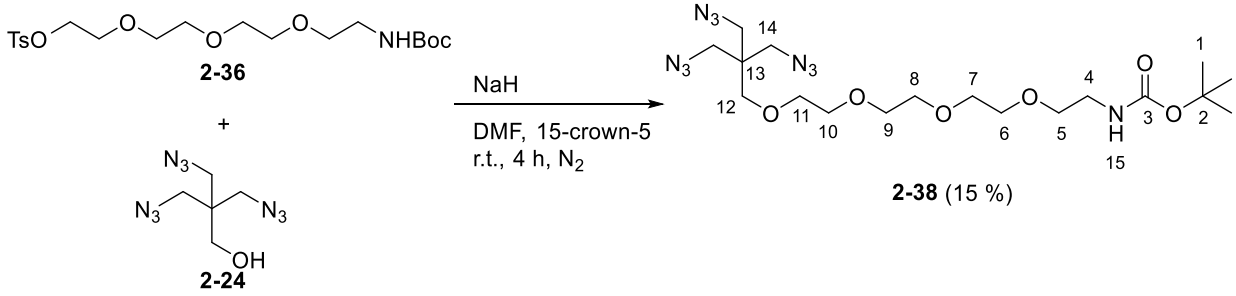

The azide **2-24** (500 mg, 2.37 mmol, 1.00 eq) was dissolved in dry DMF (2 mL) and NaH (60 % in mineral oil, 189 mg, 4.74 mmol, 2.00 eq) and 15-crown-5 (5.00 µL, 24.0 µmol, 0.01 eq) was added. The suspension was stirred for five minutes at room temperature followed by the addition of a solution of tosylate **2-36** (1.91 g, 4.26 mmol, 1.80 eq) in dry DMF (3 mL). The mixture was stirred for 4.5 hours at room temperature. The reaction was quenched by adding

MeOH (5 mL). After removing the solvent in vacuo, the residue was dissolved in deionized water (5 mL) and extracted with EtOAc (2x 4 mL) and DCM (2x 4 mL). The combined organic layers were washed with saturated NaCl solution (15 mL) and dried with $MgSO_4$. The solvent was removed in vacuo and the crude product purified by column chromatography (silica, cyclohexane/EtOAc, 4:1 -> 2:1, v/v). After removing the solvent, the product was obtained as a slightly yellow oil.

Yield: 177 mg, (0.36 mmol, 15 %). **^{1}H-NMR** (400 MHz, $CDCl_3$): δ = 5.02 (br, 1H, H-15), 3.68-3.57 (m, 12H, H-6-11), 3.57-3.47 (m, 2H, H-5), 3.38-3.23 (m, 10H, H-4+12+14) 1.42 (s, 9H, H-1) ppm. **^{13}C-NMR** (100 MHz, $CDCl_3$): δ = 156.0 (C_q, C-3), 79.2 (C_q, C-2), 70.9, 70.7, 70.7, 70.6, 70.4, 70.3, 70.3, 69.6 (CH_2, C-5/6/7/8/9/10/11/12), 51.6 (CH_2, C-14) 44.8 (C_q, C-13), 40.4 (CH_2, C-4), 28.5 (CH_3, C-1), ppm. **IR** (ATR): $\tilde{\nu}$ = 3358 (br), 2977 (m), 2930 (m), 2874 (s), 2095 (vs), 1705 (vs), 1503 (s), 1452 (s), 1388 (w), 1358 (s), 1281 (vs), 1242 (vs), 1110 (vs), 1041 (m), 1003 (w), 938 (m), 895 (w), 874 (m), 779 (w), 728 (w), 642 (m), 608 (m) cm^{-1}.

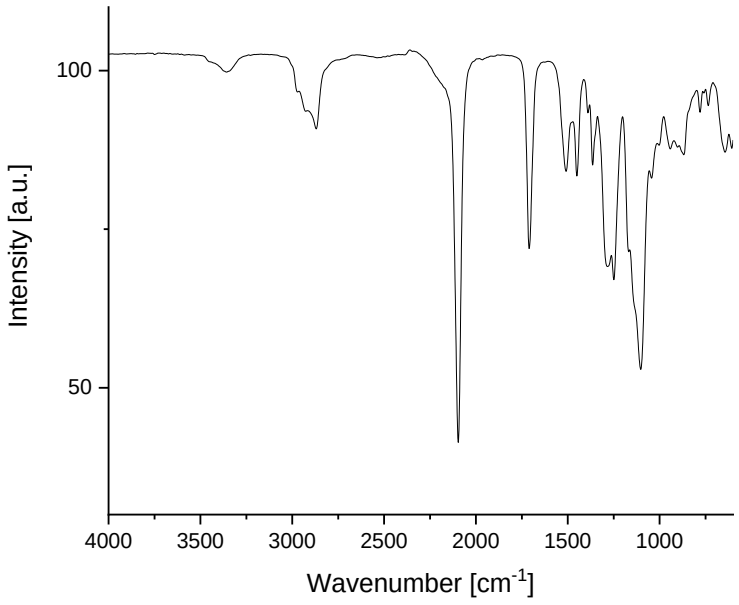

Figure S2-33: FT-IR ATR of *tert*-butyl (15-azido-14,14-bis(azidomethyl)-3,6,9,12-tetraoxapentadecyl)-carbamate (**2-38**).

15-Azido-14,14-bis(azidomethyl)-3,6,9,12-tetraoxapentadecan-1-amine (2-13)[4]

2-38 **2-13** (67 %)

The protected amine **2-38** (177 mg, 0.36 mmol, 1.00 eq) was dissolved in $CHCl_3$ (3 mL) and TFA (4.48 mL, 58.2 mmol, 160 eq) was added. The reaction mixture was stirred for 4 h at room temperature and the solvent was removed in vacuo. The residue was dissolved in $CHCl_3$ (5 mL) and washed with saturated $NaHCO_3$ and NaCl solution. The combined organic layers were dried with $MgSO_4$, and the solvent removed in vacuo. The crude product was obtained as slightly yellow oil and used without further purification.

Yield: 90 mg, (0.24 mmol, 67 %). **^{1}H-NMR** (400 MHz, $CDCl_3$): δ = 3.68-3.57 (m, 14H, H-2-9), 3.35-3.31 (m, 8H, H-10+12), 3.05-2.96 (m, 2H, H-2) ppm. **^{13}C-NMR** (100 MHz, $CDCl_3$): δ = 71.0, 70.7, 70.6, 70.6, 70.5, 70.3, 70.3, 69.7 (CH_2, C-3/4/5/6/7/8/9/10), 51.6 (CH_2, C-12), 44.8 (C_q, C-11), 41.0 (CH_2, C-2) ppm. **IR** (ATR): $\tilde{\nu}$ = 3371 (br), 2865 (s), 2099 (vs), 1675 (vs), 1444 (vs), 1383 (m), 1352 (m), 1285 (s), 1255 (s), 1200 (s), 1093 (vs), 998 (w), 934 (m), 882 (m), 823 (m), 793 (m), 715 (m), 655 (m) cm^{-1}.

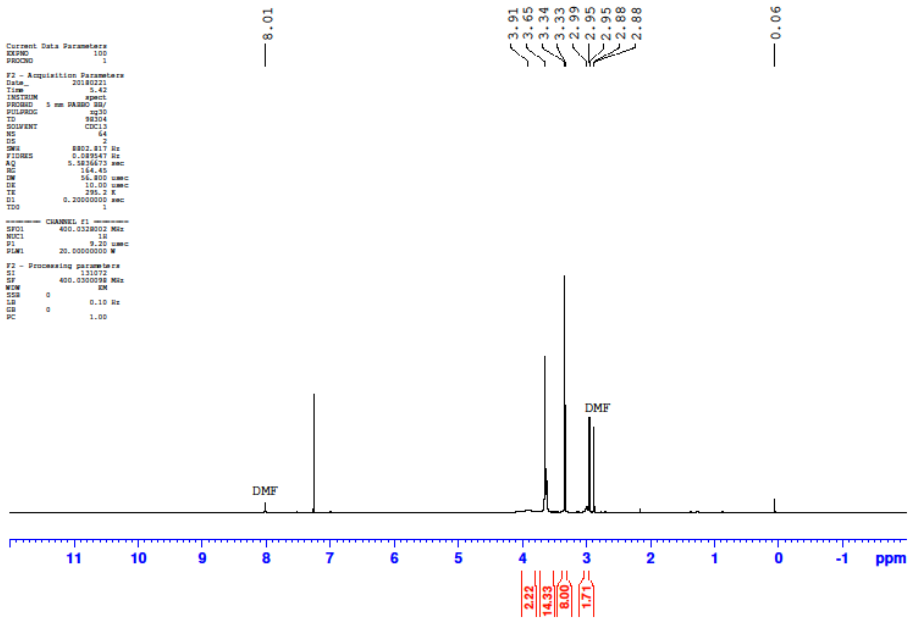

Figure S2-34: ^{1}H-NMR spectrum of 15-azido-14,14-bis(azidomethyl)-3,6,9,12-tetraoxapentadecan-1-amine (**2-13**).

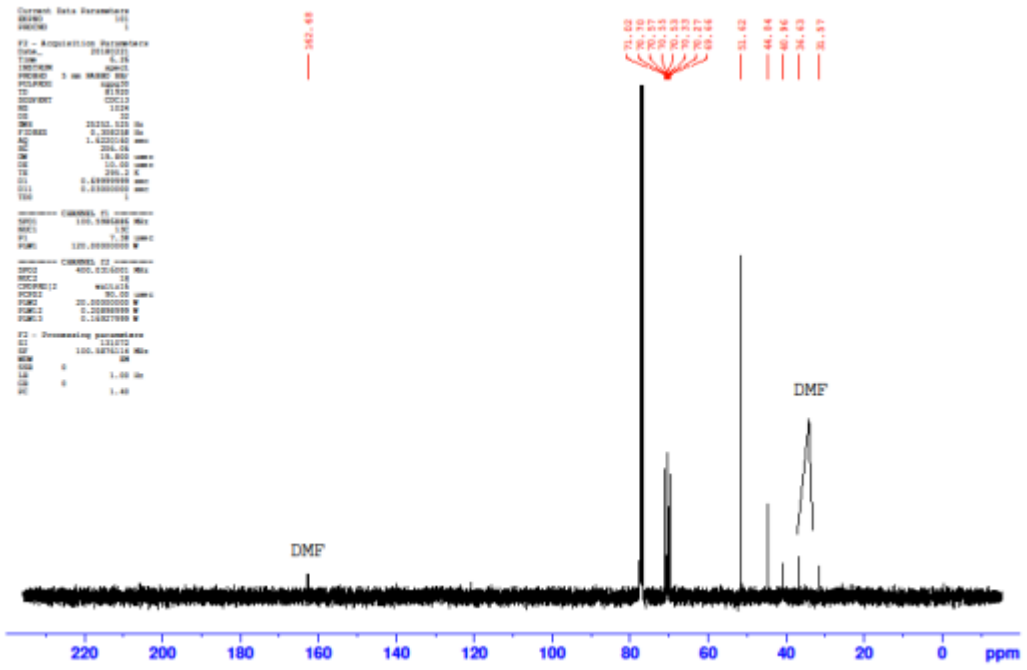

Figure S2-35: ^{13}C-NMR spectrum of 15-azido-14,14-bis(azidomethyl)-3,6,9,12-tetraoxapentadecan-1-amine (**2-13**).

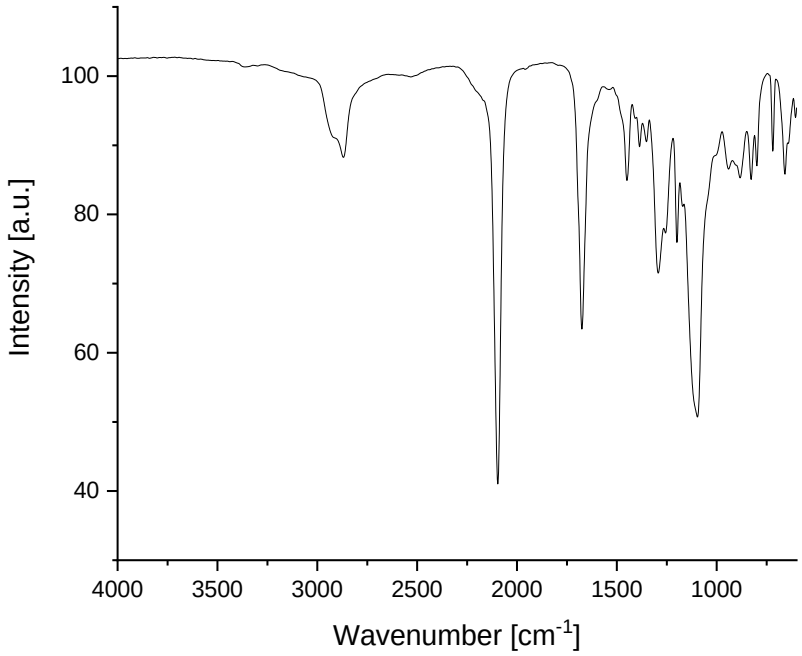

Figure S2-36: FT-IR ATR spectrum of 15-azido-14,14-bis(azidomethyl)-3,6,9,12-tetraoxapentadecan-1-amine (**2-13**).

7.1.2 Functionalization of milled DND and synthesis of ND conjugates

7.1.2.1 Milling of detonation nanodiamond

Acid-purified detonation nanodiamond (Gansu Lingyun Corp, see main article for details) was milled according to the procedure described in ref. 35 in the main manuscript. In brief, 25 g of grey, unmilled DND powder was dispersed in 500 mL DD-water using an ultrasonic bath. Then, the turbid dispersion was milled in an attrition mill at 4000 rpm for 2 hours. The final concentration of the black, clear dispersion (450 mL) was 51.3 mg mL^{-1}.

Zeta potential: 44 mV (DD-water, intrinsic pH = 5.5), **Surface loading** (TGA): no significant surface loading = Δm (150-450 °C) = <1 %; **Particle size** (DLS, DD-water): 10 % ≤ 2.3 nm, 50 % ≤ 3.3 nm, 90 % ≤ 5.1 nm, **FT-IR** (KBr**):** $\tilde{\nu}$ = 3432 (br), 2969 (w), 2923 (w), 2888 (w), 1712 (m), 1629 (vs), 1370 (vw), 1365 (w), 1320 (m), 1293 (m), 1253 (m), 1128 (s), 1090 (s), 946 (m), 810 (w), 774 (w), 684 (w) cm^{-1}.

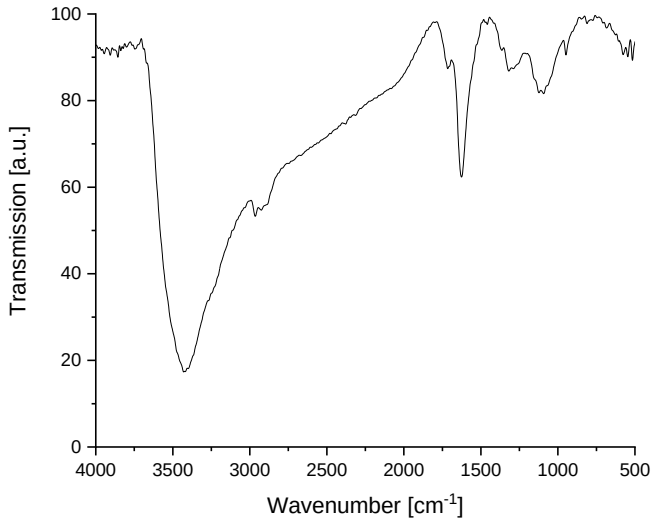

Figure S2-37: FT-IR spectrum (KBr pellet) of ND **2-1**.

7.1.2.2 Functionalization of milled detonation nanodiamond

ND-phenethyl azide (2-2)

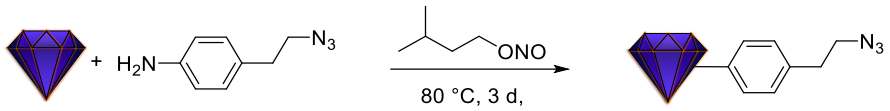

Milled ND (1, 95.0 mg) was dispersed in 5 mL MQ-water and dispersed. The reaction was heated to 80 °C, then 4-(2-azidoethyl)aniline (0.12 g, 0.74 mmol) and isopentyl nitrite (0.24 g, 0.27 mL, 2 mmol) were added. The reaction mixture was stirred at 80 °C for 3 days and washed in Eppendorf tubes in totally 12 mL volume with MQ-water (2x, 15k RPM), acetone (5x, 10k RPM) and MQ-water (2x, 15k RPM). Subsequent drying at 80 °C in vacuum yielded 88 mg of ND 2 as a grey powder. **Zeta potential**: 24 mV (DD-water, intrinsic pH = 4.5), **Surface loading** (TGA): 63 mmol g^{-1} = Δm (150-450 °C) = 9.2 %; **Particle size** (DLS, DD-water): 10 % ≤ 53 nm, 50 % ≤ 76 nm, 90 % ≤ 121 nm, **FT-IR** (DRIFTS**):** $\tilde{\nu}$ = 3381 (br), 2952 (m), 2872 (m), 2105 (vs,), 1712 (m), 1686 (s), 1540 (m), 1351 (m), 1294 (m), 1258 (m), 1130 (w), 1040 (vw), 959 (vw), 901 (w), 848 (m), 822 (m), 791 (w), 756 (vw) cm^{-1}.

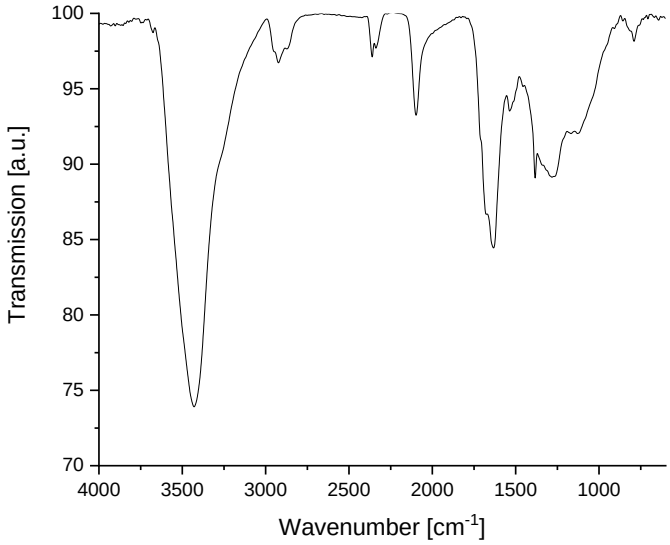

Figure S2-38: FT-IR spectrum (KBr pellet) of ND **2-2**.

ND-benzoic acid (2-3)

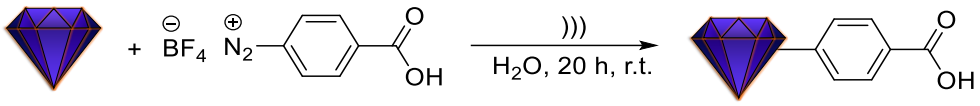

A dispersion of milled ND (**2-1**, 1.00 g) was diluted with 150 mL MQ-H_2O and mixed with 4-carboxybenzenediazonium tetrafluoroborate (10.0 g, 42.4 mmol). The reaction mixture was then dispersed using an ultrasonic horn (output 80 W) for 20 h. After the reaction the dispersion was washed with 100 mL of each acetone (9x), MQ-H_2O (1x), acetone/MQ-H_2O (2:1, 3x), MQ-H_2O (3x) at 6.000 RPM. After drying at 80 °C in vacuum, 890 mg of ND 3 were obtained as a dark-grey powder. **Zeta potential**: -27.5 mV (DD-water, intrinsic pH=5.1), **Surface loading** (TGA): 47 mmol/g = Δm (150-450 °C) = 5.7 %; **Particle size** (DLS, DD-water): 10 % ≤ 60 nm, 50 % ≤ 82 nm, 90 % ≤ 141 nm, **FT-IR** (DRIFTS**):** $\tilde{\nu}$ = 3381 (br), 2980 (s), 2887 (m), 1716 (m,), 1462 (m), 1381 (m), 1252 (m), 1153 (m), 1072 (m), 813 (w) cm^{-1}.

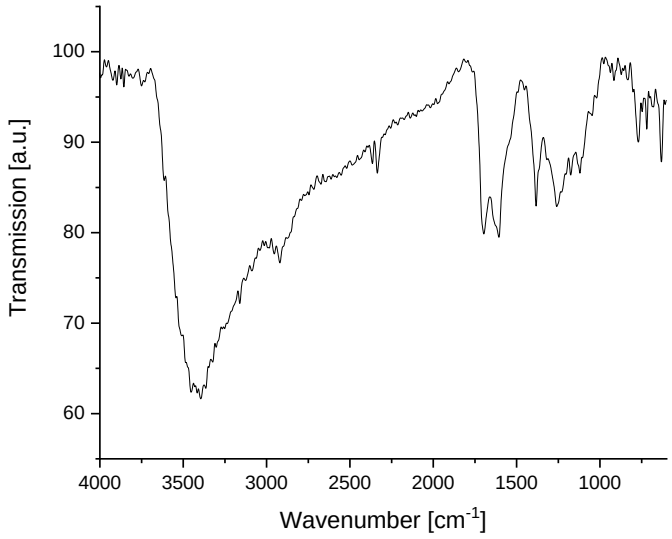

Figure S2-39: FT-IR spectrum (KBr pellet) of ND **2-3**.

General procedure for the preparation of ND 2-4, 2-5, 2-7, 2-41 by thioester formation

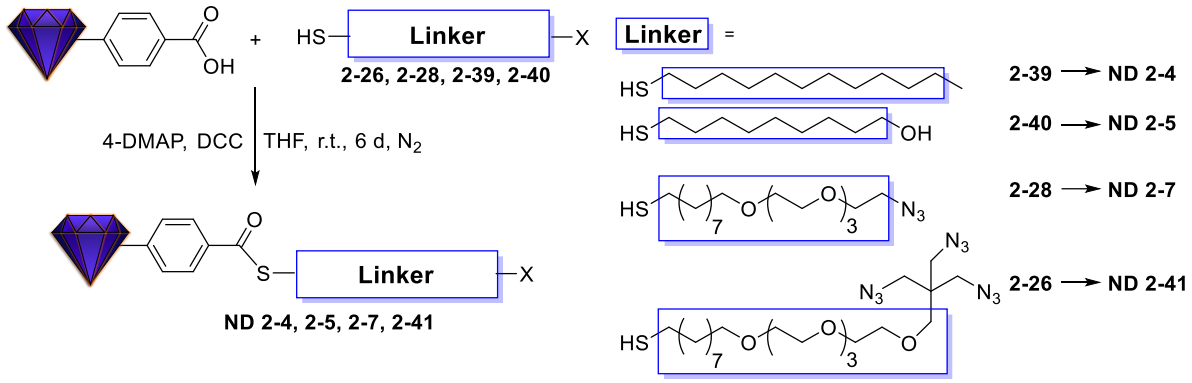

Figure S40: Schematic representation of thioester formation of ND **2-4**, **2-5**, **2-7** and **2-41**.

The general procedure is presented in the main article.

ND 2-41: Zeta potential: 14 mV (DD-water, intrinsic pH=5.5). **Particle size:** (DLS, DD-water): 10 % ≤ 80 nm, 50 % ≤ 119 nm, 90 % ≤ 196 nm. **Surface loading (TGA):** 10.6 % (150-450 °C). **FT-IR (KBr):** 3418 (br), 2934 (vs), 2853 (s), 2103 (m), 1705 (vs), 1639 (vs), 1606 (vs), 1538 (s), 1452 (m), 1366 (vs), 1229 (vs), 1169 (m), 1148 (s), 1110 (s), 866 (m), 775 (m) cm^{-1}.

The analytical data of ND **2-4**, **2-5** and **2-7** are presented in the main text.

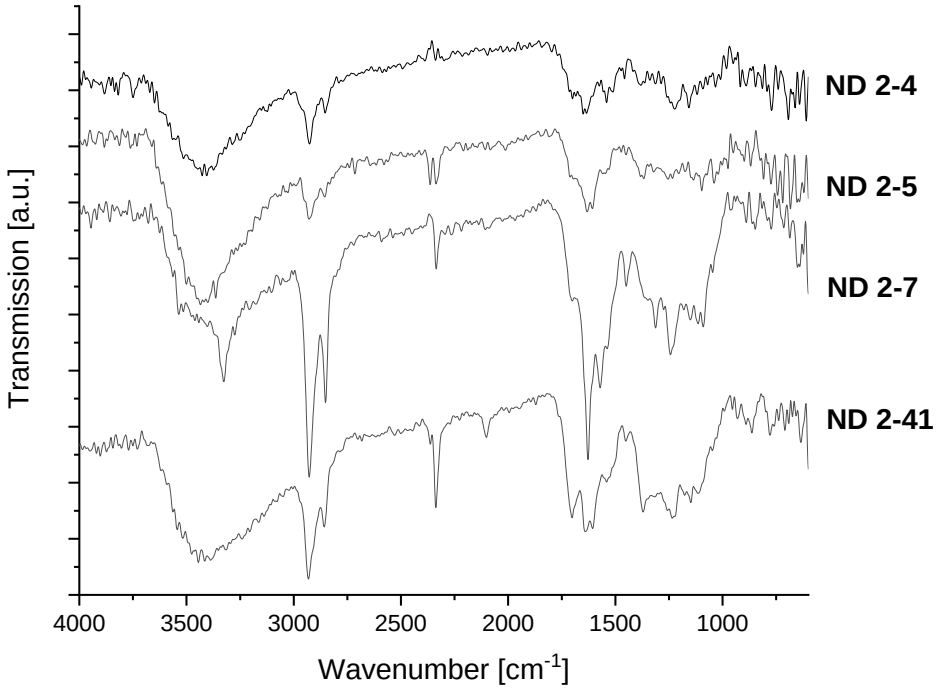

Figure S2-41: FT-IR spectra (KBr pellet) of ND **2-4, 2-5, 2-7, 2-41**.

General procedure for the preparation of ND 2-6, 2-42 and 2-43 by amide formation

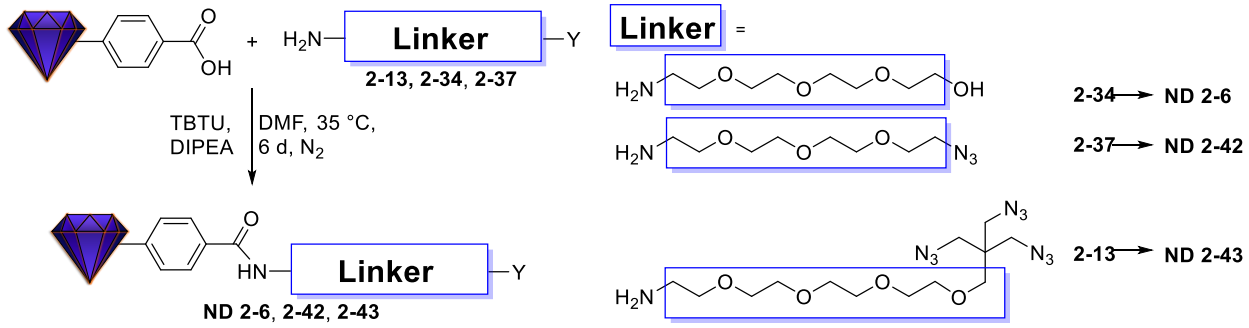

Figure S2-42: Schematic representation of amid formation of ND **2-6**, **2-42** and **2-43**.

The general procedure is presented in the main article together with the analytical data of ND **2-6**.

ND 2-42: Zeta potential: 31 mV (DD-water, intrinsic pH=6.0). **Particle size:** (DLS, DD-water): 10 % ≤ 51 nm, 50 % ≤ 84 nm, 90 % ≤ 174 nm. **Surface loading (TGA):** 9.8 % (150-450 °C). **FT-IR (KBr):** 3465 (br), 2923 (s), 2096 (s), 1711 (m), 1641 (vs), 1534 (s), 1439 (w), 1358 (m), 1282 (s), 1237 (m), 1117 (vs), 1029 (s) cm^{-1}.

ND 43: Zeta potential: 24 mV (DD-water, intrinsic pH=6.0). **Particle size:** (DLS, DD-water): 10 % ≤ 80 nm, 50 % ≤ 133 nm, 90 % ≤ 246 nm. **Surface loading (TGA):** 11.2 % (150-450 °C). **FT-IR (KBr):** 3383 (br), 2969 (vs), 2923 (s), 2885 (s), 2108 (vs), 1704 (w), 1641 (s), 1547 (w), 1452 (w), 1372 (m), 1300 (s), 1124 (vs), 1093 (vs), 1042 (s), 954 (s) cm^{-1}

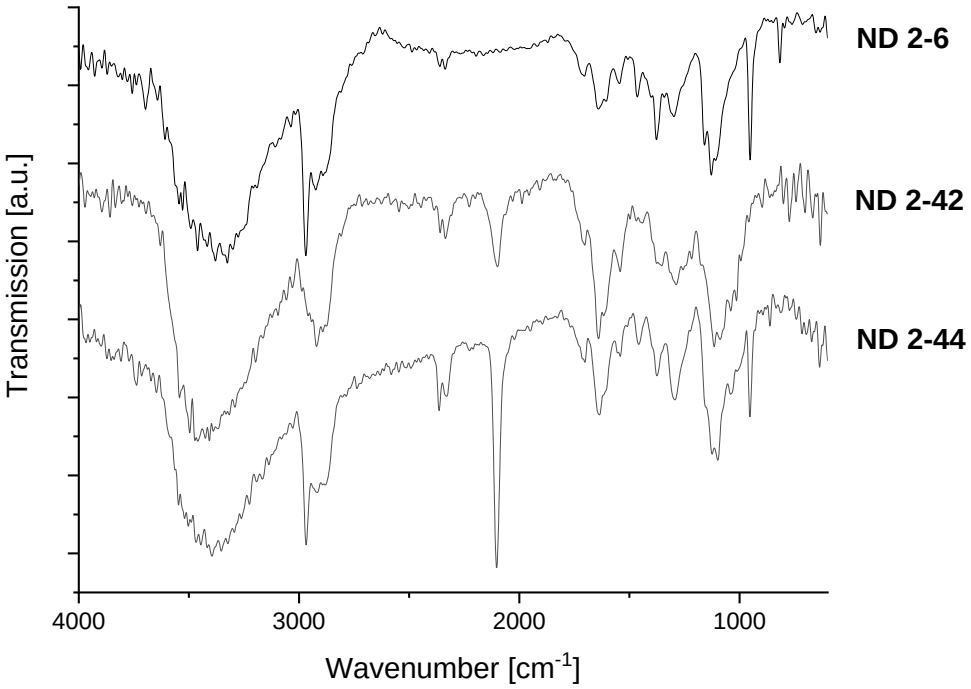

Figure S2-43: FT-IR spectra (KBr pellet) of ND **2-6, 2-42, 2-43**.

General procedure for the preparation of ND conjugates 2-8, 2-9, 2-10, 2-11, 2-12

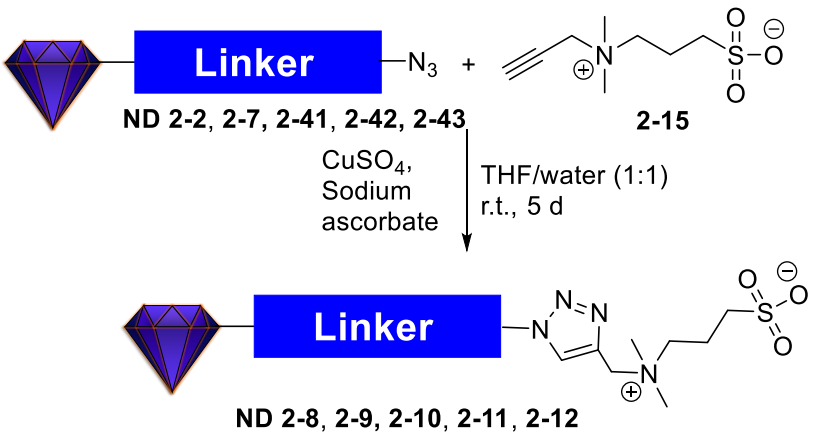

Figure S2-44: Schematic representation of a click reaction to ND **2-8**, **2-9**, **2-10**, **2-11** and **2-12**.

The general procedure for the preparation of ND **8-12** is presented in the main article together with their analytical data.

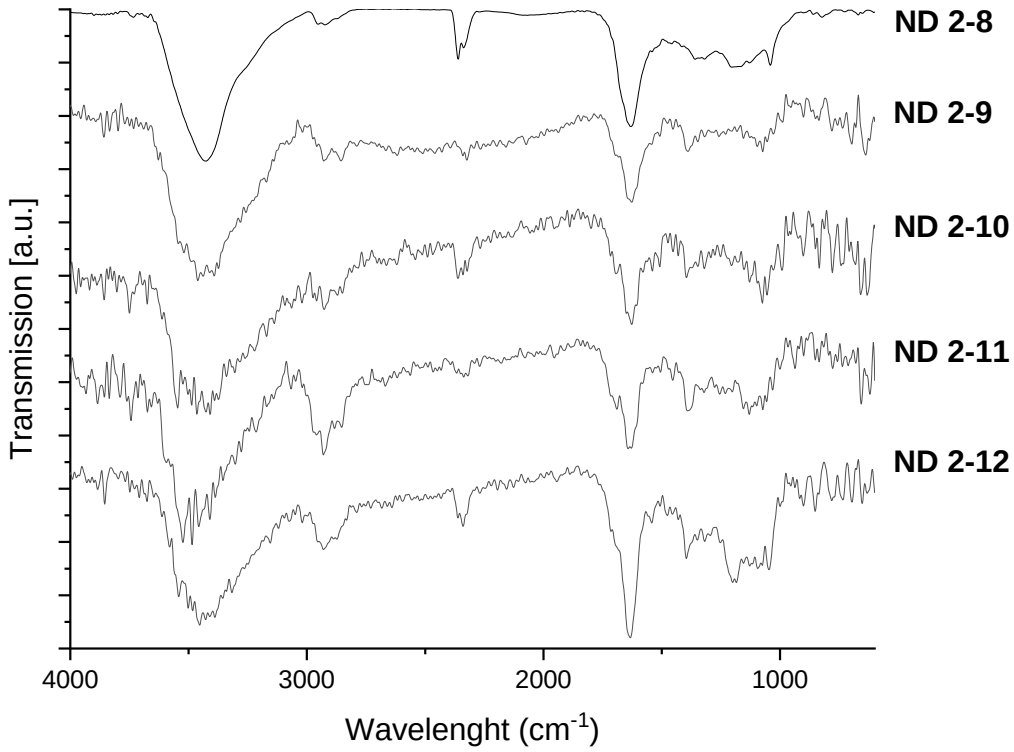

Figure S2-45: FT-IR spectra (KBr pellet) of ND **2-8, 2-9, 2-10, 2-11** and **2-12**.

7.1.3 Thermogravimetric analysis of ND 2-2–2-11 with and without FBS incubation

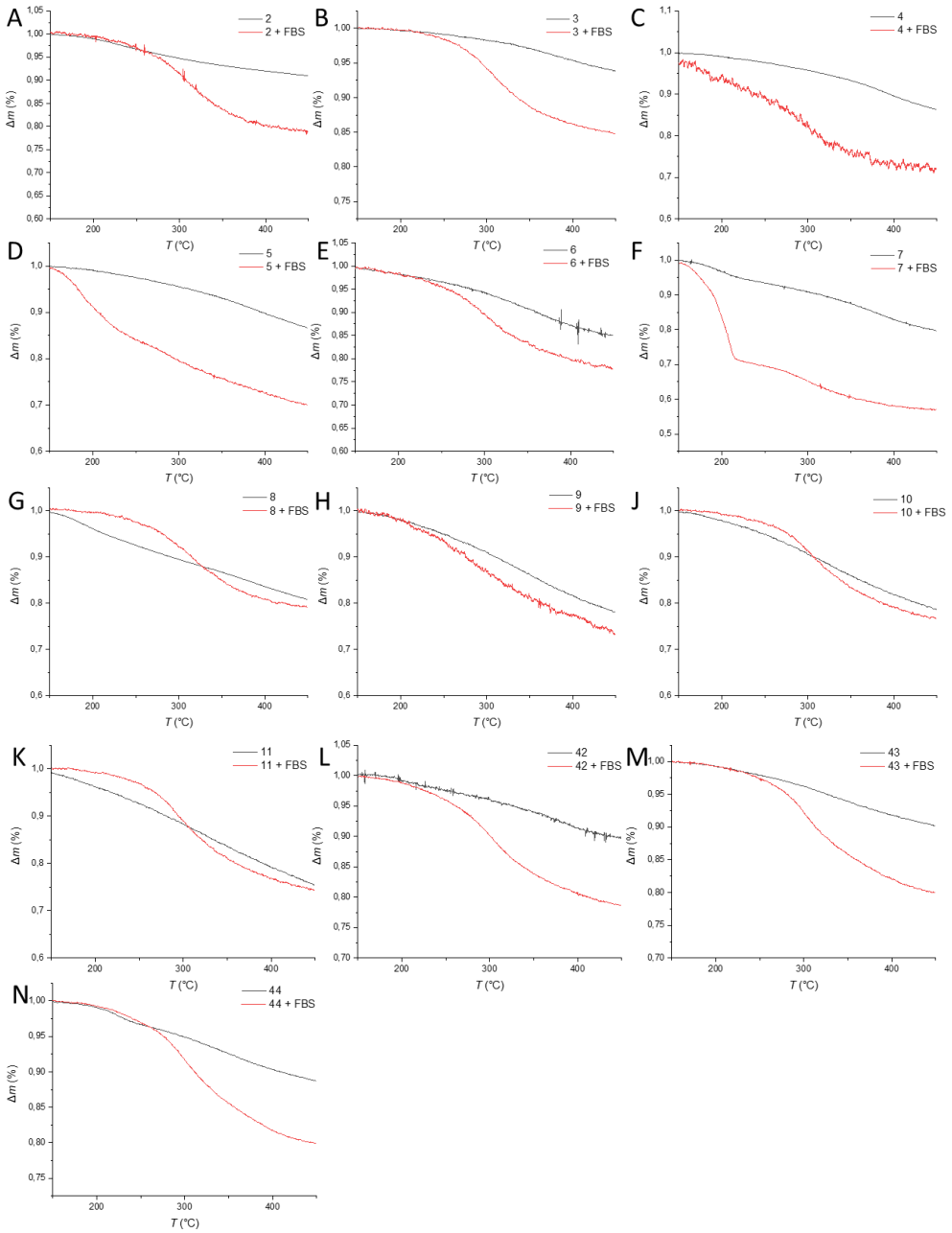

Figure S2-46: Thermogravimetric analysis curves of ND **2-2**–**2-11** (A-K) and ND **2-41**–**2-43** (L-N).

(TGA data for ND **2-1** and ND **2-12** with and without FBS are shown in the main manuscript.)

7.1.4 Colloidal stability of ND 2-1–2-12 in different media

7.1.4.1 Colloidal stability of ND 2-1–2-12 in FBS/water 1:5 (v/v) (red 0 d, green 2 d, blue 3 d)

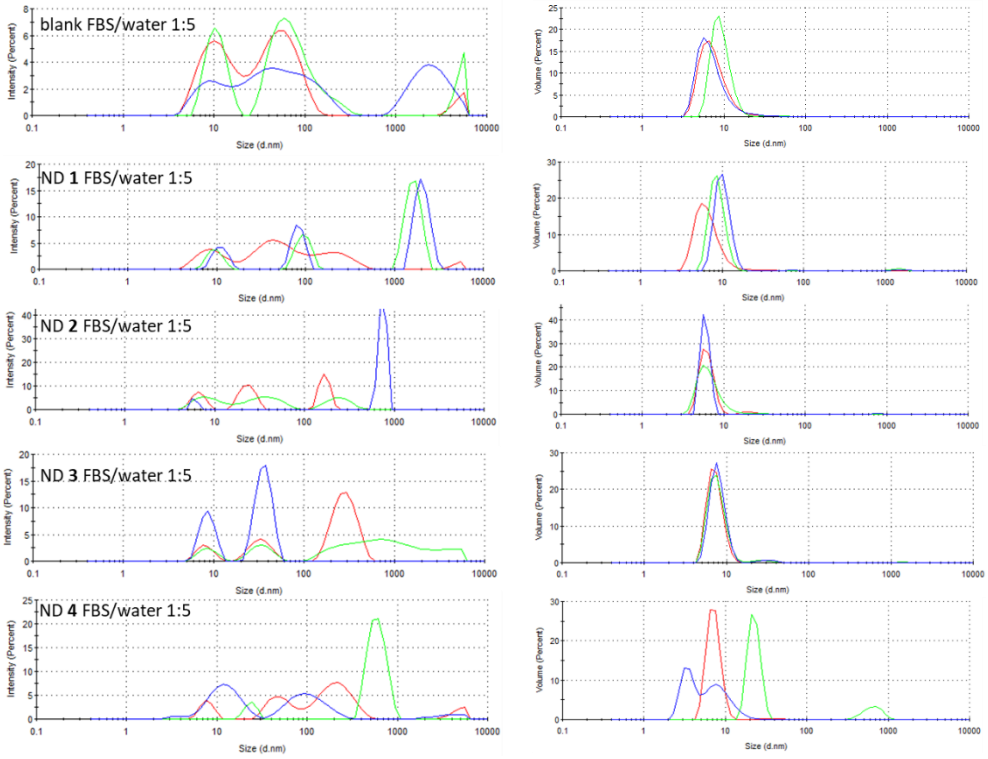

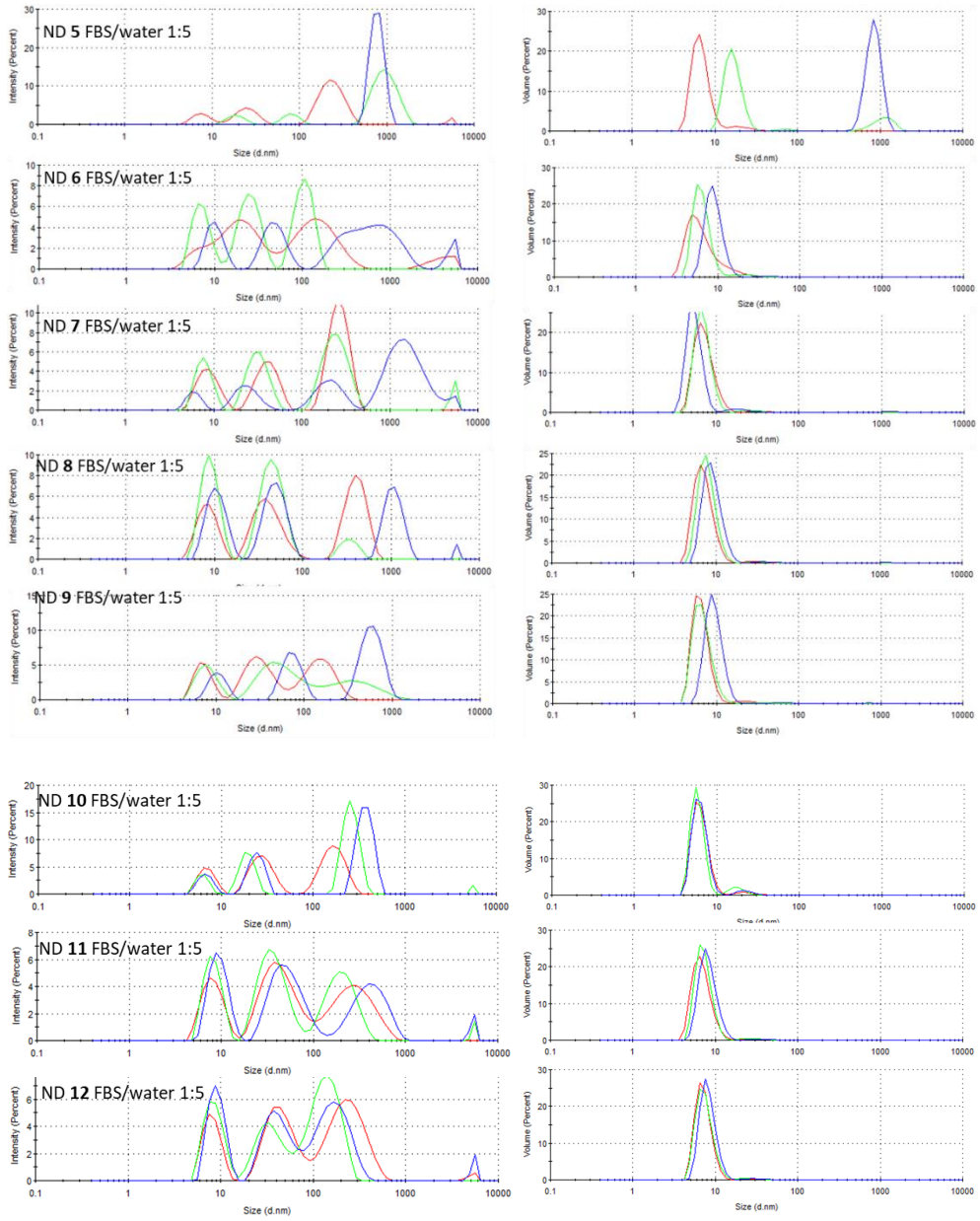

Figure S2-47: Dynamic light scattering spectra of ND **2-1–2-12** in FBS/water 1:5 (v/v) in intensity (left) and volume (right, color code red 0 day, green 2 days and blue 3 days.

7.1.4.2 Colloidal stability of ND 2-1–2-12 in DMEM/water 1:9 + 1% FBS (v/v)

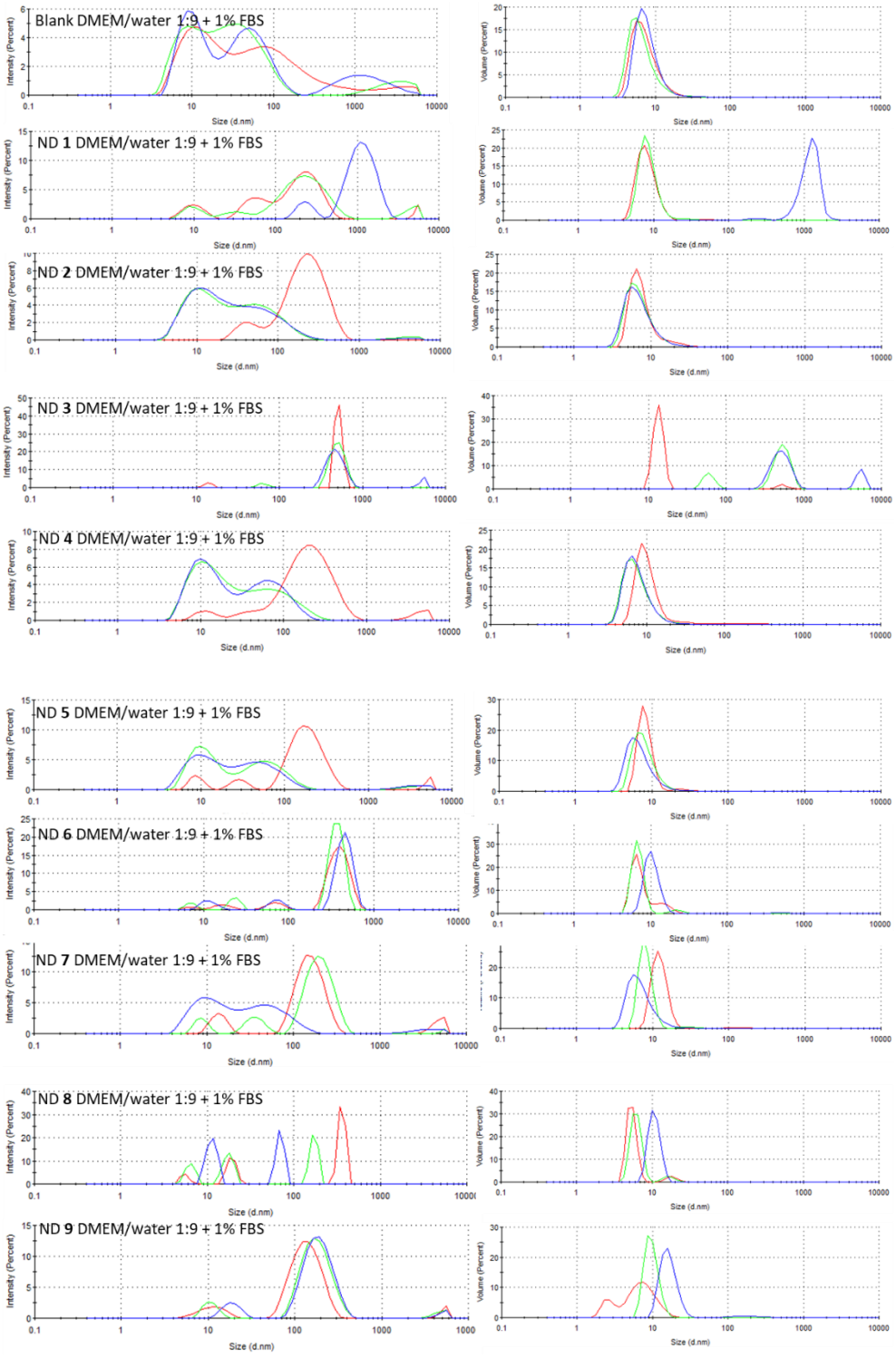

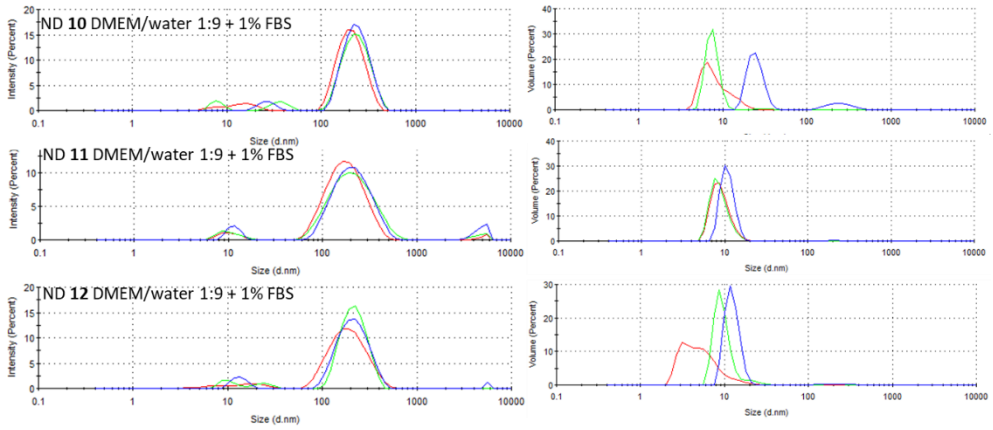

Figure S2-48: Dynamic light scattering spectra of ND **2-1**–**2-12** in DMEM/water 1:9 + 1% FBS (v/v) in intensity (left) and volume (right, color code red 0 day, green 2 days and blue 3 days.

7.1.4.3 Colloidal Stability of ND 2-1–2-12 in DMEM/FBS 9:1 (v/v)

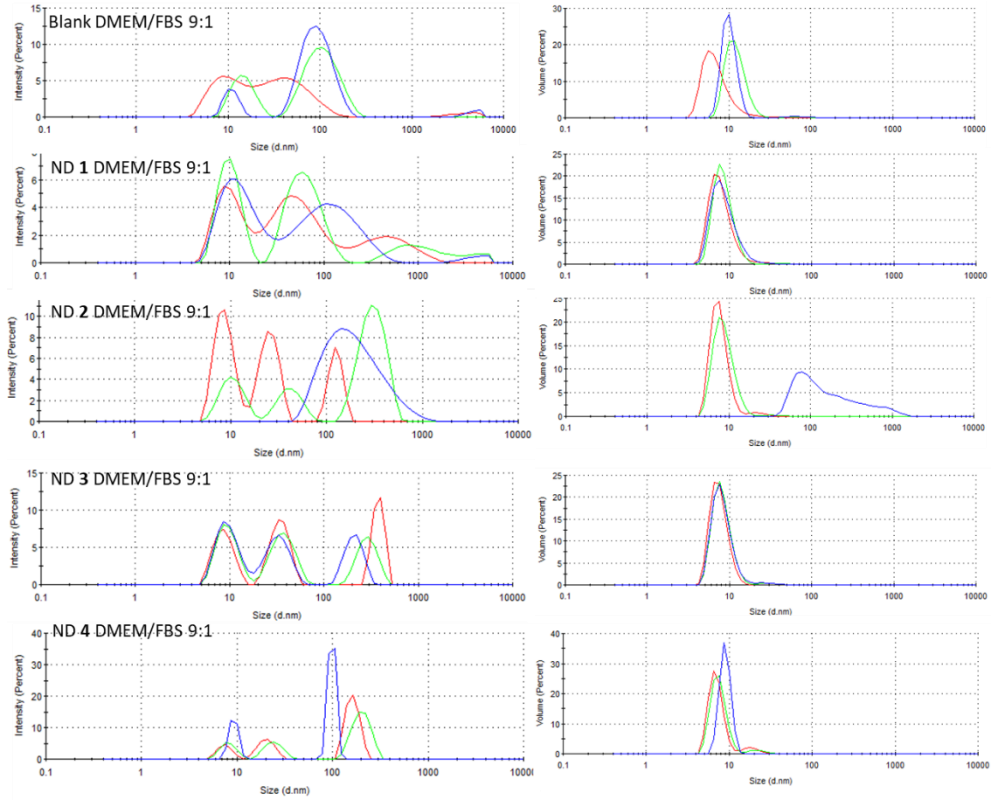

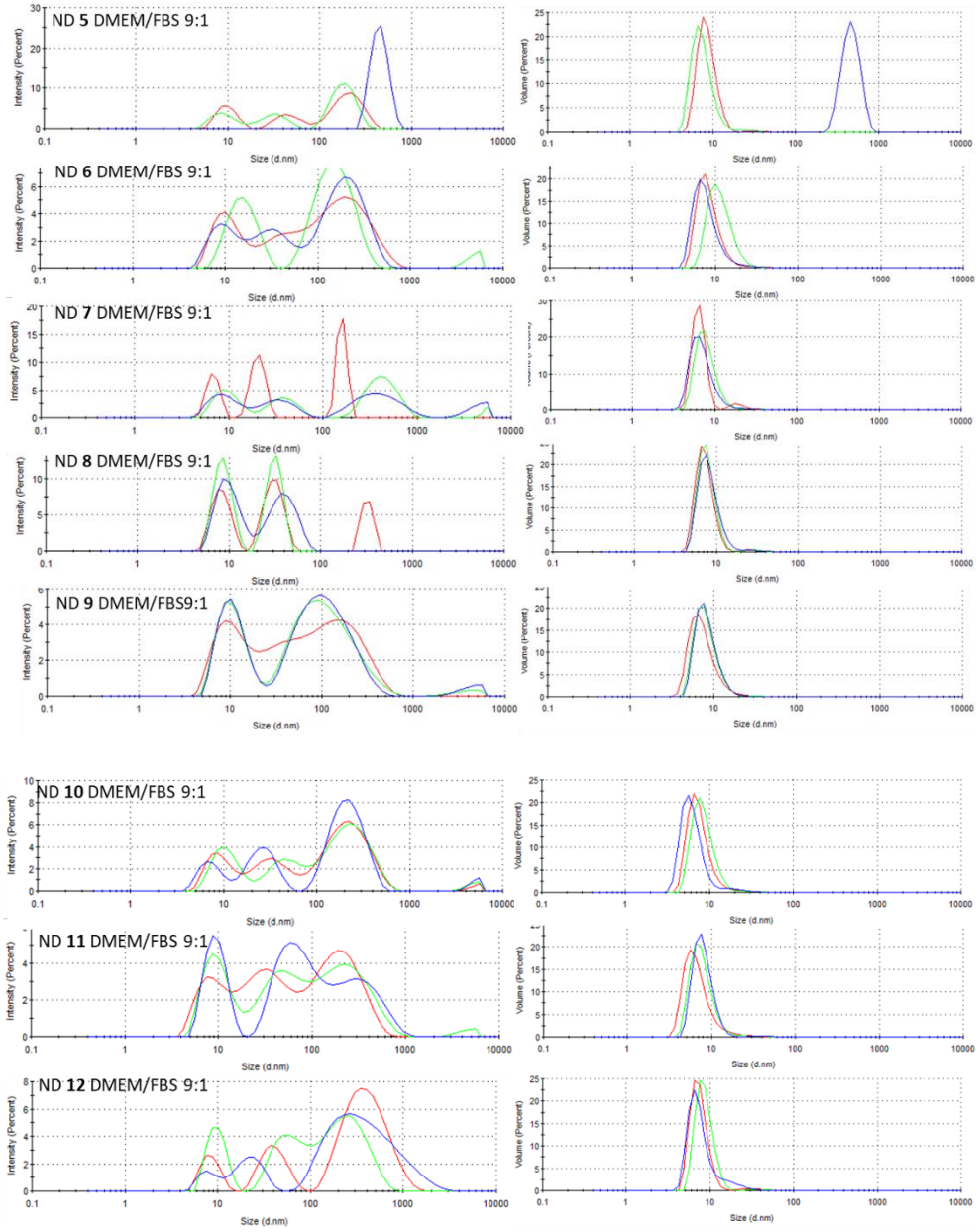

Figure S49: Dynamic light scattering spectra of ND **1-12** in DMEM/FBS 9:1 (v/v) in intensity (left) and volume (right, color code red 0 day, green 2 days and blue 3 days.

7.1.5 Particle size distribution of ND 2-1–2-12 and pristine DND in aqueous solution by dynamic light scattering

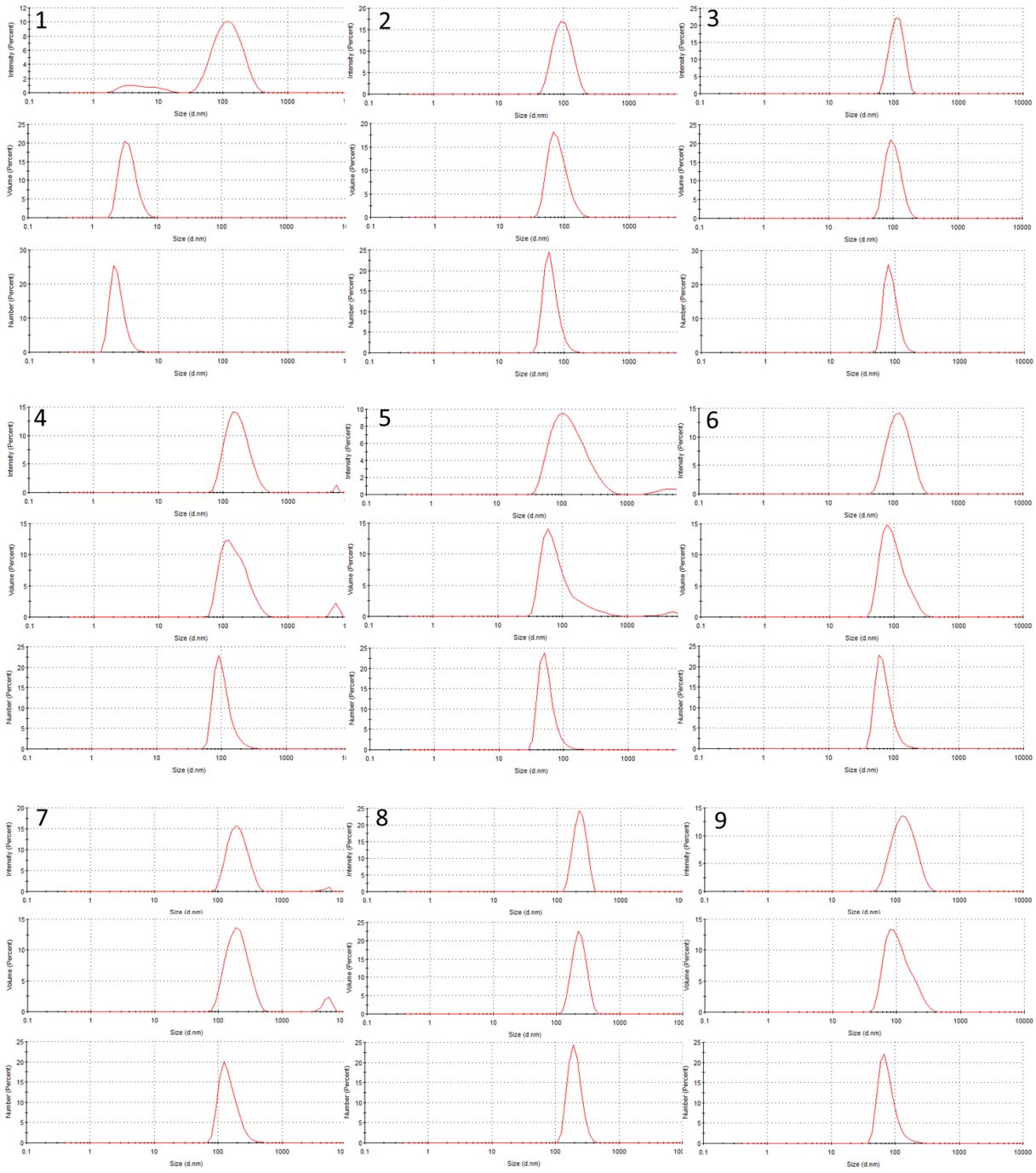

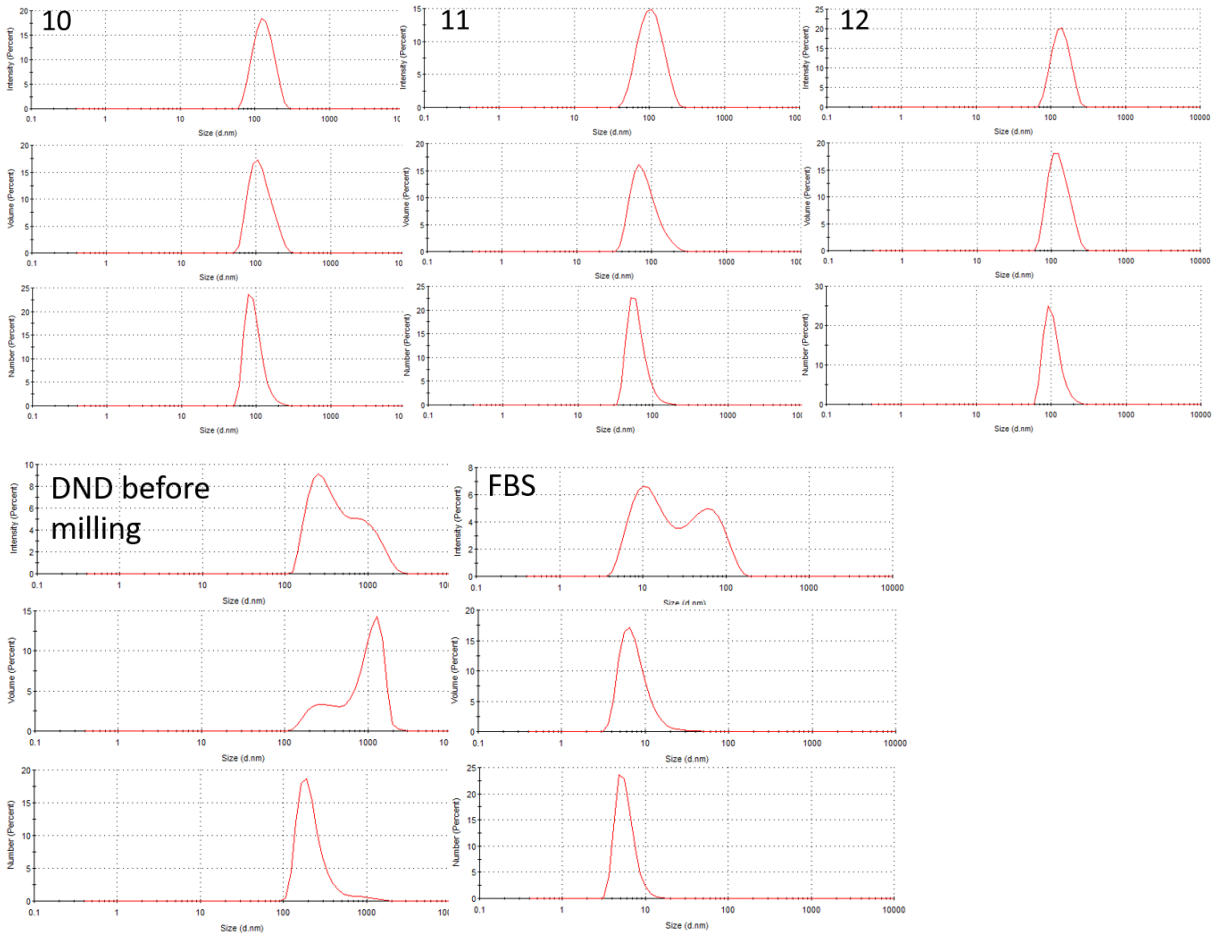

Figure S2-50: Dynamic light scattering spectra of ND **2-1**–**2-12**, DND before milling and FBS in DD-water as a distribution of intensity (top), volume (middle) and number (bottom) in percent.

7.1.6 Particle size of ND 2-1, ND 2-3 and ND 2-12 measured by AFM

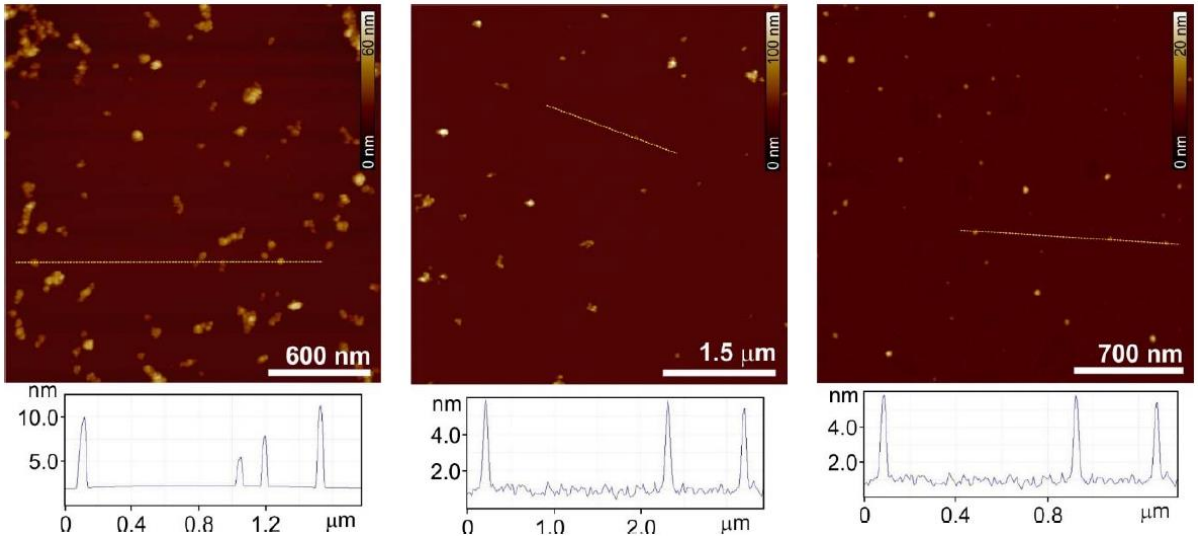

Figure S2-51: AFM images of ND **2-1** (left), ND **2-3** (center) and ND **2-12** (right) deposited on a plasma-etched silicon wafer by dropcasting followed by blow-drying with nitrogen.

7.1.7 Interaction of different ND conjugates with *E. coli* bacteria

Chemically competent cells of *E. coli* TOP10 [F–*mcr*A Δ(*mrr*-*hsd*RMS-*mcr*BC) Φ80*lac*ZΔM15 Δ*lac*X74 *rec*A1 *ara*D139 Δ(*ara leu*) 7697 *gal*U *gal*K *rps*L (StrR) *end*A1 *nup*G] were transformed with the vector pETM11 (EMBL) which carries the kanamycin resistance gene as a selection marker.

A single clone from an agar plate containing 50 µg/mL kanamycin was used to inoculate 10 µL of LB medium with antibiotic. Six mL of the overnight culture were centrifuged for 1 min at 16,000 x g and the supernatant discarded. The harvested cells were washed with 2 mL phosphate-buffered saline (PBS, 137 mM NaCl, 2.7 mM KCl, 10 mM Na_2HPO_4, 1.8 mM KH_2PO_4), centrifuged, and resuspended in 2 mL PBS. The optical density of the cells measured at 600 nm in a cuvette of 1 cm path length was 6.23.

Aliquots of 50 µL cells in PBS were prepared and mixed with 6 µL of previously sonicated nanodiamonds (NDs) (1 mg/mL stock) and 4 µL PBS to obtain a final concentration of 0.1 NDs mL^{-1}. A blank sample was prepared without NDs. Cells were incubated for 1 h at 27 °C in a thermomixer comfort (Eppendorf) with shaking (700 rpm). After this time, 30 µL of cells/ND

and the blank sample were transferred to a 96-well 2.0 mL DeepWell™ plate (Thermo Scientific™ Nunc™) and 1.17 mL LB medium was added. The plate was sealed with an air permeable adhesive foil (Breathe-EASIER™, 6" x 3.25", Diversified Biotech). Incubation proceeded at 37 °C/750 rpm in a TIMIX incubator during 7 h.

Samples were taken at different periods of time and the optical density of cultures was measured in a 96-well plate at 600 nm using appropriate dilutions in a total volume of 100 µL.

For experiments with a final concentration of 0 .5 NDs mL^{-1}, 10 mL of the overnight culture were centrifuged, and processed as mentioned above. Aliquots of 30 µl of cells in PBS were incubated with 30 µl of ND and the *E. coli* growth was measured as previously described.

All experiments were performed in duplicates and the average of two measurements was plotted against the growth time using a nonlinear curve fitting in OriginPro 9.1 (OriginLab).

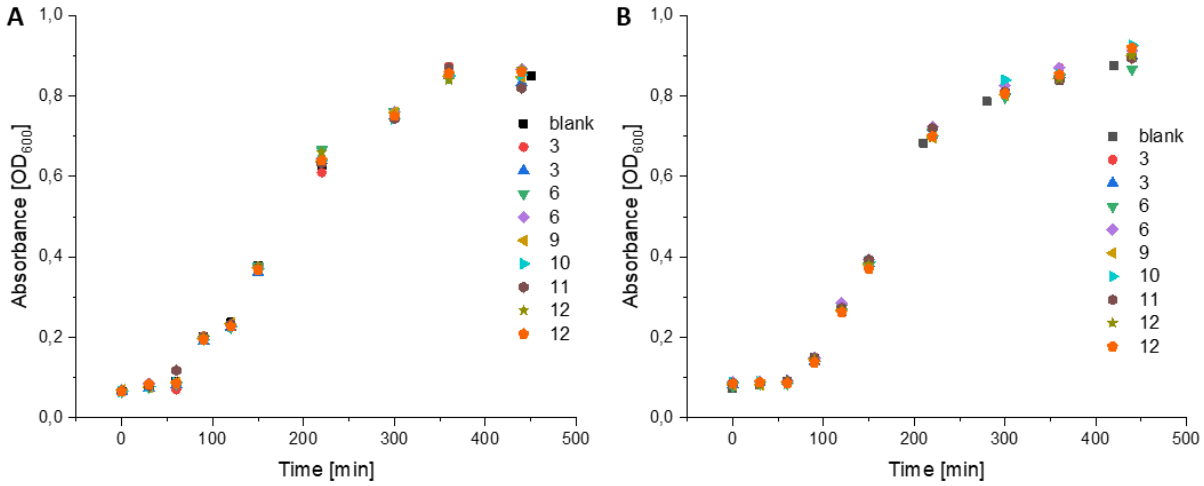

Figure S2-52: *E. Coli* growth curves with 0.1 mg mL^{-1} (A) and 0.5 mg mL^{-1} (B) of each ND (sample numbers given for each individual curve)

7.1.8 Supplementary References

[1] V. S. Gontijo, P. F. Espuri, R. B. Alves, L. F. de Camargos, F. V. D. Santos, W. A. de Souza Judice, M. J. Marques, R. P. Freitas, *Eur. J. Med. Chem.* **2015**, *101*, 24.
[2] C. Kim, G. Y. Tonga, B. Yan, C. S. Kim, S. T. Kim, M.-H. Park, Z. Zhu, B. Duncan, B. Creran, V. M. Rotello, *Org. Biomol. Chem.* **2015**, *13*, 2474.

[3] K. Brunner, J. Harder, T. Halbach, J. Willibald, F. Spada, F. Gnerlich, K. Sparrer, A. Beil, L. Möckl, C. Bräuchle et al., *Angew. Chem. Int. Ed.* **2015**, *54*, 1946.
[4] C. K. Kim, P. Ghosh, C. Pagliuca, Z.-J. Zhu, S. Menichetti, V. M. Rotello, *J. Am. Chem. Soc.* **2009**, *131*, 1360.
[5] S.-L. Niu, G. Ulrich, P. Retailleau, J. Harrowfield, R. Ziessel, *Tetrahedron Lett.* **2009**, *50*, 3840.
[6] A. Gansäuer, A. Okkel, L. Schwach, L. Wagner, A. Selig, A. Prokop, *Beilstein J. Org. Chem.*, **2014**, *10*, 1630.

7.2 Chapter 3 - Supporting Information

The following section is slightly modified and reproduced from the manuscript of A. Sigaeva‡, V. Merz‡, R. Sharmin, S. R. Hemelaar, R. Schirhagl*, A. Krueger*.

7.2.1 Organic Synthesis

The synthesis of the basic structure of organic molecules was recently reported by us[1] and is based on the work of Rotello and coworkers.[2,3]

1,1,1-Triphenyl-12,15,18,21-tetraoxa-2-thiatricosan-23-yl methane-sulfonate (3-12)

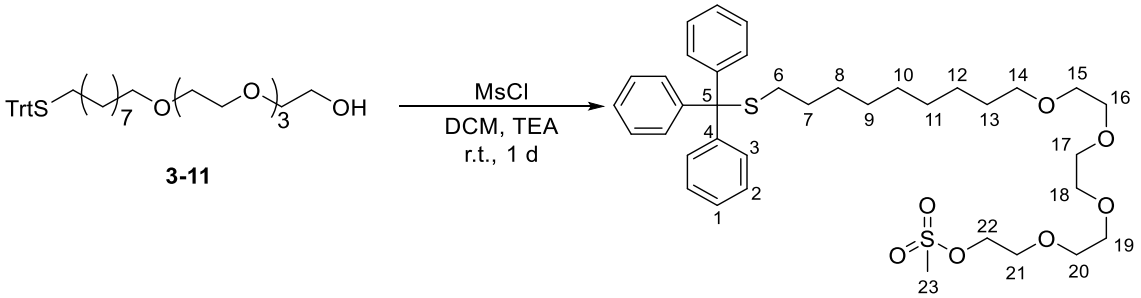

3-12 (85 %)

The glycol precursor **3-11** (5.6 g, 9.41 mmol, 1.00 eq) was dissolved in dry DCM and Triethylamine (TEA) (2.60 mL, 18.8 mmol, 2.00 eq) was added. After cooling the mixture in an ice bath methanesulfonyl choride (1.10 mL, 14.1 mmol, 1.50 eq) was added dropwise. After 60 min at 0 °C, the reaction mixture was warmed to room temperature and stirred for 1 d. Upon completion, the reaction mixture was concentrated in vacuo. The crude product was dissolved in DCM (70 mL) and washed three times with 0.1 M HCl (100 mL), neutralized with saturated $NaHCO_3$-solution and washed with MQ-water three times. The organic layer was dried with Na_2SO_4 and the solvent removed in vacuo. The crude product was purified by column chromatography (silica, cyclohexane/EtOAc, 2:5, v/v). After removing the solvent, the product was obtained as a slightly yellow oil.

Yield: 4.66 g (6.94 mmol, 74 %). $\mathbf{R_f}$ (EtOAc/cyclohexane, 5:2): 0.29. **^{1}H-NMR** (400 MHz, $CDCl_3$): δ = 7.44-7.38 (m, 6H, H-3), 7.34-7.24 (m, 6H, H-2), 7.24-7.17 (m, 3H, H-1), 4.38 (m, 2H, H-22), 3.80-3.53 (m, 14H, H-15 – H-21) 3.43 (t, $^3J_{14,13}$ = 6.8 Hz, 2H, H-14), 3.07 (s, 3H, H-23) 2.12 (t, $^3J_{6,7}$ = 7.4 Hz, 2H, H-6), 1.59-1.48 (m, 2H, H-13), 1.39-1.26 (m, 2H, H-7)

1.26-0.95 (m, 10H, H-8 – H-12) ppm. **^{13}C-NMR** (100 MHz, $CDCl_3$): δ = 145.2 (C_q, C-4), 129.7 (CH, C-2), 127.9 (CH, C-3), 126.6 (CH, C-1), 71.6, 70.8, 70.7, 70.6, 70.2, 69.4, 69.1 ($(CH_2)_9$, C-14/15/16/17/18/19 /20/21/22), 66.5 (C_q, C-5), 37.9 (CH_3, C-23), 32.2 (CH_2, C-6), 29.7, 29.5, 29.5, 29.2, 29.1, 28.7, 26.2 ($(CH_2)_7$, C-7/8/9/10/11/12/13) ppm. **HRMS** (ESI,+): found: 695.30399 $[M]^+$; calc. for $[M]^+$: 695.30467. **FT-IR (ATR):** $\tilde{\nu}$ = 3055 (w), 3024 (w), 2925 (s), 2854 (s), 1595 (w), 1486 (m), 1444 (m), 1351 (s), 1246 (m), 1174 (s), 1105 (s), 1018 (w), 970 (w), 918 (w), 798 (w), 744 (m), 700 (s), 619 (w) cm^{-1}. **UV/Vis** (acetonitrile): λ_{max}(log ε) = 256 (5.37), 290 (4.74), 320 (4.72) ($c = 2.0 \cdot 10^{-5}$ mol L^{-1}) nm.

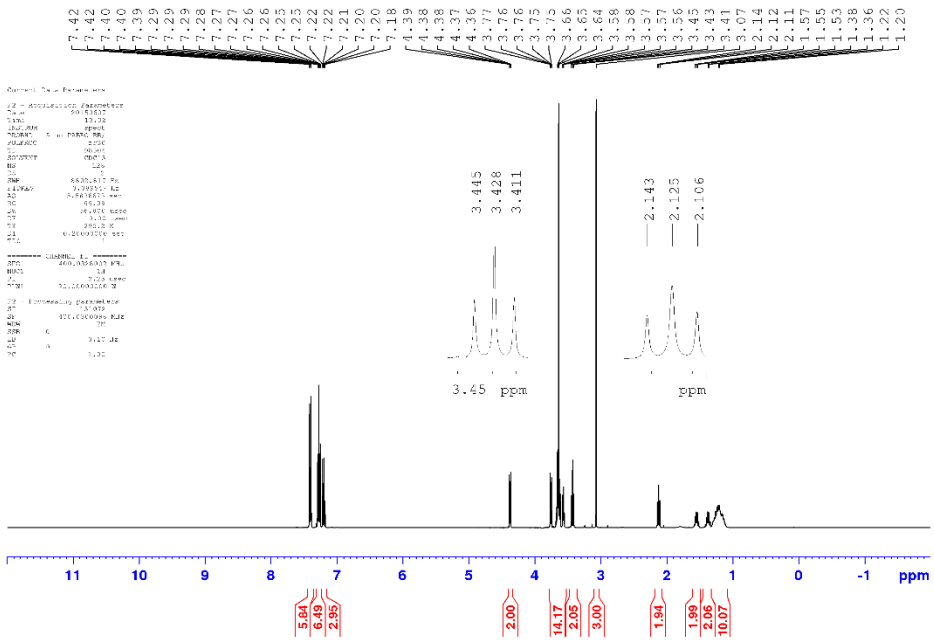

Figure S3-1: ^{1}H-NMR of 1,1,1-triphenyl-12,15,18,21-tetraoxa-2-thiatricosan-23-yl methanesulfonate (**3-12**).

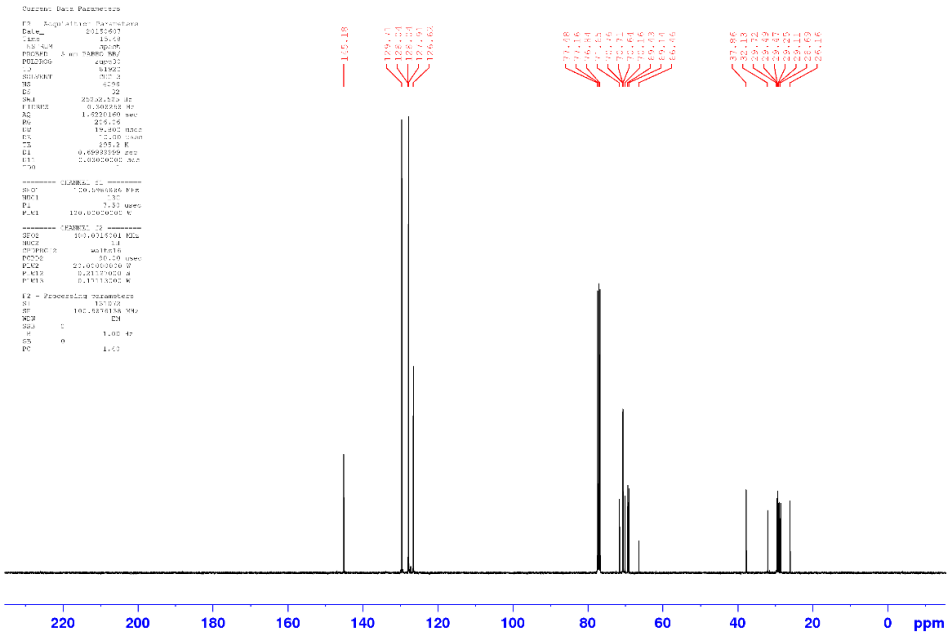

Figure S3-2: ^{13}C-NMR spectrum of 1,1,1-triphenyl-12,15,18,21-tetraoxa-2-thiatricosan-23-yl methane-sulfonate (**3-12**).

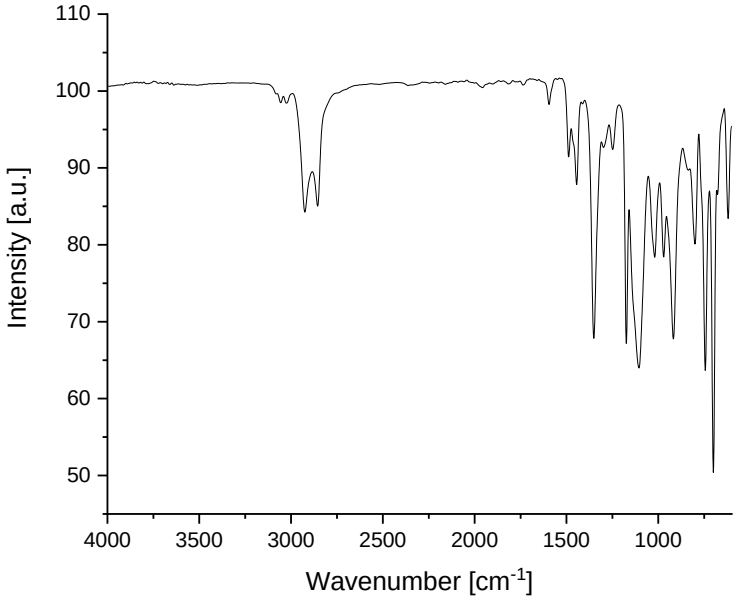

Figure S3-3: FT-IR ATR of 1,1,1-triphenyl-12,15,18,21-tetraoxa-2-thiatricosan-23-yl methane-sulfonate(**3-12**).

***N*,*N*-dimethyl-1,1,1-triphenyl-12,15,18,21-tetraoxa-2-thiatricosan-23-amine (3-13)**[3]

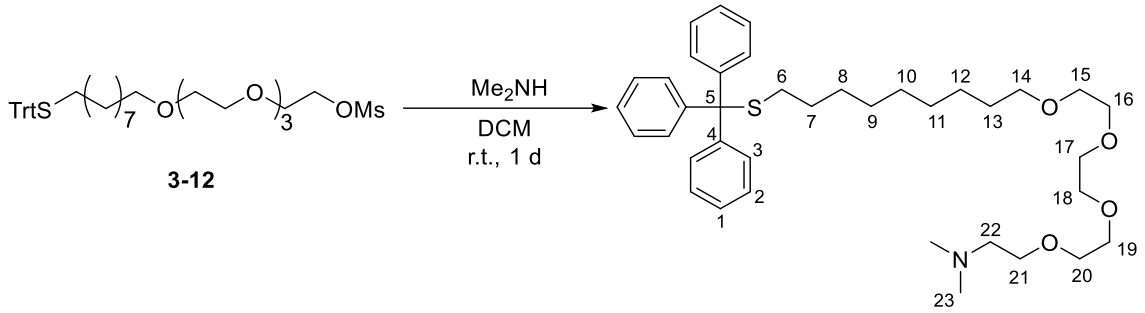

The mesylate **3-12** (2.38 g, 3.53 mmol, 1.00 eq) was added to an emulsion of DCM (25 mL) and a 40-%-solution of dimethylamine in water (8.00 mL, 70.0 mmol, 20.0 eq). and stirred for 1 d at room temperature. After one day, the reaction mixture was extracted with of deionized water and DCM. The organic layer was separated and the solvent removed in vacuo before purifying the crude product by column chromatography (silica, cyclohexane/EtOAc, 1:4, v/v). By adding TEA (5 %) to the eluent, the product was isolated. After removing the solvent, the product was obtained as a slightly yellow oil.

Yield: 9.69 g (1.54 mmol, 44 %). **R_f** (EtOAc/cyclohexane/TEA, 76:19:5): 0.33. **^{1}H-NMR** (400 MHz, $CDCl_3$): δ = 7.44-7.38 (m, 6H, H-3), 7.34-7.24 (m, 6H, H-2), 7.24-7.17 (m, 3H, H-1), 3.71-3,55 (m, 14H, H-15 – H-21) 3.42 (t, $^3J_{13,14}$ = 6.8 Hz, 2H, H-14), 2.50 (t, $^3J_{21,22}$ = 5.8 Hz 2H, H-22) 2.26 (s, 6H, H-23), 2.12 (t, $^3J_{6,7}$ = 7.4 Hz, 2H, H-6), 1.61-1.49 (m, 2H, H-13), 1.43-1.32 (m, 2H, H-7) 1.32-1.06 (m, 10H, H-8 – H-12) ppm. **^{13}C-NMR** (100 MHz, $CDCl_3$): δ = 144.4 (C_q, C-4), 129.5 (CH, C-2), 126.7 (CH, C-3), 126.4 (CH, C-1), 71.4, 70.5, 70.5, 70.5, 70.5, 70.3, 69.9, 68.9 ($(CH_2)_8$, C-14/15/16/17/18/19/20/21), 66.2 (C_q, C-5), 58.6 (CH_2, C-22), 45.6 (CH_3, C-23), 31.8 (CH_2, C-6), 29.5, 29.2, 29.2, 29.0, 28.8, 28.4, 25.9 ($(CH_2)_7$, C-7/8/9/10/11/12/13) ppm. **HRMS** (ESI,+): Gef.: 622,39246 ; calc.: 622,39246. **FT-IR(ATR):** $\tilde{\nu}$ = 2925 (m), 2854 (m), 1489 (w), 1444 (m), 1351 (w), 1296 (w), 1113 (m), 1036 (w), 847 (w), 744 (s), 700 (s), 619 (w) cm^{-1}. **UV/Vis** (acetonitrile): λ_{max}(log ε) = 280 (4.18), 332 (3.89), (c = 2.57 · 10^{-5} mol L^{-1}) nm.

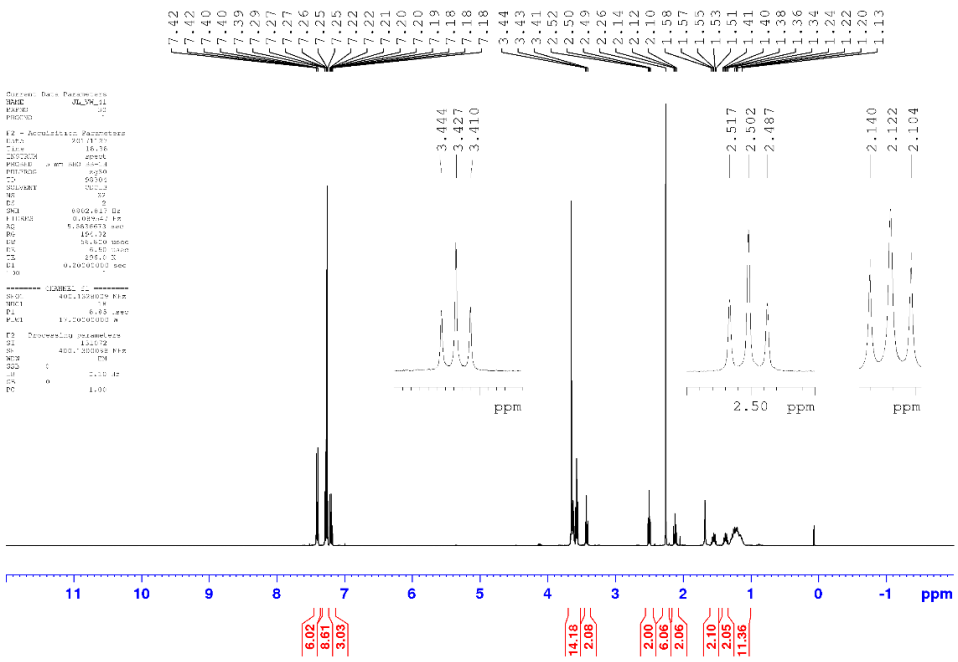

Figure S3-4: ^{1}H-NMR spectrum of *N,N*-dimethyl-1,1,1-triphenyl-12,15,18,21-tetraoxa-2-thiatricosan-23-amine (**3-13**).

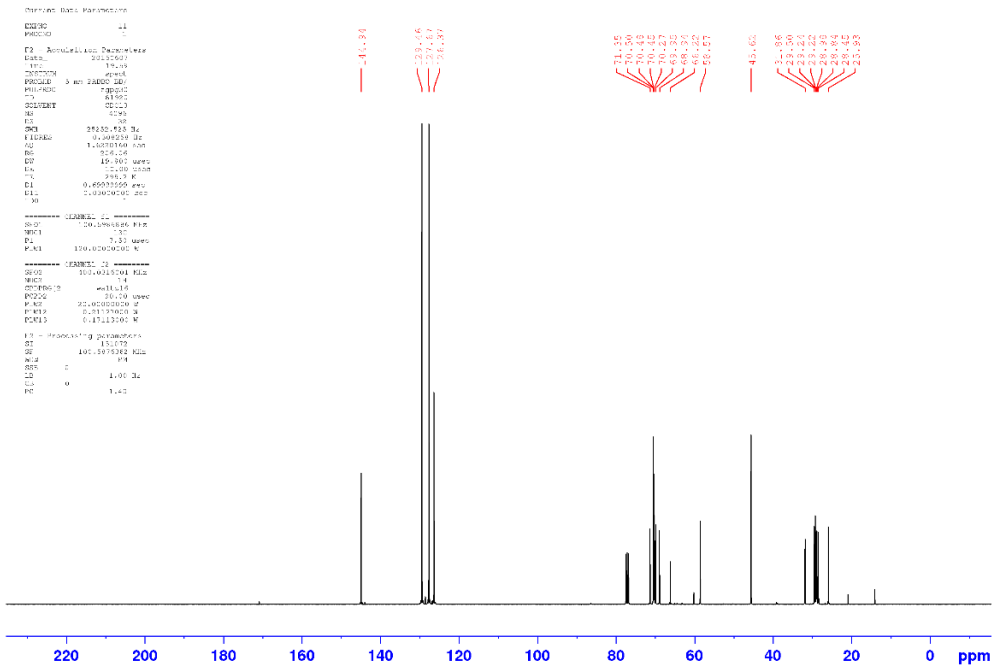

Figure S3-5: ^{13}C-NMR spectrum of *N,N*-dimethyl-1,1,1-triphenyl-12,15,18,21-tetraoxa-2-thiatricosan-23-amine (**3-13**).

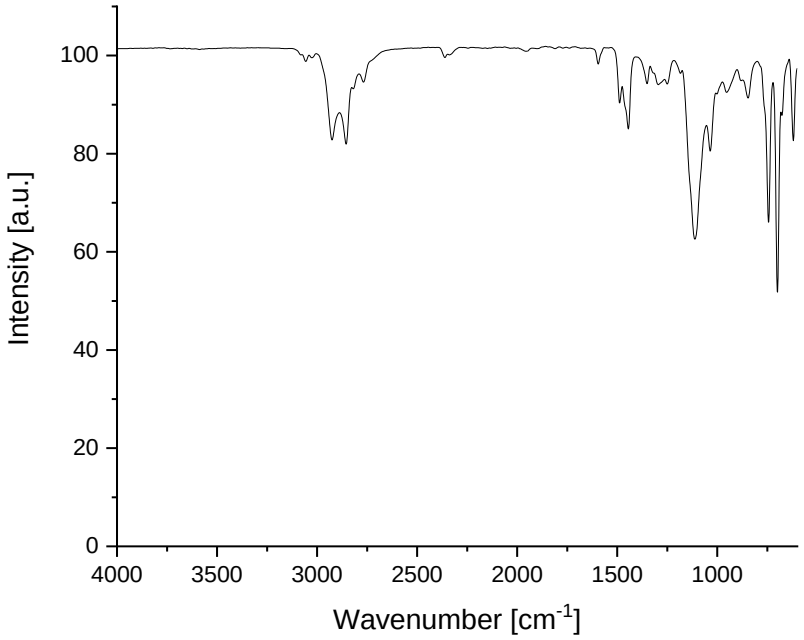

Figure S3-6: FT-IR ATR spectrum of *N,N*-dimethyl-1,1,1-triphenyl-12,15,18,21-tetraoxa-2-thiatricosan-23-amine (**3-13**).

24,24-Dimethyl-1,1,1-triphenyl-12,15,18,21-tetraoxa-2-thia-24-azaheptacosan-24-ium-27-sulfonate (3-14)[16]

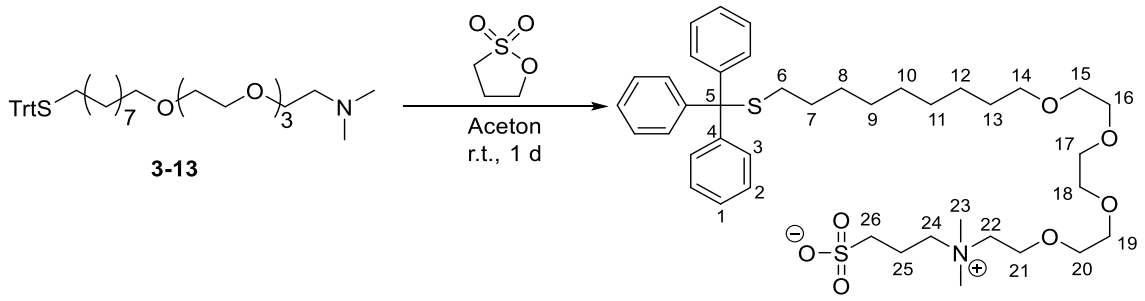

The amine **3-13** (960 mg, 1.54 mmol, 1.00 eq) was dissolved in dry acetone (45 mL) and 1,3-propanesultone (410 mg, 3.40 mmol, 2,20 eq) was added and the mixture was stirred for 1 d at room temperature. The resulting solid was filtered and washed with EtOAc/cyclohexane (1:4, v/v). After drying it in vacuo, a colorless solid was obtained.

Yield: 3,15 g (4.2 mmol, 94 %). **^{1}H-NMR** (400 MHz, $CDCl_3$): δ = 7.42-7.37 (m, 6H, H-3), 7.31-7.24 (m, 6H, H-2), 7.23-7.16 (m, 3H, H-1), 4.00-3.88 (m, 2H, H-24), 3.84-3.73 (m, 2H, H-26), 3.71-3,58 (m, 12H, H-15 – H-20), 3.58-3,51 (m, 2H, H-21), 3.41 (t, $^3J_{13,14}$ = 6.9 Hz, 2H, H-14), 3.22 (s, 6H, H-23), 2.90 (t, $^3J_{21,22}$ = 6.3 Hz 2H, H-22), 2.34-2.20 (m, 2H, H-25), 2.12 (t, $^3J_{6,7}$ = 7.4 Hz, 2H, H-6), 1.61-1.47 (m, 2H, H-13), 1.43-1.32 (m, 2H, H-7) 1.32-1.02 (m, 10H, H-8 – H-12) ppm. **^{13}C-NMR** (100 MHz, $CDCl_3$): δ = 145.4 (C_q, C-4), 129.9 (CH, C-2), 128.1 (CH, C-3), 126.8 (CH, C-1), 71.8, 70.9, 70.8, 70.7, 70.5, 70.5, 70.3 ($(CH_2)_8$, C-14/15/16/17/18/19/20/21), 66.7 (C_q, C-5), 65.5 (CH_2, C-24), 65.2 (CH_2, C-26), 59.0 (CH_2, C-25), 52.2 (CH_3, C-23), 47.9 (CH_2, C-22) 32.4 (CH_2, C-6), 29.9, 29.7, 29.5, 29.4, 29.3, 28.9, 26.4 ($(CH_2)_7$, C-7/8/9/10/11/12/13) ppm. **HRMS** (ESI,+): found: 744.39671 $[M]^+$; calc. for $[M]^+$: 744.39622. **FT-IR (ATR):** $\tilde{\nu}$ = 3450 (br), 3055 (vw), 3022 (vw), 2925 (m), 2854 (m), 1733 (w), 1666 (w), 1597 (w), 1487 (m), 1442 (m), 1176 (s), 1105 (s), 1035 (s), 742 (s), 698 (s), 607 (m) cm^{-1}. **UV/Vis** (acetonitrile): λ_{max} (log ε) = 255 (5.34), 328 (4.91), ($c = 2.15 \cdot 10^{-5}$ mol L^{-1}) nm.

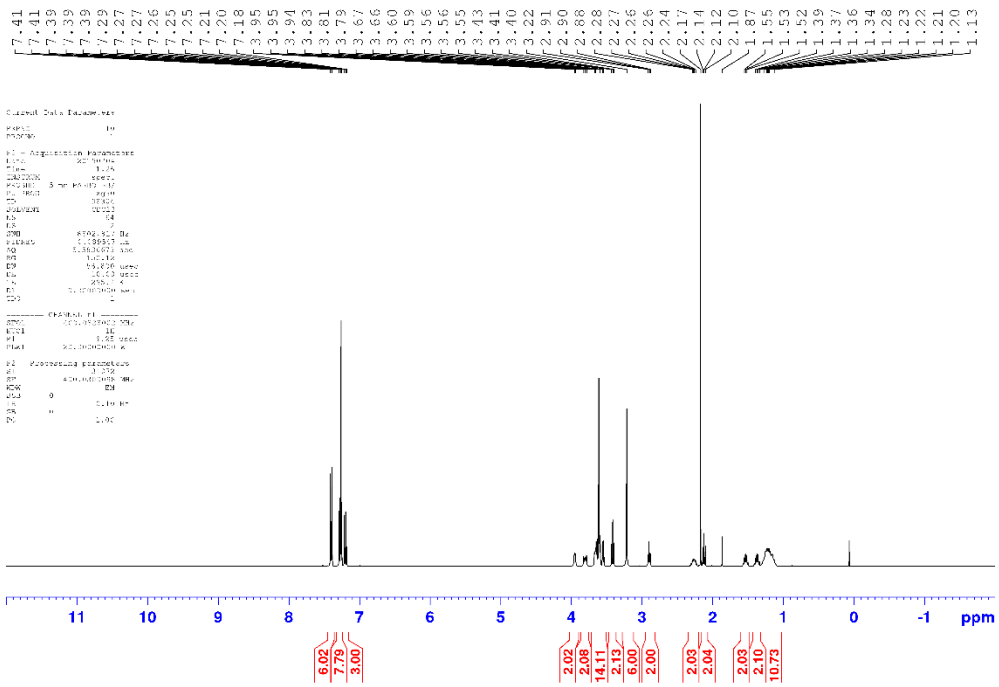

Figure S3-7: ^{1}H-NMR spectrum of 24,24-dimethyl-1,1,1-triphenyl-12,15,18,21-tetraoxa-2-thia-24-azaheptacosan-24-ium-27-sulfonate (**3-14**).

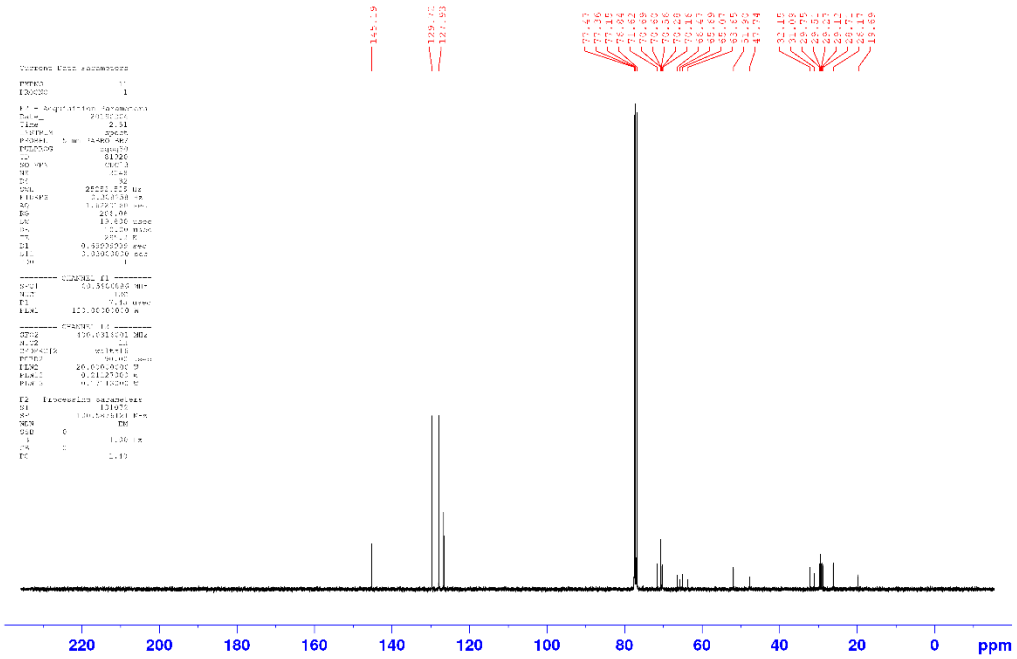

Figure S3-8: ^{13}C-NMR spectrum of 24,24-dimethyl-1,1,1-triphenyl-12,15,18,21-tetraoxa-2-thia-24-azaheptacosan-24-ium-27-sulfonate (**3-14**).

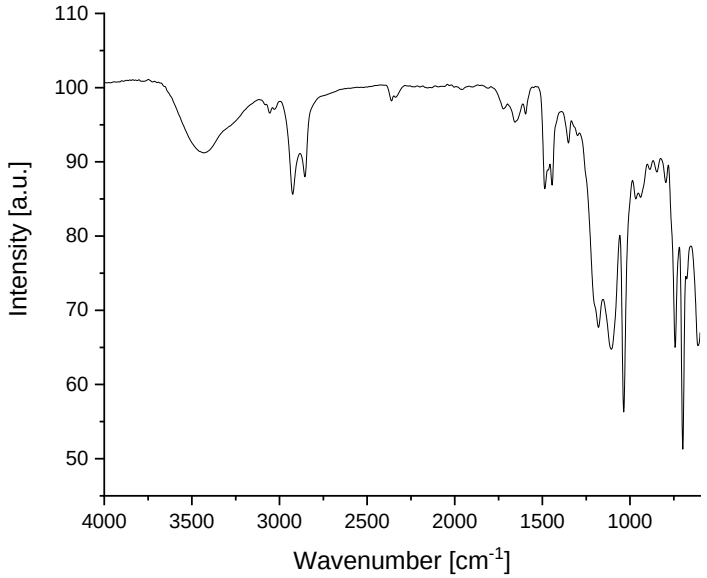

Figure S3-9: FT-IR ATR spectrum of 24,24-dimethyl-1,1,1-triphenyl-12,15,18,21-tetraoxa-2-thia-24-azaheptacosan-24-ium-27-sulfonate (**3-14**).

25-mercapto-4,4-dimethyl-7,10,13,16-tetraoxa-4-azapentacosan-4-ium-1-sulfonate (3-5)

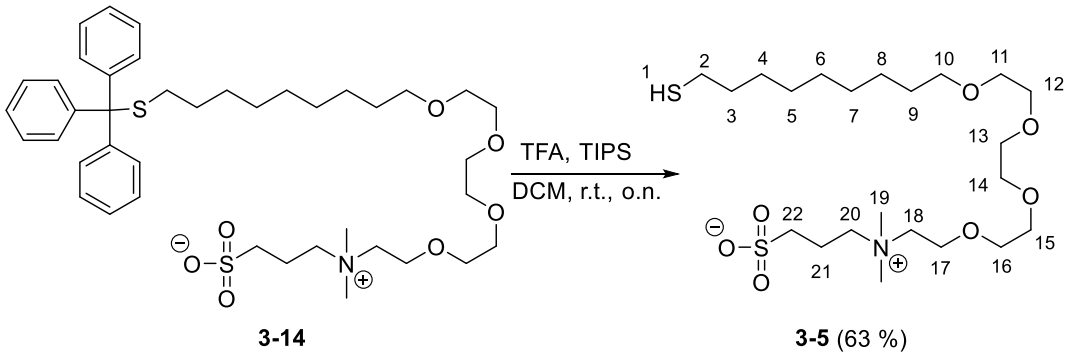

3-14 **3-5** (63 %)

The protected thiol **3-14** (70 mg, 94 µmol, 1.00 eq) was dissolved in dry DCM (0.7 mL) and TFA (0.15 mL, 1.90 mmol, 20.00 eq), TFAH (0.04 mL, 0.30 mmol, 3.00 eq) and TIPS (0.06 mL, 0.30 mmol, 3.00 eq) were added. After adding TFA, the mixture turns yellow. The reaction mixture was stirred overnight (16 h) at room temperature. The solvent was removed in vacuo and the crude product was washed with diethyl ether (3x, 1.5 mL). After drying the product in vacuo, a whitish solid was obtained which is melting at room temperature to form a slightly yellow oil.

Yield: 22 mg (44 µmol, 63 %). **^{1}H-NMR** (400 MHz, $CDCl_3$): δ = 3.99-3.86 (m, 2H, H-20), 3.82-3.70 (m, 2H, H-22), 3.71-3.58 (m, 12H, H-11 – H-16), 3.58-3.50 (m, 2H, H-17), 3.42 (t, $^{3}J_{10,9}$ = 6.9 Hz, 2H, H-10), 3.23 (s, 6H, H-19), 2.96-2.85 (m, 3H, H-18+H-1), 2.51 (t, $^{3}J_{2,3}$ = 7.4 Hz, 2H, H-2), 2.36-2.14 (m, 2H, H-21), 1.66-1.49 (m, 4H, H-3+H-9) 1.45-1.15 (m, 10H, H-4 – H-8) ppm. **^{13}C-NMR** (100 MHz, $CDCl_3$): δ = 71.8, 70.8, 70.8, 70.7, 70.7, 70.4, 70.3, 69.1 ($(CH_2)_8$, C-10/11/12/13/14/15/16/17), 65.3 (CH_2, C-20), 65.0 (CH_2, C-22), 57.1 (CH_2, C-21), 52.1 (CH_3, C-19), 47.9 (CH_2, C-18), 34.0 (CH_2, C-2), 29.6, 29.5, 29.4, 29.0, 28.3 26.0, 24.7 ($(CH_2)_7$, C-3/4/5/6/7/8/9) ppm. **HRMS** (ESI,+): found: 524.26701 $[M]^+$; calc. for $[M]^+$: 524.26862. **FTIR (ATR):** $\tilde{\nu}$ = 3440 (br), 2934 (s), 2856 (s), 2549 (w), 1764 (m), 1458 (m), 1207 (s), 1122 (vs), 1038 (s), 964 (w), 942 (w), 802 (m), 702 (m), 595 (m). **UV/Vis** (acetonitrile): λ_{max}(log ε) = 232 (4,57), 270 (4,28), 278 (4,29), 308 (4,66), 328 (7,32), (c = $2.19 \cdot 10^{-5}$ mol L^{-1}) nm.

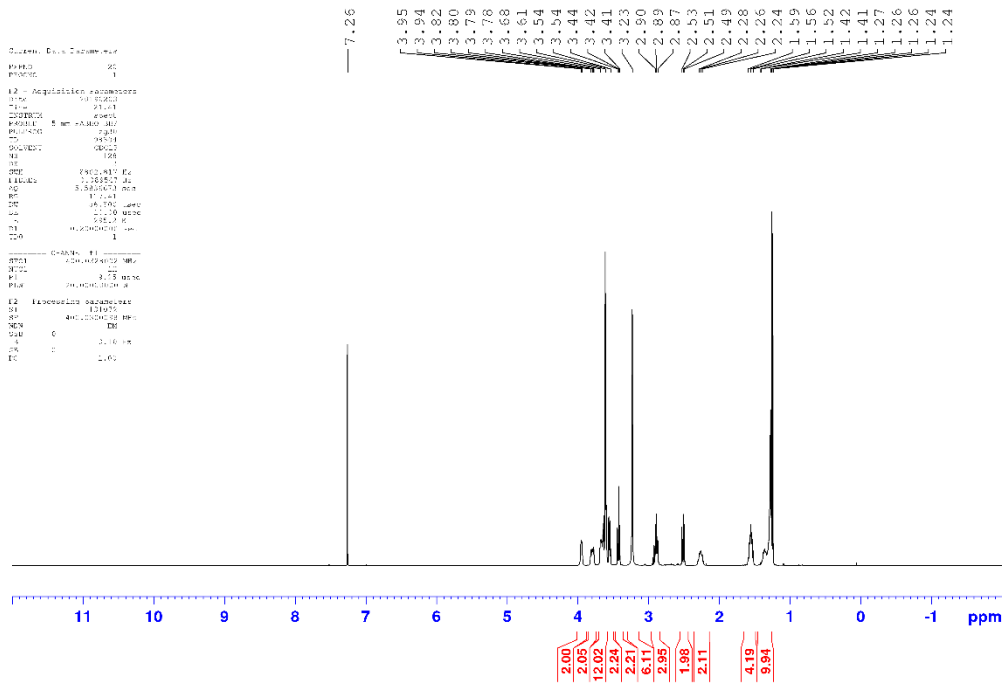

Figure S3-10: ^{1}H-NMR spectrum of 25-mercapto-4,4-dimethyl-7,10,13,16-tetraoxa-4-azapentacosan-4-ium-1-sulfonate (**3-5**).

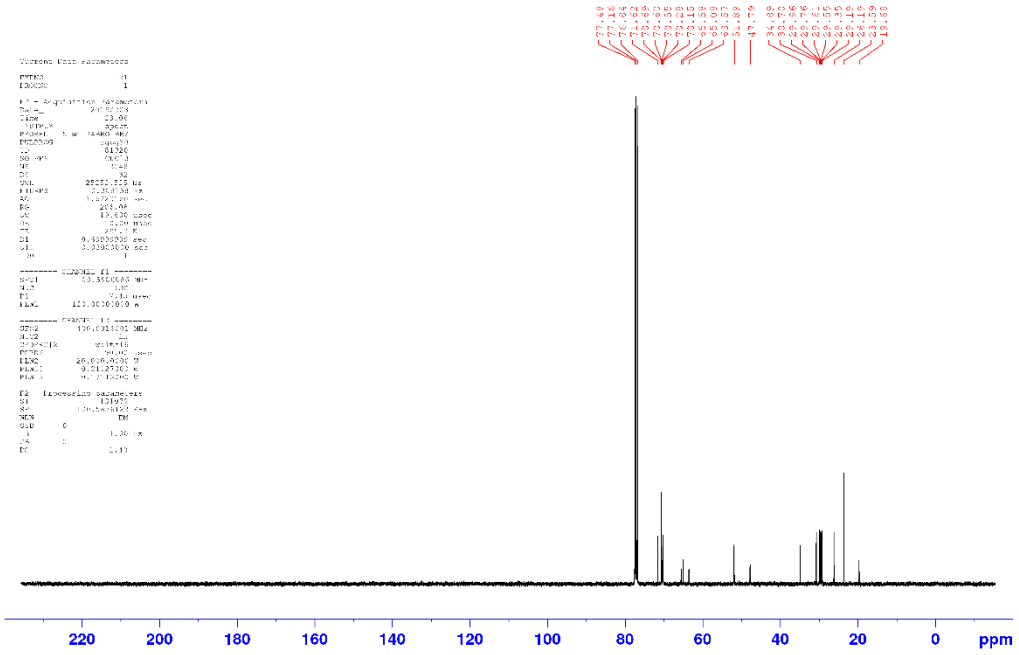

Figure S3-11: ^{13}C-NMR spectrum of 25-mercapto-4,4-dimethyl-7,10,13,16-tetraoxa-4-azapentacosan-4-ium-1-sulfonate (**3-5**).

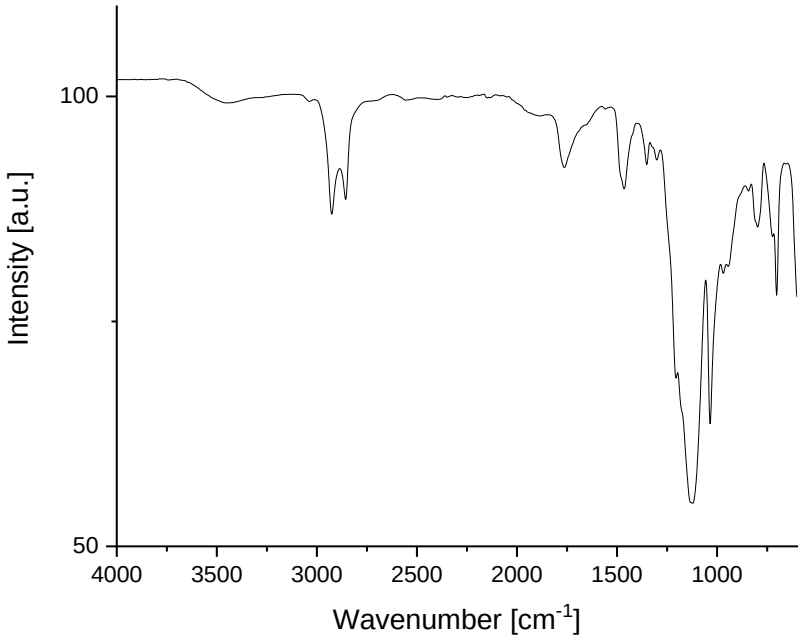

Figure S3-12: FT-IR ATR spectrum of 25-mercapto-4,4-dimethyl-7,10,13,16-tetraoxa-4-azapentacosan-4-ium-1-sulfonate (**3-5**).

7.2.2 Nanodiamond Functionalization

Benzoic acid functionalized ND 3-3

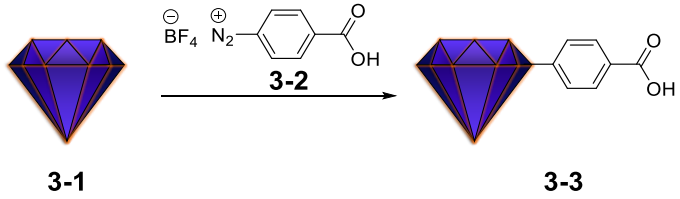

Figure S3-13: Functionalization of HPHT fND **3-1** with diazonium salt **3-2**.

As received fND **3-1** (2 mg, 1 mg/mL) was mixed with the diazonium salt **3-2** (10 mg in 4 mL MQ-water) in a chamber of a mini mill Pulverisette 23 for 1 h at 50 Hz vibration mode with 10x2 mm steel beads. The chamber was opened in minute 5, 20 and 45 to release the overpressure of nitrogen. After the reaction, the fNDs were washed with water, acetone, THF, dry THF in consecutive dispersion-centrifugation (16000 rpm, 10 min) steps. One part of the dispersion was then washed again in acetone and water for further analytics. The dispersion appears grey in dispersion and whitish grey when dry. As the amount of fND was too low to be able to carry out all characterizations, a larger batch of non-fluorescent but otherwise identical HTHP ND (non-fND) was functionalized using the same procedure. The thermogravimetric data have been obtained from this nonfluorescent batch of **3-3**.

*ND **3-1** (fND):* **Zeta potential**: -30.5 mV (DD-water, intrinsic pH=5.5), **Particle size** (DLS, DD-water): 10 % ≤ 71 nm, 50 % ≤ 287 nm, 90 % ≤ 887 nm.

*ND **3-1** (non-fND):* **Zeta potential**: -36 mV (DD-water, intrinsic pH=5.4), **Surface loading** (TGA): Δm(150-300 °C) = 0.3 %, **Particle size** (DLS, DD-water): 10 % ≤ 71 nm, 50 % ≤ 110 nm, 90 % ≤ 197 nm, **FT-IR** (DRIFTS): $\tilde{\nu}$ = 3600 (br), 1760 (m), 1604 (m), 1181 (m), 863 (s) cm^{-1}.

*ND **3-3** (fND):* **Zeta potential**: -28.2 mV (DD-water, intrinsic pH=5.5), **Particle size** (DLS, DD-water): 10 % ≤ 97 nm, 50 % ≤ 184 nm, 90 % ≤ 387 nm, **FT-IR** (DRIFTS): $\tilde{\nu}$ = 3400 (br), 2951 (vw), 2930 (vw), 2853 (vw), 2637 (br), 2521 (br), 1936 (w), 1704 (s), 1604 (s), 1411 (s),

1259 (m), 1179 (w), 1111 (w), 1021 (w), 963 (vw), 911 (vw), 863 (m), 788 (m), 710 (w), 634 (vw) cm^{-1}.

*ND **3-3** (non-fND):* **Zeta potential**: -28.8 mV (DD-water, intrinsic pH=5.6), **Surface loading** (TGA): 0.30 mmol/g = Δm(150-300 °C) = 3.8 %; **Particle size** (DLS, DD-water): 10 % ≤ 137 nm, 50 % ≤ 246 nm, 90 % ≤ 478 nm, **FT-IR** (DRIFTS): $\tilde{\nu}$ = 3400 (br), 2951 (vw), 2930 (vw), 2853 (vw), 2637 (br), 2521 (br), 1936 (w), 1704 (s), 1604 (s), 1411 (s), 1259 (m), 1179 (w), 1111 (w), 1021 (w), 963 (vw), 911 (vw), 863 (m), 788 (m), 710 (w), 634 (vw) cm^{-1}.

Thioester formation to ND **3-6**

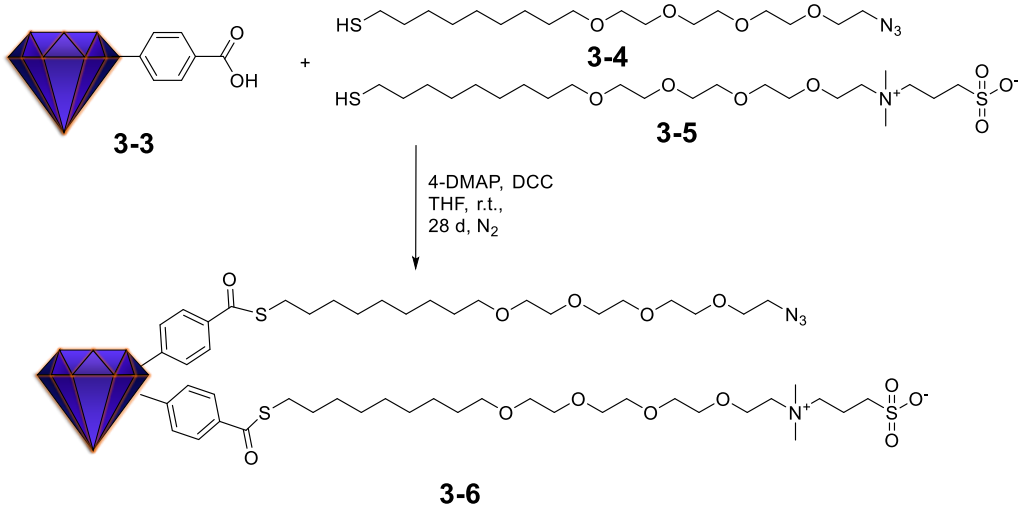

Figure S3-14: Thioester formation on the ND surface.

To perform this reaction, the ND **3-3** was washed two times in THF and two times in dry THF. The dispersion was mixed with DCC (42 mg, 202 mmol) and 4-DMAP (5 mg, 40 mmol) respective zwitterion (27 mg, 53 mmol) and azide (20 mg, 53 mmol) linker for a thioester formation. The reaction was stirred 28 days at room temperature and after 8 days, the same amount of starting materiel and linker was added to the reaction. After 28 days, water was used to quench the reaction and wash the fNDs free from organic material. Used solvents were THF, water, acetone, dichloromethane, acetone and bidestilled water.

*ND **3-3** (fND):* **Zeta potential**: -34.5 mV (DD-water, intrinsic pH=5.4), **Particle size** (DLS, DD-water): 10 % ≤ 153 nm, 50 % ≤ 266 nm, 90 % ≤ 531 nm, **FT-IR** (DRIFTS): $\tilde{\nu}$ = 3383 (br), 2930 (m), 2853 (m), 2102 (vw), 1704 (m), 1652 (m) 1604 (s), 1535 (s), 1408 (vs), 1271 (w),

1215 (vw), 1184 (w), 1021 (w), 1103 (w), 1039 (m), 1015 (m), 867 (w), 788 (m), 710 (w) cm^{-1}.

*ND **3-6** (non-fND):* **Zeta potential**: -25 mV (DD-water, intrinsic pH=5.4), **Surface loading** (TGA): 0.21 mmol/g = Δm(150-300 °C) = 11.8 %, **Particle size** (DLS, DD-water): 10 % ≤ 175 nm, 50 % ≤ 216 nm, 90 % ≤ 266 nm, **FT-IR** (DRIFTS): $\tilde{\nu}$ = 3383 (br), 2930 (m), 2853 (m), 2102 (vw), 1704 (m), 1652 (m) 1604 (s), 1535 (s), 1408 (vs), 1271 (w), 1215 (vw), 1184 (w), 1021 (w), 1103 (w), 1039 (m), 1015 (m), 867 (w), 788 (m), 710 (w) cm^{-1}.

7.2.3 Antibody Purification, Modification and Binding on ND

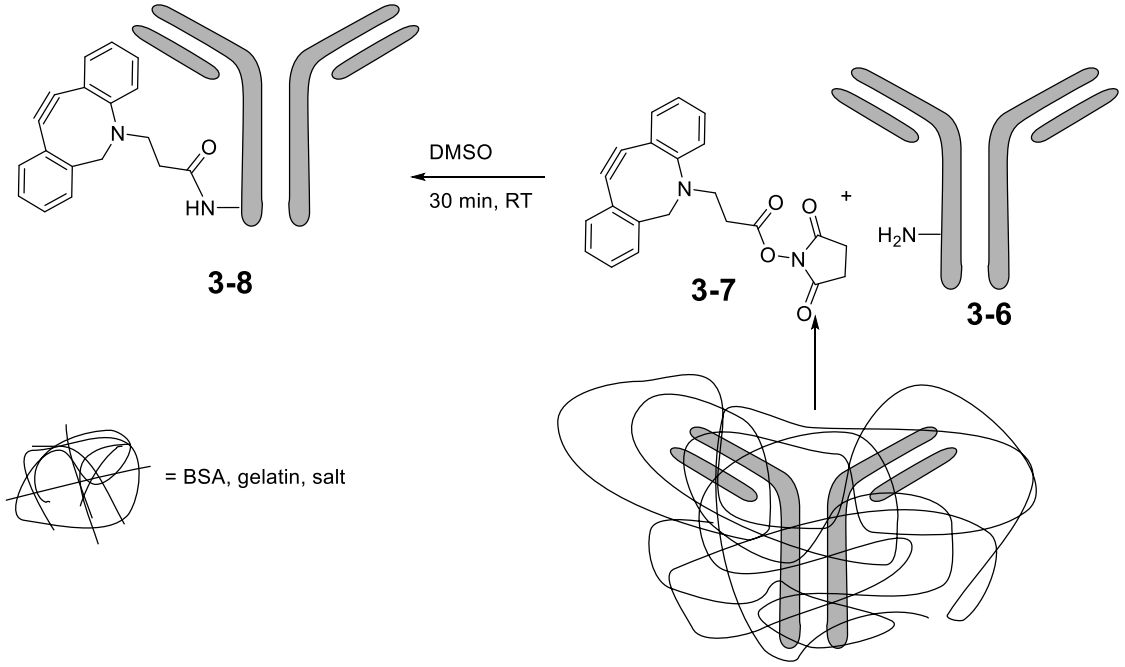

Figure S3-15: Schematic illustration of antibody purification and functionalization with a clickable DBCO-NHS ester.

For the click reaction, the antibody (ab) had to be purified. By using *Pierce™ Antibody clean-up kit* from *Thermo Scientific* the antibody was cleaned in a two-step procedure. In the first step the antibody was desalted using *Zeba™ Spin Desalting Columns*, 7K MWCO, and in the second step *Melon™ Gel IgG Spin Purification Kit* was used bind non-antibody serum proteins.

Cleaning with *Zeba™ Spin Desalting Columns*, 7K MWCO:

In this column, the resin is mixed with buffer. The column must be washed and dried by centrifugation. Therefore, the column's bottom cap must be removed and the top cap should be loosening to avoid vacuum build up in the column while it is centrifuged (RCF = 1500, 1 min). Since a rotor with a settled angel was used, the column must be marked and put every time in the same orientation. It was 300 µL melon puffer added and washed 3 times. To desalt the antibody, the antibody mixture **3-6** (50 µL, 1 mg/mL) was applied to the dry column and centrifuged again at the same speed 2 min. After 2 min, the column is loaded with 15 µm bidestilled water and centrifuged again 2 min.

Cleaning with *Melon^{TM} Gel IgG Spin Purification Kit*:

The BSA/Gelatin removal was done using a 100 µL Melon gel column. To prepare the column, the melon gel was centrifuged as described above (4000xG 1x 1 min) and washed two times with melon buffer (4000xG 2x 10 s). The gel was incubated with the antibody mixture **3-6** (in bidest. water/BSA mixture) for 10 min and centrifugate 1 min at 4000xG to a total volume of 35 µL.

Preparation of clickable antibodies

The preparation of the clickable antibodies **3-8** was performed with DBCO-NHS-ester in DMSO (1 µg/µL). A total of 10 µL (10-fold excess) was added to the 35 µL antibody solution **3-6**. Additionally, 90 µL of DMSO were added. The reaction was shaken at r.t. 30 min. To stop the reaction, Tris-HCl buffer (pH = 8, 100 mM) was added and the mixture shaken for additional 5 min. The excess of ester and Tris-HCl was adsorbed on a Zeba column (see above for procedure).

Coupling of prefunctionalized ND 3-9 with the clickable antibody 3-8

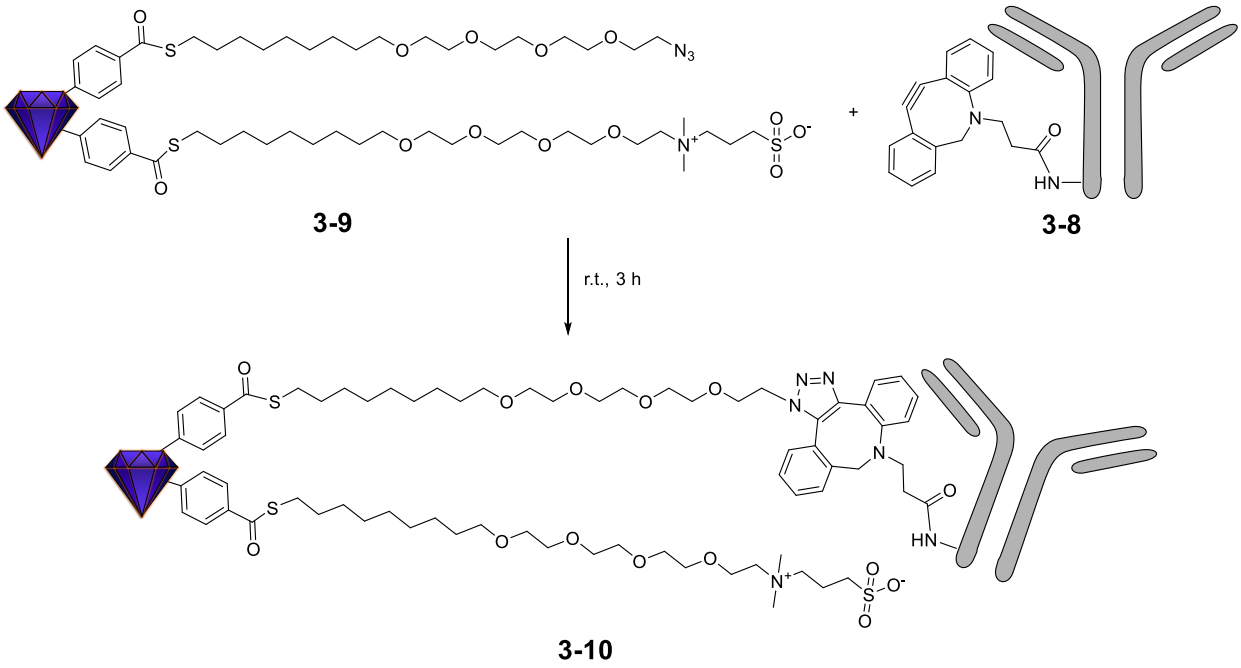

Figure S3-16: Click reaction between antibodies and azide moieties of the functionalized fND.

As soon as the antibody was purified and reacted with the ester, the click reaction was initiated to prevent decomposition related to the poor stability of the antibodies and dibenzocyclooctyne. Therefore, the antibody solution was mixed with 1 mg of fND **3-8** (1 mg/mL) and incubated at r.t. 3 h. After 3 h, the reaction mixture was washed three times with bidestilled water in consecutive dispersion centrifugation (10000xG 10 min) steps and stored at 4 °C.

7.2.4 Supplementary References

[1] V. Merz, J. Lenhart, Y. Vonhausen, M. E. Ortiz-Soto, J. Seibel, A. Krueger. Zwitterion-Functionalized Detonation Nanodiamond with Superior Protein Repulsion and Colloidal Stability in Physiological Media. *Small*, **2019**, *15*, 1901551.

[2] C. Kim, G. Y. Tonga, B. Yan, C. S. Kim, S. T. Kim, M.-H. Park, Z. Zhu, B. Duncan, B. Creran, V. M. Rotello. Regulating exocytosis of nanoparticles via host-guest chemistry. *Org. Biomol. Chem.* **2015**, *13*, 2474–2479.

[3] C. K. Kim, P. Ghosh, C. Pagliuca, Z.-J. Zhu, S. Menichetti, V. M. Rotello. Entrapment of hydrophobic drugs in nanoparticle monolayers with efficient release into cancer cells. *J. Am. Chem. Soc.* **2009**, *131*, 1360–1361.

7.3 Chapter 4 - Supporting Information

The following section is slightly modified and reproduced from V. Merz, J. Merz, M. Kirchner, J. Lenhart, T. B. Marder, A. Krueger, Pyrene-Based "Turn-Off" Probe with Broad Detection Range for Cu^{2+}, Pb^{2+} and Hg^{2+} Ions, *Chem. Eur. J.* **2021**, *27*, 8118–8126., *with permission from Wiley-VCH.*

7.3.1 Organic Synthesis

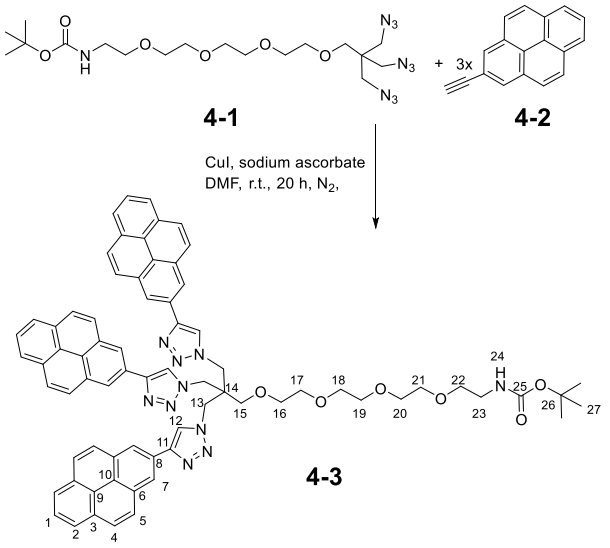

Under an N_2 atmosphere, azide **4-1** (0.80 g, 1.6 mmol, 1.0 eq) and alkyne **4-2** (1.50 g, 6.6 mmol, 4.1 eq) were dissolved in DMF (20 mL) and degassed under a stream of nitrogen in an ultrasonic bath for 15 min. Sodium ascorbate (1.31 g, 6.6 mmol, 4.1 eq) and CuI (0.42 g, 1.6 mmol, 1.0 eq) were then added and the mixture was stirred at room temperature for 20 h. The solvent was removed, and the residue was dissolved in CH_2Cl_2 and water. The organic phase was washed with brine and the combined aqueous solutions extracted with CH_2Cl_2 were dried with magnesium sulfate and concentrated under reduced pressure. The crude product was purified by column chromatography (eluent CyH / EtOAc, 1:1 $\rightarrow$ 0:1, v/v). After evaporation of the solvent, **4-3** was obtained as a yellowish solid.

Yield: 0.6 g (0.51 mmol, 32 %). M.p.: 180-220 °C. $\mathbf{R_f}$ (cyclohexane/EtOAc, 1:1): 0.05. **^{1}H NMR** (400 MHz, $CDCl_3$): δ = 8.94 (s, 3H, H-12), 8.73 (s, 6H, H-7), 8.16 (d, $^3J_{2,1}$ = 7.6 Hz, 6H, H-2), 8.13-8.03 (m, 12H, H-4+5), 7.99 (dd, $^3J_{1,2}$ = 7.6 Hz, 3H, H-1), 4.81 (br, 1H, H-24), 4.69 (s, 6H, H-

13), 3.90-3.81 (m, 4H, H-18/19/20/21), 3.79-3.74 (m, 2H, H-18/19/20/21), 3.74-3.64 (m, 2H, H-18/19/20/21), 3.42-3.33 (m, 2H, H-16), 3.32-3.27 (m, 2H, H-17), 3.27 3.19 (m, 2H, H-22), 3.18-3.01 (m, 4H, H-15+23), 1.36 (s, 9H, H-27) ppm. **^{13}C NMR** (100 MHz, $CDCl_3$): δ = 156.0 (C_q, C-25), 148.2 (C_q, C-11), 131.8 (C_q, C-8), 131.2 (C_q, C-6), 128.1 (CH, C-4), 127.9 (C_q, C-3), 127.5 (CH, C-5), 126.2 (CH, C-1), 125.4 (CH, C-2), 124.7 (C_q, C 9/10), 124.6 (C_q, C 9/10), 124.2 (CH, C-12), 122.1 (CH, C 7), 79.3 (C_q, C 26), 77.4 (CH, C-16), 70.8 (CH_2, C 17-22), 70.7 (CH_2, C 17-22), 70.6 (CH_2, C 17-22), 70.5 (CH_2, C-17-22), 70.1 (CH_2, C 17-22), 70.0 (CH_2, C 17-22), 68.3 (CH_2, C-15), 49.7 (CH_2, C-13), 46.5 (C_q, C-14), 40.2 (CH_2, C-23), 28. 5 (CH_3, C-27) ppm. **FT-IR (ATR):** $\tilde{\nu}$ = 3127 (w), 3039 (w), 2966 (w), 2868 (m), 1704 (vs), 1608 (m), 1504 (s), 1437 (s), 1365 (s), 1275 (m), 1245 (vs), 1170 (vs), 1137 (vs), 1095 (vs), 1040 (vs), 1006 (w), 962 (vw), 879 (vs), 839 (vs), 819 (vs), 759 (m), 727 (s), 706 (vs), 660 (m), 608 (w) cm^{-1}. **HRMS** (ESI,+): found: 1164.5000 $[M]^+$; calc. for $[M]^+$: 1164.5010.

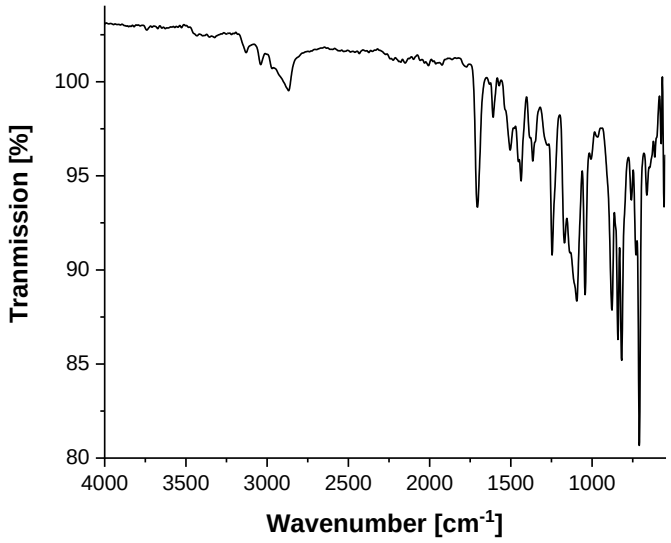

Figure S4-1. FT-IR ATR spectrum of *tert*-butyl (15-(4-(pyren-2-yl)-1H-1,2,3-triazol-1-yl)-14,14-bis((4-(pyren-2-yl)-1H-1,2,3-triazol-1-yl)methyl)-3,6,9,12-tetraoxapentadecyl)carbamate (**4-3**).

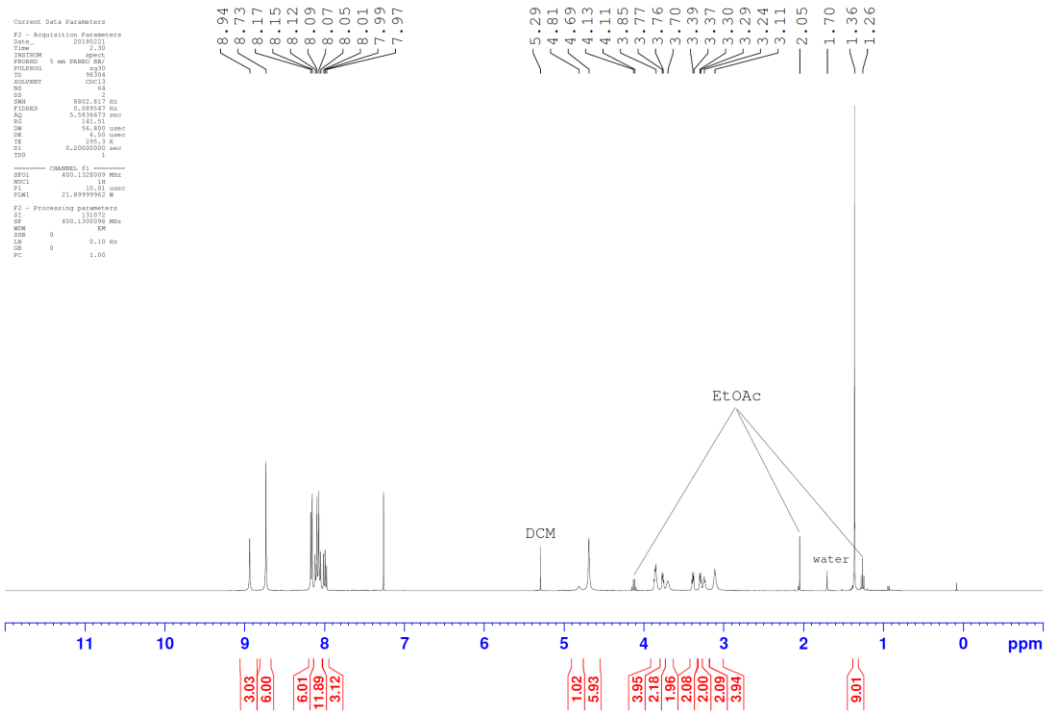

Figure S4-2. ^{1}H NMR spectrum of (15-(4-(pyren-2-yl)-1H-1,2,3-triazol-1-yl)-14,14-bis((4-(pyren-2-yl)-1H-1,2,3-triazol-1-yl)methyl)-3,6,9,12-tetraoxapentadecyl)carbamate (**4-3**).

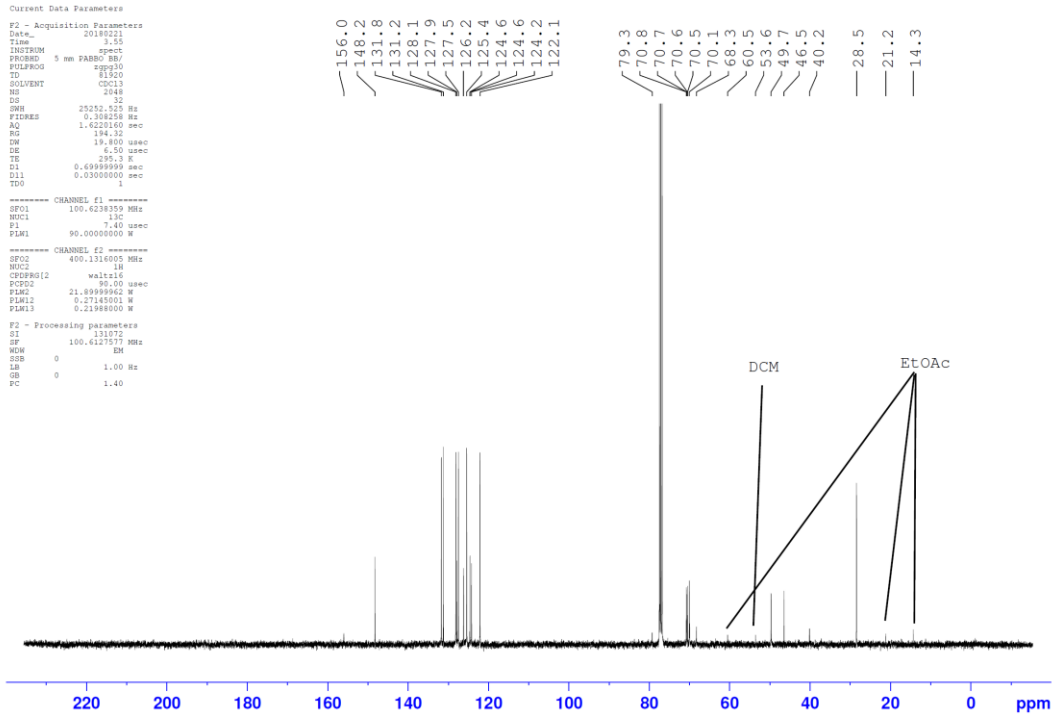

Figure S4-3. ^{13}C{^{1}H} NMR spectrum of (15-(4-(pyren-2-yl)-1H-1,2,3-triazol-1-yl)-14,14-bis((4-(pyren-2-yl)-1H-1,2,3-triazol-1-yl)methyl)-3,6,9,12-tetraoxapentadecyl)carbamate (**4-3**).

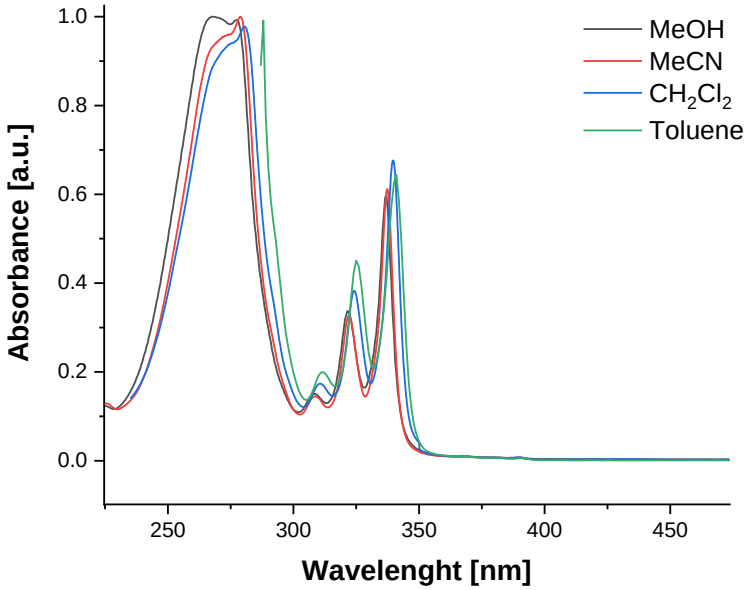

Figure S4-4. UV/Vis spectra of **4-3** in methanol, acetonitrile, dichloromethane and toluene (conc. = 4.29 x 10^{-6} mol L^{-1}).

7.3.2 Bindfit calculations

Snapshots of the data obtained from bindfit (http://app.supramolecular.org/bindfit/)

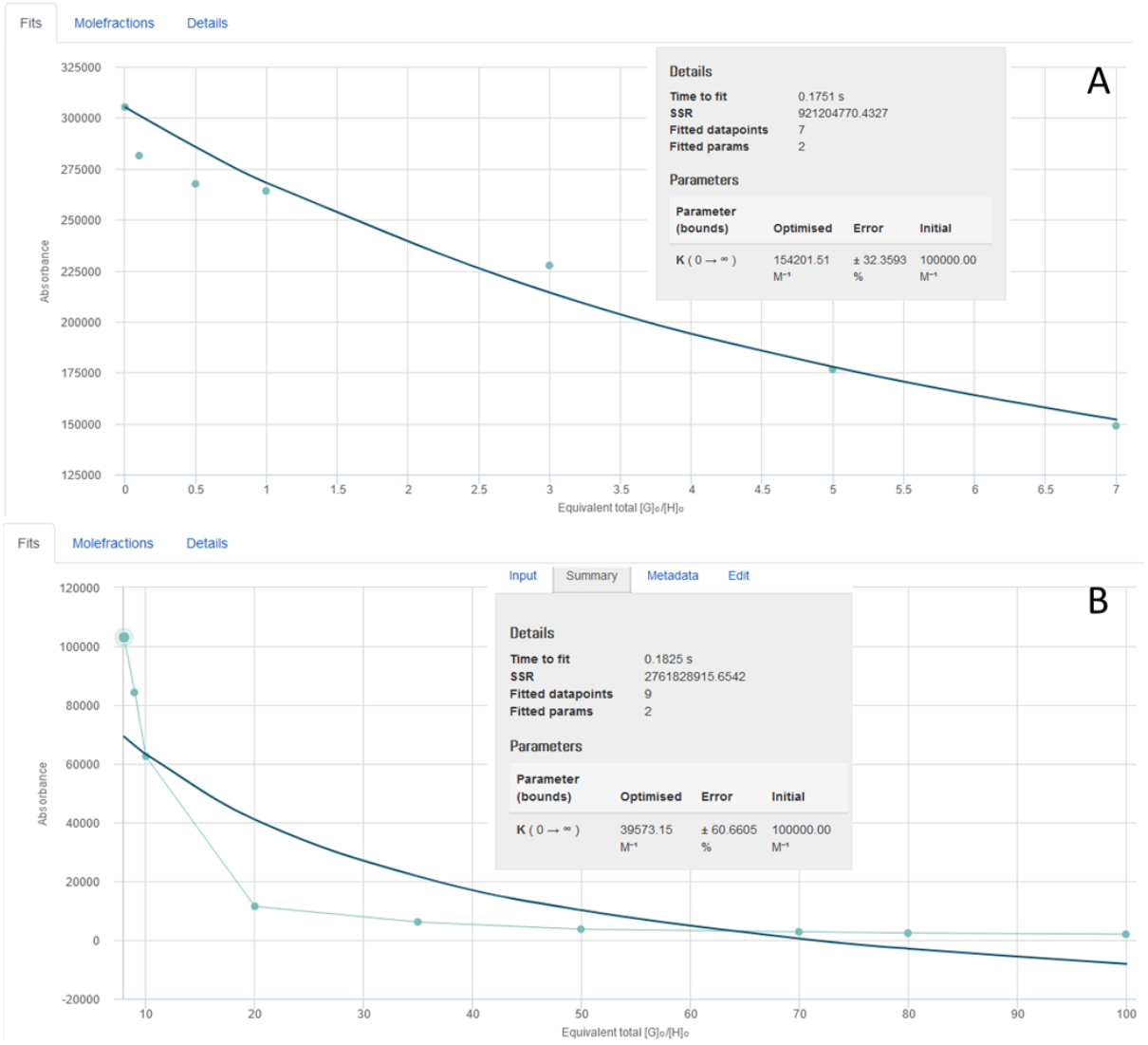

Figure S4-5. Bindfit plots for Cu^{2+}-titration for A) <10 eq, B) >10 eq using Nelder-Mead fit for 1:1 stoichiometry.

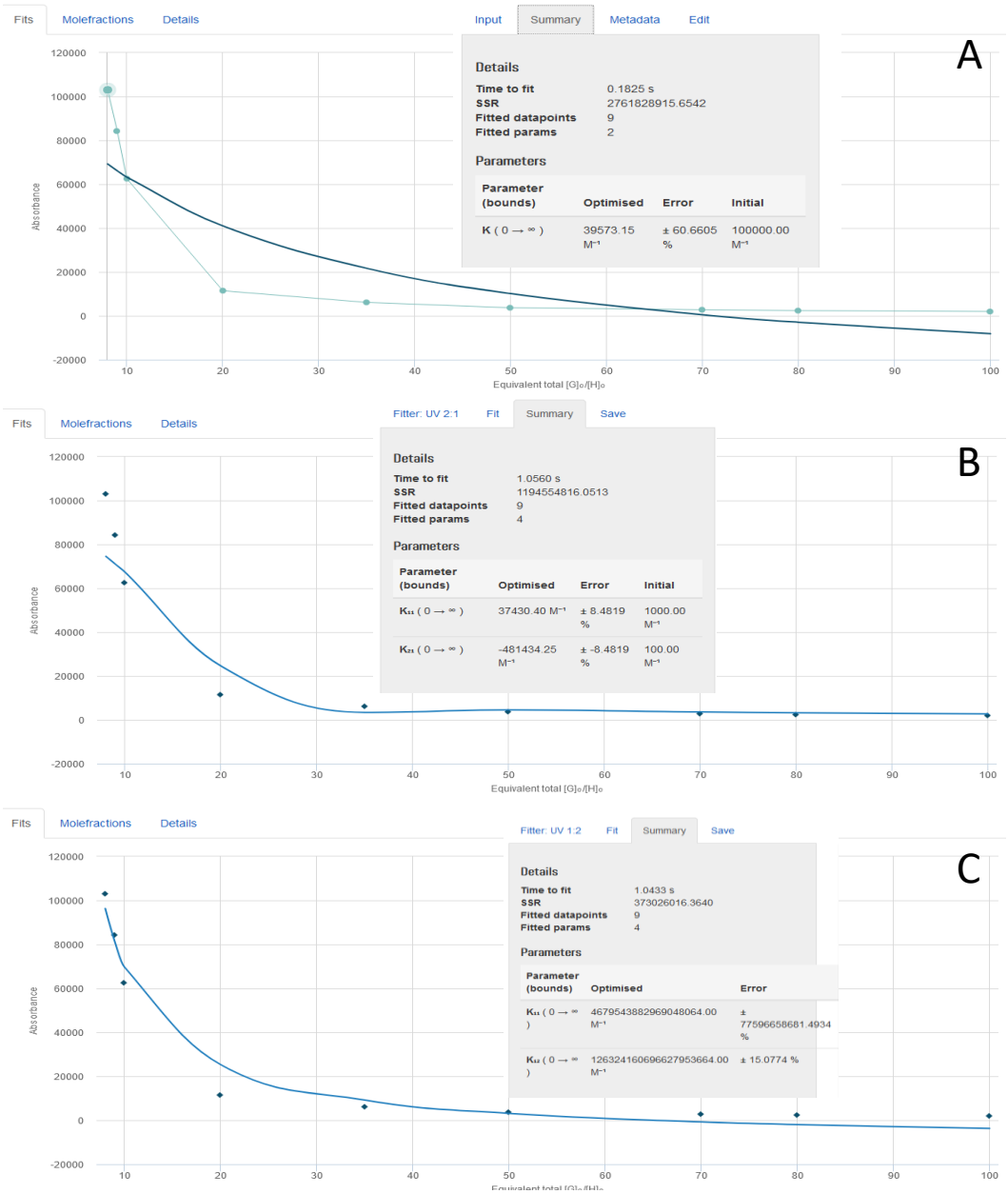

Figure S4-6. Bindfit plots for Cu^{2+}-titration for >10 eq A) 1:1, B) 2:1 C) 1:2 stoichiometry using Nelder-Mead fit resulting with negative K_{21} for 2:1 and K_{11} = 4.6 x 10^8 M^{-1} for 1:2 stoichiometry.

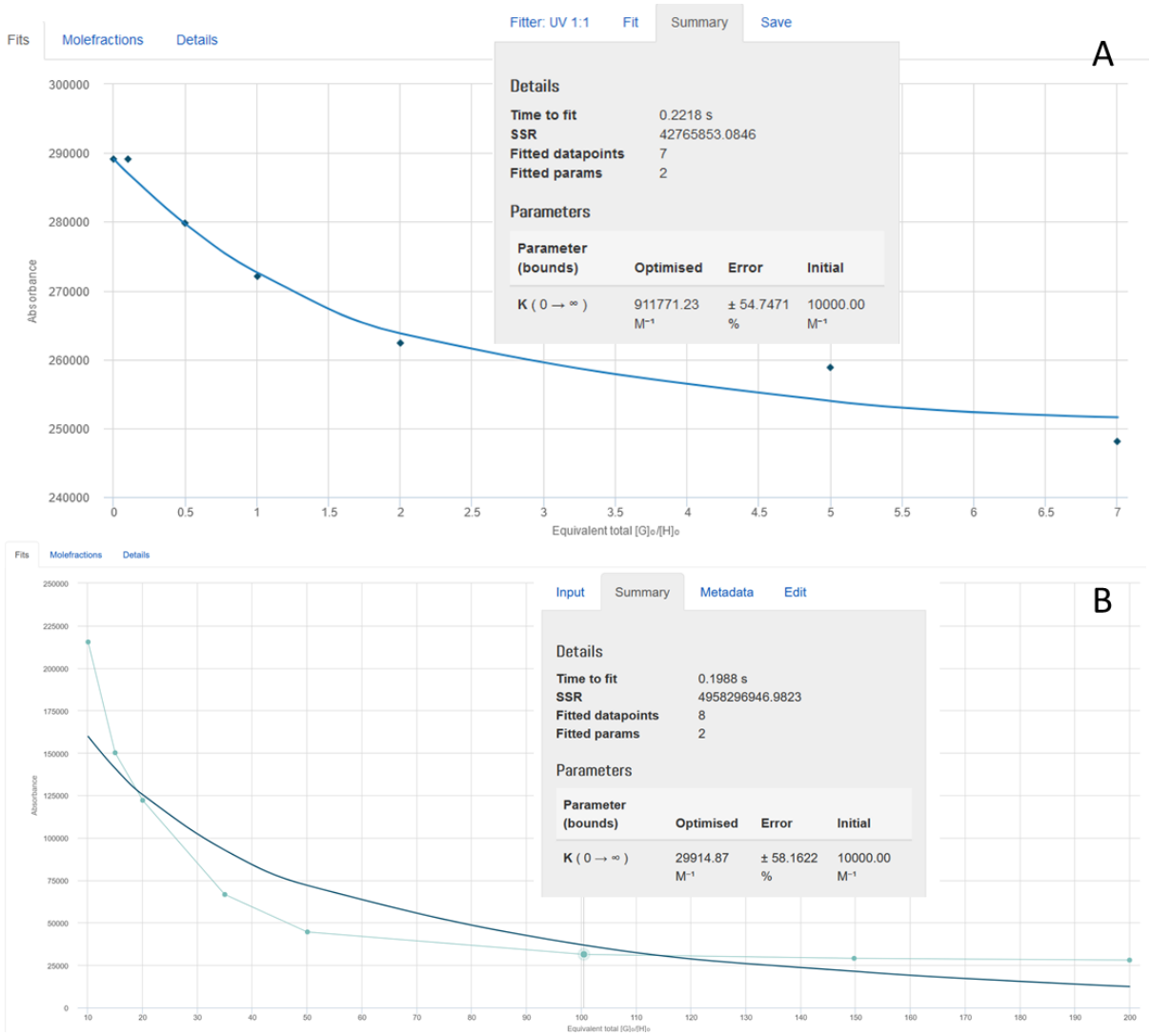

Figure S4-7. Bindfit plots for Hg^{2+}-titration for A) <10 eq, B) >10 eq using Nelder-Mead fit for 1:1 stoichiometry.

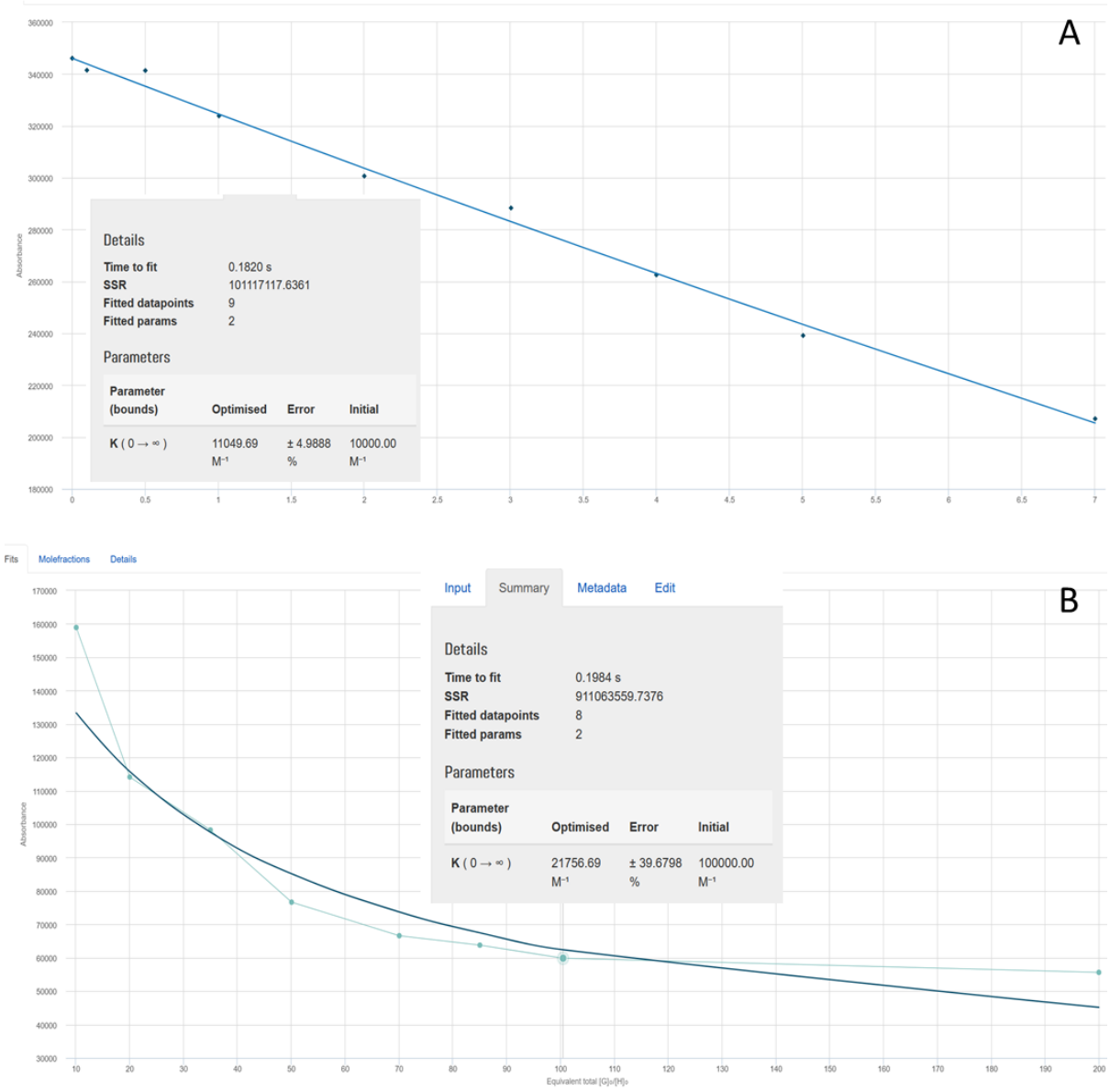

Figure S4-8. Bindfit plots for Pb^{2+}-titration for A) <10 eq, B) >10 eq using Nelder-Mead fit for 1:1 stoichiometry.

7.3.3 Dynamic Light Scattering Measurements

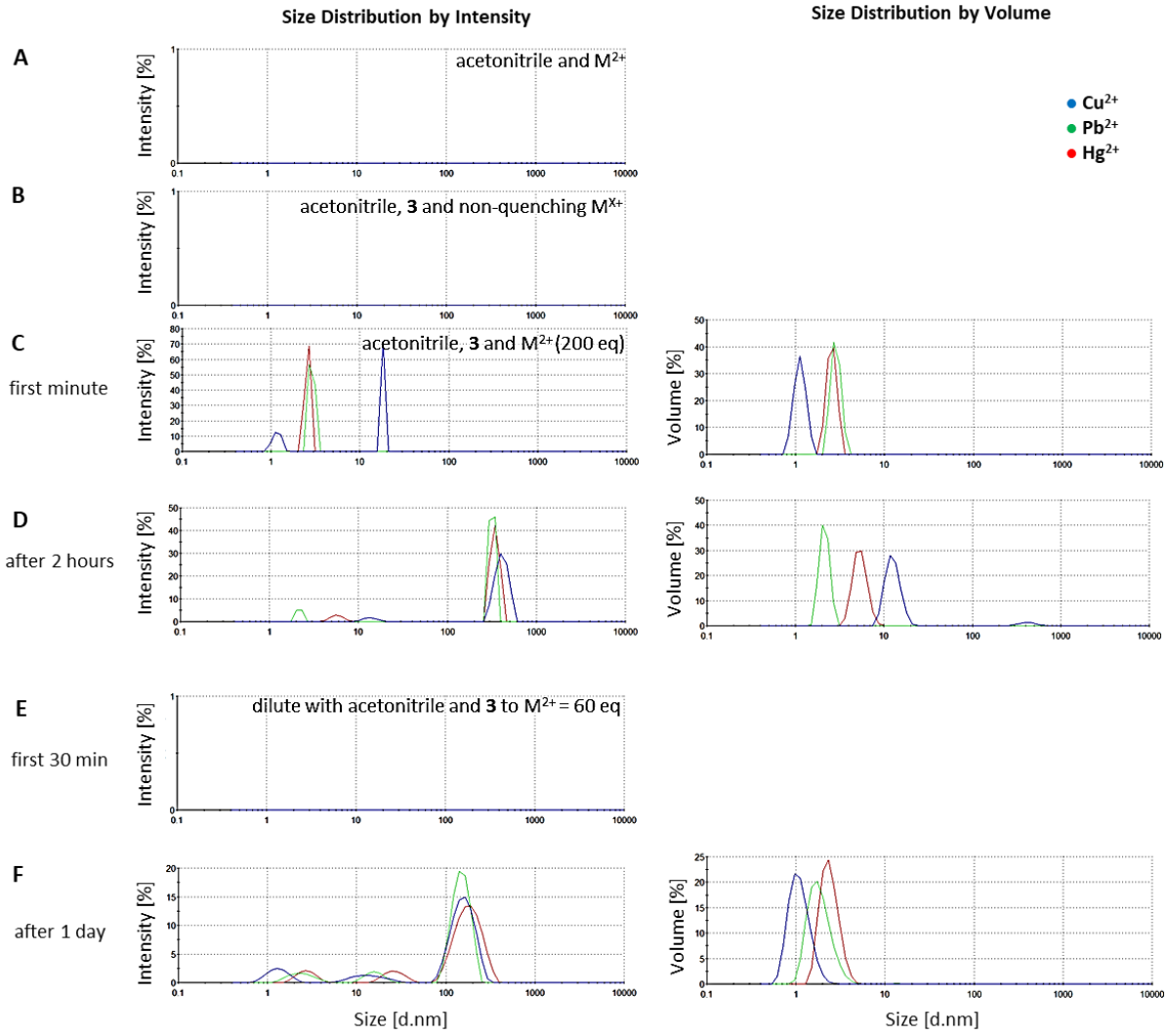

Figure S4-9. DLS size measurement (diameter) in acetonitrile with A) perchlorate salts, B) chemosensor and non-quenching perchlorate salts, C) first minute of chemosensor **4-3** (5×10^{-6} mol L^{-1}, 1 eq) in presence of 200 eq M^{2+}, D) after 2 hours, E) first 30 minutes of diluted mixture with sensor **3**, acetonitrile and 60 eq M^{2+}, F) after one day.

7.3.4 Titration Results

Benesi-Hildebrand-Plot

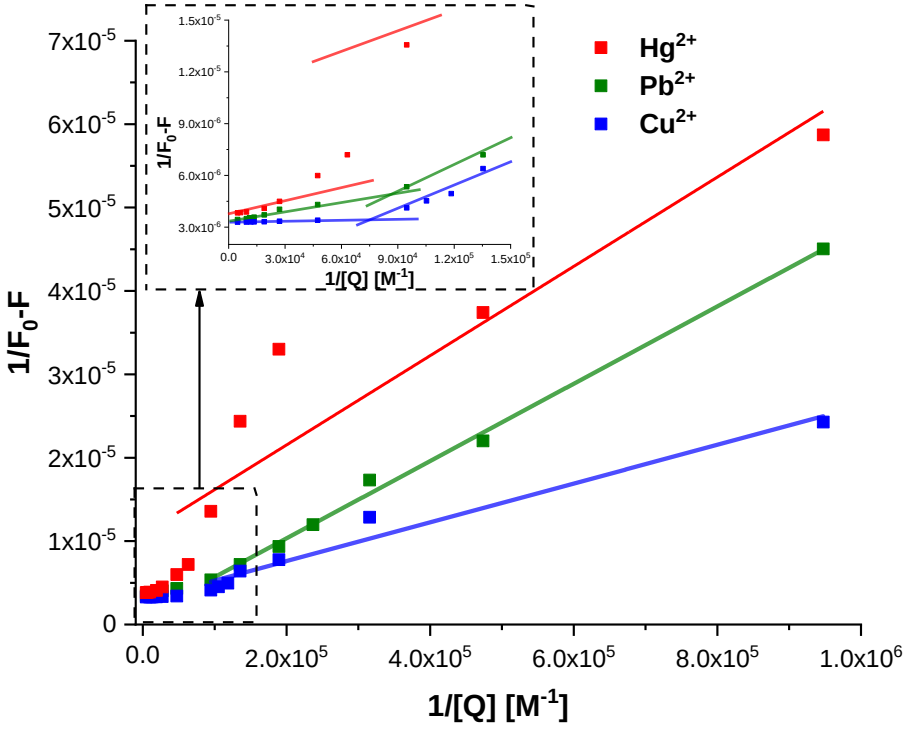

Figure S4-10. Double reciprocal Benesi-Hildebrand plot of Cu^{2+} (blue), Pb^{2+} (green) and Hg^{2+} (red) titration to **4-3** with partial regression line for 0-10 eq and 10-200 eq. Inset: zoomed area for 10–200 eq.

The binding constants of the BH-plot and the bindfit methods differ greatly. Because the BH method is only suitable for linear plots, it is not suitable for mixed quenching mechanisms as present here. All linear approximations required for the BH plot ignore the non-linear progression of the values and lead to unsatisfactory results. This is particularly noticeable for the course of the titration with Hg^{2+}, in the range from 0-10 eq, in which the best linear fit does not even comprise any of the experimental values.

^{1}H-NMR-Titration

NMR titration experiments in DMSO-d_6 to investigate the ^{1}H-NMR shifts upon addition of the three quenchers.

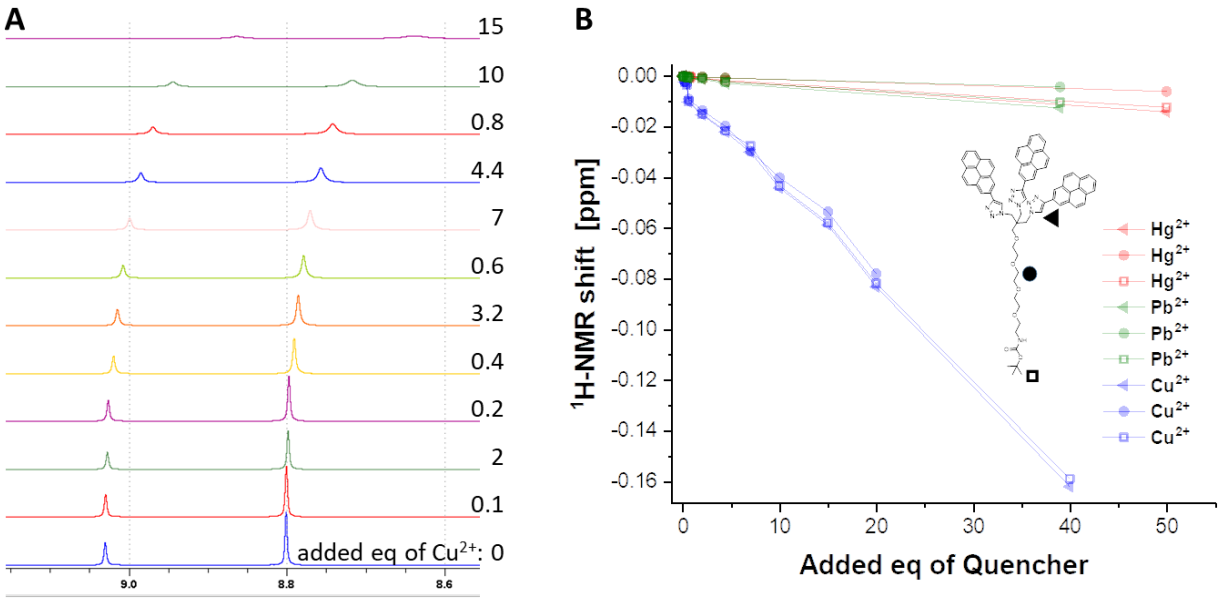

Figure S4-11. ^{1}H NMR titration results: A) with Cu^{2+} as observed for the aromatic proton signals of pyrene (7-H, 9.2 ppm) and triazole (8.8 ppm), B) the plot of the respective protons shift of the triazole (triangle), the TEG-CH_2 (circle) and the CH_3 of the Boc group (square) for the respective metal ions.

After the addition of Cu^{2+} (Figure S12, left) the signals not only begin to shift evenly, but also become broader and smaller, which makes it difficult to interpret the spectra from 20 eq Cu^{2+}. Unfortunately, the data show (Figure S12, right) a very linear course without any saturation, which does not allow a calculation of the binding constant. However, the NMR experiments clearly support the results from the fluorescence experiments that Cu^{2+} changes the physical properties of **4-3** most strongly. It is clearly shown by the small difference in the shift, that the triazole proton (star) is always the most shifted, followed by the protons of the Boc-protective group (square) and the CH_2-backbone of the TEG chain (circle). This information suggests that the interaction between **4-3** and the metal ion, as shown in Scheme 1, occurs with the whole molecule.

Screening Experiments using Different Non-Perchlorate Salts

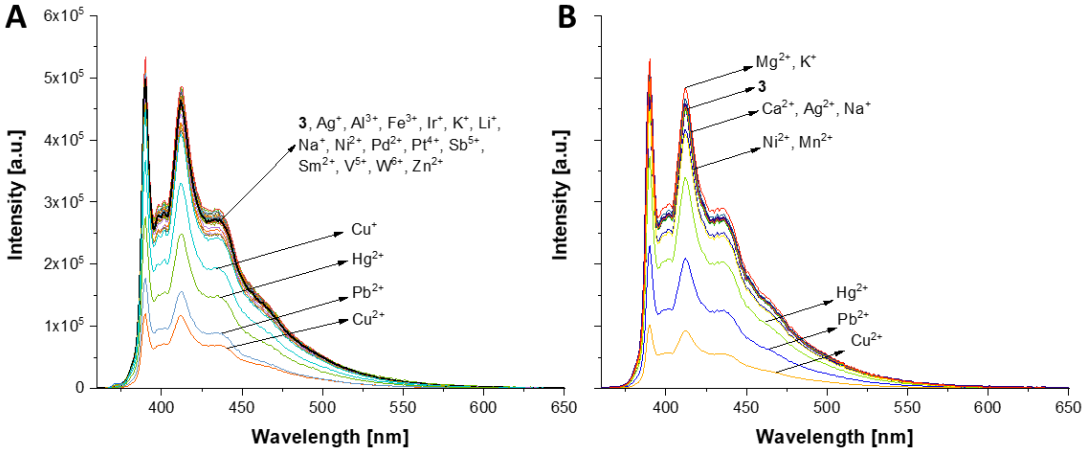

Figure S4-12. A) Fluorescence spectra in acetonitrile of sensor **4-3** in the presence of 10 eq of the following salts: $AgNO_3$, $AlCl_3$, $FeCl_3$, $C_{18}H_{30}Ir_2O_2$, CuI, $CuOAc_2$, $HgOAc_2$, KOH, KI, LiOH, LiAc, NaOH, NaI, $NiBr_2$, $PbOAc_2$, $PdAc_2$, $PdCl_2$, $PtCl_6H_2$, $(BrC_6H_4)_3NSbCl_6$, SmI_2, VOF_3, $H_2Na_6O_{40}W_{12}$, $ZnCl_2$ and B) respective perchlorate salts.

Magnification of Figure 4-2A

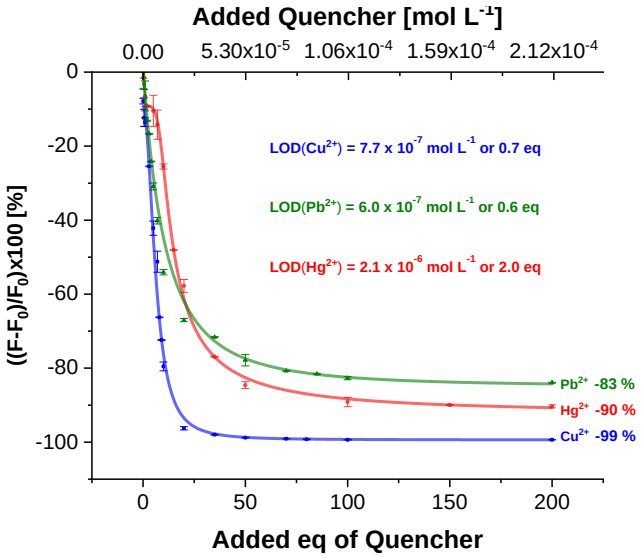

Figure S4-13. Magnification of Figure 2 A (Fluorescence titration spectra of sensor **4-3** at 1.02 x 10^{-6} mol L^{-1} with the quencher ions Cu^{2+}(blue), Pb^{2+} (green) and Hg^{2+} (red), with error bars given for all data points).

7.4 Chapter 5 - Supporting Information

The following section is slightly modified and reproduced from the manuscript of V. Merz, J. Merz, T. B. Marder, A. Krueger.

Initial fluorescence measurement indicated the formation of excimers as indicated by the strong intensity band around 470 nm in the fluorescence spectrum (see **Figure S5-1**).

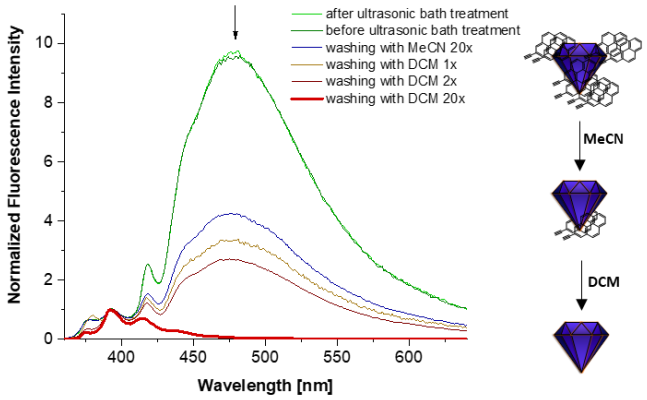

Figure S5-1. Normalized fluorescence spectrum of the washing process of the samples before the titration measurement in doubly distilled water.

However, it was found that this excimer band originated from unreacted 2-ethynyl pyrene **5-2** adsorbed on the ND surface. The triply pyrene functionalized head groups of sensor **5-3** do not show this excimer emission due to the sterically demanding spatial arrangement of the pyrenes. Normally, the concentration of unreacted **5-2** should have been reduced to a minimum using the established purification protocol. To remove the adsorbed pyrene **5-2**, the obtained sample of **5-3** was dispersed in warm acetonitrile and DCM (about 30-40 ° C) respectively in an ultrasonic bath for 30 min and subsequently centrifuged. The purified precipitate was then washed again with acetone and water and fluorescence measurements were carried out in double-distilled water under an argon atmosphere. Dispersing in an ultrasonic bath in water is

not sufficient to remove the residual **5-2** (**Figure S5-1** green spectrum). Washing with MeCN halved the intensity of the excimer band after 20 washes, and subsequent washing with DCM caused the excimer band to disappear. The protocol was therefore modified to ensure the complete removal of residual 2 by the conformation of the absence of the excimer band.

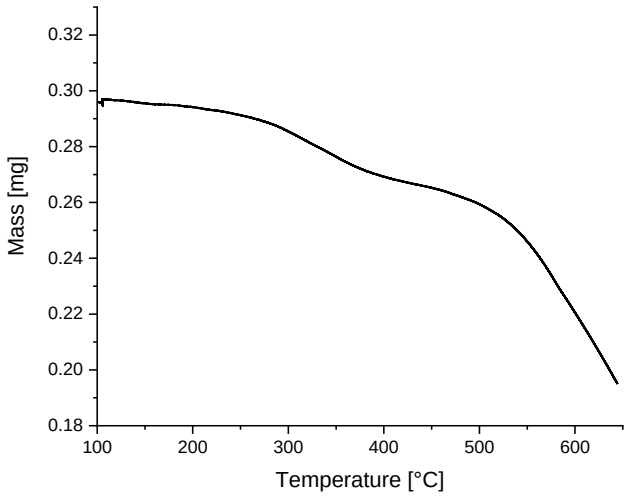

Figure S5-2: Thermogravimetric analysis of ND **3**

Snapshots of the data obtained from bindfit (http://app.supramolecular.org/bindfit/)

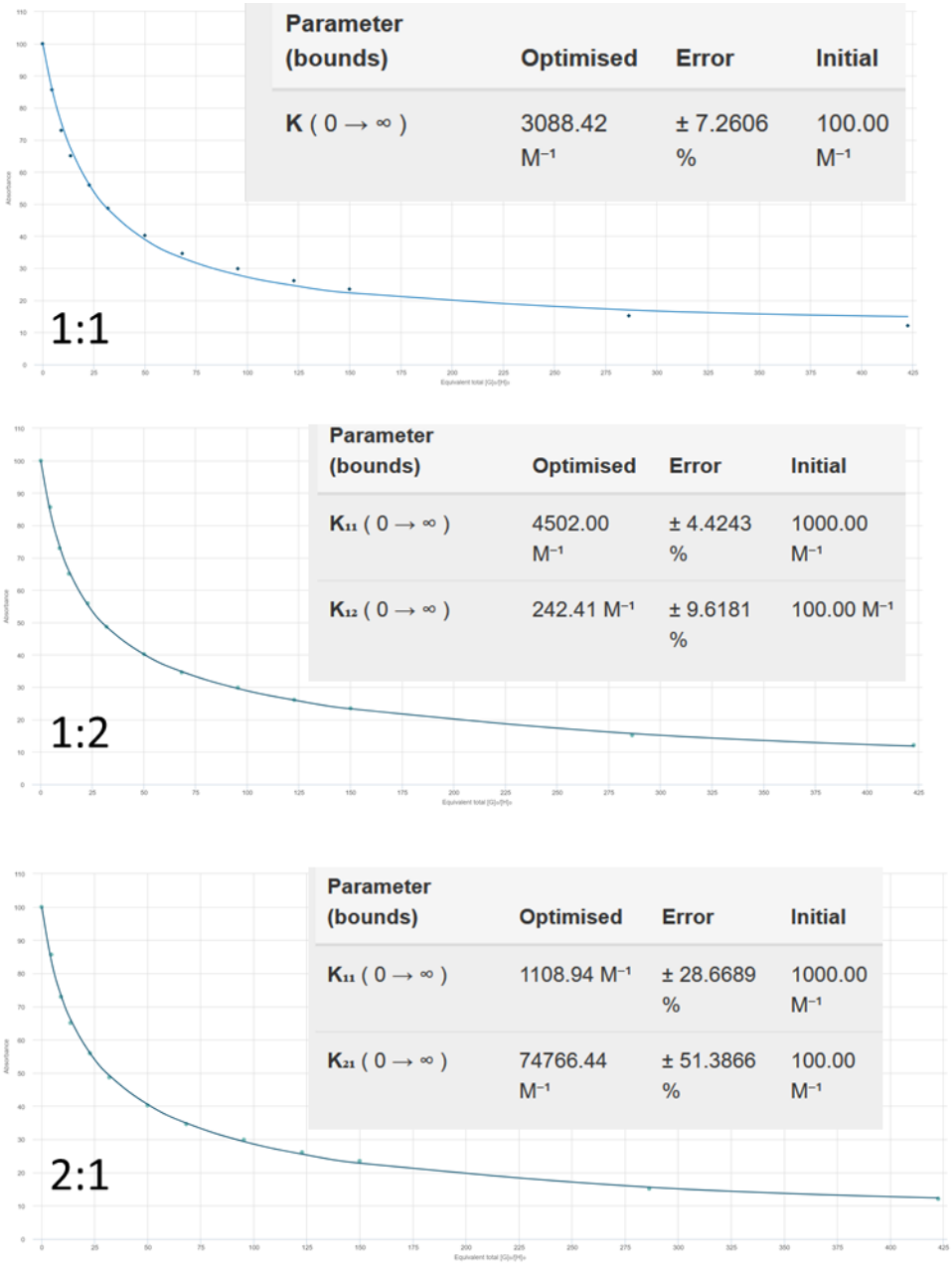

Figure S5-3: Bindfit plots for Cu^{2+}-titration using Nelder-Mead fit for 1:1, 1:2 and 2:1 stoichiometry.

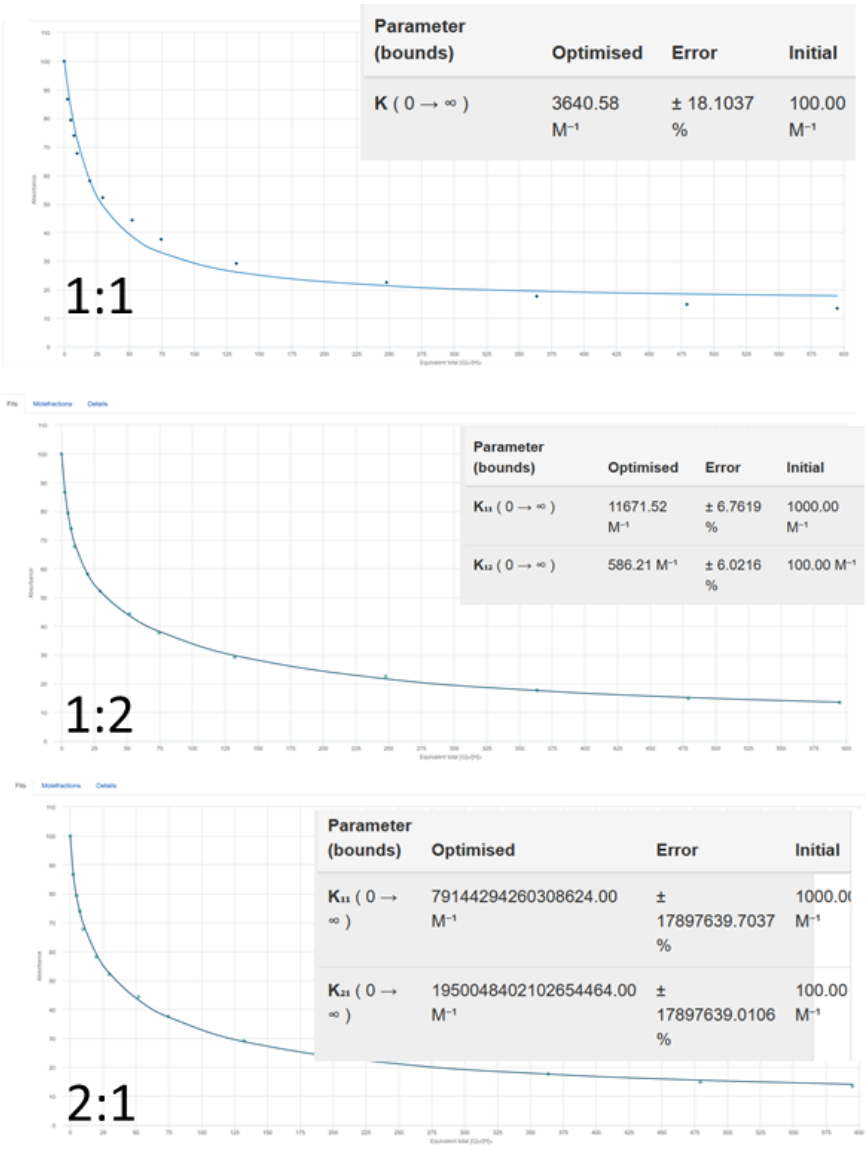

Figure S5-4: Bindfit plots for Pb^{2+}-titration using Nelder-Mead fit for 1:1, 1:2 and 2:1 stoichiometry.

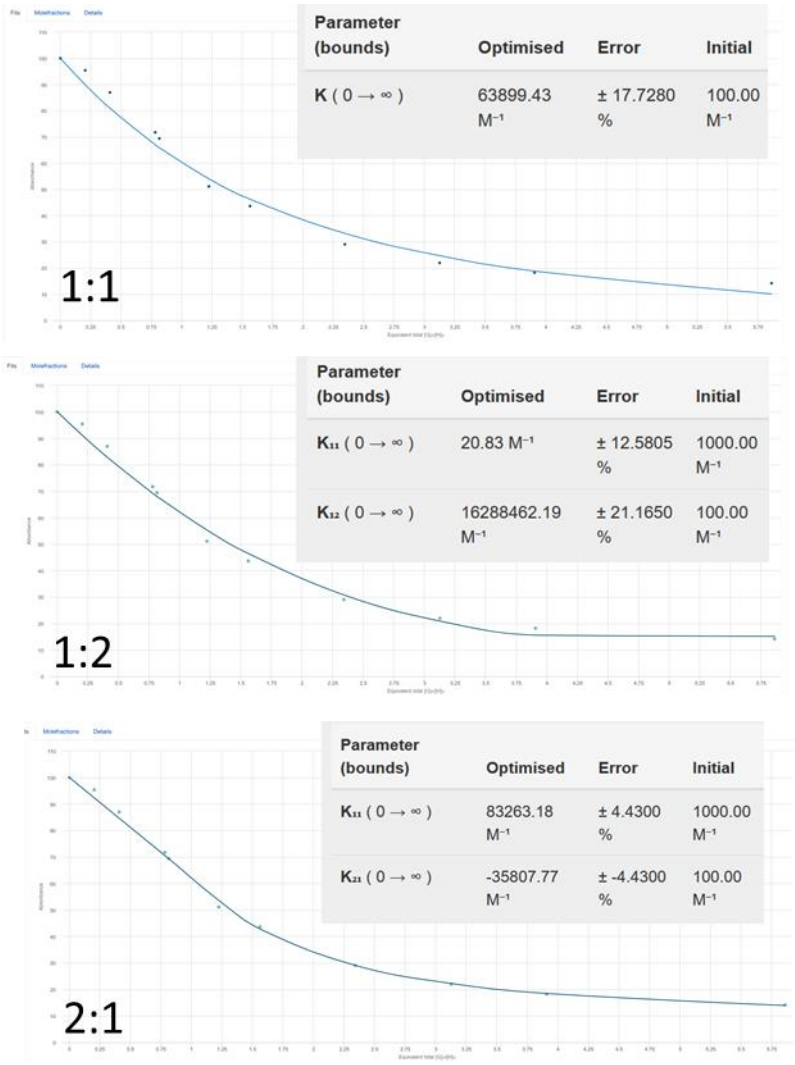

Figure S5-5: Bindfit plots for Hg^{2+}-titration using Nelder-Mead fit for 1:1, 1:2 and 2:1 stoichiometry.

Erklärung zur Autorenschaft

Titel der Dissertation: Functionalization and Investigation of Nanodiamonds for Biomedical- and Sensor Applications, Titel der Publikation: Zwitterion-Functionalized Detonation Nanodiamond with Superior Protein Repulsion and Colloidal Stability in Physiological Media, V. Merz, J. Lenhart, Y. Vonhausen, M. E. Ortiz-Soto, J Seibel, A. Krueger, *Small* **2019**, 15, 1901551

Viktor Merz (VM), Julian Lenhart (JL), Yvonne Vonhausen (YV), Maria E. Ortiz-Soto (MEOS), Jürgen Seibel (JS), Anke Krueger (AK),

Autor	VM	JL	YV	MEOS	JS	AK
Konzeptionierung des Forschungsprojektes	X					X
Synthese der organischen Verbindungen	X	X	X			
Charakterisierung der organischen Verbindungen	X	X	X			
Funktionalisierung der Nanodiamanten	X					
Charakterisierung der Nanodiamant-Proben	X					
Untersuchungen der kolloidalen Stabilität	X					
Auswertung der Ergebnisse	X					
Diskussion der Ergebnisse	X			X		X
Grafische Auftragung und Formatierung der Ergebnisse für die Publikation	X					
Planung der Bakterienexperimente	X			X	X	X
Durchführung und Auswertung der Bakterienexperimente				X		
Verfassen der Veröffentlichung	X			X		X
Korrektur der Veröffentlichung	X				X	X
Koordination der Veröffentlichung						X

Die Mitautoren der in dieser (teil-)kumulativen Dissertation verwendeten Manuskripte sind sowohl über die Nutzung als auch über die angegebenen Eigenanteile informiert und stimmen dem zu.

Autor 1 (Viktor Merz) **Hauptautor/in** ☐ Verweis: E-Mail hinterlegt	Autor 2 (Julian Lenhart) **Koautor/in** ☒ Verweis: E-Mail hinterlegt	Autorin 3 (Yvonne Vonhausen) **Koautor/in** ☒ Verweis: E-Mail hinterlegt
Autorin 4 (Maria E. Ortiz-Soto) **Koautor/in** ☒ Verweis: E-Mail hinterlegt	Autor 5 (Jürgen Seibel) **Koautor/in** ☒ Verweis: E-Mail hinterlegt	Autorin 6 (Anke Krueger) **Korrespondenzautor/in** ☐ Verweis: E-Mail hinterlegt

Würzburg, 30.04.2021 _____(Datum)

Prof. Dr. Anke Krueger (Betreuerin)

Titel der Dissertation: Functionalization and Investigation of Nanodiamonds for Biomedical- and Sensor Applications, Titel der Publikation: Pyrene-Based "Turn-Off" Probe with Broad Detection Range for Cu^{2+}, Pb^{2+} and Hg^{2+} Ions, V. Merz, J. Merz, M. Kirchner, J. Lenhart, T. B. Marder, A. Krueger, *Chem. Eur. J.* **2021**, *27*, 8118–8126

Viktor Merz (VM), Julia Merz (JM), Maximilian Kirchner (MK), Julian Lenhart (JL), Todd B. Marder (TBM), Anke Krueger (AK),

Autor	VM	JM	MK	JL	TBM	AK
Konzeptionierung des Forschungsprojektes	X	X				X
Synthese der organischen Verbindungen	X		X	X		
Charakterisierung der organischen Verbindungen	X					
Fluoreszenz-Titrationen mit dem Sensor	X	X		X		
NMR-Titrationen mit dem Sensor	X					
Auswertung der Ergebnisse	X					
Diskussion der Ergebnisse	X	X				X
Grafische Auftragung und Formatierung der Ergebnisse für die Publikation	X					
Verfassen der Veröffentlichung	X	X				X
Korrektur der Veröffentlichung	X	X			X	X
Koordination der Veröffentlichung						X

Die Mitautoren der in dieser (teil-)kumulativen Dissertation verwendeten Manuskripte sind sowohl über die Nutzung als auch über die angegebenen Eigenanteile informiert und stimmen dem zu.

Autor 1 (Viktor Merz) **Hauptautor/in** ☐ Verweis: E-Mail hinterlegt	Autorin 2 (Julia Merz) **Koautor/in** ☐ Verweis: E-Mail hinterlegt	Autor 3 (Maximilian Kirchner) **Koautor/in** ☒ Verweis: E-Mail hinterlegt
Autor 4 (Julian Lenhart) **Koautor/in** ☒ Verweis: E-Mail hinterlegt	Autor 5 (Todd B. Marder) **Koautor/in** ☒ Verweis: E-Mail hinterlegt	Autorin 6 (Anke Krueger) **Korrespondenzautor/in** ☐ Verweis: E-Mail hinterlegt

Würzburg, 30.07.2021 _____

(Datum) Prof. Dr. Anke Krueger (Betreuerin)

Affidavit

I hereby confirm that my theses entitled "***Functionalization and Investigation of Nanodiamonds for Biomedical and Sensor Applications***" is the result of my own work. I did not receive any help or support from commercial consultants. All sources and/or materials applied are listed and specified in the thesis. Furthermore, I confirm that this thesis has not yet been submitted as part of another examination process neither in identical nor similar form.

Würzburg, 30.07.2021

_____

Signature

Eidesstaatliche Erklärung

Hiermit erkläre ich an Eides statt, die Dissertation „***Functionalization and Investigation of Nanodiamonds for Biomedical and Sensor Applications***" eigenständig, d.h. insbesondere selbstständig und ohne Hilfe eines kommerziellen Promotionsberaters angefertigt und keinen anderen als die von mir angegebenen Quellen und Hilfsmittel verwendet zu haben. Ich erkläre außerdem, dass die Dissertation weder in gleicher noch ähnlicher Form bereits in einem anderen Prüfungsverfahren vorgelegen hat.

Würzburg, 30.07.2021

_____

Unterschrift